Modelling charge-sign dependent modulation of cosmic rays in the heliosphere

EE Vos

20068034

Thesis submitted for the degree *Philosophiae Doctor* in Space Physics at the Potchefstroom Campus of the North-West University

Promoter: Prof MS Potgieter

October 2016

North-West University

Doctoral Thesis

Modelling charge-sign dependent modulation of cosmic rays in the heliosphere

Author:
EE Vos

Promoter:
MS Potgieter

October 2016

To Jana – my wife, companion and best friend.

"The important thing is not to stop questioning.
Curiosity has its own reason for existing."
– Albert Einstein

Abstract

The solar minimum of cycle 23/24 has seen exceptionally quiet levels of solar activity and heliospheric modulation, which resulted in the highest cosmic ray (CR) spectrum ever recorded at Earth in December 2009 by the PAMELA detector. This solar minimum has been extensively observed by PAMELA in terms of CR intensities and presents a unique opportunity to study the heliosphere in light of CR modulation. A three-dimensional numerical model was used to simulate the transport and modulation of CRs, with the aim of reproducing a selection of PAMELA proton, electron and positron energy spectra, taken during the 2006 to 2009 minimum period. In doing so, various improvements were made to the model, such as using a new Smith-Bieber modification for the heliospheric magnetic field and utilizing the parallel computing capability of the graphics processing unit (GPU). New local interstellar proton, electron and positron spectra were also constructed using PAMELA, AMS-02 and Voyager 1 measurements as constraints over certain energy ranges, in addition to GALPROP solutions. A key objective of this study was to uncover and investigate the effects that drifts had on CRs, which present itself as charge-sign dependent modulation. Since the PAMELA and Ulysses missions overlapped between mid-2006 and mid-2009, simultaneous measurements from these were used to calculate the global radial and latitudinal gradients for protons in the inner heliosphere. Negative latitudinal gradients were found ($-0.05 \pm 0.01\,\%/^\circ$ at 1.63 GV), which is a consequence of charge-sign dependent modulation and indicative of the drift patterns experienced by positively charged CRs during an $A < 0$ solar polarity cycle. A comparative study revealed that the intensities of positively charged CRs increased significantly more from 2006 to 2009 than the negatively charged CR component – a result that can only be explained with drift theory. All of these characteristic signatures of charge-sign dependent modulation were reproduced through modelling, which subsequently facilitated a comprehensive study of drifts at energies beyond the observable ranges of PAMELA and AMS-02. In essence, this work provides substantial proof that all modulation processes played a role during the minimum period of cycle 23/24 and contributed to the observed energy spectra, including drifts.

Keywords: Cosmic rays, numerical modelling, heliosphere, modulation, particle drifts, particle diffusion, solar minimum, galactic protons, galactic electrons, galactic positrons.

Opsomming

Die son-minimum van siklus 23/24 het buitengewone stil vlakke van sonaktiwiteit en heliosferiese modulasie getoon, wat gelei het tot die hoogste kosmiese strale (KSe) spektrum wat al ooit aangeteken was by die Aarde in Desember 2009 deur die PAMELA detektor. Hierdie son-minimum is op groot skaal waargeneem deur PAMELA in terme van KS intensiteite, en bied 'n unieke geleentheid om die heliosfeer te bestudeer wat betref KS modulasie. 'n Drie-dimensionele numeriese model is gebruik om die transport en modulasie van KSe te simuleer, met die doel om 'n seleksie van PAMELA proton, elektron en positron energie spektra, waargeneem gedurende die 2006 tot 2009 minimum periode, te herproduseer. Sodoende is verskeie verbeteringe tot die model aangebring, soos om 'n nuwe Smith-Bieber modifikasie vir die heliosferiese magneetveld te gebruik en om die parallele berekeningsvermoë van die grafiese verwerkingseenheid te benuttig. Nuwe lokale interstellêre proton, elektron en positron spektra is ook gekonstrueer deur PAMELA, AMS-02 en Voyager 1 metings te gebruik as beperkings oor sekere energie gebiede, bykomend tot GALPROP oplossings. 'n Belangrike doelwit van hierdie studie is om die effekte wat dryf op KSe het, wat voorkom as ladings-afhanklike modulasie, bloot te lê en te ondersoek. Omdat die PAMELA en Ulysses missies geoorvleul het vanaf middel-2006 tot middel-2009, is gelyktydige metings van hierdie instrumente gebruik om die globale radiale en breedtegraad gradiënte van protone in die binneste heliosfeer te bereken. Negatiewe breedtegraad gradiente is gevind ($-0.05 \pm 0.01\,\%/^\circ$ by $1.63\,\mathrm{GV}$), wat 'n gevolg is van ladings-afhanklike modulasie en 'n aanduiding van die dryf patrone wat positief gelaaide KSe ervaar gedurende 'n $A < 0$ son-polariteit siklus. 'n Vergelykende studie het getoon dat die intensiteite van positief gelaaide KSe aansienlik meer toegeneem het vanaf 2006 tot 2009 as die negatief gelaaide KS komponent – 'n resultaat wat slegs met dryf teorie verklaar kan word. Al hierdie kenmerkende eienskappe van ladings-afhanklike modulasie is bevredigend gesimuleer deur modellering, wat gevolglik gehelp het om dryf by energieë buite die waarneembare grense van PAMELA en AMS-02 volledig te bestudeer. In wese verskaf hierdie werk aansienlike bewyse dat alle modulasie prosesse 'n rol gespeel het gedurende die minimum periode van siklus 23/24, en bygedra het tot die waargenome energie spektra, insluitend dryf.

Sleutelwoorde: Kosmiese strale, numeriese modellering, heliosfeer, modulasie, deeltjie dryf, deeltjie diffusie, sonaktiwiteit, galaktiese protone, galaktiese elektrone, galaktiese positrone.

Contents

Nomenclature

1D	One-Dimensional
2D	Two-Dimensional
3D	Three-Dimensional
ACR	Anomalous Cosmic Ray
ADI	Alternating Direction Implicit
API	Application Programming Interface
BS	Bow Shock
CIR	Corotating Interaction Region
CPU	Central Processing Unit
CR	Cosmic Ray
CUDA	Compute Unified Device Architecture
DC	Diffusion Coefficient
FLS	Fast Latitude Scan
GCR	Galactic Cosmic Ray
GPU	Graphics Processing Unit
HCS	Heliospheric Current Sheet
HMF	Heliospheric Magnetic Field
HP	Heliopause
ISM	Interstellar Medium
LIS	Local Interstellar Spectrum
LISM	Local Interstellar Medium
MF	Modulation Factor
MFP	Mean Free Path
MHD	Magnetohydrodynamic
NLGC	Non-Linear Guiding Center
NM	Neutron Monitor
QLT	Quasi-Linear Theory
SDE	Stochastic Differential Equation
SEP	Solar Energetic Particle
SSN	Sunspot Number
SW	Solar Wind

TPE	Transport Equation
TS	Termination Shock

Chapter 1

Introduction

When galactic cosmic rays (GCRs) enter the heliosphere, they are subject to various modulation processes that govern their transport. While in the heliosphere, the energy-dependent intensities of these cosmic rays (CRs) are decreased through their interaction with the solar wind (SW) and the heliospheric magnetic field (HMF), a process referred to as heliospheric modulation. Numerical models are generally used to solve the Parker transport equation (TPE) – an equation that combines all of the modulation processes and describes the transport of CRs (*Parker*, 1965) – in order to obtain energy spectra of CR intensities at Earth and throughout the heliosphere. CRs and numerical models are indirectly used in this way as a probe to study the heliosphere and the physics associated with heliospheric modulation. However, *in situ* measurements of CR intensities are required for comparison and validation of numerical results.

The goal of this work is to study the heliospheric modulation of GCR particles and antiparticles during the recent unique solar minimum of cycle 23/24, for the time period between 2006 and 2009. This is done using a comprehensive three-dimensional (3D) numerical model, which includes all of the important modulation processes in the heliosphere, in combination with measurements from the Earth-orbiting satellite detector, PAMELA (a Payload for Antimatter Matter Exploration and Light-nuclei Astrophysics). Measurements of CR intensities from Ulysses and the Voyager spacecraft are also used for comparison with model predictions. Global radial and latitudinal gradients in the inner heliosphere are studied by combining measurements from Ulysses and PAMELA for the time during which these missions overlapped.

According to drift theory, charged CRs are known to undergo unique drift patterns in the presence of the HMF. An important consequence of drifts is that oppositely charged particles experience drift motions in opposite directions, a phenomenon referred to as charge-sign dependent modulation, and a key theme of this study. The subsequent modulation caused by drifts therefore leads to characteristic "signatures", or features, that are reflected in the intensities of CRs. Between 2006 and 2009, PAMELA took simultaneous measurements of both positive and negatively charged CRs and thereby

observed the effects of drifts on CRs for both drift directions. In this study, it is shown that characteristic drift features are clearly observable in PAMELA measurements and can be successfully reproduced through modelling. These results provide strong evidence that points toward the presence of gradient, curvature and current sheet drifts in the heliosphere during the solar minimum period of cycle 23/24. Insights gained from this study will shed light on how this unique solar minimum developed.

This study is arranged in the following chapters:

Chapter 2 is devoted to introductory discussions of the physics related to CRs and the heliosphere in general. Topics like the major populations of CRs, the structure and features of the heliosphere, as well as the Sun and its contribution to the observed $\sim$ 11-year and $\sim$ 22-year solar activity cycles are covered. Overviews are given of the SW, the termination shock (TS), the HMF and the heliospheric current sheet (HCS). Neutron monitor (NM) counts are used to show how drifts along the HCS influence CR intensities over solar cycles. Brief discussions of the PAMELA, Ulysses, Voyager, and AMS-02 missions are given.

The modulation model used in this study is discussed in detail in **Chapter 3**, along with the Parker TPE and the underlying numerical scheme that is used to solve the TPE. Diffusion and drift theories are explained, and it is shown how these modulation processes are applied in the model. The advantages and basic concept of using a graphics processing unit (GPU) to perform parallel computations, as was done with the model in this study, are mentioned and discussed. A brief history of numerical modulation models is also given.

In **Chapter 4** the numerical model is applied to the modulation of GCR protons. A new and reliable very local interstellar spectrum (LIS) for protons is constructed and used as an input spectrum in the model. After calculating the necessary input parameters, the model is used to reproduce a selection of PAMELA proton energy spectra. These results, along with PAMELA measurements, are discussed in detail. Voyager 1 and 2 measurements are compared to radial profiles of proton intensities from the model to verify modulation in the inner and outer heliosphere. This chapter is also devoted to a study of the global radial and latitudinal gradients, where gradients predicted by the model in the inner heliosphere are compared to observations from PAMELA and the Kiel Electron Telescope on board Ulysses. Chapter 4 concludes with a report of the diffusion and drift coefficients obtained from this study of proton modulation.

The numerical model is applied to GCR electron modulation in **Chapter 5**. By using PAMELA, AMS-02 and Voyager 1 measurements, as was done for protons, a new and more reliable electron very LIS is proposed. This LIS is subsequently used in the model to reproduce semesterly averaged electron energy spectra from PAMELA between July 2006 and December 2009. These modelling results are discussed and the diffusion and

drift coefficients that were obtained are presented.

In **Chapter 6** the study of electron modulation from Chapter 5 is extended by including positron antiparticles. It is shown that, when considering both electron and positron observations, a better constrained set of modulation parameters can be obtained. Using these parameters, simultaneous electron and positron observations from PAMELA are reproduced through modelling. These results are shown and discussed in detail. Since electrons and positrons only differ in the charge they carry, they experience drifts in opposite directions. Emphasis is therefore given to the role that drifts play in this study.

The focus of **Chapter 7** is on charge-sign dependent modulation and further highlights the significance of drifts in the heliosphere during the solar minimum of cycle 23/24. In this chapter the results from the previous chapters are combined and analyzed with the aim of identifying the effects of charge-sign dependent modulation. A comparative study of the measured and computed intensities of GCR protons and electrons is conducted, followed by a similar study of electrons and positrons. The intensity-time profiles of various particles are compared to each other and the electron to proton and electron to positron ratios are calculated.

A comprehensive summary of this work, as well as the key conclusions that can be drawn from the results presented here, are given in **Chapter 8**.

Extracts from this thesis, which include contributions from the PAMELA collaboration, were published in the following peer-reviewed journals:

- Adriani, O., G.C. Barbarino, G.A. Bazilevskaya, *et al.*, Time dependence of the proton flux measured by PAMELA during the 2006 July-2009 December solar minimum, *Astrophysical Journal*, 765, 91, 2013.

- Potgieter, M.S., E.E. Vos, M. Boezio, N. De Simone, V. Di Felice, and V. Formato, Modulation of galactic protons in the heliosphere during the unusual solar minimum of 2006 to 2009, *Solar Physics*, 289, 391–406, 2014.

- Adriani, O., G.C. Barbarino, G.A. Bazilevskaya, *et al.*, Time dependence of the e^- measured by PAMELA during the 2006 July – 2009 December solar minimum, *Astrophysical Journal*, 810, 142, 2015.

- Potgieter, M.S., E.E. Vos, R. Munini, M. Boezio, V. Di Felice, Modulation of galactic electrons in the heliosphere during the unusual solar minimum of 2006 – 2009: A modeling approach, *Astrophysical Journal*, 810, 141, 2015.

- Vos, E.E., M.S. Potgieter, New modeling of galactic proton modulation during the minimum of solar cycle 23/24, *Astrophysical Journal*, 815, 119, 2015.

- Vos, E.E., M.S. Potgieter, Global gradients for cosmic ray protons in the heliosphere during the solar minimum of cycle 23/24, *Solar Physics*, In press, 2016.

- Adriani, O., G.C. Barbarino, G.A. Bazilevskaya, *et al.*, Time dependence of the electron and positron components of the cosmic radiation measured by the PAMELA experiment between July 2006 and December 2015, *Physical Review Letters*, 116, 241105, 2016.

The following manuscript has also been submitted to a peer-reviewed journal:

- Di Felice, V., R. Munini, M.S. Potgieter, and E.E. Vos, New evidence for charge-sign dependent modulation during the solar minimum of 2006 to 2009, *Astrophysical Journal*, Submitted, 2016.

Aspects of this study were presented at various international conferences. Contributions to conference proceedings include the following:

- Vos, E.E., M.S. Potgieter, M. Boezio, N. De Simone, V. Di Felice, and V. Formato, Modulation mechanisms for galactic protons during the unusual solar minimum of 2009, *Proceedings of the* 33*rd International Cosmic Ray Conference*, 2013.

- Vos, E.E., M.S. Potgieter, M. Boezio, V. Di Felice, N. De Simone, and V. Formato, Modulation of galactic electrons during the unusual solar minimum of 2009, *Proceedings of the* 33*rd International Cosmic Ray Conference*, Rio de Janeiro, Brazil, 2013.

- Potgieter, M.S., R.R. Nndanganeni, E.E. Vos, and M. Boezio, A heliopause spectrum for electrons, *Proceedings of the* 33*rd International Cosmic Ray Conference*, Rio de Janeiro, Brazil, 2013.

- Potgieter, M.S., R.R. Nndanganeni, E.E. Vos, M. Boezio, and R. Munini, A very local interstellar spectrum for galactic electrons, *Proceedings of the* 33*rd International Cosmic Ray Conference*, Rio de Janeiro, Brazil, 2013.

- Munini, R., The Pamela Collaboration, and M.S. Potgieter, R. du T. Strauss, and E.E. Vos, Solar modulation of galactic cosmic rays electrons and positrons over the 23rd solar minimum with the PAMELA experiment, *Proceedings of the* 33*rd International Cosmic Ray Conference*, Rio de Janeiro, Brazil, 2013.

- Potgieter M.S., E.E. Vos, and R.R. Nndanganeni, The first very local interstellar spectra for galactic protons, helium and electrons, *Proceedings of the* 14*th ICATPP Conference on Cosmic Rays for Particle and Astroparticle Physics*, Como, Italy, 8, 204-211, 2014.

- Potgieter, M.S. and E.E. Vos, A global view of the modulation of cosmic ray protons in the heliosphere for the solar minimum period up to 2009, *Proceedings of the 15th Annual International Astrophysics Conference*, Cape Coral, USA, In press, 2016.

Chapter 2

Cosmic Rays and the Heliosphere

2.1 Introduction

This chapter is devoted to discussing the theoretical background of the heliosphere, CRs and heliospheric modulation in general. Special attention is given to the primary features of the heliosphere, namely the SW, the HMF and the HCS. The $\sim$ 11-year solar activity cycle, and the $\sim$ 22-year magnetic polarity cycle are other important aspects that will be discussed in light of the heliospheric modulation of CRs. Particle drifts form a central theme of this study, so that a good understanding of the mechanism behind this modulation process is necessary, as well as how drifts lead to charge-sign dependent modulation. This chapter concludes with an overview of the PAMELA, and AMS-02 satellite detectors, and the Ulysses and Voyager spacecraft. Measurements from these spacecraft and detectors, in particular PAMELA, were used throughout this study as validation for CR intensities calculated with a numerical modulation model.

2.2 Cosmic Rays

CRs, first observed by Viktor Hess (1883-1964) during the renowned balloon flights in 1911 and 1912, are charged particles with energies ranging from the order of MeV to as high as 10^{20} eV. The composition of CRs vary with energy, but are mainly composed of atomic nuclei (most of which are protons) above $\sim$ 100 MeV, followed by smaller abundances of electrons, positrons, antiprotons, as well as traces of heavier nuclei (e.g. *Lave et al.*, 2013). These charged particles are subjected to solar modulation conditions inside the heliosphere, which affect both their energy and intensity. Modulated CRs that reach the Earth serve as an indirect probe that provides us with valuable information about unexplored regions of the heliosphere (e.g. *Heber*, 2001).

Generally, CRs found in the heliosphere are classified into four major populations, the first of which is GCRs. These CRs originate from far outside the solar system where

they are accelerated up to very high energies (ranging from a few hundred keV to as high as 3.2×10^{20} eV) by, among other, supernovae explosions and remnants, active galactic nuclei and pulsars (e.g. *Tanimori et al.*, 1998; *Büsching and Potgieter*, 2008; *Fisk and Gloeckler*, 2012). CRs are also accelerated by the outward propagating supernova shockwave through a mechanism called diffusive shock acceleration, which is a version of Fermi type acceleration (e.g. *Ptuskin*, 2005). The energy spectrum of GCRs has the form of a power law that goes like $j \propto E^{-\gamma}$, with the spectral index $\gamma \approx 2.6$, E the kinetic energy in MeV/nuc, and j the differential intensity, normally measured in units of particles/m^2/s/sr/MeV. At energies below ~ 30 GeV, the spectral index of GCRs measured at Earth changes due to solar modulation effects that become increasingly important.

Solar energetic particles (SEPs) are another class of CRs that originate from the Sun and are related to solar flares (e.g. *Forbush*, 1946) and coronal mass ejections, as well as interplanetary shocks (see *Cliver*, 2000 for a detailed review). These particles are intermittently observed at Earth, especially during solar maximum activity. SEPs that are observed rarely reach energies as high as ~ 1 GeV for protons, and ~ 100 MeV for electrons (e.g. *Grechnev et al.*, 2008; *Usoskin*, 2008; *Dresing et al.*, 2014).

A third class of CRs is anomalous cosmic rays (ACRs). These particles enter the heliosphere as neutral interstellar atoms, unaffected by the HMF, after which they become singly ionized, either through charge-exchange or photo-ionization (e.g. *Pesses et al.*, 1981). These ions are then "picked up" by the HMF, now called pick-up ions, and transported to the TS where they become accelerated through various mechanisms, still considered as controversial (see *Fichtner*, 2001 for an earlier review, and also *Heber*, 2001). For updated reviews see *Fisk et al.* (2006), *Florinski* (2009) and *Strauss et al.* (2010b).

Jovian electrons, discovered in 1973 by Pioneer 10 during the Jupiter fly-by, form the fourth class of CR particles which in this case originate from Jupiter's magnetosphere and is known to be a relatively strong source of electrons at energies ~ 30 MeV (e.g. *Simpson et al.*, 1974; *Chenette et al.*, 1974). These electrons, dominating at the lower end of the electron spectrum, are primarily found within the first ~ 10 AU from the Sun. See *Ferreira* (2005), *Heber and Potgieter* (2006), *Dunzlaff et al.* (2010) and *Nndanganeni* (2016) for detailed studies of the transport of Jovian electrons in the heliosphere. SEPs, ACRs and Jovian electrons were not considered in this study.

2.3 Structure of the Heliosphere

Due to a pressure difference, the solar corona is not confined to the Sun's surface, but continually expands into interplanetary space at supersonic speeds. As our solar system moves through space, this outward expanding SW, consisting of a continuous stream

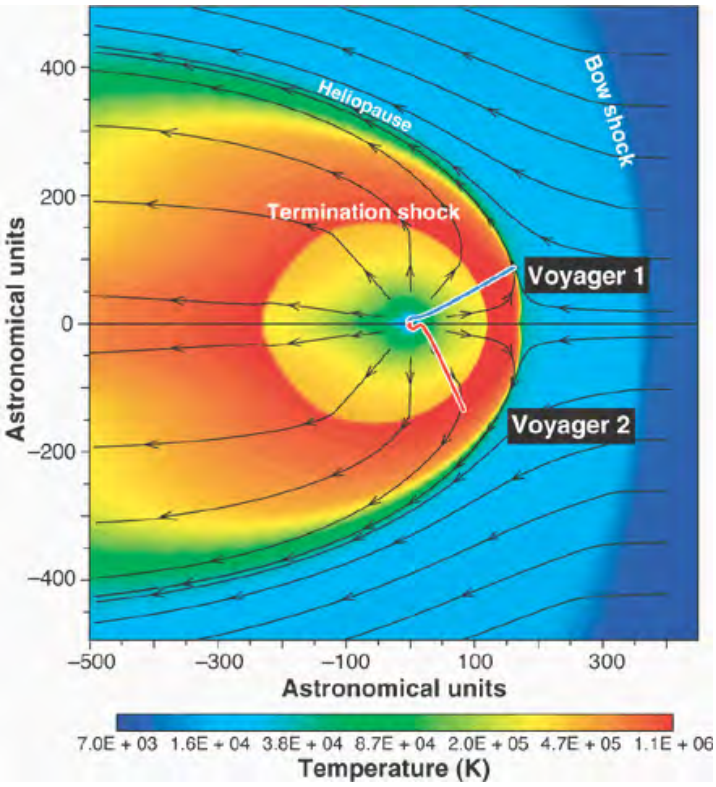

Figure 2.1: A hydrodynamic simulation of the heliosphere giving the temperatures throughout the heliosphere. From this meridional cut, the positions of the TS, HP and the BS are clearly illustrated, along with the indicated Voyager 1 and 2 trajectories. At the TS, the SW plasma heats up to 10^6 K as the SW plasma speed transitions from supersonic to subsonic. Figure taken from *Zank* (1999).

of ionized gas, eventually encounters and interacts with the interstellar medium (ISM) to form a spherical quasi-static "bubble" that serves as a defining boundary between the SW plasma and the ISM. It is at this boundary, referred to as the heliopause (HP), that the SW plasma turns around and merges with the surrounding local interstellar medium (LISM). This region of space, occupied by the outward flowing SW plasma, is called the heliosphere and it encloses the borders of our solar system and beyond. The structure of the heliosphere is therefore primarily determined by the SW, as well as the interstellar "wind".

Figure 2.1 shows a hydrodynamic simulation of the heliosphere in the meridional plane, giving the plasma temperatures (taken from *Zank*, 1999). From this simulation, the general structure and various regions within and around the heliosphere are apparent, where the TS, bow shock (BS) and HP are labelled. See also *Pogorelov et al.* (2013) and *Opher et al.* (2015) for comprehensive reviews of the global properties and dynamics of the heliosphere.

As the SW expands outward, the SW ram pressure becomes equal to the external interstellar thermal pressure at a heliocentric distance of between 70 AU and 100 AU, causing the supersonic SW plasma to rapidly decrease to subsonic speeds (e.g. *Whang*

and Burlaga, 2000). At this point the SW plasma interacts violently with the interstellar gas, resulting in the formation of the TS (*Florinski et al.*, 2003). It is at the TS that the SW is slowed down. The region beyond the TS up to the HP is known as the inner heliosheath.

Discontinuities in various SW parameters occur at the TS, such as a sudden decrease in the SW speed and increases in temperature and density. In addition, the HMF is also compressed, as measured by both Voyager 1 and 2 spacecraft (e.g. *Müller et al.*, 2006; *Richardson et al.*, 2008). The TS is considered to be a dynamic shock, and its position varies depending on the solar cycle. Evidence of this was found when Voyager 1 crossed the TS at a distance of ~ 94 AU from the Sun (*Stone et al.*, 2005), followed by Voyager 2, which crossed at a distance of ~ 10 AU closer than that of Voyager 1 (*Stone et al.*, 2008; *Manuel et al.*, 2014, 2015).

The BS is situated beyond the HP, probably at a distance of ~ 350 AU from the Sun, which includes a region known as the outer heliosheath. The existence of the BS became controversial but seems to be settled (see *Scherer and Fichtner*, 2014). Concerning the propagation of CRs into the heliosphere, it has been shown by *Scherer et al.* (2011), *Strauss and Potgieter* (2014a) and *Luo et al.* (2015) that galactic protons already experience modulation in this outer region of the heliosphere.

2.4 The Sun and Solar Activity

Our Sun is a main-sequence yellow dwarf with an effective temperature of 5.778×10^3 K, and is classified as a star of spectral type G2V (*Stix*, 2004). By mass it consists of about 70 % hydrogen, 28 % helium and 2 % heavier nuclei. The Sun also possesses a magnetic field, similar to that of a typical magnetic dipole, where the Northern and Southern hemispheres have opposite polarities. As the SW expands, it convects the solar magnetic field outward across the heliosphere to form what is known as the HMF. It is well known that the HMF is the primary influencing factor of, and driving force behind, the CR modulation cycle throughout the heliosphere.

Sunspots are dark regions that form on the photosphere of the Sun, and have a lower temperature than their surrounding environment. Sunspots also possess intense magnetic fields and usually appear in groups. Sunspot observations, therefore, directly reflect on the current state of the Sun and thereby provide us with valuable information about the solar cycle and solar activity (*Moore and Rabin*, 1985; *Hathaway*, 2010).

It follows from sunspot observations taken over time (from WDC-SILSO, Royal Observatory of Belgium, Brussels) that there is a clear quasi-periodic variation in solar activity, with an apparent periodicity of ~ 11 years, during which the SSN fluctuates between successive maxima and minima, referred to as solar maximum and minimum. SSNs, therefore, effectively serve as the primary index for solar activity.

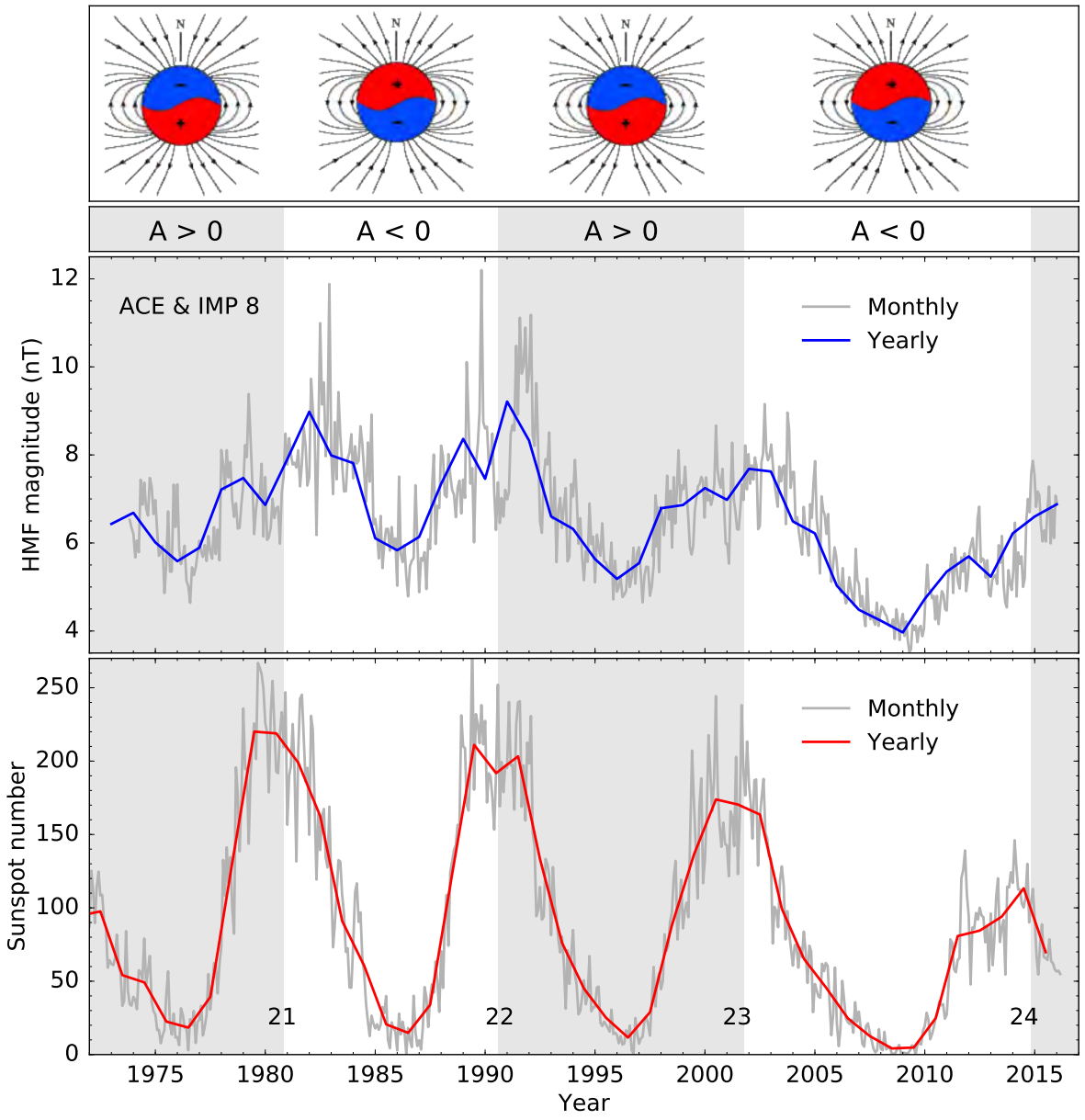

Figure 2.2: A correlation exists between the HMF magnitude (middle panel) and the 11-year cycle of the SSN (bottom panel). Both quantities fluctuate between solar minimum conditions (low SSN counts) and solar maximum conditions (high SSN counts). The grey lines represent monthly averages, while the blue and red lines represent yearly averages. The solar cycle numbers are shown in the bottom panel and are assigned according to each cycle from solar minimum to solar maximum and back to solar minimum. The $A < 0$ and $A > 0$ 22-year solar magnetic polarity cycles are shown in the panel above the HMF. Approximate time spans of these cycles are given by the alternating shaded bands. The inserted illustrations in the top panel shows the solar magnetic configuration for each polarity epoch. Magnetic field data from ACE and IMP8 were obtained from http://nssdc.gsfc.nasa.gov/ and SSN data were obtained from http://sidc.oma.be/.

Apart from the 11-year cycle in SSNs, observations by *Hale and Nicholson* (1925) revealed that the Sun also exhibits a periodic variation in solar magnetic polarity, now with a 22-year periodicity. After every 11-year cycle, the solar magnetic field undergoes a polarity reversal so that after every two successive 11-year cycles the Sun's polarity

assumes its initial configuration, hence the 22-year cycle. This is known as the Hale cycle (*Babcock*, 1961; *Leighton*, 1969). When the solar magnetic field points outward in the Northern hemisphere and inward in the Southern hemisphere, the HMF is said to be in an $A > 0$ polarity cycle, whereas during an $A < 0$ polarity cycle, the solar magnetic field points inward in the Northern- and outward in the Southern hemispheres respectively.

In addition to the polarity reversal, the HMF magnitude also shows a fluctuating pattern that correlates with the SSN counts. Figure 2.2 gives a plot of the HMF magnitude (as measured by IMP8 and ACE) from 1970 to 2017 in the middle panel, along with the SSN counts in the bottom panel. Schematic illustrations of the solar magnetic field configuration for the $A > 0$ and $A < 0$ polarity epochs are also shown. These magnetic configurations become more structured toward solar minimum conditions (as shown in the illustrations) and less structured during solar maximum conditions. It is evident that the HMF magnitude is significantly smaller during solar minimum conditions (with an average magnitude of $\sim 5\,\mathrm{nT}$) compared to solar maximum conditions (with magnitudes between about $8\,\mathrm{nT}$ and $12\,\mathrm{nT}$). See *Balogh et al.* (2008) and *Hathaway* (2010) for detailed discussions of the HMF and the solar cycle in general.

Not surprisingly, the SW is also correlated to solar activity, as well as the tilt angle of the so-called HCS, which is a thin neutral sheet where the oppositely directed open magnetic field lines from the Sun meet. These topics, along with their relation to the solar cycle, are discussed in detail in the following sections.

2.5 The Solar Wind and Termination Shock

Early cometary studies on the orientations of ionic comet tails led scientists to propose various theories as attempts to explain their observations. Biermann published a series of papers between 1951 and 1957 wherein he first postulated the existence of a continuous emission of solar particles, which was, in those days, known as the "solar corpuscular radiation" (*Biermann*, 1961; see also *Fichtner*, 2001, and references therein). Biermann based his postulate on the fact that the ion tails of comets passing close by the Sun always point radially away from the Sun, a phenomenon that couldn't result from solar radiation pressure. In 1958, Eugene Parker presented his theory of this corpuscular radiation, calling it the "solar wind", in which he describes it as a supersonic magnetized fluid (*Parker*, 1958). *Parker* (1963) showed that the only way in which the Sun could remain in equilibrium was if the solar corona was expanding at supersonic speeds.

During solar minimum conditions, the Sun's global magnetic field has its simplest form, and there can be distinguished between two different types of coronal magnetic field structures: regions containing open magnetic field lines and regions containing

closed magnetic field lines. These structures eventually result in different SW and interplanetary magnetic field properties. In regions that contain closed field lines, the magnetic field is perpendicular to the radial SW outflow, which presumably inhibits the outflow. Such regions, called slow SW streams, are generally found at low heliographic latitudes, where the SW has typical velocities of $\sim 400\,\mathrm{km/s}$ (*Feldman et al.*, 2005; *Miralles and Sánchez Almeida*, 2011; *Manoharan*, 2012). Conversely, fast SW streams, associated with open magnetic field structures, originate from large unipolar coronal holes located at higher heliographic latitudes near the solar poles (e.g. *Ofman*, 2004). Typical velocities of the SW in these regions are about 800 km/s (see reviews by *Cranmer*, 2009, and *Wang*, 2009). Other readily observed transient phenomena that appear in the SW include, among other, corotating interaction regions (CIRs), which are regions of high compression that are formed when fast SW streams catch up with slower SW streams (see *Heber et al.*, 1999a, for an overview of CIRs).

The existence of these different SW regions readily imply a latitudinal dependence in the SW speed, which has been confirmed by the Ulysses spacecraft (e.g. *Phillips et al.*, 1995). Figure 2.3 shows the daily average SW speed measured by Ulysses during its three fast latitude scans (FLSs) as a function of heliographic latitude. The first and third FLSs (top and bottom panels), both of which took place during solar minimum, show a clear latitudinal dependence in the speed profile. The slow SW streams are observed in the equatorial region between $\sim 20°$S and $\sim 20°$N, with SW speeds around 400 km/s to 500 km/s, whereas the fast SW streams appear at latitudes $\gtrsim 20°$ in the Northern and Southern hemispheres, with SW speeds between 700 km/s and 800 km/s. For solar maximum, however, there appears to be a mixture of fast and slow SW streams so that no well-defined speed profile is visible, as seen from the middle panel of Figure 2.3 (*Richardson et al.*, 2001; *Heber and Potgieter*, 2006). Superimposed on the Ulysses SW measurements in the bottom panel is the assumed latitudinal dependence used for modelling purposes (black line). The inserts on the right show images of the SW outflow taken by the Solar and Heliospheric Observatory (SOHO) spacecraft, overlaid with polar plots of the SW speed. These were taken during overlapping time periods that correspond to those in the left panels. The red and blue segments of the polar plots represent the inward and outward directed regions of magnetic polarity respectively.

Concerning the radial dependence of the SW speed, *Sheeley et al.* (1997) found that the SW, across all latitudes, accelerates within 0.1 AU from the Sun, after which it becomes a steady flow at 0.3 AU. This is illustrated in Figure 2.4, which shows the SW speed measurements from Voyager 1 and 2, and Pioneer 10, as a function of radial distance. At ~ 84 AU the Voyager 2 measurements show a sudden decrease in speed, which corresponds to the TS crossing. As with Figure 2.3, this behaviour in the radial direction is emulated by the theoretical approximations of the SW speed profile, where the fast and slow SW components are represented by the solid and dashed lines. Within

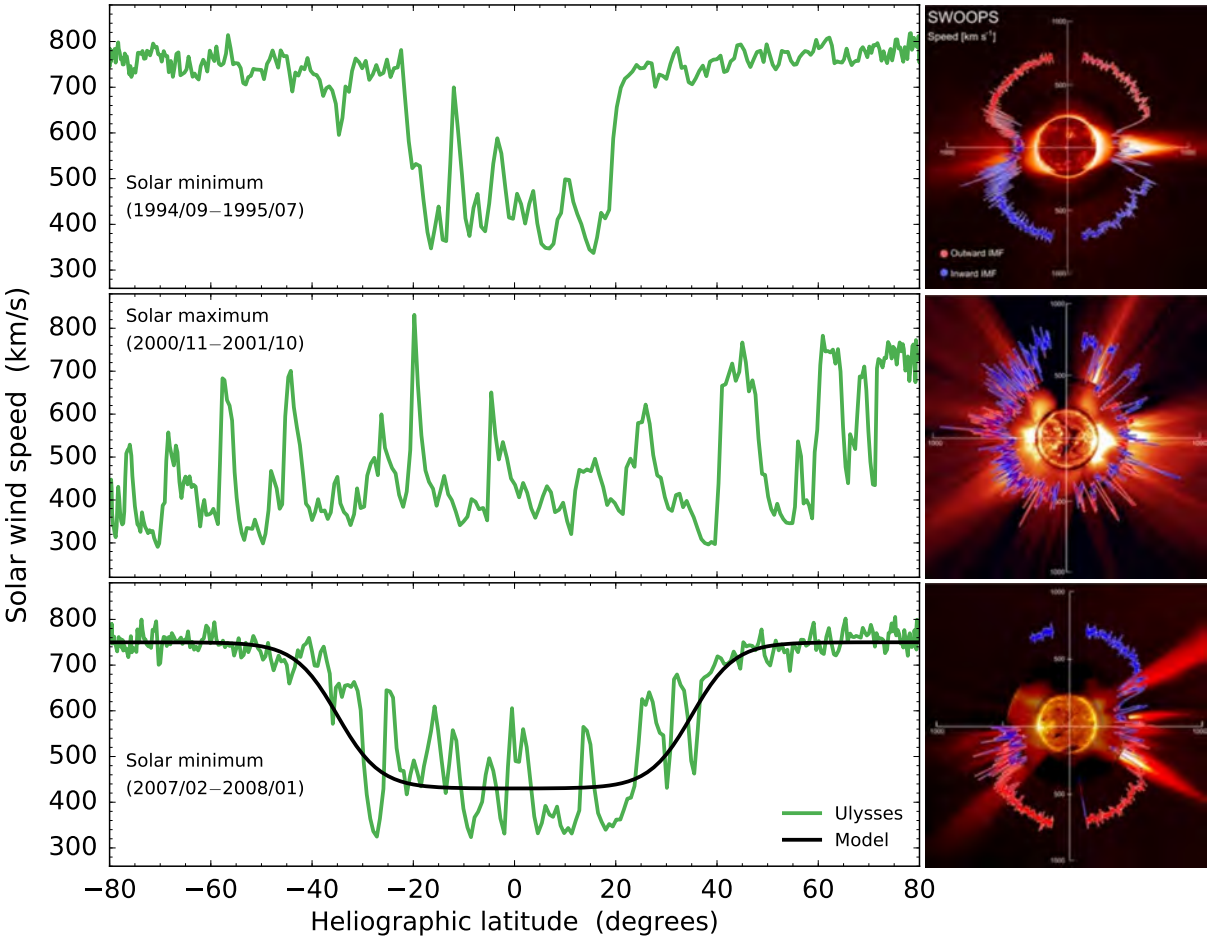

Figure 2.3: The latitudinal dependence of the SW speed during Ulysses' FLSs. The top and bottom panels show the daily averaged SW speed measurements from Ulysses' first and third FLSs, both taken during solar minimum conditions (green lines), while the middle panel shows the SW speed from the second FLS taken during solar maximum conditions (data obtained from http://cohoweb.gsfc.nasa.gov/). The respective dates that correspond to these FLSs are given in the legend. The theoretical approximation for the latitudinal dependence of the SW speed, as used for modelling purposes in this study, is given by the black line in the bottom panel. The inserts on the right show images of the SW outflow taken by the SOHO spacecraft during time periods that overlap with those in the left panels, and overlaid by polar plots of the SW speed. The blue and red segments of the polar plots represent the inward and outward directed magnetic field regions respectively (taken from *McComas et al.*, 2008).

the first 0.1 AU, the SW accelerates, after which, beyond 0.3 AU, it expands at a constant supersonic speed. Since the supersonic flow cannot steadily decelerate to subsonic flow, the supersonic flow energy is dissipated discontinuously in a shock, i.e. the TS, which occurred at $\sim$ 84 AU when Voyager 2 crossed the TS. The above-mentioned Pioneer and Voyager spacecraft mostly remained within the slow SW stream. See *Marsch et al.* (2003), *Kojima et al.* (2004), *Ashbourn and Woods* (2005) and *Schwenn* (2006) for studies and detailed reviews of the SW and its behaviour over the solar cycle.

To construct a coherent model for the SW speed profile that is axially symmetric, it is assumed for this study that the radial and latitudinal dependencies are independent

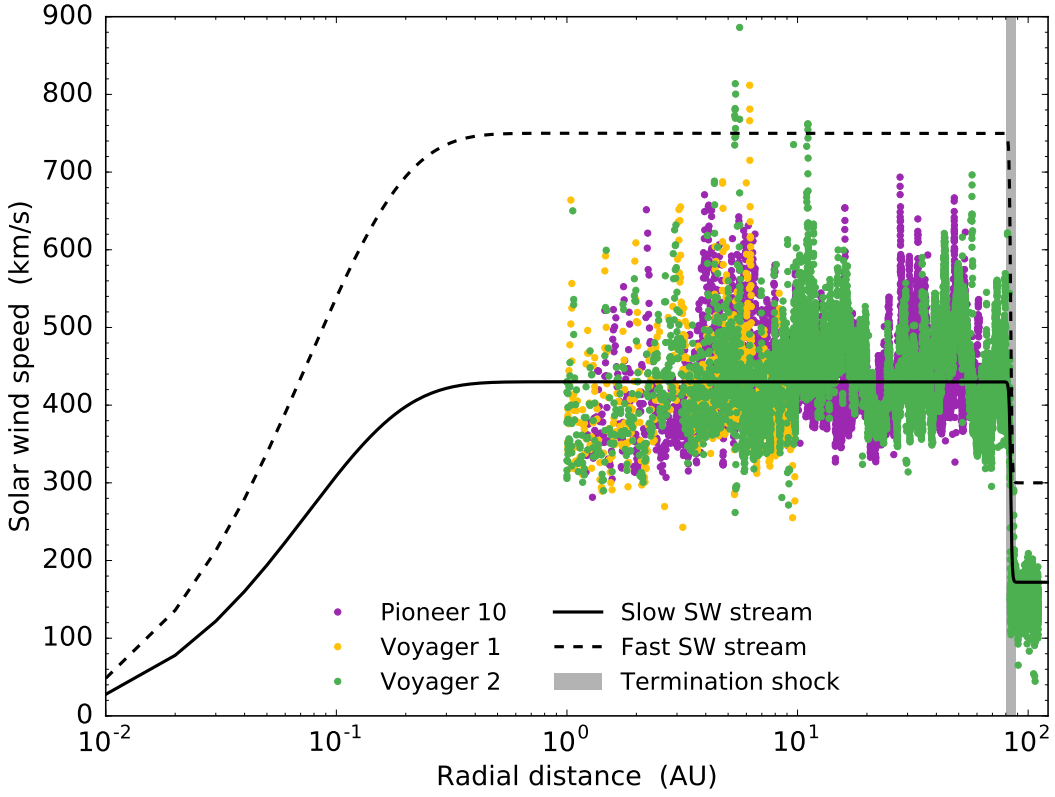

Figure 2.4: The radial dependence of the SW speed is shown using spacecraft measurements (coloured symbols), and corresponding theoretical approximations (solid and dashed lines). Three sets of SW speed measurements are shown, namely Pioneer 10 (purple symbols), Voyager 1 (orange symbols) and Voyager 2 (green symbols). The solid and dashed lines represent the approximated theoretical radial dependence for the slow and fast SW streams, respectively. The TS occurs at 84 AU, as indicated by Voyager 2 measurements. Data obtained from http://cohoweb.gsfc.nasa.gov/.

of each other, so that the outward directed SW velocity, $\mathbf{V}_{sw}(r,\theta)$, can be written as

$$\mathbf{V}'_{sw}(r,\theta) = V'_{sw}(r,\theta)\,\mathbf{e}_r = V_0 V_r(r) V_\theta(\theta)\mathbf{e}_r, \tag{2.1}$$

with r the radial distance from the Sun (in AU), θ the polar angle (or colatitude), $V_0 = 400\,\mathrm{km/s}$ and $\mathbf{e}_r$ the unit vector in the radial direction. The characteristic SW latitude dependence $V_\theta(\theta)$ (for solar minimum conditions), represented by the solid black line in Figure 2.3, is given by

$$V_\theta(\theta) = 1.475 \mp 0.4\tanh\left[6.8\left(\theta - \frac{\pi}{2} \pm \xi\right)\right], \tag{2.2}$$

where the top and bottom signs correspond to the Northern (for $0 \leq \theta \leq \frac{\pi}{2}$) and Southern (for $\frac{\pi}{2} < \theta \leq \pi$) hemispheres respectively, with $\xi = 20\pi/180$. The effect of ξ is to establish the polar angle at which V begins to transition from the slow to the fast SW speed. For this study, which focused on CR modulation during solar minimum

conditions, the slow SW stream was confined within a region of 20° above and below the 90° equatorial plane.

According to this model, it can be seen from Figure 2.3 that the fast SW in the polar regions now has a maximum speed of 750 km/s, while the slow SW in the equatorial region has a minimum speed of 430 km/s. This combination of parameters (for Equation 2.2) was chosen to give the best fit to the SW speed data from Ulysses' third FLS. As previously mentioned, no clear latitudinal dependence exists for solar maximum conditions, so that $V_\theta(\theta)$ is simply assumed to be unity in Equation 2.1 during such conditions (not considered in this study). Apart from the altered parameters, a similar SW model approach was used in numerous studies, e.g. *Hattingh* (1998), *Ferreira* (2002), *Langner* (2004), *Strauss* (2010) and *Manuel* (2013).

The radial dependence, $V_r(r)$, inside the TS is given by

$$V_r(r) = 1 - \exp\left[\frac{40}{3}\left(\frac{r_\odot - r}{r_0}\right)\right], \tag{2.3}$$

with $r_\odot = 0.005\,\text{AU}$ the Sun's radius, and $r_0 = 1\,\text{AU}$. For a heliosphere without a TS, the radial SW speed profile would, according to the above equation, remain at a constant velocity throughout the heliosphere. Conversely, for a heliosphere that includes a TS, the radial speed profile would typically look like the modelled curves of Figure 2.4, which, in this case, is given by

$$V_{sw}(r,\theta) = V'_{sw}\left(r_{TS},\theta\right)\frac{s+1}{2s} - V'_{sw}\left(r_{TS},\theta\right)\frac{s-1}{2s}\tanh\left(\frac{r - r_{TS}}{L}\right), \tag{2.4}$$

with r_{TS} the radial position of the TS (in this case 84 AU), $L = 1.2\,\text{AU}$ the shock scale length, and $s = 2.5$ the shock compression ratio in the downstream region (further away from the Sun, beyond the shock). The shock compression ratio is defined by $s = V_1/V_2$, with V_1 the flow speed in the upstream region (closer to the Sun, ahead of the shock) and V_2 the flow speed in the downstream region. See also *Li et al.* (2008) and *Potgieter et al.* (2014b).

2.6 The Heliospheric Magnetic Field

According to magnetohydrodynamic (MHD) fluid theory, the existence of an interplanetary magnetic field simply follows from the concept of having a magnetic field frozen into a fluid. Within this frame of reference, one can think of an outward flowing plasma that virtually drags the frozen-in field along with it, resulting in a magnetic structure that corresponds to the plasma flow. However, for the radially expanding SW, this only applies to regions where the plasma flow dominates the frozen-in magnetic field, which occur at distances beyond a heliocentric distance of $\sim 2.5 r_\odot$, which describes a surface

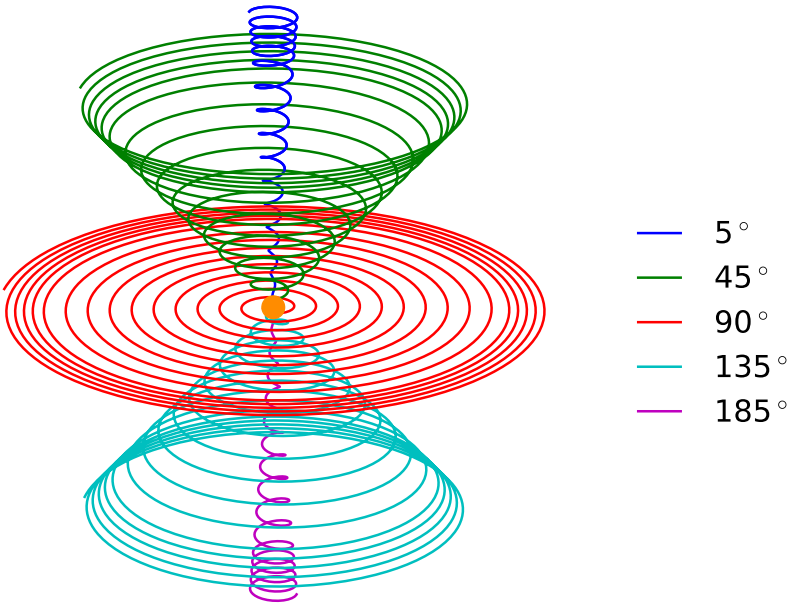

Figure 2.5: The Parker magnetic field has the basic form of Archimedian spirals. Shown here are illustrations of the HMF lines propagating outward at polar angles of 5°, 45°, 90°, 135° and 185°, according to the legend, with the Sun situated at the center. The HMF lines are compressed beyond the position of the TS up to the HP, as a result of the slower SW in the heliosheath region.

referred to as the solar source surface (*Wang and Sheeley*, 1995; *Lockwood and Stamper*, 1999). At this distance the open magnetic field lines become approximately radial so that they are carried off into interplanetary space to become the HMF. Conversely, at distances closer to the Sun, the magnetic field dominates the plasma outflow. See also *Smith* (2008).

The overall behaviour of charged CR particles depend primarily on the HMF line configuration and its embedded turbulence. The HMF, therefore, plays a critical role in heliospheric modulation in that it essentially determines the transport of CRs in the heliosphere.

2.6.1 The Parker Magnetic Field

It is apparent that, since the Sun rotates about an axis perpendicular to the equatorial plane, the HMF exhibits a spiral structure, which is known as the Parker spiral (*Parker*, 1963). The Parker model is basically a SW hydrodynamic model which ignores the magnetic field as long as the acceleration of the coronal plasma is unaffected. The magnetic field is simply added to serve as a "tracer" in the SW flow (e.g. *Smith*, 2008). See *Parker* (2001) for a review on early HMF developments.

The analytical model that describes the Parker spiral for radial distances $r \geq r_{\odot}$, as derived by *Parker* (1958), is given by the expression

$$\mathbf{B} = B_n \left(\frac{r_0}{r}\right)^2 (\mathbf{e}_r - \tan\psi \mathbf{e}_\phi) \left[1 - 2H\left(\theta - \theta'\right)\right], \tag{2.5}$$

where $\mathbf{e}_r$ and $\mathbf{e}_\phi$ are unit vectors in the radial and azimuthal directions respectively, and B_n used to determine the HMF magnitude at $r_0 = 1\,\mathrm{AU}$ (Earth), with

$$\tan\psi = \frac{\Omega\left(r - r_{\odot}\right)\sin\theta}{V_{sw}}, \tag{2.6}$$

with $\Omega = 2.67 \times 10^{-6}\,\mathrm{rad/s}$ the average angular rotation speed of the Sun, V_{sw} the SW speed, and ψ the Parker spiral angle, defined to be the angle between the radial direction and the direction of the average HMF at a given position. The Heaviside step function, H in Equation 2.5, determines the polarity of the magnetic field which causes the HMF to change direction across the HCS, and is given by

$$H\left(\theta - \theta'\right) = \begin{cases} 0 & \text{for } \theta < \theta' \\ 1 & \text{for } \theta > \theta', \end{cases} \tag{2.7}$$

with θ' the polar position of the HCS. The basic HMF structure resembles that of Archimedean spirals traversing cones of constant heliographic latitude, as shown by the graphical representation in Figure 2.5, for various polar angles between 5° and 185°. Beyond the position of the TS, the HMF lines are compressed as a result of the slower moving SW in the heliosheath region. During an $A > 0$ polarity cycle, the HMF lines will be directed outward in the Northern hemisphere, and inward in the Southern hemisphere (with opposite directions for an $A < 0$ cycle). In general, the spiral angle ψ in the equatorial plane at Earth is typically 45°, and increases with distance to 90° at $r \gtrsim 10\,\mathrm{AU}$.

The magnetic field magnitude of Equation 2.5, $|\mathbf{B}|$, is given by

$$B = B_n \left(\frac{r_0}{r}\right)^2 \sqrt{1 + (\tan\psi)^2}, \tag{2.8}$$

from which it is evident that B decreases as r^{-2} at the poles. It is known however that, since the solar surface near the poles are granular and turbulent regions that constantly change with time, the radial magnetic field lines in these regions are in a state of unstable equilibrium. This turbulence results in transverse magnetic field components in the polar regions which regularly lead to deviations from the smooth Parker field geometry (*Jokipii and Kóta*, 1989, and *Forsyth et al.*, 1996). The net effect of these deviations is a highly irregular and compressed field line. As a result, the average magnetic field magnitude in the polar regions is greater than that of regions away from the poles. The

structure of the HMF at the polar regions is a topic that is under debate (*Thomas and Smith*, 1980; *Roberts et al.*, 2007; *Smith*, 2011; *Sternal et al.*, 2011).

2.6.2 The Jokipii-Kóta Modification

Jokipii and Kóta (1989) suggested a modification to the Parker spiral field by introducing a parameter $\delta(\theta)$, which increases the field strength at large radial distances in the polar regions. With this modification, the Parker spiral field becomes

$$\mathbf{B} = B_n \left(\frac{r_0}{r}\right)^2 \left[\mathbf{e}_r + \left(\frac{r\delta(\theta)}{r_\odot}\right)\mathbf{e}_\theta - \tan\psi \mathbf{e}_\phi\right] \left[1 - 2H\left(\theta - \theta'\right)\right], \tag{2.9}$$

where the magnitude thereof is given by

$$B = B_n \left(\frac{r_0}{r}\right)^2 \sqrt{1 + (\tan\psi)^2 + \left(\frac{r\delta(\theta)}{r_\odot}\right)^2}. \tag{2.10}$$

The effect of this modification is that B now decreases as r^{-1} in the polar and equatorial regions. The modification is given by

$$\delta(\theta) = \frac{\delta_m}{\sin\theta}, \tag{2.11}$$

with $\delta_m = 8.7 \times 10^{-5}$, so that $\delta(\theta) = 0.002$ near the poles and $\delta(\theta) \approx 0$ in the equatorial plane. This modification, therefore, brings about the required changes in the HMF in the polar regions without altering the field noticeably in the equatorial plane. A further consequence of the $1/\sin\theta$ dependence of $\delta(\theta)$ is that the magnetic field is kept divergence free, i.e. $\nabla \cdot \mathbf{B} = 0$ (e.g. *Langner*, 2004).

This modification is qualitatively supported by Ulysses's HMF measurements over the polar regions (*Balogh et al.*, 1995). For further applications of this modification, where $\delta(\theta) = 0.002$ throughout the whole heliosphere, see e.g. *Haasbroek and Potgieter* (1995), *Jokipii et al.* (1995), *Hattingh* (1998), *Potgieter and Ferreira* (1999), *Potgieter* (2000) and *Vos* (2012). Similar modifications to the Parker HMF model has been used by e.g. *Ferreira* (2002), *Langner* (2004), *Ndiitwani* (2005) and *Strauss* (2010). *Moraal* (1990) also suggested a modification that has the same compensating physical effects as the Jokipii-Kóta modification.

2.6.3 The Smith-Bieber Modification

Led by magnetic field observations, *Smith and Bieber* (1991) introduced yet another modification where they proposed that the magnetic field is not fully radial below the Alfvén radius, i.e. below the radius at which the magnetic field and solar corona rotate in phase, presumably between $10r_\odot$ and $30r_\odot$. This modification, parameterized by

the ratio of the tangential (azimuthal) magnetic field component to that of the radial component, is incorporated in Equation 2.6, which gives

$$\tan\psi = \frac{\Omega(r-b)\sin\theta}{V_{sw}(r,\theta)} - \frac{rV_{sw}(b,\theta)}{bV_{sw}(r,\theta)}\left(\frac{B_T(b)}{B_R(b)}\right), \tag{2.12}$$

where $b = 20r_\odot$, so that $B_T(b)/B_R(b) \approx -0.02$ according to an estimate by *Smith and Bieber* (1991). This modification changes the geometry of the HMF so that, as a result, it affects the polar field magnitude. See also earlier work of *Haasbroek* (1993), *Haasbroek et al.* (1995) and *Minnie* (2002) for the implementation of this modification in numerical models. In this study, the Smith-Bieber modification to the HMF was used for modelling purposes and builds on the work of *Vos* (2012) and *Potgieter et al.* (2014a) and the recent work of *Raath* (2014) and *Raath et al.* (2015a).

2.6.4 Fisk Type Fields

Apart from the above-mentioned modifications, the Archimedean Parker spiral has become the standard and generally accepted model for the HMF. This model has been set up under the assumption that the Sun rotates rigidly about its axis. However, according to e.g. *Bartusiak* (1994), the Sun actually undergoes differential rotation, where the solar poles rotate $\sim 20\,\%$ slower than the solar equator, the former and latter of which have rotation periods of ~ 25 days and ~ 32 days, respectively. *Fisk* (1996) pointed out that a correction had to be made to the Parker spiral model to account for this, assuming that the HMF footpoints are connected to the differentially rotating photosphere. According to the Fisk model, the HMF exhibits a behaviour which comes from two simultaneous rotational "modes", namely the rigid rotation of the HMF about the solar magnetic axis (at a rate Ω) and the differential rotation ω (dependent on latitude) about a virtual axis inclined at an angle β with respect to the solar rotational axis. This simply means that the HMF acquires a θ-component which is absent in the Parker HMF. See *Zurbuchen* (2007), *Burger et al.* (2008), *Engelbrecht* (2008) and *Sternal et al.* (2011) for detailed discussions of the Fisk field.

When these footpoint trajectories of the HMF can be approximated by circles offset from the Sun's rotational axis by β, the components of the Fisk field are

$$\begin{aligned} B_r &= B_n\left(\tfrac{r_0}{r}\right)^2 \\ B_\theta &= B_r\tfrac{(r-r_{ss})}{V_{sw}}\sin\beta\sin\left(\phi + \tfrac{\Omega(r-r_{ss})}{V_{sw}}\right) \\ B_\phi &= B_r\tfrac{(r-r_{ss})}{V_{sw}}\left[\omega\sin\beta\cos\theta\cos\left(\phi + \tfrac{\Omega(r-r_{ss})}{V_{sw}}\right) + \sin\theta(\omega\cos\beta - \Omega)\right], \end{aligned} \tag{2.13}$$

with r_{ss} the solar surface radius (*Zurbuchen et al.*, 1997). This set of equations describe what is known as the type I Fisk field, whereas for $\beta = 90°$ Equation 2.13 simplifies to the so-called type II Fisk field. Figure 2.6 schematically shows the HMF magnetic

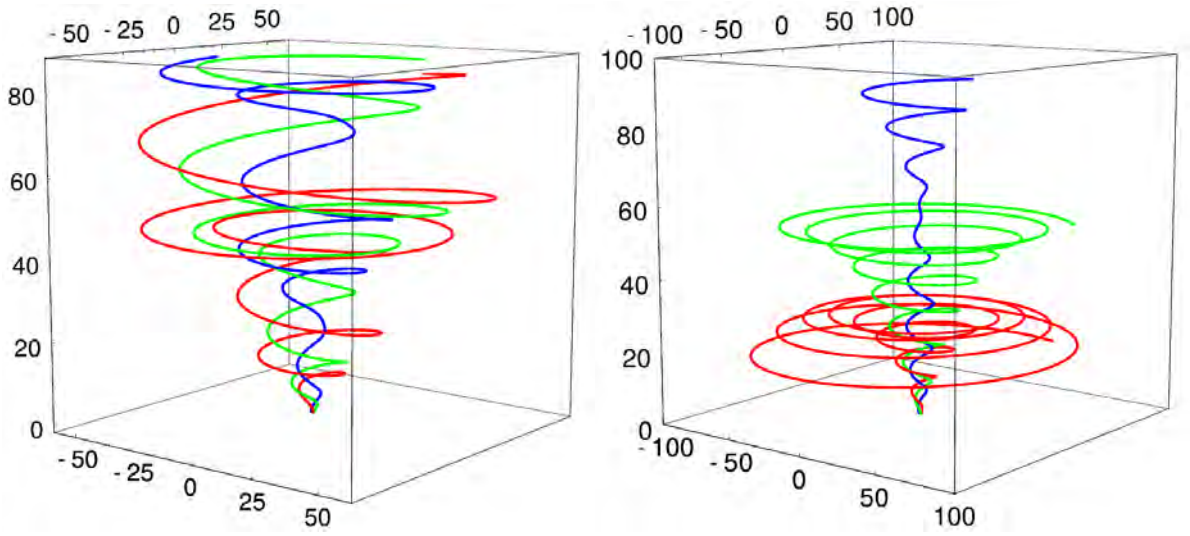

Figure 2.6: HMF lines for the type I (left) and type II (right) Fisk field. The field lines originate from 30° colatitude, but at different longitudes. Radial distances are in AU, with the Sun at the center. Figures taken from *Burger and Hattingh* (2001).

field lines of both types of Fisk fields. Even though the existence of a Fisk HMF might be supported by a tilt angle varying with time, causing regular meridional HMF components (*Kóta*, 1997, 1999), no observational evidence of its existence has been found by *Roberts et al.* (2007), which still leaves the Fisk HMF model as a controversial topic. Recently however, *Sternal et al.* (2011) presented a study based on electron measurements from Ulysses/KET that supports the possible existence of such a field.

A modification of the Fisk HMF has also been proposed by *Burger and Hitge* (2004), known as the Fisk-Parker hybrid field. In this hybrid field the HMF is considered to be a pure Parker field in the equatorial and polar regions, but a pure Fisk field at mid-latitudes, so that in the intermediate regions the HMF is a combination of both Parker and Fisk fields. See also *Burger and Hattingh* (2001), *Burger et al.* (2008), *Engelbrecht* (2008) and *Hitge and Burger* (2010) for detailed discussions of the Fisk-Parker hybrid HMF. Since the Fisk field is inherently three dimensional and time-dependent, the increased complexity of incorporating such a field in a numerical model requires the introduction of a very complicated diffusion tensor in the transport process (*Effenberger et al.*, 2012), which is beyond the scope of study for this work.

2.7 The Heliospheric Current Sheet

As previously mentioned, the magnetic field in the Northern and Southern hemispheres have opposite polarities. These hemispheres are divided by a 3D corotating current sheet, which serves as the heliospheric magnetic equator where the open magnetic field lines from the poles meet. After every $\sim$ 11-year solar cycle the HMF changes sign across this neutral sheet, so that the magnetic field direction in the two hemispheres alternate

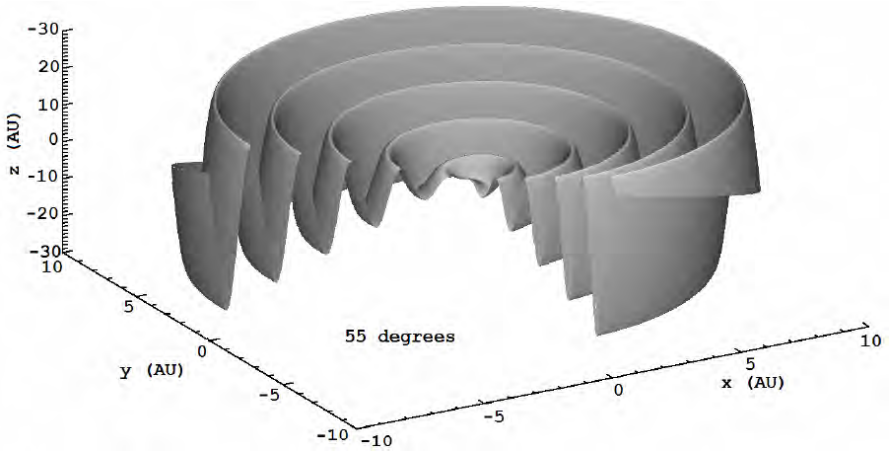

Figure 2.7: A schematic illustration of the HCS. The open magnetic field lines from the poles (which are at opposite polarities) are separated by the current sheet. Figure taken from *Strauss* (2013).

with each consecutive cycle. Since the magnetic dipole axis of the Sun is misaligned by an angle α (called the HCS tilt angle), with respect to the solar rotational axis (e.g. *Hoeksema*, 1992), the solar magnetic equator also does not coincide with the heliographic equator. As a result, the HCS is not confined to a plane near the equatorial regions, but instead has a wavy appearance. The amount of waviness is determined by the tilt angle, which in turn is correlated with solar activity.

Figure 2.7 shows a schematic illustration of the structure of the HCS for a tilt angle of 55°. During low levels of solar activity, the tilt angle becomes small, with typical values between 5° and 10°, so that the magnetic equator and the heliographic equator become closely aligned, resulting in relatively small current sheet waviness. For solar maximum, however, the wavy structure's amplitude increases to tilt angle values as high as 75°. See e.g. *Smith* (2001).

The effects of the HCS were first observed in magnetic field measurements from the early Pioneer missions (*Smith*, 1989). These measurements indicated that the HMF alternated polarity in adjacent regions or "sectors", which led to the so-called "sector-structure" explanation (*Wilcox and Ness*, 1965). It was only later realized by *Alfven* (1977) that these alternating polarity sectors were, in fact, separated by a current sheet which the Pioneer spacecraft repeatedly crossed (see also e.g. *Levy*, 1976).

The existence of the HCS is evident from magnetic field synoptic charts taken of the solar surface at $2.5r_{\odot}$. Figure 2.8 shows two such charts taken during solar cycle 23 (obtained from the Wilcox Solar Observatory at http://wso.stanford.edu). These charts show the magnetic field strength and polarity in the Northern and Southern hemispheres during high levels of solar activity (top panel), in February 2003, and low levels of solar activity (bottom panel), in October 2009. The HCS, identified by the bold black contour line, separates the regions of opposite polarity, indicated by the dark and light shades of grey. The wavy structure of the HCS can also be seen in Figure 2.8,

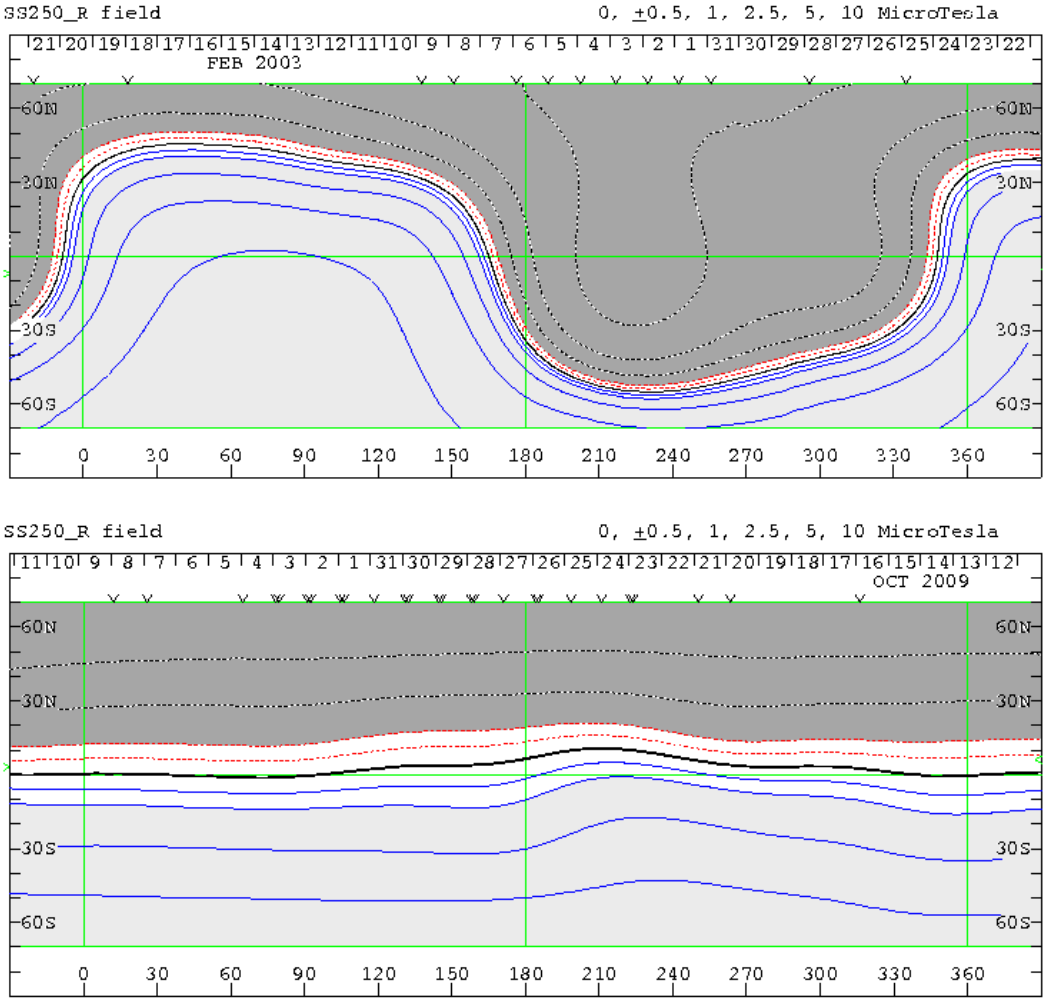

Figure 2.8: The computed source surface field maps (0° to 360° in azimuthal angle) during high levels of solar activity in February 2003 (top panel), and low levels of solar activity in October 2009 (bottom panel). The solar polar magnetic field strength is indicated by the contour lines, where the bold black line corresponds to the HCS. The different shades of grey correspond to different polarities. Figures obtained from the Wilcox Solar Observatory at http://wso.stanford.edu.

especially during high levels of solar activity, when the current sheet extends to larger polar angles for large tilt angle values. This wavy structure, first suggested by *Thomas and Smith* (1981), plays a key role in CR modulation and particle drift motions, which will be discussed in the next section.

A theoretical expression of this wavy HCS for a constant radial SW was derived by *Jokipii and Thomas* (1981), and is given by

$$\theta' = \frac{\pi}{2} + \sin^{-1}\left\{\sin\alpha \sin\left[\phi + \frac{\Omega\,(r - r_{\odot})}{V_{sw}}\right]\right\}. \tag{2.14}$$

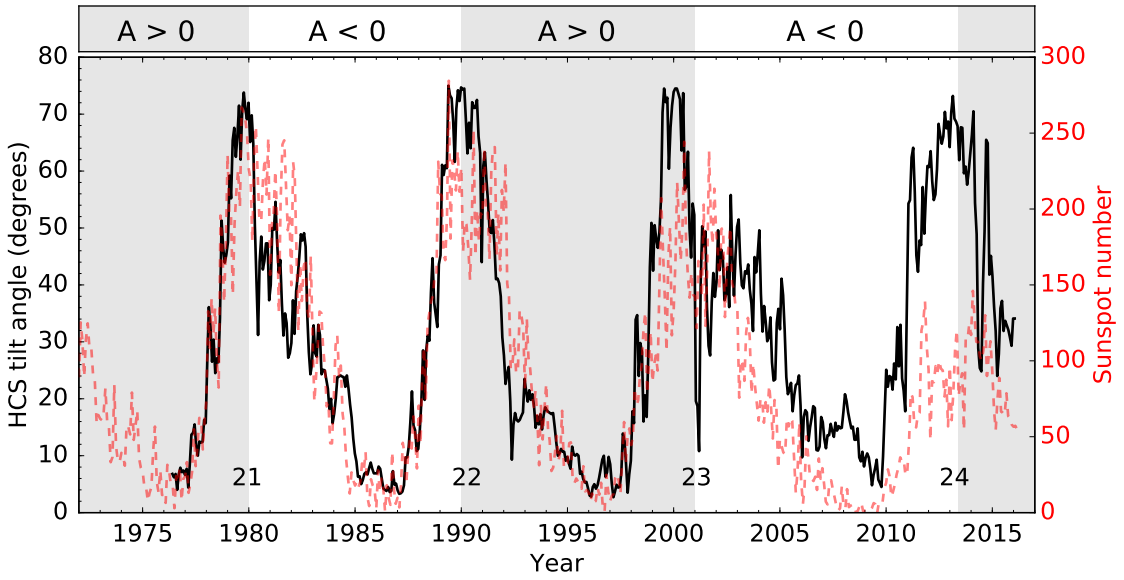

Figure 2.9: The computed HCS tilt angle (α), as a function of time, from the radial model (black line). The HCS tilt angle is correlated with the SSN, which is given by the vertical axis on the right and the dashed red line. As a result, the tilt angle is often used as a proxy for solar activity. The alternating shaded bands give approximate time spans of the $A > 0$ and $A < 0$ polarity cycles. Data obtained from the Wilcox Solar Observatory at http://wso.stanford.edu/.

For sufficiently small values of α, the above equation reduces to

$$\theta' \approx \frac{\pi}{2} + \alpha \sin\left[\phi + \frac{\Omega\,(r - r_{\odot})}{V_{sw}}\right], \tag{2.15}$$

where θ' is the polar extent of the HCS.

Since the waviness of the HCS is correlated with solar activity, which is a function of time, the HCS's waviness also exhibits a time dependence that is reflected in the tilt angle. Figure 2.9 shows a graph of the HCS tilt angle as a function of time computed from the so-called radial model, which is considered to be more accurate than the classic "line-of-sight" model. The HCS tilt angle is correlated with solar activity and also shows a clear 11-year cycle that is related to SSN counts (given by the dashed red line) and the HMF strength. The HCS tilt angle, therefore, is generally considered as a good proxy for solar activity in CR modulation studies. See *Kóta and Jokipii* (1983) and the recent work of *Strauss et al.* (2012) for simulations of CR modulation using a 3D approximation of the HCS. A more recent study by *Raath et al.* (2015b) investigates the effect of the HCS on the heliospheric modulation of CRs, in particular during periods of high solar activity when the current sheet extends to high heliographic latitudes.

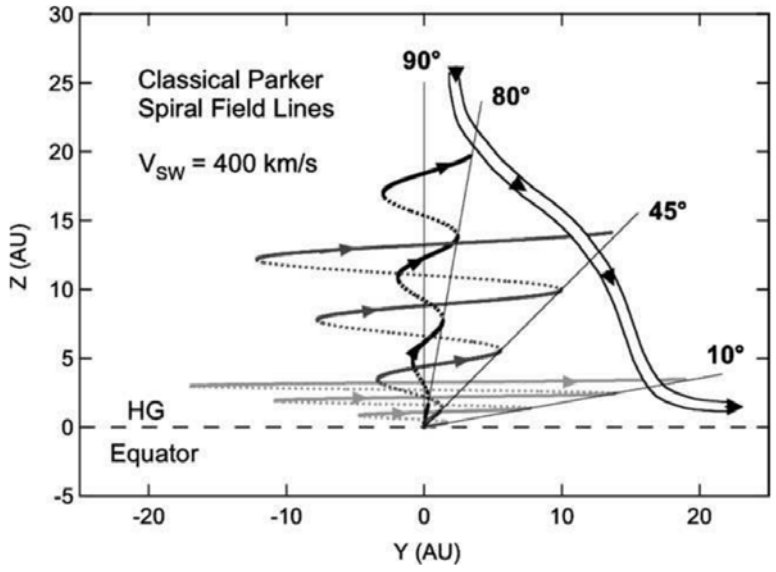

Figure 2.10: A schematic representation of Parker magnetic field lines at various latitudes, along with the possible drift motions of positively charged particles during an $A > 0$ magnetic polarity cycle (as shown by the broad-outlined line). Figure taken from *McKibben* (2005).

2.8 Cosmic Ray Modulation over the Solar Cycle

It is known that the guiding-centers of charged particles undergo gradient and curvature drift motions in the presence of a magnetic field. The HCS, therefore, as well as the global HMF, have significant influences on the transport of CRs in the heliosphere (*Jokipii et al.*, 1977; *Potgieter*, 1984; *Burger*, 1987). Since the HMF has opposite polarities in the regions separated by the HCS, particle drift motions are induced along the HCS. For an $A > 0$ cycle, when the HMF is directed outward in the Northern hemisphere and inward in the Southern hemisphere, positively charged particles undergo drift motions from the polar regions toward the equatorial region, and outward along the HCS, as illustrated in Figure 2.10. Negatively charged particles drift in opposite directions. This phenomenon is referred to as charge-sign dependent modulation. During an $A < 0$ cycle, the drift directions of positive and negative CRs are reversed.

Consequently, the amount of waviness of the HCS, as well as the drift direction, directly influence the ability of charged particles to reach certain regions in the heliosphere. These drift motions do, however, only contribute significantly to CR modulation during solar minimum conditions, when the HMF exhibits a well-ordered structure (e.g. *Ferreira and Potgieter*, 2004, and *Ndiitwani et al.*, 2005).

When CRs reach the Earth, they collide with molecules in the atmosphere, producing air showers of secondary particles. These secondary particles are then detected by ground-based neutron monitors, giving an indication of the CR flux at Earth (*Usoskin et al.*, 2011, 2015). As an example of long-term observations of the modulation of GCRs, Figure 2.11 gives a graph of NM counts, measured by the Hermanus NM, as a function of

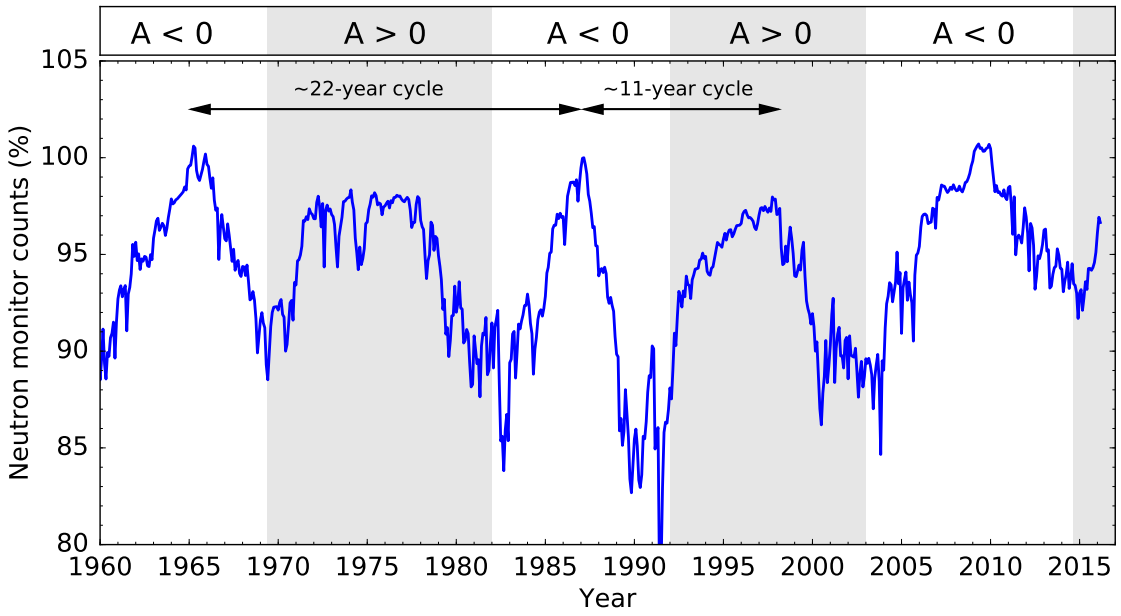

Figure 2.11: NM counts given as a function of time, as measured by the Hermanus NM. These counts are normalized with respect to March 1987, which is at 100 %. The $\sim$ 11-year and $\sim$ 22-year cycles are clearly distinguished. The cutoff rigidity for CRs at Hermanus, South Africa, is 4.6 GV. Approximate time spans for the $A > 0$ and $A < 0$ polarity cycles are given by the alternating shaded bands. Data obtained from http://www.nwu.ac.za/neutron-monitor-data.

time from 1960 until present. As could be expected, the 11-year solar activity cycle also gives rise to an 11-year CR modulation cycle, which is identified by times of increased CR flux in NM counts that occurred around 1965, 1976, 1987, 1997, and recently in 2009. However, a comparison of this figure with Figures 2.2 and 2.9 reveals that the observed CR flux is anticorrelated with solar activity, meaning that higher CR fluxes are measured during solar minimum conditions.

Furthermore, the 22-year cycle, related to the HMF polarity reversal, can also be identified from Figure 2.11. During $A < 0$ polarity cycles, peaks are formed through heliospheric modulation, while for $A > 0$ polarity cycles, the modulated flux has plateau shapes. These features can be ascribed to the drift motions experienced by charged CR particles. Another feature that is evident from NM counts are the intermittent decreases in intensity. These sudden decreases, referred to as Forbush decreases, are supposedly related to violent transient solar events (like coronal mass ejections) that lead to the formation of propagating diffusion barriers such as corotating interaction regions (e.g. *Potgieter*, 2008). For a comprehensive review of CR modulation, see *Potgieter* (2013b).

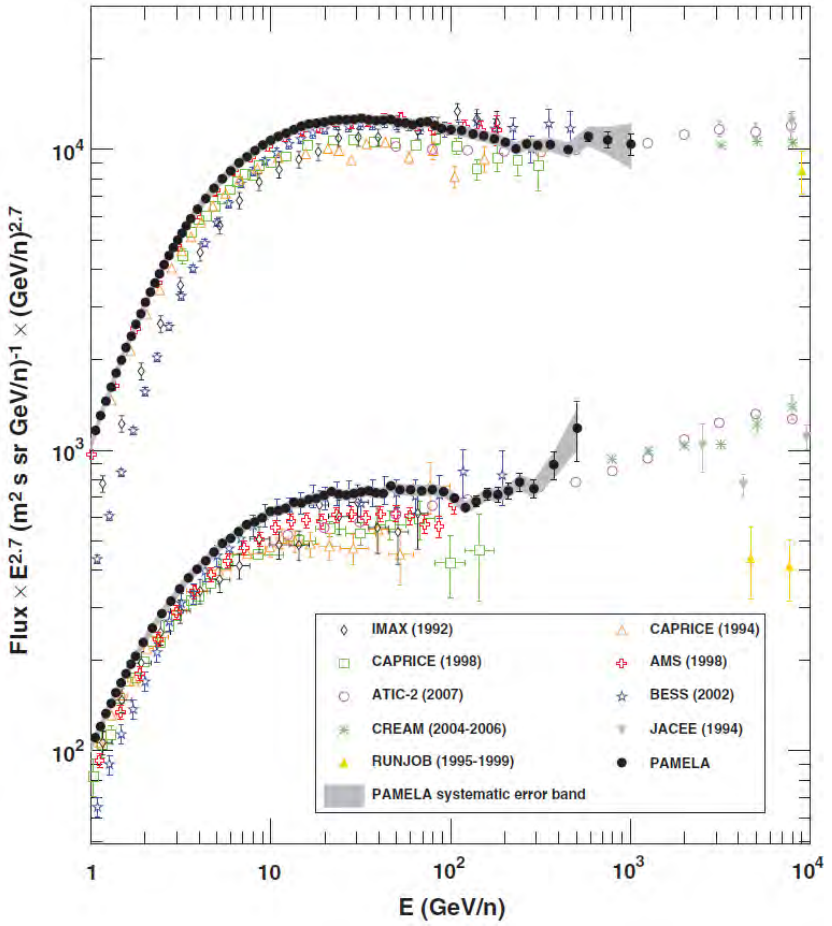

Figure 2.12: Absolute proton and helium fluxes measured by PAMELA in the rigidity range between 1 GeV and 1.2 TeV, compared to measurements made during previous balloon-borne and satellite-borne experiments (*Adriani et al.*, 2011a and references therein). The error bars on the PAMELA data indicate statistical uncertainties (within one standard deviation) and the grey shaded region represents the estimated systematic uncertainty. Figure taken from *Adriani et al.* (2011a).

2.9 Spacecraft and Satellite Missions

2.9.1 The PAMELA Mission

Since June 2006, the space-borne PAMELA detector has been measuring CR intensities of particles as well as antiparticles at 1 AU (*Picozza et al.*, 2007; *Adriani et al.*, 2009b). The instrument is built around a 0.43 T permanent magnet spectrometer and comprise of various sub-detectors that enable it to detect CRs over a wide energy range. The primary scientific objective for PAMELA is to study the antimatter component of CRs, i.e. antiprotons and positrons, in order to address various questions in CR physics, like particle production and propagation in the galaxy, dark matter detection and charge-sign dependent modulation of low-energy CRs in the heliosphere (e.g. *Casolino et al.*, 2008b; *Boezio et al.*, 2009; *Picozza et al.*, 2009; *Adriani et al.*, 2009a). As PAMELA orbits the Earth at altitudes between 350 km and 600 km, it travels through the Earth's

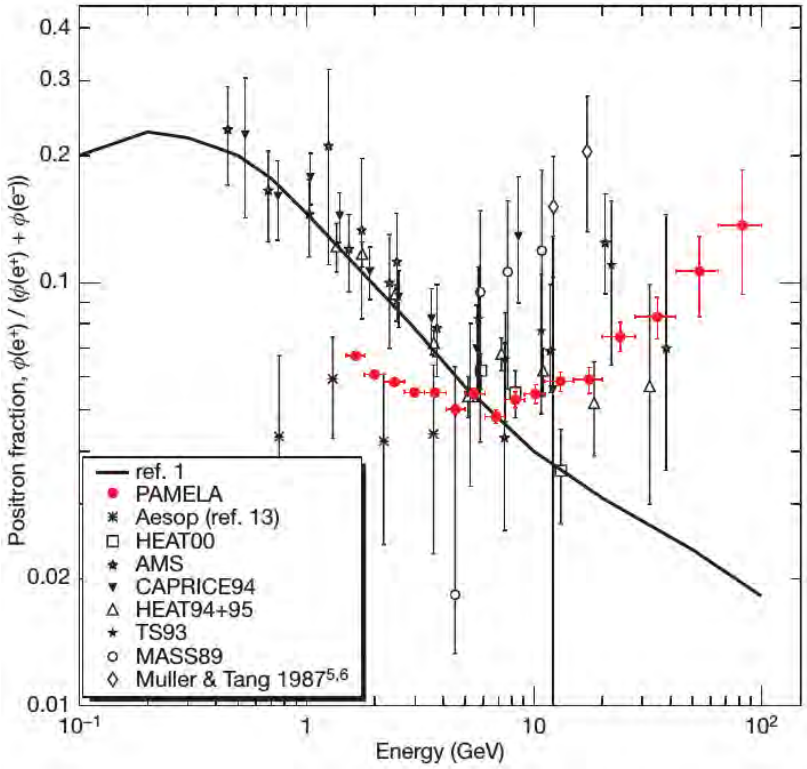

Figure 2.13: The PAMELA positron fraction (red symbols) shown with measurements from other experiments (see *Adriani et al.*, 2009c and references therein). The solid line shows a calculation for the production of secondary positrons during galactic propagation that exclude reacceleration processes. Figure taken from *Adriani et al.* (2009c).

magnetosphere as well as the Van Allen radiation belts. This also allows PAMELA to study the high-energy trapped particle components in these belts and their temporal fluctuations. Another objective for the PAMELA mission is to study SEPs. Such an event was observed by PAMELA in December 2006, which evidently was the first time that a single instrument took direct measurements of an SEP event in the energy range between $\sim 80\,\mathrm{MeV}$ and $3\,\mathrm{GeV}$ (*Adriani et al.*, 2011b; *Adriani et al.*, 2015a).

Proton and helium spectra across a rigidity interval of $1\,\mathrm{GV}$ and $1.2\,\mathrm{TV}$ were also published by *Adriani et al.* (2011a) for the time period between 2006 and 2008. This is shown in Figure 2.12, along with measurements from other experiments. It follows that PAMELA measurements are consistent with those of other experiments, taking into account the statistical and systematic uncertainties of the latter, where differences at low energies can be ascribed to solar modulation. Prominent conclusions were drawn from these results, namely that the proton and helium spectra between $30\,\mathrm{GeV}$ and $1.2\,\mathrm{GeV}$ have different spectral indices of $\gamma_\mathrm{p} = -2.820 \pm 0.003$ and $\gamma_\mathrm{He} = 2.732 \pm 0.005$, respectively, when fitting a single power law to the data (where errors represent statistical uncertainties). PAMELA observations also revealed a hardening in the proton and helium spectra above $200\,\mathrm{GV}$, a feature that was not predicted by standard galactic propagation models. This hardening could be interpreted as an indication of different

populations of CR sources.

Figure 2.13 shows the positron fraction measured by PAMELA compared with measurements from other experiments (see *Adriani et al.*, 2009c and references therein). As a result of modulation, the PAMELA measurements below $\sim 5\,\mathrm{GeV}$ are lower than the computed reference spectrum from GALPROP (solid line) and most of the measurements from other experiments. Above $\sim 10\,\mathrm{GeV}$ the PAMELA positron fraction increases with energy, which is contrary to GALPROP calculations that assume that positrons are mainly created in secondary production processes when CR nuclei interact with interstellar gas. These assumptions have been challenged by PAMELA, which was the first instrument to make definitive measurements of the anomalous CR positron abundance above $\sim 100\,\mathrm{GeV}$. See also e.g. *Mocchiutti et al.* (2011), *Menn et al.* (2013), *Adriani et al.* (2014) and references therein for more on PAMELA results in general.

PAMELA's goal to study solar modulation led to a detailed investigation of the 24^{th} solar minimum period between 2006 and 2009 in terms of CR energy spectra (*Adriani et al.*, 2013a, 2015b). The resulting measurements from PAMELA proved to be extremely valuable to heliospheric modulation studies, in particular for studying the effects of drifts on CRs. Consequently, measurements from PAMELA over this time period play a key role in this study and serve as a benchmark for modelling results.

For detailed studies on the analysis and interpretation of PAMELA measurements, see e.g. the PhD theses of *Di Felice* (2010), *De Simone* (2011), *Formato* (2013) and *Munini* (2015). See also http://pamela.roma2.infn.it/index.php for more on the PAMELA instrument and mission.

2.9.2 The Ulysses Mission

Ulysses was the first spacecraft to explore the heliosphere at higher latitudes and to take measurements over the polar regions of the Sun. Since its launch in October 1990 and the Jupiter fly-by in February 1992, the spacecraft has been orbiting the Sun in an elliptical orbit at an inclination of 80.2° relative to the solar equator. The instruments that comprised Ulysses enabled it to study the SW plasma, the HMF, as well as planetary, solar and GCR particles. Among these is the Kiel Electron Telescope (KET), which forms part of the Ulysses Cosmic and Solar Particle Investigation (COSPIN). The KET measures protons and helium in the energy range from 6 MeV to above 2 GeV and electrons in the energy range from 3 MeV to a few GeV. See *Wenzel et al.* (1992), *Marsden* (2001) and *Heber* (2011) for reviews of the Ulysses mission and results of the KET. See also http://www.cosmos.esa.int/web/ulysses for more on the Ulysses spacecraft and the instruments on board.

During its lifetime, Ulysses completed three FLSs, during each of which it travelled from the Sun's Southern polar regions (around 80°S) to the Northern polar regions (around 80°N), at distances between $\sim 2.5\,\mathrm{AU}$ and 1.2 AU from the Sun, all within time

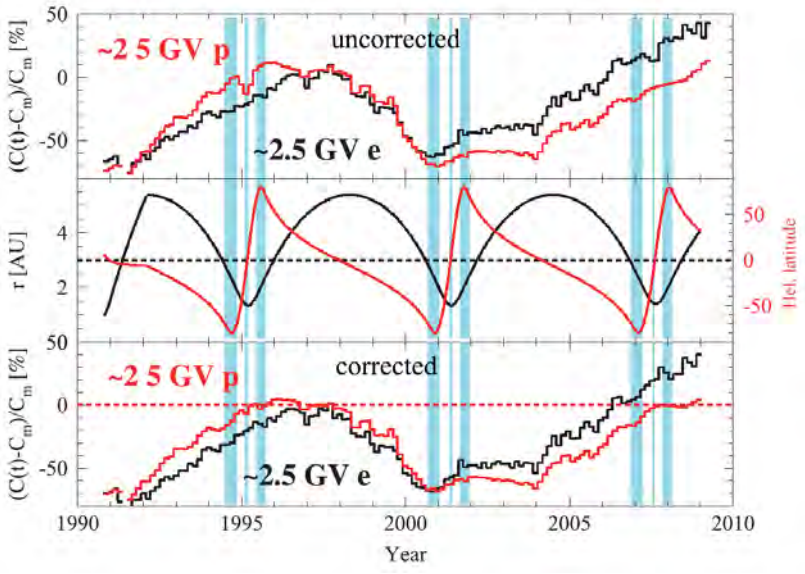

Figure 2.14: Ulysses KET count rates of protons (red) and electrons (black). Uncorrected count rates as measured along Ulysses' orbit are shown in the top panel, while "1 AU equivalent" count rates are shown in the bottom panel. The latter count rates were calculated by correcting for the varying radial distance and latitude along the Ulysses orbit by using the radial and latitudinal gradients determined by *Heber et al.* (1996a, 1999b, 2002b), *Clem et al.* (2002) and *Heber et al.* (2008). The middle panel gives the radial distance (black) and latitude (red) of Ulysses. The vertical blue shaded regions represent the FLS periods. Figure taken from *Heber et al.* (2009).

periods of less than a year. The first and third FLSs took place during $A > 0$ and $A < 0$ solar minimum periods respectively, while the second FLS was conducted during solar maximum conditions. This enabled Ulysses to study the spatial and time dependence of CR behaviour during different modulation conditions (*Heber and Potgieter*, 2006; *Heber et al.*, 2009; *Smith*, 2011; *Heber and Potgieter*, 2008).

Some key topics that were studied with Ulysses' instruments are the following: Jovian electrons were used to investigate the properties of particle propagation in the inner heliosphere at high heliolatitudes. These low-energy electrons measured by Ulysses were also used to find a diffusion tensor suitable to the modulation of electrons (e.g. *Ferreira et al.*, 2001a, 2001b). Recurrent variations in particle intensities were also studied at high heliolatitudes. These variations were observed with the occurrence of recurrent fast and slow SW streams, along with depressions in CR flux that were associated with CIRs. However, variations in CRs were still observed in the absence of these recurrent events, even at polar latitudes (e.g. *Kunow et al.*, 1995, 1999; *Paizis et al.*, 1999). A primary aspect that Ulysses was well-suited to investigate was global CR gradients. During Ulysses' first and second FLSs it confirmed the expectation of positive latitudinal gradients during solar minimum and an isotropic GCR distribution at solar maximum. During the third FLS Ulysses KET measured very small positive and negative latitudinal gradients for 2.5 GV electrons ($\sim 0.2 \pm 0.05\,\%/^\circ$) and 1.63 GV protons

($-0.04 \pm 0.01\,\%/^\circ$) respectively (*Heber et al.*, 2008; *Gieseler and Heber*, 2016). Latitudinal gradients occur as a result of charge-sign dependent modulation, so that many studies of this phenomenon have been conducted using Ulysses/KET measurements – see e.g. *Heber et al.* (2002a, 2002b), *Ferreira et al.* (2003) and *Ndiitwani et al.* (2005). Significant insight also resulted from Ulysses KET measurements regarding CR propagation, namely that perpendicular diffusion in the polar direction has to be enhanced latitudinally. This enhancement, which is discussed in more detail in the next chapter, is related to the different SW regimes observable during solar minimum.

Figure 2.14 gives an overview of $\sim 2.5\,\mathrm{GV}$ electron and proton count rates as measured along Ulysses' orbit (top panel), along with the "1 AU equivalent" count rates (bottom panel), where corrections have been made for the radial and latitudinal variation in Ulysses' orbit. The difference in how electron (black) and proton (red) count rates develop with time is a result of long-term charge-sign dependent modulation. During an $A > 0$ polarity cycle (between ∼1990 and ∼2000) protons drift into the heliosphere via the polar regions and gain quick access to Earth's position, while for an $A < 0$ cycle (between ∼2002 and 2012) protons take longer to reach Earth since they drift into the heliosphere along the HCS (reversed scenarios hold for electrons). The Ulysses KET count rates are consistent with these predictions from drift theory (*Potgieter*, 2014a).

In this study, the radial and latitudinal gradients between the positions of Ulysses and PAMELA are calculated for the time that these two missions overlapped during recent solar minimum of cycle 23/24. PAMELA measurements and Ulysses count rates are used, in addition to model intensities, where an analysis similar to *De Simone et al.* (2011) and *Gieseler and Heber* (2016) is followed.

2.9.3 The Voyager Missions

The Voyager 1 and 2 spacecraft were launched in 1977 with the purpose of studying the outer regions of our solar system as well as Jupiter, Saturn and their moons (*Kohlhase and Penzo*, 1977). After about 12 years of flight, the Voyager program was extended in order to continue studying the outer heliosphere and ultimately the very local interstellar environment, as part of the Voyager Interstellar Mission. Many of the instruments and scientific investigations on board the Voyager spacecraft have been disabled or are defective, however, most instruments related to CR measurements and heliospheric studies are still active. See e.g. *Behannon et al.* (1977), *Bridge et al.* (1977), *Krimigis et al.* (1977), *Scarf and Gurnett* (1977) and *Stone et al.* (1977) for more about the various investigations and scientific instruments on board the Voyager spacecraft. See also http://voyager.jpl.nasa.gov/ for more resources on the Voyager spacecraft and their interstellar mission.

Significant milestones were reached by the Voyager spacecraft after completing their primary mission. In December 2004, Voyager 1 crossed the TS at a distance of 94 AU

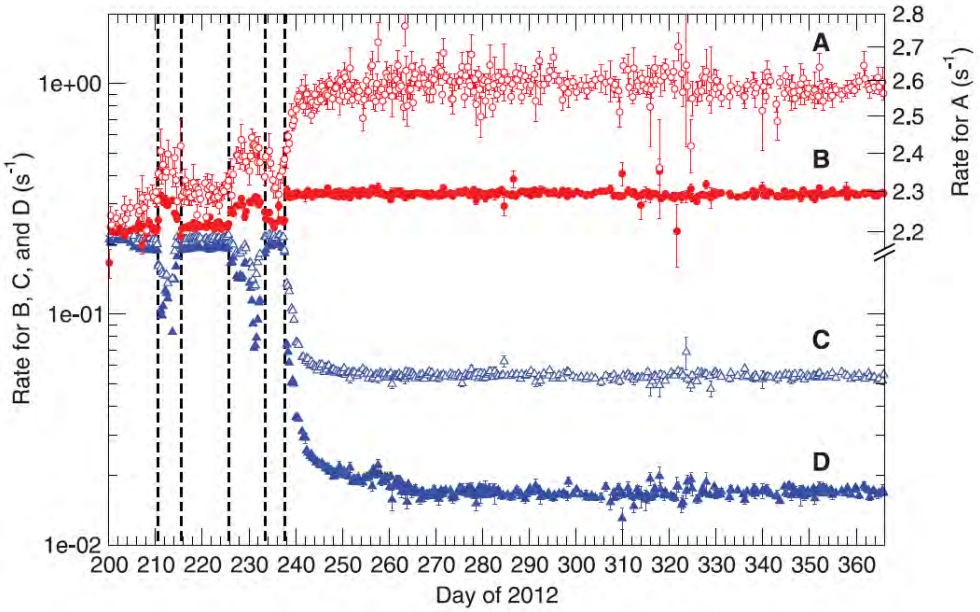

Figure 2.15: Voyager 1 counting rates at 6-hourly averaged intervals, as a function of day number in 2012. In August of 2012, Voyager 1 crossed the HP after brief encounters with regions depleted of heliospheric ions between days 210 to 215 and 226 to 233 (indicated by the vertical dashed lines). After day 238, Voyager 1 entered the ISM, which is evident from the increase in GCR counts and decrease in low-energy particles from the heliosphere. See text for an explanation of the various energetic particle species denoted by A, B, C and D. Counting rates for B, C and D are given by the left y-axis, while counting rates for A are given by the upper right y-axis. Figure taken from *Stone et al.* (2013).

from the Sun in the Northern hemisphere, after which Voyager 2 crossed the TS in August 2007 at a closer distance of 84 AU from the Sun in the Southern hemisphere (see *Decker et al.*, 2005; *Stone et al.*, 2005; *Richardson et al.*, 2008). On August 25, 2012, after travelling $\sim$ 8 years through the heliosheath, Voyager 1 measured a sudden decrease in the intensity of low-energy particles by a factor of more than 10^3, along with a 9.3 % increase in GCR intensities. This region turned out to be part of the interface between the SW plasma and the very local interstellar environment, referred to as the HP region, and the crossing of the HP by Voyager 1 at 122 AU was consequently confirmed (*Burlaga et al.*, 2013; *Gurnett et al.*, 2013; *Krimigis et al.*, 2013; *Stone et al.*, 2013; *Webber and McDonald*, 2013). The crossing of the HP is still considered as controversial by *Fisk and Gloeckler* (2014) and *Gloeckler and Fisk* (2015).

Figure 2.15 shows 6-hourly averaged counting rates of four different energetic particle species over the time period that Voyager 1 crossed the HP. The different sets of symbols denoted by "A" and "B" represent GCR nuclei (mainly $>$ 70 MeV protons) from the High Energy Telescope 1 (HET1) and GCR electrons with energies between 6 MeV and $\sim$ 100 MeV from the Electron Telescope, respectively. Protons with energies between 7 MeV and 60 MeV from HET1 are primarily ACRs before day 238 and GCRs thereafter (denoted by C). Filled blue symbols (D) are measurements of low-energy particles, primarily protons between 0.5 MeV and $\sim$ 30 MeV that were accelerated at the TS and

in the heliosheath. Brief encounters with regions depleted of heliospheric ions occurred during time periods between day 210 to 215 and day 226 to 233. After day 238 Voyager 1 entered a broad depletion region that is being interpreted as the ISM.

This achievement by Voyager 1 has proven to be invaluable for CR modulation studies, since low-energy (below $\sim 600\,\mathrm{MeV}$) *in situ* measurements of interstellar electrons, protons, helium, carbon and oxygen are now possible. Such measurements were used extensively throughout this study to determine the correct shape and absolute value of the very local interstellar spectra for electrons and protons. At the time of writing, the Voyager 1 and 2 spacecraft were at distances of 134.7 AU and 111.0 AU from the Sun, respectively.

2.9.4 AMS-02

The Alpha Magnetic Spectrometer (AMS-02) is a high-energy CR detector that has been installed as an external module on the international space station since May 2011. The AMS-02 instrument is built around a powerful superconducting magnet, with a field measuring 0.87 T at the center, that enables it to determine the charge of particles. It is designed to conduct long-term CR measurements over a span of $\sim 20\,\mathrm{years}$, during which it will explore the field of particle physics by studying the composition of CRs with extreme accuracy, searching for primordial antimatter as well as studying the nature of dark matter. Other primary goals of AMS-02 include measuring the antiproton to proton and electron to positron ratios, and to collect data up to TeV energies (e.g. *Aguilar et al.*, 2013).

First results from AMS-02 were reported by *Aguilar et al.* (2013), followed by high statistics measurements of the positron fraction between 0.5 GeV and 500 GeV by *Accardo et al.* (2014). These measurements extend the energy range of previous measurements to higher energies, along with an increase in accuracy. Consequently, a previously unobserved behaviour of the positron fraction was discovered at very high energies, namely that above $\sim 200\,\mathrm{GeV}$ the positron fraction is no longer increasing. Better clarification of the origin of this new behaviour will require more measurements up to higher energies.

Aguilar et al. (2014a) published electron and positron energy spectra as measured by AMS-02 between May 2011 and November 2013. These are shown in Figure 2.16 (red symbols) and compared to measurements from PAMELA (*Adriani et al.*, 2011c, 2013b), Fermi-LAT (*Ackermann et al.*, 2012), MASS (*Grimani et al.*, 2002), CAPRICE (*Boezio et al.*, 2000), AMS-01 (*Alcaraz et al.*, 2000b) and HEAT (*DuVernois et al.*, 2001), all of which are multiplied by E^3. Below $\sim 30\,\mathrm{MeV}$, the AMS-02 and PAMELA measurements are notably different. Since these measurements were taken during different times in the solar cycle, the consequent differences can be ascribed to the heliospheric modulation.

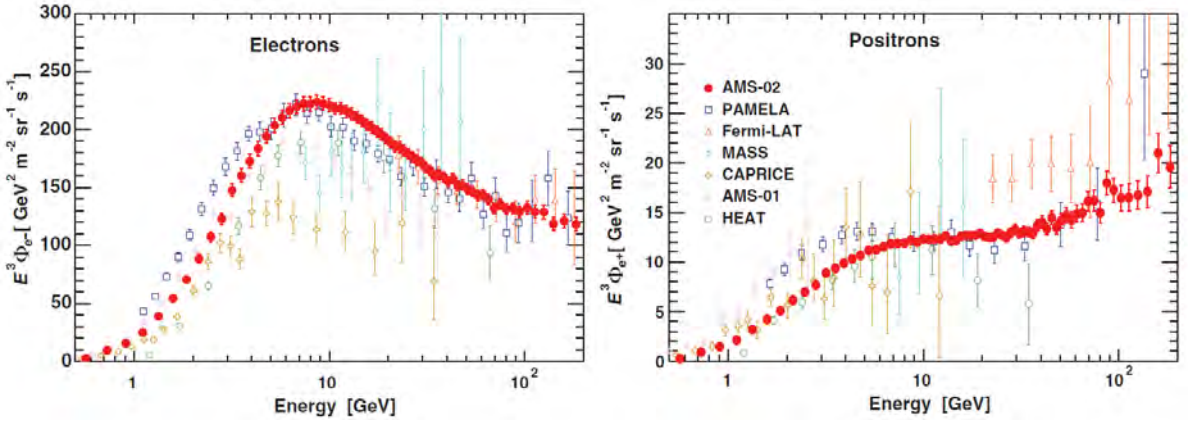

Figure 2.16: AMS-02 electron (left) and positron (right) differential intensities (red symbols), multiplied by E^3, as a function of energy. Also shown, according to the legend, are measurements from other experiments for comparison (see text for references). Figures taken from *Aguilar et al.* (2014a).

AMS-02 energy spectra of protons, electrons and positrons are used in this study to assist in normalizing the very LIS between 30 GeV and 50 GeV. See *Aguilar et al.* (2014b) for measurements of the total lepton intensities, and *Aguilar et al.* (2015) for measurements of the proton energy spectrum. See also http://www.ams02.org/ for more on the AMS-02 experiment.

2.10 Summary

This chapter gave an overview of some of the key features of the heliosphere as they pertain to CR modulation. The four major classes of CRs were discussed namely GCRs, SEPs, ACRs and Jovian electrons. Each of these groups of particles originate from different sources or regions, within the heliosphere and beyond. This study focuses on the GCRs.

In Section 2.3, the structure of the heliosphere was discussed using a hydrodynamic simulation that shows the spatial variation of the plasma temperature. From this simulation the main heliospheric structures result in apparent discontinuities. Moving outward from the Sun, these structures are the TS (at $\sim$ 90 AU), the HP (at $\sim$ 122 AU) and the BS (some distance beyond the HP). The TS is also known to be the primary source region of ACRs.

The structure of the heliosphere, including all the discontinuous boundaries it contains, is determined by the SW. The SW is therefore considered the main impetus that drives the heliosphere. As discussed in Section 2.5, the SW has two distinct components, namely the fast and slow SW streams, which are formed presumably as a result of the structure of the solar magnetic dipole field. The SW is accelerated within 0.3 AU to supersonic speeds – $\sim$ 400 km/s in the slow SW streams near the equatorial regions,

and $\sim 800\,\mathrm{km/s}$ in the fast SW streams at the polar regions – after which it slows down to subsonic speeds at the TS. Frozen into the SW is the solar magnetic field, so that the SW essentially carries the solar magnetic field out into the heliosphere to become the HMF.

Another important solar phenomenon that was discussed in Section 2.4 is the solar activity cycle. It has been established from SSN observations that the Sun has an $\sim$ 11-year sunspot (or solar activity) cycle, going from quiet solar conditions (or solar minimum) to very active solar conditions (or solar maximum) and back to solar minimum. During such an $\sim$ 11-year cycle, from one solar minimum to the next, the Sun's polarity reverses. A configuration where the solar magnetic field points outward in the Northern hemisphere and inward in the Southern hemisphere is referred to as an $A > 0$ polarity epoch, while an $A < 0$ polarity epoch refers to the opposite configuration. Figure 2.2 gives a detailed explanation of the solar activity cycle and also shows how the HMF magnitude measured at Earth is also correlated with the this cycle. During solar minimum the SW is structured, with fast SW streams in the polar regions and slow SW streams in the equatorial regions, as described above. This structure in the SW breaks down during solar maximum conditions, so that the slow and fast SW streams occur seemingly randomly at all latitudes (see Figure 2.3).

In Section 2.6 the structure of the HMF has been examined in light of three related HMF models. The pure Parker field has for long been considered as the standard model to describe the HMF. However, the pure Parker field has turned out to be too simplistic, which led to various modified versions of this model, namely the Jokipii-Kòta modification and the Smith-Bieber modification. A Fisk HMF model has also been proposed and developed as an attempt to account for effects caused by the differentially rotating nature of the Sun.

The HCS, as discussed in Section 2.7, is a 3D corotating structure that is formed as a result of the magnetic dipole structure of the Sun. Open magnetic field lines that emanate from the polar regions of the Sun (at opposite polarities) meet at this thin neutral current sheet. Even though the HCS is generally located near the equatorial regions, it has a wavy appearance – a result of the misalignment of the Sun's rotational and magnetic axes by the so-called HCS tilt angle. The tilt angle determines the waviness of the HCS and also serves as a proxy for solar activity, seeing that it too is correlated with the solar activity cycle (see Figure 2.9).

When combined, the HMF and HCS lead to gradient, curvature and current sheet drifts of charged CR particles. During an $A > 0$ polarity epoch, for example, positively charged particles drift into the heliosphere over the polar regions, and outward along the HCS and equatorial region. Over an $\sim$ 11-year solar cycle, during which the HMF polarity reverses, the drift directions of charged particles also reverse. After two consecutive $\sim$ 11-year cycles, the Sun's polarity returns to it's original configuration, giving

rise to a $\sim$ 22-year cycle called the Hale cycle. Drifts are essentially determined by the HMF polarity and also influenced by the waviness of the HCS. Consequently, CR intensities also undergo $\sim$ 11-year and $\sim$ 22-year cycles that are driven by alternating drift directions. These cycles are clearly observable in NM counts (see Figure 2.11). Since a particle's charge also determines its drift direction, oppositely charged CRs experience opposite drifts. This phenomenon of charge-sign dependent modulation is a key result of drift theory, and forms a central theme of this study.

Section 2.9 concluded with an overview of important satellite and spacecraft missions. The PAMELA mission along with some results were discussed, followed by discussions of the Ulysses spacecraft and the COSPIN/KET investigation, the Voyager spacecraft and the AMS-02 instrument on the International Space Station. PAMELA measurements were mainly used throughout this study, with particular focus on the period from 2006 to 2009.

Chapter 3

Numerical Modulation Model

3.1 Introduction

When GCRs enter the heliosphere, they are subject to various modulation processes. The four major modulation mechanisms are: outward convection by the SW, adiabatic deceleration due to the expanding SW, diffusion along and across the HMF and gradient, curvature and current sheet drifts in the HMF. These modulation processes are responsible for altering the differential intensities of CRs as a function of energy, position and time, and were first combined by *Parker* (1965) into a comprehensive TPE.

The focus of this work is to simulate the transport of CRs within the heliosphere by including all of the above-mentioned modulation processes into a full 3D numerical model. This chapter is therefore devoted to gaining a better understanding of the inner workings of such a model. The relevant theory behind the modulation processes is discussed, where special emphasis is given to diffusion and drifts. An overview of the Parker TPE is given, as well as the numerical method that is used in order to obtain CR energy spectra solutions throughout the heliosphere.

This study builds on the previous work of *Vos* (2012) and *Potgieter et al.* (2014a). Recent improvements that have been made to the modulation model are discussed, in particular the implementation of GPU computing and the advantages that this technology has to offer with regard to parallel processing.

3.2 The Transport Equation

Within a heliocentric spherical coordinate system that rotates with the Sun, the time-dependent TPE, as derived by *Parker* (1965), which describes the transport and modulation of CRs in the heliosphere, is given by

$$\underbrace{\frac{\partial f}{\partial t}}_{\text{a}} = -(\underbrace{\mathbf{V}_{sw}}_{\text{b}} + \underbrace{\langle \mathbf{v}_d \rangle}_{c}) \cdot \nabla f + \underbrace{\nabla \cdot (\mathbf{K}_s \cdot \nabla f)}_{d} + \underbrace{\frac{1}{3} (\nabla \cdot \mathbf{V}_{sw}) \frac{\partial f}{\partial \ln p}}_{e} + \underbrace{Q}_{f} \tag{3.1}$$

for the omnidirectional distribution function $f(\mathbf{r}, p, t)$ of CRs, where f is a function of position $\mathbf{r}$, particle momentum p and time t. The transport and modulation mechanisms contained in Equation 3.1 are: (a) time-dependent changes in the CR distribution function, (b) outward convection caused by the radially expanding SW velocity $\mathbf{V}_{sw}$ within the corotating frame, (c) CR gradient and curvature drift motions in the global HMF in terms of the averaged pitch angle guiding center drift velocity $\langle \mathbf{v}_d \rangle$, (d) spatial diffusion caused by the irregular HMF through the symmetric diffusion tensor $\mathbf{K}_s$, (e) adiabatic energy changes (deceleration or acceleration) determined by the SW divergence ($\nabla \cdot \mathbf{V}_{sw}$), and (f) possible additional sources of CRs within the heliosphere (for example, Jovian electrons), as they appear from left to right in Equation 3.1. See e.g. *Potgieter* (1998), *Fisk* (1999) and *Potgieter* (2013a, 2013b) for overviews of all the heliospheric transport processes and CR modulation in general.

Even though the numerical model includes a TS, the effects of diffusive shock acceleration (Fermi I) and stochastic acceleration (Fermi II) on CRs are excluded for the purpose of this study. For an overview of modulation models that account for these acceleration mechanisms in the TPE, see *Jokipii* (1986), *Potgieter and Moraal* (1988), *Langner* (2004), *Strauss* (2010) and *Ngobeni and Potgieter* (2010). See *Gleeson and Axford* (1967) for a rederivation of the TPE, as well as *Gleeson and Axford* (1968), *Jokipii and Parker* (1970) and *Schlickeiser* (2002) for details on further refinement of the TPE.

For this study the TPE is solved in a coordinate system that rotates with the Sun, which allows the use of a time-stationary expression for the HMF. This, in turn, enables one to obtain a time-independent solution for the TPE in Equation 3.1. That is,

$$\mathbf{V}_{sw} = \mathbf{V}^*_{sw} - \mathbf{\Omega} \times \mathbf{r} = V_{sw}\mathbf{e}_r - \Omega\, r \sin\theta \mathbf{e}_\phi, \tag{3.2}$$

where $\mathbf{V}^*_{sw}$ is the stationary SW velocity and $\mathbf{\Omega}$ is the rotational velocity of the Sun. In this case, the partial derivative of f with respect to time simply reduces to zero in Equation 3.1. Since the primary focus of this work is on particles of galactic origin, the source term in the TPE is also disregarded.

Even though the TPE is written in terms of momentum in Equation 3.1, it is generally solved in numerical modulation studies in terms of rigidity, which is defined as

$$P = \frac{pc}{q} = \frac{mvc}{Ze}, \tag{3.3}$$

where

$$\mathbf{p} = m\mathbf{v} = \frac{m_0\mathbf{v}}{\sqrt{1 - v^2/c^2}} \tag{3.4}$$

is the particle's momentum, $q = Ze$ its charge, v the speed (with $v = |\mathbf{v}|$), m the relativistic mass, m_0 the rest-mass and c the speed of light in a vacuum. For a relativistic particle, then, the total energy in terms of momentum is given by

$$E_p^2 = (T_p + E_{0\,p})^2 = p^2c^2 + m_0^2c^4, \tag{3.5}$$

with T_p the total kinetic energy and $E_{0\,p}$ the rest-mass energy of the particle ($E_0 = 0.938\,\text{GeV}$ for protons and $E_0 = 5.11 \times 10^{-4}\,\text{GeV}$ for electrons). In terms of rigidity, the total energy of such a particle is given by

$$E_p^2 = (T_p + E_{0\,p})^2 = P^2(Ze)^2 + E_{0\,p}^2. \tag{3.6}$$

If E is the total energy per nucleon, T the kinetic energy per nucleon and A the number of nucleons in the particle (i.e. the mass number), then the total energy per particle can be written as

$$A^2E^2 = (AT + AE_0)^2 = P^2(Ze)^2 + A^2E_0^2. \tag{3.7}$$

The kinetic energy per nucleon in terms of particle rigidity is

$$T = \sqrt{P^2\left(\frac{Ze}{A}\right)^2 + E_0^2} - E_0, \tag{3.8}$$

so that, conversely, the rigidity can be written in terms of kinetic energy per nucleon as

$$P = \left(\frac{A}{Ze}\right)\sqrt{(T + E_0)^2 - E_0^2} = \left(\frac{A}{Ze}\right)\sqrt{T\,(T + 2E_0)}. \tag{3.9}$$

These equations allow for the definition of another useful quantity, namely the ratio of particle speed to the speed of light, β, given by

$$\beta = \frac{v}{c} = \frac{pc}{mc^2} = \frac{PZe}{AE} = \frac{PZe}{\sqrt{P^2(Ze)^2 + A^2E_0^2}} = \frac{P}{\sqrt{P^2 + \left(\frac{A}{Ze}\right)^2 E_0^2}} \tag{3.10}$$

in terms of rigidity, or by

$$\beta = \frac{v}{c} = \frac{pc}{mc^2} = \frac{\sqrt{E_p^2 - E_{0\,p}^2}}{E_p} = \frac{\sqrt{E^2 - E_0^2}}{E} = \frac{\sqrt{T(T + 2E_0)}}{T + E_0} \tag{3.11}$$

in terms of kinetic energy. The relation between rigidity, kinetic energy and β is therefore summarized by

$$P = \frac{A}{Z}\sqrt{T\left(T + 2E_0\right)} = \left(\frac{A}{Z}\right)\beta\left(T + E_0\right). \tag{3.12}$$

3.2.1 Deriving an Expression for Differential Intensity

The particle density within a region d^3r, for particles with momenta between $\mathbf{p}$ and $\mathbf{p} + d\mathbf{p}$, is related to the full CR distribution function (which includes a pitch angle distribution) by

$$n = \int F(\mathbf{r}, \mathbf{p}, t)d^3p = \int_p p^2 \left[\int_\Omega F(\mathbf{r}, \mathbf{p}, t)d\Omega\right] dp, \tag{3.13}$$

where $d^3p = p^2 dp d\Omega$. The differential particle density, U_p, is related to n by

$$n = \int U_p(\mathbf{r}, p, t)dp, \tag{3.14}$$

which leads to

$$U_p(\mathbf{r}, p, t) = \int_\Omega p^2 F(\mathbf{r}, \mathbf{p}, t)d\Omega. \tag{3.15}$$

The omni-directional (i.e. pitch angle) average of $F(\mathbf{r}, \mathbf{p}, t)$ is calculated as

$$f(\mathbf{r}, p, t) = \frac{\int_\Omega F(\mathbf{r}, \mathbf{p}, t)d\Omega}{\int_\Omega d\Omega} = \frac{1}{4\pi}\int_\Omega F(\mathbf{r}, \mathbf{p}, t)d\Omega, \tag{3.16}$$

which leads to

$$U_p(\mathbf{r}, p, t) = 4\pi p^2 f(\mathbf{r}, p, t). \tag{3.17}$$

The differential intensity, in units of particles/unit area/unit time/unit momentum/unit solid angle, is defined as

$$j_p = \frac{vU_p(\mathbf{r}, p, t)}{\int_\Omega d\Omega} = \frac{vU_p(\mathbf{r}, p, t)}{4\pi} = vp^2 f(\mathbf{r}, p, t). \tag{3.18}$$

The particle speed can be eliminated from the above equation through substitution, where

$$\frac{\partial p}{\partial E} = \frac{1}{v}, \tag{3.19}$$

and with the relation $jdE = j_p dp$, so that

$$j(\mathbf{r}, p, t) = \frac{v}{4\pi} U_p \frac{dp}{dE} = \frac{1}{4\pi} U_p = p^2 f(\mathbf{r}, p, t), \tag{3.20}$$

where $j(\mathbf{r}, p, t)$ is the differential intensity in units of particles/area/time/energy/solid angle (see also *Strauss*, 2010).

3.2.2 The Diffusion Tensor

For a magnetic field without a θ-component, an HMF-aligned coordinate system has one axis parallel to the mean HMF in the $r\phi$-plane ($\mathbf{e}_\parallel$), another perpendicular to the first in the $\mathbf{e}_\theta$ direction ($\mathbf{e}_1$), and a third axis in the $r\theta$-plane perpendicular to the first two ($\mathbf{e}_2$), forming a right-handed coordinate system. Within such a system, an asymmetrical diffusion tensor can be set up, which consists of a symmetrical diffusion tensor $\mathbf{K}_s$ (as in Equation 3.1) and an asymmetrical drift tensor $\mathbf{K}_A$ (e.g. *Effenberger et al.*, 2012). This tensor contains the necessary diffusion and drift coefficients that determine the extent to which charged particles are transported and modulated, and is given by

$$\begin{aligned} \mathbf{K} &= \mathbf{K}_s + \mathbf{K}_A \\ \mathbf{K} &= \begin{bmatrix} \kappa_\parallel & 0 & 0 \\ 0 & \kappa_{\perp\theta} & 0 \\ 0 & 0 & \kappa_{\perp r} \end{bmatrix} + \begin{bmatrix} 0 & 0 & 0 \\ 0 & 0 & \kappa_A \\ 0 & -\kappa_A & 0 \end{bmatrix} = \begin{bmatrix} \kappa_\parallel & 0 & 0 \\ 0 & \kappa_{\perp\theta} & \kappa_A \\ 0 & -\kappa_A & \kappa_{\perp r} \end{bmatrix}. \end{aligned} \tag{3.21}$$

The diffusion coefficients (DCs) in the symmetrical tensor describe particle diffusion parallel to the mean HMF ($\kappa_\parallel$), as well as in the polar ($\kappa_{\perp\theta}$) and radial ($\kappa_{\perp r}$) directions perpendicular to it, while the coefficients in the asymmetrical tensor describe gradient, curvature and current sheet drifts experienced by particles. Figure 3.1 shows schematic illustrations of the directions in which these diffusion (left panel) and drift (right panel) coefficients operate with respect to the mean HMF.

By combining the symmetrical and asymmetrical tensors, it is possible to rewrite the TPE in a more compact form, as

$$-\mathbf{V}_{sw} \cdot \nabla f + \nabla \cdot (\mathbf{K} \cdot \nabla f) + \frac{1}{3} (\nabla \cdot \mathbf{V}_{sw}) \frac{\partial f}{\partial \ln p} = 0, \tag{3.22}$$

where the average guiding center drift velocity $\langle \mathbf{v}_A \rangle$ is now included in the asymmetrical tensor $\mathbf{K}$. Take note that both the source term Q and the time-dependent changes $\frac{\partial f}{\partial t}$ in Equation 3.1 have now been set to zero.

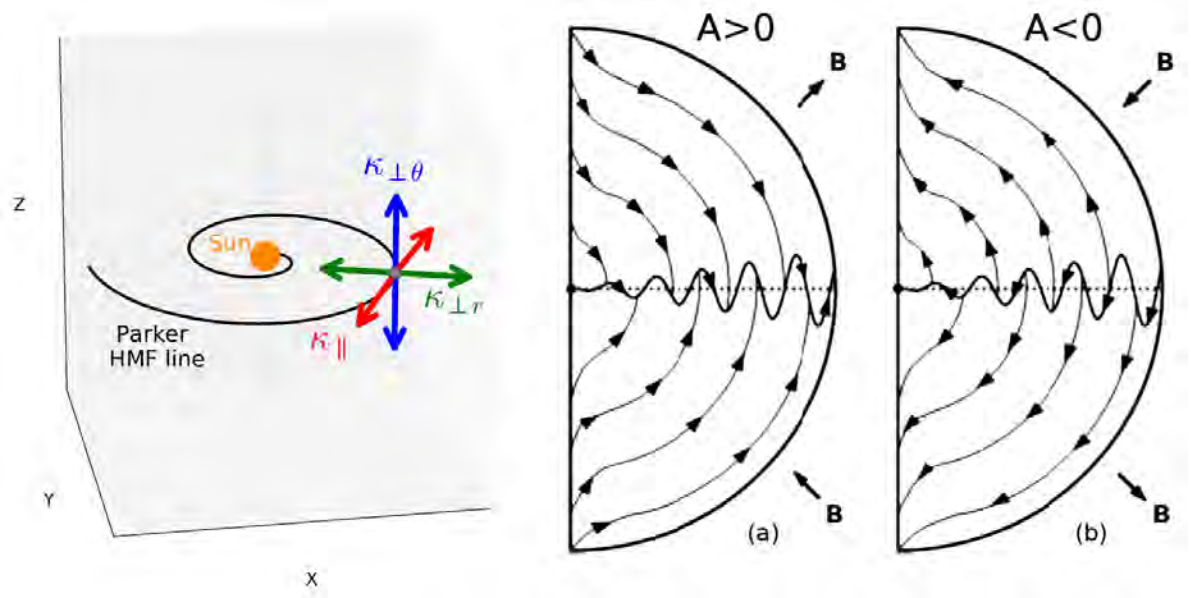

Figure 3.1: *Left panel:* The parallel and perpendicular components of the symmetrical diffusion tensor are illustrated here, with respect to a Parker HMF line in the equatorial plane emanating from the Sun. Diffusion directions parallel to the HMF line are represented by the red arrows ($\kappa_{\parallel}$), while diffusion in the radial ($\kappa_{\perp r}$) and polar ($\kappa_{\perp\theta}$) directions perpendicular to the HMF line are represented by the green and blue arrows respectively. *Right panel:* The global drift patterns (including current sheet drifts) for positively charged particles are illustrated here, for both the $A > 0$ (a) and $A < 0$ (b) magnetic polarity cycles (*Heber and Potgieter*, 2006).

3.2.3 The Transport Equation in Spherical Coordinates

Since the geometry of the heliosphere is assumed to be spherical, it is convenient to rewrite Equation 3.22 in terms of spherical coordinates. The HMF-aligned coordinate system is related to the spherical coordinate system by

$$\begin{aligned} \mathbf{e}_{\parallel} &= \cos\psi \mathbf{e}_r - \sin\psi \mathbf{e}_{\phi} \\ \mathbf{e}_1 &= \mathbf{e}_{\theta} \\ \mathbf{e}_2 &= \mathbf{e}_{\parallel} \times \mathbf{e}_1 = \sin\psi \mathbf{e}_r + \cos\psi \mathbf{e}_{\phi}, \end{aligned} \tag{3.23}$$

where ψ is the spiral angle, defined as the angle between the parallel component of the magnetic field (in the $\mathbf{e}_{\parallel}$ direction) and the radial direction $\mathbf{e}_r$. This coordinate system will be referred to as the magnetic coordinate system. The asymmetrical diffusion tensor $\mathbf{K}$ can therefore also be written in terms of spherical coordinates by specifying the appropriate transformation matrix $\mathbf{T}$, for which it is required that $\det(\mathbf{T}) = 1$. This matrix is given by

$$\mathbf{T} = \begin{bmatrix} \cos\psi & 0 & \sin\psi \\ 0 & 1 & 0 \\ -\sin\psi & 0 & \cos\psi \end{bmatrix}, \tag{3.24}$$

so that the diffusion tensor in Equation 3.21 in spherical coordinates is

$$\begin{bmatrix} \kappa_{rr} & \kappa_{r\theta} & \kappa_{r\phi} \\ \kappa_{\theta r} & \kappa_{\theta\theta} & \kappa_{\theta\phi} \\ \kappa_{\phi r} & \kappa_{\phi\theta} & \kappa_{\phi\phi} \end{bmatrix} = \mathbf{TKT}^T \tag{3.25}$$

$$= \begin{bmatrix} \cos\psi & 0 & \sin\psi \\ 0 & 1 & 0 \\ -\sin\psi & 0 & \cos\psi \end{bmatrix} \begin{bmatrix} \kappa_{\parallel} & 0 & 0 \\ 0 & \kappa_{\perp\theta} & \kappa_A \\ 0 & -\kappa_A & \kappa_{\perp r} \end{bmatrix} \begin{bmatrix} \cos\psi & 0 & -\sin\psi \\ 0 & 1 & 0 \\ \sin\psi & 0 & \cos\psi \end{bmatrix}$$

$$= \begin{bmatrix} \kappa_{\parallel}\cos^2\psi + \kappa_{\perp r}\sin^2\psi & -\kappa_A\sin\psi & \left(\kappa_{\perp r} - \kappa_{\parallel}\right)\cos\psi\sin\psi \\ \kappa_A\sin\psi & \kappa_{\perp\theta} & \kappa_A\cos\psi \\ \left(\kappa_{\perp r} - \kappa_{\parallel}\right)\cos\psi\sin\psi & -\kappa_A\cos\psi & \kappa_{\parallel}\sin^2\psi + \kappa_{\perp r}\cos^2\psi \end{bmatrix}.$$

The TPE in Equation 3.1 can now be written in terms of spherical coordinates as

$$\begin{aligned} &\left[\frac{1}{r^2}\frac{\partial}{\partial r}\left(r^2K_{rr}\right) + \frac{1}{r\sin\theta}\frac{\partial}{\partial\theta}\left(K_{\theta r}\sin\theta\right) + \frac{1}{r\sin\theta}\frac{\partial K_{\phi r}}{\partial\phi} - V_{sw}\right]\frac{\partial f}{\partial r} \\ +\ &\left[\frac{1}{r^2}\frac{\partial}{\partial r}\left(rK_{r\theta}\right) + \frac{1}{r^2\sin\theta}\frac{\partial}{\partial\theta}\left(K_{\theta\theta}\sin\theta\right) + \frac{1}{r^2\sin\theta}\frac{\partial K_{\phi\theta}}{\partial\phi}\right]\frac{\partial f}{\partial\theta} \\ +\ &\left[\frac{1}{r^2\sin\theta}\frac{\partial}{\partial r}\left(rK_{r\phi}\right) + \frac{1}{r^2\sin\theta}\frac{\partial K_{\theta\phi}}{\partial\theta} + \frac{1}{r^2\sin^2\theta}\frac{\partial K_{\phi\phi}}{\partial\phi} - \Omega\right]\frac{\partial f}{\partial\phi} \\ +\ &K_{rr}\frac{\partial^2 f}{\partial r^2} + \frac{K_{\theta\theta}}{r^2}\frac{\partial^2 f}{\partial\theta^2} + \frac{K_{\phi\phi}}{r^2\sin^2\theta}\frac{\partial^2 f}{\partial\phi^2} \\ +\ &\frac{2K_{r\phi}}{r\sin\theta}\frac{\partial^2 f}{\partial r\partial\phi} + \frac{1}{3r^2}\frac{\partial}{\partial r}\left(r^2V_{sw}\right)\frac{\partial f}{\partial\ln p} = 0, \end{aligned} \tag{3.26}$$

where it is assumed that the SW is axisymmetrical and directed radially outward, i.e. $\mathbf{V}_{sw} = V_{sw}\mathbf{e}_r$. This version of the TPE is rearranged to isolate the various terms that contribute to diffusion, drift, convection and adiabatic energy losses, so that Equation 3.26 now becomes:

$$\begin{aligned} &\overbrace{\left[\frac{1}{r^2}\frac{\partial}{\partial r}\left(r^2K_{rr}\right) + \frac{1}{r\sin\theta}\frac{\partial K_{\phi r}}{\partial\phi}\right]\frac{\partial f}{\partial r} + \left[\frac{1}{r^2\sin\theta}\frac{\partial}{\partial\theta}\left(K_{\theta\theta}\sin\theta\right)\right]\frac{\partial f}{\partial\theta}}^{\text{diffusion}} \\ +\ &\overbrace{\left[\frac{1}{r^2\sin\theta}\frac{\partial}{\partial r}(rK_{r\phi}) + \frac{1}{r^2\sin^2\theta}\frac{\partial K_{\phi\phi}}{\partial\phi} - \Omega\right]\frac{\partial f}{\partial\phi}}^{\text{diffusion}} \\ +\ &\overbrace{K_{rr}\frac{\partial^2 f}{\partial r^2} + \frac{K_{\theta\theta}}{r^2}\frac{\partial^2 f}{\partial\theta^2} + \frac{K_{\phi\phi}}{r^2\sin^2\theta}\frac{\partial^2 f}{\partial\phi^2} + \frac{2K_{r\phi}}{r\sin\theta}\frac{\partial^2 f}{\partial r\partial\phi}}^{\text{diffusion}} \end{aligned} \tag{3.27}$$

$$+ \overbrace{\left[-\langle \mathbf{v}_A \rangle_r\right] \frac{\partial f}{\partial r} + \left[-\frac{1}{r}\langle \mathbf{v}_A \rangle_\theta\right] \frac{\partial f}{\partial \theta} + \left[-\frac{1}{r\sin\theta}\langle \mathbf{v}_A \rangle_\phi\right] \frac{\partial f}{\partial \phi}}^{\text{drift}}$$
$$- \overbrace{V_{sw}\frac{\partial f}{\partial r}}^{\text{convection}}$$
$$+ \overbrace{\frac{1}{3r^2}\frac{\partial}{\partial r}\left(r^2 V_{sw}\right)\frac{\partial f}{\partial \ln p}}^{\text{adiabatic energy losses}} = 0.$$

The first three lines in the above equation contain the terms that describe the diffusion of CR particles, the fourth line contains the particle drift motions, and the fifth and sixth lines give the convection and adiabatic energy losses respectively.

3.3 Particle Diffusion

As a result of turbulent irregularities and fluctuations in the HMF, CRs undergo diffusion in the heliosphere through a process called pitch angle scattering, which can be described by quasi-linear theory (QLT), first introduced by *Jokipii* (1966). Such turbulence, generally interpreted either as waves (*Schlickeiser*, 1988) or dynamical turbulence (e.g. *Bieber and Matthaeus*, 1991), are described by the DCs that make up the elements of the asymmetrical tensor $\mathbf{K}$. Each DC is related to a mean free path (MFP) λ by

$$\kappa = \frac{v}{3}\lambda, \tag{3.28}$$

whereby each DC (in units of area/time) are transformed to a more tangible variable (in units of length). For the case when κ is the drift coefficient, λ is referred to as the drift scale (λ_A). A detailed study of the diffusion and drift coefficients in light of turbulence theory is beyond the scope of this study. See e.g. *Hattingh* (1998), *Minnie* (2006) and *Engelbrecht* (2008, 2013) for in depth studies about the elements of the diffusion tensor.

3.3.1 Parallel Diffusion

An expression for the pitch angle averaged parallel diffusion, in terms of the pitch angle Fokker-Planck coefficient $D_{\mu\mu}$, can be derived from the Fokker-Planck equation using the method of *Earl* (1974). It then follows that

$$\kappa_\parallel = \frac{v^2}{8}\int_{-1}^{1} \frac{\left(1-\mu^2\right)^2}{D_{\mu\mu}} d\mu, \tag{3.29}$$

where $D_{\mu\mu}$, which is essentially the rate of particle scattering, depends on the turbulence model considered (*Schlickeiser*, 2002; *Shalchi and Schlickeiser*, 2004). See *Teufel and Schlickeiser* (2002, 2003) for the derivation of piecewise continuous expressions for the parallel MFPs for two distinct turbulence models, namely dynamical magnetic slab turbulence and random sweeping slab turbulence. See *Langner* (2004), *Ndiitwani* (2005), *Engelbrecht* (2008), *Burger et al.* (2008) and *Strauss* (2010) for applications of these MFPs to numerical modulation studies.

The MFPs derived from such turbulence approaches often pose problems when it comes to reproducing observed CR energy spectra through modelling of heliospheric modulation. Consequently, a more simplified approach is followed for describing the DC rigidity dependence used in this study. This approach is found to be a good approximation to QLT (see also *Langner*, 2004; *Strauss*, 2010; *Nndanganeni*, 2016). For the spatial dependence, the parallel DC ($\kappa_{\parallel}$) is considered to be inversely proportional to the HMF magnitude.

The general expression used in this study to describe the parallel diffusion of protons, electrons and positrons is given by

$$\kappa_{\parallel} = \kappa_{\parallel 0}\,\beta\,\frac{B_0}{B}\left\{\frac{\left(\frac{P}{P_0}\right)^{c_3}+\left(\frac{P_k}{P_0}\right)^{c_3}}{1+\left(\frac{P_k}{P_0}\right)^{c_3}}\right\}^{\frac{c_2-c_1}{c_3}}\left(\frac{P}{P_0}\right)^{c_1}, \tag{3.30}$$

with $\kappa_{\parallel 0}$ a constant in units of $6\times10^{20}\,\mathrm{cm^2/s}$, and where $P_0 = 1\,\mathrm{GV}$ and $B_0 = 1\,\mathrm{nT}$ are added to obtain the correct units. Furthermore, c_1 and c_2 are dimensionless constants that respectively determine the slope of the rigidity dependence below and above a rigidity P_k, with c_3 another dimensionless constant (whose value varies between ~ 2 and ~ 7) that determine the smoothness of the transition between the P^{c_1} slope and the P^{c_2} slope at P_k. The rigidity dependence for $\kappa_{\parallel}$ is therefore essentially a double power law. Exact values for these variables are given in later chapters, for each of the particle species considered in this study.

Figure 3.2 shows a graph of the parallel MFPs ($\lambda_{\parallel}$) at Earth for GCR protons (top panel) and electrons (bottom panel). The solid black lines give the upper and lower limits for $\lambda_{\parallel}$ that followed from this study. These MFPs are based on Equation 3.30 and were required to reproduce simultaneously observed proton, electron and positron energy spectra from PAMELA between 2006 and 2009 (discussed in later chapters). The shaded regions represent the *Palmer* (1982) consensus values as a reference. Also shown are results from *Teufel and Schlickeiser* (2003) and *Shalchi and Schlickeiser* (2004), who used the damping model of dynamical turbulence to calculate electron and proton MFPs at Earth for two different turbulence geometries, namely slab turbulence (dashed red lines) and 2D turbulence (dashed green lines). For a detailed discussion of

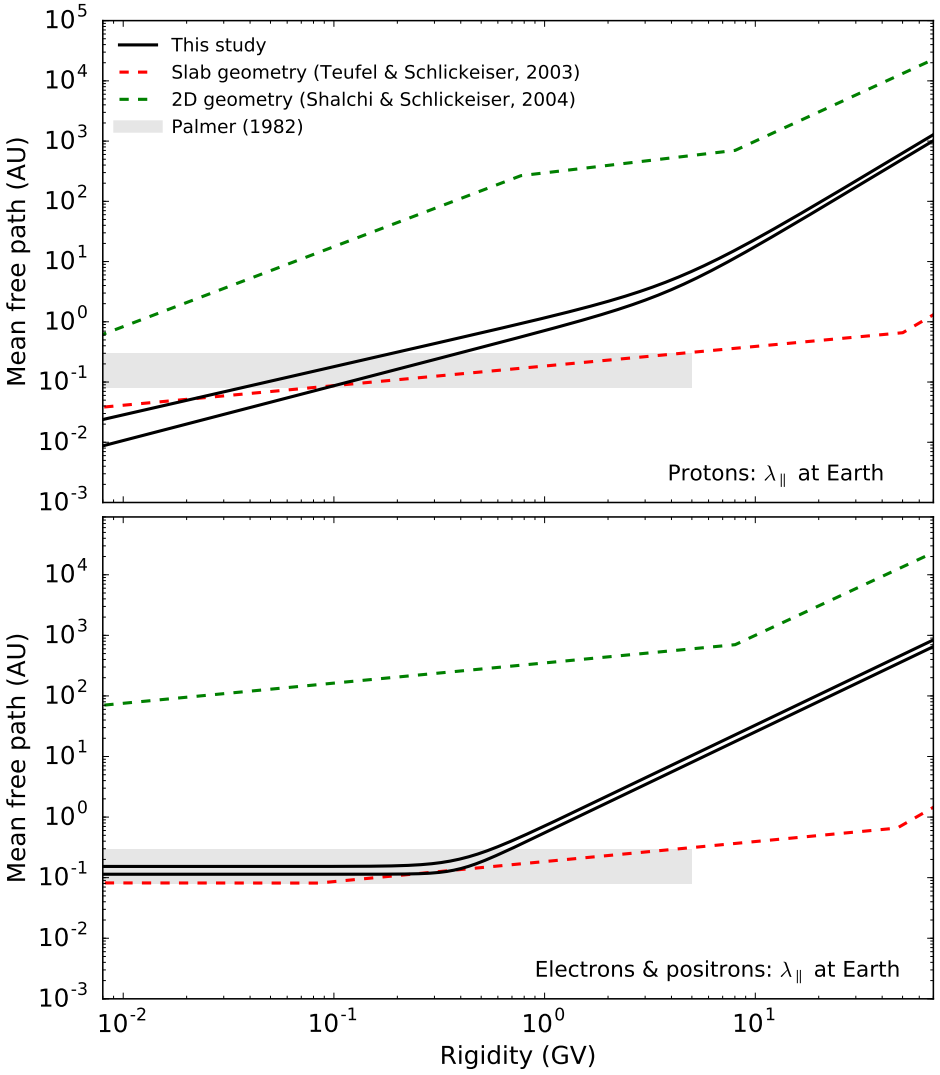

Figure 3.2: *Top panel:* The upper and lower limits of the parallel MFPs ($\lambda_\parallel$) for galactic protons at Earth, as used in this study, is given by the solid black lines, as a function of rigidity. The difference between these two sets of MFPs correspond to time-dependent changes (which are discussed further in Chapters 4 to 6). The red and green dashed lines represent the parallel MFPs obtained from the damping model of dynamical turbulence for two different turbulence geometries, namely pure slab geometry (from *Teufel and Schlickeiser*, 2003) and pure 2D geometry (from *Shalchi and Schlickeiser*, 2004) at Earth. The shaded region represents the Palmer consensus values as a reference (*Palmer*, 1982). *Bottom panel:* Similar to the top panel, but for galactic electrons and positrons at Earth.

these turbulence approaches, as well as a composite slab/2D approach to turbulence, see *Shalchi and Schlickeiser* (2004) and references therein.

For the rigidity range shown in Figure 3.2, the 2D turbulence geometry yields MFPs that are orders of magnitude larger than the slab turbulence geometry and serves to illustrate the scale of the variability that can occur depending on the assumed turbulence geometry. In comparison, the range of $\lambda_\parallel$ values that were obtained from this study is much more concise and still in general agreement with the magnitudes suggested by turbulence theory. Since these MFPs are based on PAMELA measurements, they give a

reliable estimate of what the parallel MFPs are expected to have been during 2006 and 2009, especially when considering that their rigidity dependence also exhibit important qualitative characteristics from turbulence theory.

The $\lambda_{\parallel}$ rigidity dependence from this study varies between $P^{0.8}$ and $P^{0.9}$ below $\sim$ 3 GV, which is steeper than the $P^{0.3}$ dependence suggested by the slab model, but weaker than the $P^{1.3}$ dependence that the 2D turbulence model assumes below $\sim$ 800 MV. Above $\sim$ 5 GV, the MFPs from this study take on a $P^{2.1}$ dependence, which, apart from the lower rigidity at which this transition occurs, is comparable to the P^{2} dependence of the slab turbulence model above $\sim$ 50 GV, and the $P^{1.6}$ dependence of the 2D turbulence model above $\sim$ 8 GV. MFPs from the latter model has a $P^{0.3}$ dependence between $\sim$ 800 MV and $\sim$ 8 GV.

In similar studies where PAMELA energy spectra between 2006 and 2009 were reproduced, *Vos* (2012) and *Potgieter et al.* (2014a) used the approach of *Jokipii and Kóta* (1989) to modify the Parker HMF model and reported a $\lambda_{\parallel}$ rigidity dependence for protons of between $P^{0.56}$ and $P^{0.28}$. When compared to the MFPs from these authors, the quantitative differences and steeper rigidity dependence for $\lambda_{\parallel}$ used here can be ascribed to the application of an improved HMF modification from *Smith and Bieber* (1991). See also *Raath et al.* (2015a) for a detailed discussion of the effect of HMF modifications on CR modulation in the heliosphere.

The rigidity dependence for the electron MFPs is also based on Equation 3.30, except that different parameter values (for $\kappa_{\parallel 0}$, c_1, c_2, c_3 and P_k) are chosen to obtain the correct shape. This is shown in the bottom panel of Figure 3.2, where the shaded region and all the lines are similar to that of protons in the top panel, as explained before. Below $\sim$ 300 MV, $\lambda_{\parallel}$ for electrons become independent of rigidity and take on constant values between $\sim$ 0.1 AU and $\sim$ 0.2 AU, while above $\sim$ 500 MV they have a $P^{1.67}$ dependence. The electron MFPs obtained from this study are based on PAMELA measurements and therefore represent a definitive set of coefficients that describe the actual diffusion and modulation experienced by electrons between 2006 and 2009. These MFPs are also well contained within the upper and lower limits of $\lambda_{\parallel}$ as suggested by the two different turbulence regimes (dashed lines).

According to the slab turbulence model of *Teufel and Schlickeiser* (2003), the rigidity dependence of $\lambda_{\parallel}$ for electrons is the same as that of protons for rigidities above $\sim$ 100 MV. Below $\sim$ 100 MV, $\lambda_{\parallel}$ becomes independent of rigidity and takes on a value of $\sim$ 0.08 AU. This is also the case for the 2D turbulence model from *Shalchi and Schlickeiser* (2004), where $\lambda_{\parallel}$ for electrons is identical to that of protons above $\sim$ 800 MV. Below $\sim$ 800 MV electron MFPs from this turbulence model maintain a $P^{0.3}$ dependence. For the current study, strong rigidity dependencies in $\lambda_{\parallel}$ for electrons (above $\sim$ 500 MV) and for protons (above $\sim$ 4 GV) were required to sufficiently increase MFPs and reduce modulation at these rigidities, in order to comply with PAMELA measurements.

Since the parallel MFPs that follow from this study were obtained by self-consistently reproducing simultaneous proton, electron and positron measurements from PAMELA, they are considered to be reliable estimates of $\lambda_{\parallel}$ values for protons and electrons during the solar minimum period from 2006 to 2009.

3.3.2 Perpendicular Diffusion

The scattering of CR particles perpendicular to the HMF can be caused either as a result of the particles' gyrocentres that are displaced transverse to the mean HMF through scattering, or due to the random walk of the magnetic field lines themselves. These processes are collectively taken into account in numerical models via the perpendicular DC $\kappa_{\perp}$. As previously mentioned, $\kappa_{\perp}$ can be subdivided into two possibly independent coefficients describing perpendicular diffusion in the radial ($\kappa_{\perp r}$) and polar ($\kappa_{\perp \theta}$) directions. It has also been established that $\kappa_{\perp}$ plays a significant role in the modulation of CRs (*Potgieter*, 1996, 2000; *Ferreira et al.*, 2000). See also *Jokipii* (2001) for further theoretical work with regard to $\kappa_{\perp}$.

In the presence of parallel diffusion, a pure field line random walk scenario gives an insufficient description of perpendicular diffusion, because particles sometimes retrace their paths after they backscatter – a process that hasn't been taken into account until the non-linear guiding center (NLGC) theory of particle diffusion proposed by *Matthaeus et al.* (2003). According to this theory, the process of perpendicular diffusion is a combination of field line random walk, backscattering from parallel diffusion and the transfer of particles across field lines due to the perpendicular complexity of the magnetic field (see also *Bieber et al.*, 2004). This theory for perpendicular diffusion was later improved by *Shalchi* (2006), who proposed an extended nonlinear guiding center theory (ENLGC), followed by a unified NLGC theory (UNLGC) by *Shalchi* (2010). See also e.g. *Shalchi* (2009) and *Pei et al.* (2010a) for overviews of nonlinear CR diffusion theories and comparisons with observations.

According to the NLGC approach, perpendicular MFPs are calculated using parallel MFPs. Figure 3.3 gives an example of the perpendicular MFPs (dashed lines) for protons (left) and electrons (right), calculated using NLGC theory and the associated parallel MFPs (solid lines), as taken from *Bieber et al.* (2004). Above $\sim 10\,\mathrm{GV}$, $\lambda_{\parallel}$ for both protons and electrons increase with a stronger rigidity dependence than at lower rigidities. Below $\sim 10\,\mathrm{MV}$, $\lambda_{\parallel}$ for electrons begin to increase, which favour observations of Jovian electrons according to *Bieber et al.* (2004). In addition to the strong rigidity dependence of both $\lambda_{\parallel}$ and $\lambda_{\perp}$, a key feature that follows from NLGC theory is that $\lambda_{\perp}$ is scaled with a weaker rigidity dependence compared to $\lambda_{\parallel}$, which is particularly evident at higher rigidities. The NLGC description of perpendicular diffusion is not followed in this study. However, the important qualitative feature of scaling $\lambda_{\perp}$ different than $\lambda_{\parallel}$, especially at higher rigidities, is incorporated.

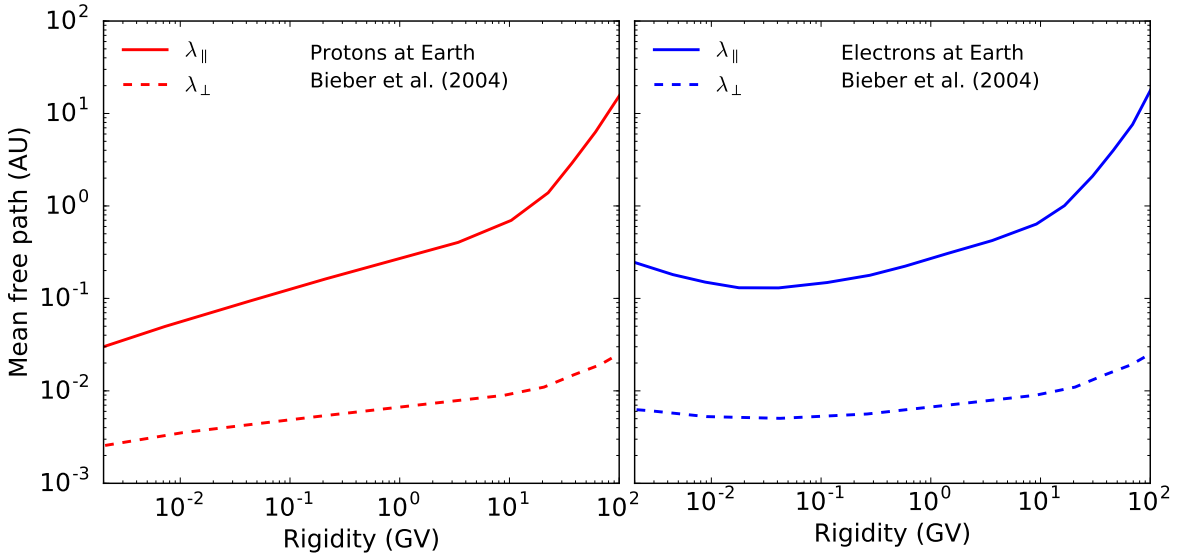

Figure 3.3: Parallel (solid lines) and perpendicular (dashed lines) MFPs calculated by *Bieber et al.* (2004) at Earth, for protons (left panel) and electrons (right panel), as a function of rigidity. The perpendicular MFPs were calculated according to NLGC theory by using the parallel MFPs shown here. No distinction is made between perpendicular diffusion in the radial and polar directions (i.e. $\lambda_\perp = \lambda_{\perp r} = \lambda_{\perp\theta}$).

In this work, for rigidities above P_k, $\kappa_\perp$ is scaled with a slightly weaker dependence compared to $\kappa_\parallel$, which, after converting to MFPs, results in a non-constant $\lambda_\perp/\lambda_\parallel$ ratio (see e.g. *Shalchi et al.*, 2004, and *Pei et al.*, 2010a). This translates to using different values for c_2 in Equation 3.30, namely $c_{2\parallel}$ for $\kappa_\parallel$ and $c_{2\perp}$ for $\kappa_\perp$. Exact values for these variables depend on the particle species and are discussed in detail in later chapters.

It also follows from this study that $\kappa_{\perp r}$ was required to be scaled by 2 % of $\kappa_\parallel$ below P_k, while $\kappa_{\perp\theta}$ had to be scaled by 1 % of $\kappa_\parallel$. This differs from what *Vos* (2012) and *Potgieter et al.* (2014a) used, but is more in line with turbulence theory. Similar scaling factors were reported by *Zhao et al.* (2014) and *Manuel et al.* (2014).

Observations from the Ulysses spacecraft (e.g. *Heber and Potgieter*, 2006, and references therein) also revealed that the latitude dependence of GCR protons is significantly weaker than predicted by classical drift models (e.g. *Potgieter and Haasbroek*, 1993), which led *Kóta and Jokipii* (1995) to propose the concept of an anisotropic $\kappa_\perp$, where $\kappa_{\perp\theta} > \kappa_{\perp r}$ in the off-equatorial regions (e.g. *Potgieter*, 1996; *Burger et al.*, 2000). The effect of such an approach to perpendicular diffusion on CR modulation was studied in detail by e.g. *Ferreira et al.* (2000).

The parallel DCs are given by

$$\kappa_{\perp r} = \kappa^0_{\perp r}\kappa_\parallel \tag{3.31}$$

and

$$\kappa_{\perp\theta} = h_{\perp\theta}\,\kappa^0_{\perp\theta}\,\kappa_\parallel, \tag{3.32}$$

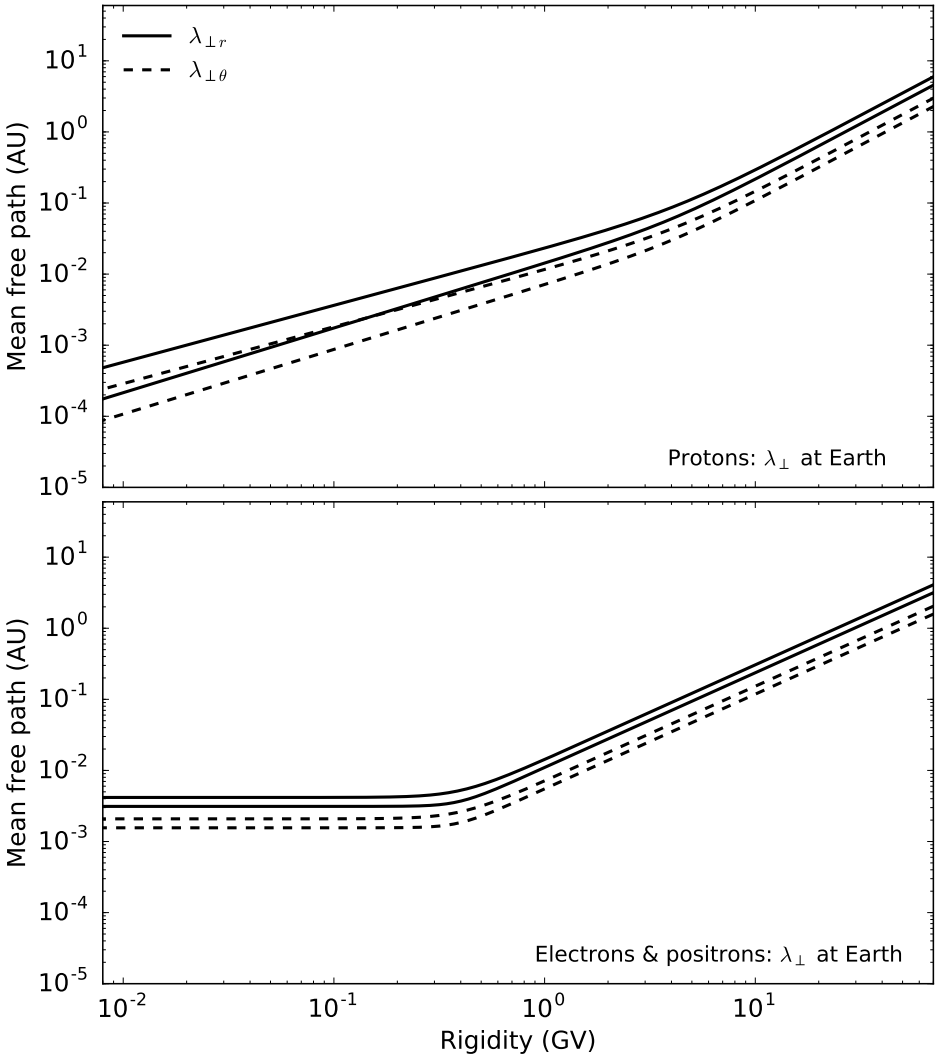

Figure 3.4: Similar to Figure 3.2, but for diffusion perpendicular to the HMF in the radial ($\lambda_{\perp r}$) and perpendicular ($\lambda_{\perp\theta}$) directions. Only results from this study are shown.

where $\kappa^0_{\perp r} = 0.02$ and $\kappa^0_{\perp\theta} = 0.01$ are the dimensionless scaling factors and $h_{\perp\theta}$ is a latitude-dependent function that takes care of the anisotropy in $\kappa_{\perp\theta}$, and is given by

$$h_{\perp\theta} = A^+ + A^- \tanh\left[\frac{1}{\Delta\theta}\left(\widetilde{\theta} - \frac{\pi}{2} + \theta_F\right)\right]. \tag{3.33}$$

Here $A^+ = \frac{d_{\perp\theta}+1}{2}$, $A^- = \frac{d_{\perp\theta}-1}{2}$ and $\Delta\theta = 1/8$, with

$$\widetilde{\theta} = \begin{cases} \theta & \text{for } \theta \geq \frac{\pi}{2} \\ \pi - \theta & \text{for } \theta < \frac{\pi}{2}, \end{cases} \tag{3.34}$$

and

$$\theta_F = \begin{cases} \frac{-35^\circ\pi}{180^\circ} & \text{for } \theta \geq \frac{\pi}{2} \\ \frac{35^\circ\pi}{180^\circ} & \text{for } \theta < \frac{\pi}{2}, \end{cases} \tag{3.35}$$

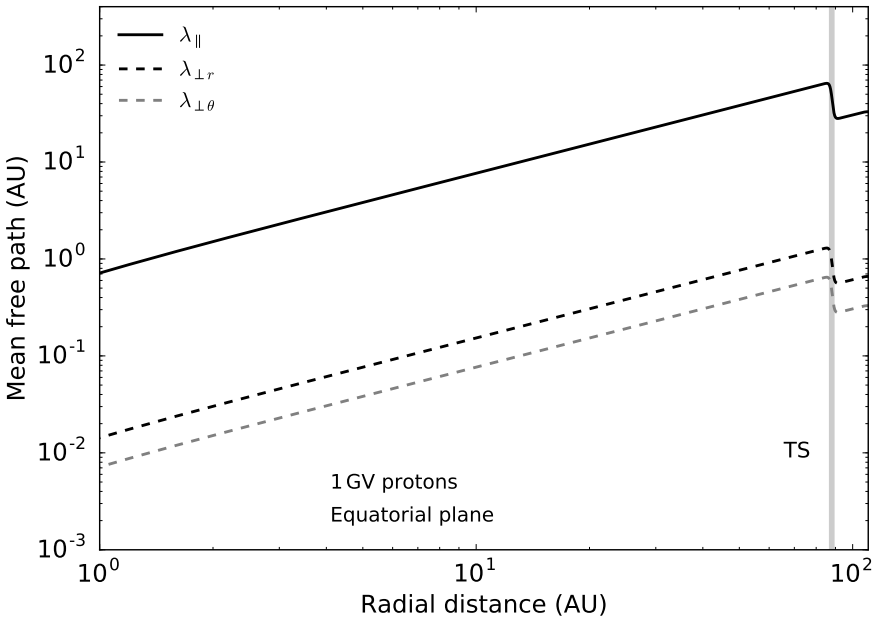

Figure 3.5: The MFPs for $\lambda_\parallel$, $\lambda_{\perp r}$ and $\lambda_{\perp\theta}$ are given as a function of radial distance, along with the drift scale λ_A (to be discussed in the next section), for 1 GV protons as used in this study. The TS position is given by the vertical shaded band at 88 AU.

where $d_{\perp\theta}$ is a dimensionless constant that determines the enhancement factor of $\kappa_{\perp\theta}$ from its value in the equatorial plane toward the poles, with respect to $\kappa_\parallel$.

Figure 3.4 is similar to Figure 3.2, but gives the rigidity dependence of $\lambda_{\perp r}$ (solid black lines) and $\lambda_{\perp\theta}$ (dashed black lines) for protons (top panel) and electrons (bottom panel) at Earth, as used in this study. Below ~ 3 GV, $\lambda_\perp$ for protons (in both the radial and polar directions), has a rigidity dependence that varies between $P^{0.8}$ and $P^{0.9}$, similar to $\lambda_\parallel$. Above ~ 5 GV, $\lambda_\perp$ has a slightly weaker $P^{1.58}$ dependence compared to $\lambda_\parallel$. The perpendicular MFPs for electrons are independent of rigidity below ~ 300 MV, with a $P^{1.34}$ dependence above ~ 500 MV. In some cases NLGC theory suggests a very weak, or even an independent, rigidity dependence for $\lambda_\perp$ below ~ 10 GV (e.g. *Pei et al.*, 2010a), which, according to the modulation model, produces excessively large modulation above ~ 1 GV.

3.3.3 Radial Dependence of the Diffusion Coefficients

Figure 3.5 gives the radial dependence of $\lambda_\parallel$, $\lambda_{\perp r}$ and $\lambda_{\perp\theta}$ for 1 GV protons (solid and dashed lines), as a function of radial distance. The parallel DC, given by Equation 3.30, scales spatially as B^{-1}, where $B \propto r^{-1}$ in the equatorial regions (from Equation 2.8). The Smith-Bieber modification applied to the HMF (see Chapter 2) also causes the HMF magnitude to have a r^{-1} dependence in the polar regions, which is different than the r^{-2} dependence for a pure Parker HMF. As a result, the radial dependence of $\lambda_\parallel$ is proportional to r for $r \gtrsim 1$ AU. For radial distances smaller than ~ 1 AU, B

becomes proportional to r^{-2}, so that $\lambda_{\parallel} \propto r^2$ in this region (see also *Raath et al.*, 2015a). Beyond the TS position, the HMF field lines are compressed, resulting in larger HMF magnitudes and in turn smaller MFPs, as shown at 88 AU in Figure 3.5.

The perpendicular MFPs ($\lambda_{\perp r}$ and $\lambda_{\perp \theta}$) have a similar radial dependence than $\lambda_{\parallel}$, which follows from Equations 3.31 and 3.32. Electron MFPs also have the same radial dependencies and differ only in magnitude. A similar radial dependence for the parallel and perpendicular MFPs was used by e.g. *Ndiitwani* (2005), *Ngobeni* (2015) and *Nndanganeni* (2016). The drift scale λ_A and the corresponding drift coefficient κ_A are discussed in the next section. A further discussion of the radial and polar dependence of the DCs is given at the end of Chapter 4.

3.4 Particle Drifts

The significance of particle drifts, not included in the original derivation of the TPE, was not realized until *Jokipii et al.* (1977) pointed out that this process might contribute to CR modulation. This was later confirmed by modulation models that included drift effects (e.g. *Potgieter and Moraal*, 1985). The global background HMF induces drift motions in CRs, which originate as a result of gradients in the HMF magnitude, the curvature of the field and any sudden changes in the field direction, like those found at the HCS (e.g. *Burger and Potgieter*, 1989), in addition to a charge asymmetry as a result of the sensitivity of drifts to the HMF polarity. See Figure 3.1 (right panel) for a schematic illustration of the drift directions experienced by positively charged particles during both magnetic polarity cycles.

The components of the average guiding center drift velocity, due to the presence of HMF gradients and curvatures, as well as the HCS, are given in the fourth line of Equation 3.27. It also follows from Equation 3.26 that the drift components, in the radial, polar and azimuthal directions, are given by

$$\begin{aligned} \langle \mathbf{v}_A \rangle_r &= -\frac{A^*}{r \sin\theta} \frac{\partial}{\partial \theta} \left(\sin\theta K_{\theta r} \right), \\ \langle \mathbf{v}_A \rangle_\theta &= -\frac{A^*}{r} \left[\frac{1}{\sin\theta} \frac{\partial}{\partial \phi} (K_{\phi\theta}) + \frac{\partial}{\partial r} (r K_{r\theta}) \right], \\ \langle \mathbf{v}_A \rangle_\phi &= -\frac{A^*}{r} \frac{\partial}{\partial \theta} (K_{\theta\phi}), \end{aligned} \tag{3.36}$$

where A^* is a constant that denotes the HMF polarity. Every ~ 11 years A alternates between a value of $+1$, for when the HMF is directed outward in the Northern hemisphere and inward in the Southern hemisphere, and a value of -1, for when the HMF is directed inward in the Northern hemisphere and outward in the Southern hemisphere. In essence,

A^* determines the drift directions of charged particles, and is given by

$$A^* = \begin{cases} +1 & \text{when } qA > 0 \\ -1 & \text{when } qA < 0, \end{cases} \tag{3.37}$$

with q the particle charge.

In the general case, the average pitch angle guiding center drift velocity is given by

$$\langle \mathbf{v}_A \rangle = \frac{pv}{3q} \frac{(\omega\tau_A)^2}{1+(\omega\tau_A)^2} \nabla \times \frac{\mathbf{B}}{B^2}, \tag{3.38}$$

where the suppression of drifts via scattering, due to the presence of turbulence, is accounted for (e.g. *Giacalone*, 1999; *Minnie et al.*, 2007; *Tautz and Shalchi*, 2012; *Ngobeni and Potgieter*, 2015). The particle gyro-frequency is given by ω, with τ_A a time scale related to scattering. The maximal Larmor radius of a particle is given by

$$r_L = \frac{mv}{qB} = \frac{P}{Bc}, \tag{3.39}$$

so that Equation 3.38 can be rewritten as

$$\begin{aligned} \langle \mathbf{v}_A \rangle &= \nabla \times \frac{pc}{q} \frac{v}{c} \frac{1}{3B} \frac{(\omega\tau_A)^2}{1+(\omega\tau_A)^2} \frac{\mathbf{B}}{B} \\ &= \nabla \times \frac{P\beta}{3B} \frac{(\omega\tau_A)^2}{1+(\omega\tau_A)^2} \frac{\mathbf{B}}{B} \\ &= \nabla \times r_L \frac{v}{3} \frac{(\omega\tau_A)^2}{1+(\omega\tau_A)^2} \mathbf{e}_B, \end{aligned} \tag{3.40}$$

where $\mathbf{e}_B = \mathbf{B}/B$ is a unit vector directed along $\mathbf{B}$.

When scattering due to turbulence is small, particles undergo a large number of gyrations before being scattered, leading to a scenario where the drift velocity can assume its so-called maximal weak scattering value. This leads to the approximation where $\omega\tau_A \gg 1$, which reduces Equation 3.40 to the well known weak-scattering limit of the guiding center drift velocity for an ensemble of charged particles (e.g. *Rossi and Olbert*, 1970; *Burger et al.*, 1985), given by

$$\begin{aligned} \langle \mathbf{v}_A \rangle^{ws} &= \nabla \times \frac{v}{3} r_L \mathbf{e}_B \\ &= \nabla \times \kappa_A \mathbf{e}_B, \end{aligned} \tag{3.41}$$

where the weak-scattering drift coefficient is introduced and given by

$$\kappa_A^{ws} = \frac{v}{3} r_L = \frac{pv}{3qB}. \tag{3.42}$$

The drift coefficient is related to the drift scale through

$$\lambda_A = \kappa_A \frac{3}{v}, \tag{3.43}$$

so that for the weak-scattering scenario, the drift scale becomes $\lambda_A^{ws} = r_L$. Even though the exact form of the suppression factor on κ_A^{ws} due to particle scattering is not yet known, it continues to be studied (e.g. *Minnie et al.*, 2007; *Burger and Visser*, 2010; *Strauss*, 2010; *Ngobeni and Potgieter*, 2015).

The average drift velocity in a Parker HMF (which can also include a Smith-Bieber modification) follows from Equation 3.41 (e.g. *Hattingh*, 1998; *Ferreira*, 2002) as

$$\begin{aligned} \langle \mathbf{v}_A \rangle &= \nabla \times \kappa_A \mathbf{e_B} \\ &= \nabla \times (\kappa_A \mathbf{e}_B) \left[1 - 2H(\theta - \theta')\right] + 2\delta(\theta - \theta')\kappa_A \mathbf{e}_B \times \nabla(\theta - \theta'), \end{aligned} \tag{3.44}$$

for both the weak-scattering and modified drift scenarios, with δ the Dirac-Delta function given by

$$\delta(\theta - \theta') = \begin{cases} \infty & \text{if } \theta = \theta' \\ 0 & \text{if } \theta \neq \theta'. \end{cases} \tag{3.45}$$

The first term in Equation 3.44 describes the particle drifts due to gradients and curvatures in the HMF, while the second term describes drift motions along the HCS.

In this study, the suppression of drifts due to scattering is taken into account, where it is assumed that $(\omega\tau_A) \propto P$. This gives

$$\kappa_A = \kappa_{A0} \frac{\beta P}{3B} \frac{\left(\frac{P}{P_{A0}}\right)^2}{1 + \left(\frac{P}{P_{A0}}\right)^2}, \tag{3.46}$$

with P_{A0} (in GV) added to retain the correct units and $\kappa_{A0} \in [0.0, 1.0]$ a dimensionless parameter that determines the amount of drift (see e.g. *Burger et al.*, 2000, and *Burger et al.*, 2008, for similar approaches).

Ngobeni (2015) studied the spatial and rigidity dependence of $\omega\tau_A$ and the effect that it has on the drift coefficient and the modulation of GCR carbon in the heliosphere. It was found that, to a first-order estimate, values for $\omega\tau_A$ range from 0 to 5. Four scenarios for $\omega\tau_A$, from *Burger et al.* (2000), *Burger and Visser* (2010) and *Engelbrecht and Burger* (2013), were considered, where it was shown that these different scenarios had significant effects on the weak scattering drift coefficient and the subsequent differential intensities at 1 AU. The choice for $\omega\tau_A$ also influenced the interplay between drifts and perpendicular diffusion in the polar direction, which alters the total drift effects experienced by CRs.

Even though *Potgieter et al.* (1989) showed that full drifts at all energies are highly

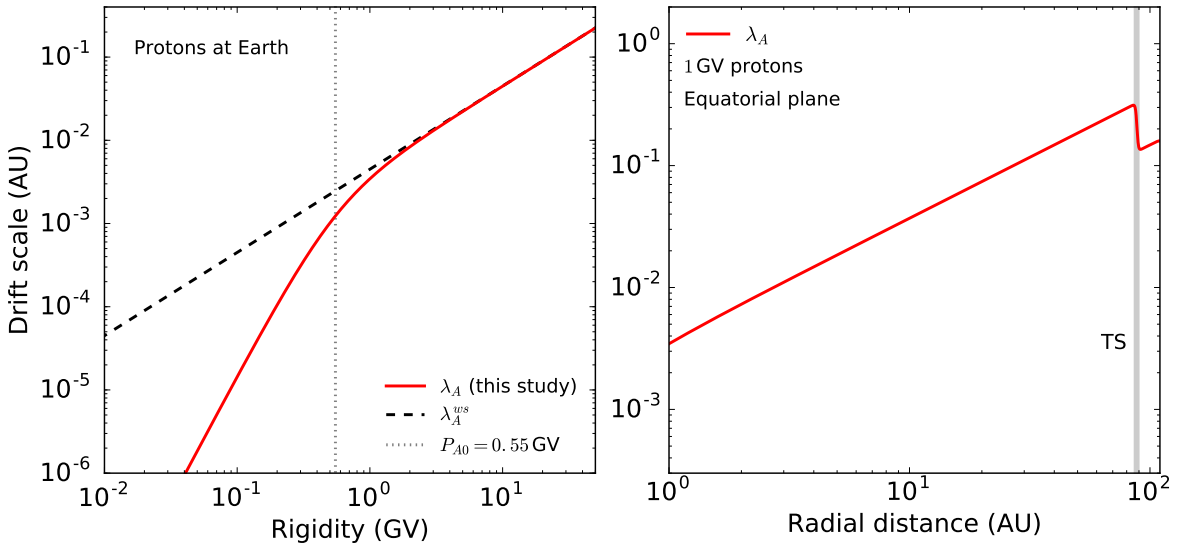

Figure 3.6: *Left panel:* The drift scale for protons at Earth, as used in this study, is given by the solid red line as a function of rigidity. Drifts are modified below $P_{A0} = 0.55$ GV, indicated by the vertical dotted line. The dashed black line shows the weak scattering limit for drifts, where scattering due to turbulence is neglected. *Right panel:* The drift scale as a function of radial distance in the equatorial plane for 1 GV protons, as used in this study. The TS position is shown by the grey band at 88 AU.

unlikely, such a scenario, as a result of the unusual minimum of solar cycle 24, is investigated in this study. It is therefore assumed that $\kappa_{A0} = 1.0$ to obtain maximum possible drift effects (100 %), with $P_{A0} = 0.55$ GV, which is comparable to what *Langner* (2004), *Strauss* (2010) and *Manuel* (2013) used. During solar maximum, however, *Ferreira and Potgieter* (2004) showed that κ_{A0} should be less than 10 % in order to reproduce observations. See also *Ndiitwani et al.* (2005).

Figure 3.6 shows the rigidity dependence (left panel) of the drift scale (λ_A) for protons at the position of Earth. The weak-scattering limit of λ_A (see Equation 3.42) is given by the dashed black line. The modified drift scenario is shown by the red line, where drifts are scaled down from the weak-scattering limit below $P_{A0} = 0.55$ GV (dotted grey line), so that drifts can be neglected for very low rigidities, i.e. $P \ll P_{A0}$. Above $\sim P_{A0}$, λ_A is proportional to P. Figure 3.6 also shows the radial dependence of λ_A for 1 GV protons in the equatorial plane (right panel). The position of the TS is given by the vertical grey band at 88 AU. At this rigidity, λ_A is representative of the Larmor gyro-radius. As discussed above, the spatial dependence of λ_A is governed by B, and therefore also by $\mathbf{V}_{sw}$. Consequently, since B changes with time, temporal changes are expected in the drift scale as well as the DCs.

3.5 The Numerical Model

3.5.1 A Brief History of Numerical Modulation Models

The numerical modelling of CR modulation in the heliosphere began with *Fisk* (1971), who, assuming a spherically symmetric heliosphere, developed the first one-dimensional (1D) steady-state numerical solution of the TPE, with radial distance as the only spatial variable. A polar angle dependence was later included in this model by *Fisk* (1975, 1976), to form an axisymmetric two-dimensional (2D) model, with further developments made by *Moraal and Gleeson* (1975). Gradient and curvature drifts for a flat HCS were included in separately developed steady-state 2D models by *Moraal et al.* (1979) and *Jokipii and Kopriva* (1979), followed by the first 2D model wherein the waviness of the HCS was emulated (*Potgieter*, 1984; see also e.g. *Potgieter and Moraal*, 1985, and *Burger*, 1987). An improved 2D wavy current sheet model was also developed by *Hattingh* (1993) and *Langner* (2004).

The first 3D steady-state model, which included particle drifts, as well as a wavy HCS, was developed by *Kóta and Jokipii* (1983) and later by *Hattingh* (1998). It was also shown by *Hattingh* (1998) and *Ferreira* (1998) that the 2D and 3D steady-state models delivered remarkably similar results, thereby validating the use of both these models. Steady-state 3D models, which included the Jovian magnetosphere as a source of low-energy electrons, were independently developed by *Fichtner et al.* (2000) and *Ferreira et al.* (2001a).

Perko and Fisk (1983) developed the first spherically symmetric time-dependent model which was later extended to two and three dimensions (*le Roux*, 1990; *Fichtner et al.*, 2001). The effects of a heliospheric TS, i.e. diffusive shock acceleration, was first incorporated into an axisymmetric model by *Jokipii* (1986), after which *Potgieter* (1989) developed a 2D shock acceleration model. In the following years *Steenkamp* (1995) independently developed a 2D shock acceleration model with a discontinuous transition in the TS, while *le Roux et al.* (1996) developed a similar model, but with a continuous TS transition. *Kissmann et al.* (2004) developed a 3D time-dependent model that could be used to study the effect of CIRs on electron intensities. *Sternal et al.* (2011) extended this time-dependent model by introducing a Fisk-type HMF.

Langner (2004) used a 2D time-dependent TS model based on various other 2D steady-state and time-dependent shock acceleration models. This model, significantly modified, was also used by *Strauss* (2010), *Ngobeni* (2015) and *Prinsloo* (2016). See also *Strauss et al.* (2010a, 2010b).

Several stochastic modulation models were also developed by *Zhang* (1999), *Florinski and Pogorelov* (2009), *Pei et al.* (2010b), *Strauss et al.* (2011a), *Strauss* (2013), *Luo et al.* (2013) and *Kopp et al.* (2014). In these models stochastic differential equations (SDEs) are used to solve the TPE in 3D. A major advantage of SDE models over finite difference

models is that CR propagation times and energy losses can be calculated from them (*Strauss et al.*, 2011b).

For this study, however, an improved 3D steady-state model of *Hattingh* (1998) is used, which includes a wavy HCS and a heliosheath, but without shock acceleration at the TS. See *Manuel* (2013) for a detailed review of the history of numerical modulation models.

3.5.2 Numerical Scheme

In order to solve the TPE within a spherical coordinate system that rotates with the Sun, Equation 3.26 can be written in a condensed form, in terms of rigidity, as

$$\begin{aligned} & a_0(r,\theta,\phi,P)\frac{\partial f}{\partial r} + b_0(r,\theta,\phi,P)\frac{\partial f}{\partial \theta} + c_0(r,\theta,\phi,P)\frac{\partial f}{\partial \phi} + d_0(r,\theta,\phi,P)\frac{\partial^2 f}{\partial r \partial \phi} \\ + \;& e_0(r,\theta,\phi,P)\frac{\partial^2 f}{\partial r^2} + l_0(r,\theta,\phi,P)\frac{\partial^2 f}{\partial \theta^2} + m_0(r,\theta,\phi,P)\frac{\partial^2 f}{\partial \phi^2} \\ + \;& s_0(r,\theta,\phi,P)\frac{\partial f}{\partial \ln P} = 0, \end{aligned} \tag{3.47}$$

with

$$\begin{aligned} a_0(r,\theta,\phi,P) &= \frac{1}{r^2}\frac{\partial}{\partial r}\left(r^2 K_{rr}\right) + \frac{1}{r\sin\theta}\frac{\partial}{\partial \theta}\left(K_{\theta r}\sin\theta\right) + \frac{1}{r\sin\theta}\frac{\partial K_{\phi r}}{\partial \phi} - V_{sw} \\ b_0(r,\theta,\phi,P) &= \frac{1}{r^2}\frac{\partial}{\partial r}\left(r K_{r\theta}\right) + \frac{1}{r^2\sin\theta}\frac{\partial}{\partial \theta}\left(K_{\theta\theta}\sin\theta\right) + \frac{1}{r^2\sin\theta}\frac{\partial K_{\phi\theta}}{\partial \phi} \\ c_0(r,\theta,\phi,P) &= \frac{1}{r^2\sin\theta}\frac{\partial}{\partial r}\left(r K_{r\phi}\right) + \frac{1}{r^2\sin\theta}\frac{\partial K_{\theta\phi}}{\partial \theta} + \frac{1}{r^2\sin^2\theta}\frac{\partial K_{\phi\phi}}{\partial \phi} - \Omega \\ d_0(r,\theta,\phi,P) &= \frac{2K_{r\phi}}{r\sin\theta} \\ e_0(r,\theta,\phi,P) &= K_{rr} \\ l_0(r,\theta,\phi,P) &= \frac{K_{\theta\theta}}{r^2} \\ m_0(r,\theta,\phi,P) &= \frac{K_{\phi\phi}}{r^2\sin^2\theta} \\ s_0(r,\theta,\phi,P) &= \frac{1}{3r^2}\frac{\partial}{\partial r}\left(r^2 V_{sw}\right). \end{aligned} \tag{3.48}$$

Equation 3.47 is a parabolic differential equation which can be solved with a modified Crank-Nicholson finite difference method, called the Alternating Direction Implicit (ADI) method. The ADI method was initially developed by *Peaceman and Rachford* (1955) and *Douglas* (1955) to solve parabolic differential equations in terms of two spatial coordinates and time, after which *Douglas* (1962) extended this method to include three spatial coordinates and time. The ADI method is applied in the numerical model

from this study, where the TPE is solved in three spatial dimensions and rigidity. See *Potgieter* (1984) for a full discussion.

The very LIS ($f_g(P)$) is taken as an input spectrum at the outer boundary of the heliosphere, which is located at $r_b = 122\,\mathrm{AU}$, for all values of θ and ϕ, while the inner boundary is taken at $r_1 > r_\odot$. At the poles (i.e. for $\theta = 0$ and $\theta = \pi$), it is assumed that $\partial f/\partial\theta = 0$, so that a symmetry exists with respect to the polar line.

Firstly, an initial solution is obtained at one third of a rigidity step forward by solving Equation 3.47 implicitly in the direction of the first spatial coordinate, i.e. the radial distance r. A second solution is then calculated at another third of a rigidity step forward, using the first solution, by solving the differential equation implicitly in the direction of the second spatial coordinate, the polar angle θ. For a solution at the final third of the rigidity step, this process is repeated for the last spatial coordinate, the azimuthal angle ϕ, using the previous two solutions. As a result, a system of linear equations is obtained which can be solved using the Thomas algorithm (e.g. *Lapidus and Pinder*, 1982). For locally developed models, *Williams* (1990) was the first to implement this numerical scheme in order to solve the TPE in three spatial coordinates, with rigidity as the fourth coordinate, for a flat HCS, followed by *Hattingh* (1998), who applied the method for a wavy HCS model.

A 3D grid is constructed across which the TPE is solved. The radial grid points $r_i = (i-1)\Delta r + r_1$, for $i = 1, 2, \ldots, N_r$, run from $r = r_1$ at the inner boundary to $r = r_b$ at the outer boundary, with the radial increments $\Delta r = (r_b - r_1)/(N_r - 1)$. The polar grid points are $\theta_j = (j-1)\Delta\theta$, for $j = 1, 2, \ldots, N_\theta$, and run from $\theta = 0^\circ$ at the north pole to $\theta = 180^\circ$ at the south pole, with increments of $\Delta\theta = \pi/(N_\theta - 1)$. The azimuthal grid points $\phi_k = (k-1)\Delta\phi$, for $k = 1, 2, \ldots, N_\phi$, run from $\phi = 0^\circ$ to $\phi = 360^\circ$ for a full solar rotation, where the azimuthal increments are $\Delta\phi = 2\pi/(N_\phi - 1)$.

Furthermore, the rigidity decreases logarithmically from an initial maximum value P_{max} to a minimum value P_{min}, so that $P_{n+1} = P_n/\exp(\Delta \ln P)$, for $n = 1, 2, \ldots$, with $\Delta \ln P > 0$ the rigidity increment. The solution, however, becomes unstable when the rigidity steps are large relative to the squares of the spatial increments, so that the value for $\Delta \ln P$ is chosen in order to improve the stability of the solution.

In terms of the grid points, the distribution function is

$$f(r_i, \theta_j, \phi_k, P_n) = f(i\Delta r, j\Delta\theta, k\Delta\phi, n\Delta \ln P) = f_{i,j,k,n}, \tag{3.49}$$

so that, from Taylor series expansions, the central finite difference approximations for the first, second and mixed derivatives of f are given by

$$\begin{aligned}
\frac{\partial f(x)}{\partial x} &= \frac{f(x+\Delta x) - f(x-\Delta x)}{2\Delta x} \\
\frac{\partial^2 f(x)}{\partial x^2} &= \frac{f(x+\Delta x) - 2f(x) + f(x-\Delta x)}{(\Delta x)^2} \\
\frac{\partial^2 f(x)}{\partial x \partial y} &= \frac{f(x+\Delta x, y+\Delta y) - f(x+\Delta x, y-\Delta y) - f(x-\Delta x, y+\Delta y)}{4\Delta x \Delta y} \\
&\quad + \frac{f(x-\Delta x, y-\Delta y)}{4\Delta x \Delta y}.
\end{aligned} \tag{3.50}$$

The error on the first two equations is $(\Delta x)^2$ and on the third it is $\Delta x \Delta y$. In terms of the grid points, these equations are written as

$$\begin{aligned}
\frac{\partial f}{\partial x} &= \frac{f_{i+1} - f_{i-1}}{2\Delta x} \\
\frac{\partial^2 f}{\partial x^2} &= \frac{f_{i+1} - 2f_i + f_{i-1}}{(\Delta x)^2} \\
\frac{\partial^2 f}{\partial x \partial y} &= \frac{f_{i+1,j+1} - f_{i+1,j-1} - f_{i-1,j+1} + f_{i-1,j-1}}{4\Delta x \Delta y}.
\end{aligned} \tag{3.51}$$

The solutions for f at the different rigidity steps are indicated by

$$\begin{aligned}
f_{i,j,k,n} &= f_{i,j,k} \\
f_{i,j,k,n+\frac{1}{3}} &= f^*_{i,j,k} \\
f_{i,j,k,n+\frac{2}{3}} &= g_{i,j,k} \\
f_{i,j,k,n+1} &= h_{i,j,k}.
\end{aligned} \tag{3.52}$$

The first solution, $f^*_{i,j,k}$, is calculated by solving Equation 3.47 implicitly in the radial direction at one third of a rigidity step backward. This is achieved by evaluating half of the central difference equations 3.50 in r at the present rigidity step and half of them at a third of a rigidity step backward. For the second solution, $g_{i,j,k}$, this process is repeated by once again solving Equation 3.47 implicitly, in terms of $f^*_{i,j,k}$, in the θ-direction. Similarly, the third solution, $h_{i,j,k}$, in terms of $f^*_{i,j,k}$ and $g_{i,j,k}$, is obtained at one full rigidity step backward by solving Equation 3.47 implicitly in the ϕ-direction. This process is repeated for all rigidity values in order to obtain a solution for the final distribution function f, which is related to the differential intensity j, by $j = P^2 f$. See *Hattingh* (1998) for a full discussion on solving the TPE numerically in 3D.

3.5.3 GPU Implementation

Over recent years, the computing power of GPUs has become readily accessible for general purpose calculations with the introduction of Nvidia's CUDA (Compute Unified

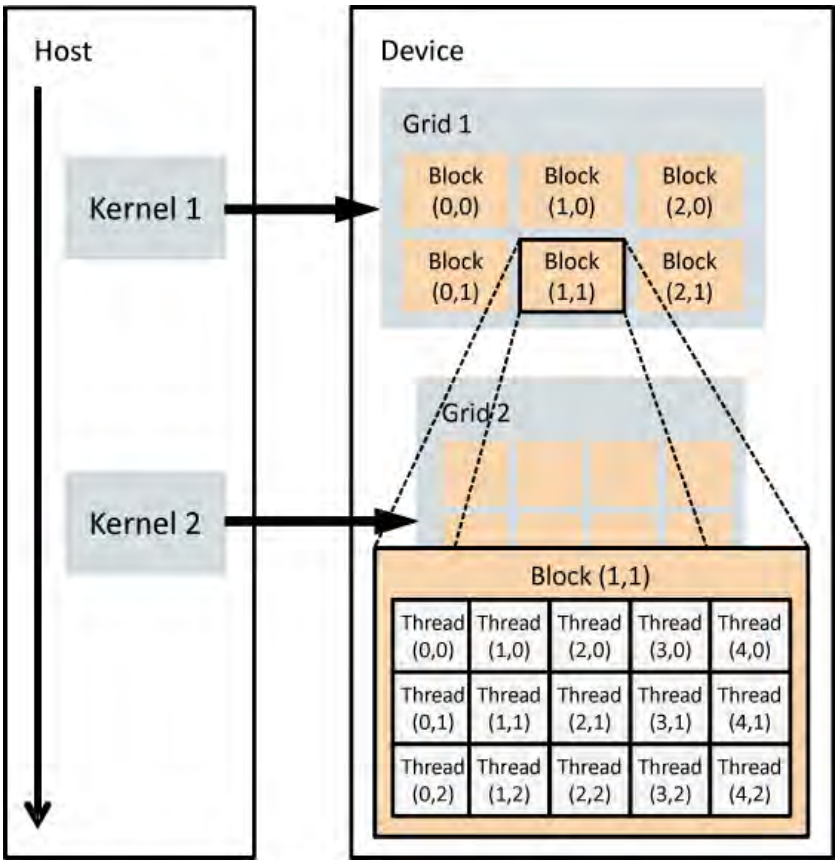

Figure 3.7: A schematic illustration of the basic CUDA execution model. Kernel functions are called from the host (CPU) to run on the device (GPU). Each invoked kernel is associated with a grid of blocks, where each block contains a number of threads. The number of blocks per grid and the number of threads per block can be specified by the user. Figure taken from https://sites.google.com/site/cudapros/website-builder.

Device Architecture) parallel computing platform and application programming interface (API) in 2007. The primary advantage of utilizing the massive parallel design of the CUDA architecture, is the significant increase in runtime performance compared to central processing units (CPUs).

CUDA is the name of the SIMT (single instruction, multiple threads) hardware architecture, as well as the C/C++-like bindings that are used to write code that can perform parallel calculations on GPUs. At the highest level, the CUDA paradigm consists of the CPU and the memory attached to it, and the GPU along with its memory. In CUDA terminology, these components are known as the `host` and the `device`, respectively, and are connected via the PCI Express bus. When a function (or `kernel`) that operates on the device side is invoked by the host, it is necessary to explicitly move any data required for (or generated by) the kernel to and from the GPU memory. During execution, a copy of the kernel function is run in parallel across multiple threads. Figure 3.7 shows a schematic illustration of the CUDA execution model. At runtime, the host calls a kernel function which is to be executed on the device. Associated with

each kernel is a grid of blocks on the device, where each block contains the same number of threads. Both the number of blocks and the number of threads per block are variables that can be set by the user. See e.g. *Kirk and Hwu* (2010) and *Sanders and Kandrot* (2010) for more information about streaming multiprocessors, warps and warp occupancy, and how these relate to making proper choices for the number of blocks and the number of threads per block, with the aim of achieving optimal performance. See also http://www.nvidia.com/object/cuda_home_new.html for more information about Nvidia's CUDA API.

Many fields of science have benefited from the gain in performance that GPUs and the CUDA API can offer, including space physics. *Dunzlaff et al.* (2015) introduced a GPU-accelerated modulation model where the CUDA API was used to solve the Parker TPE and to simulate the transport of charged particles using SDEs. In their study, a comparison was made between the runtimes of the GPU-based model and a CPU version of the same model. The latter model was also optimized with OpenMP (Open Multi-Processing), a multi-thread technique that facilitates parallel processing in CPUs. Since SDE modulation models calculate the trajectory of individual pseudo-particles, where the calculation of one trajectory is independent of all other trajectories, they lend themselves well to parallelization. The GPU model from *Dunzlaff et al.* (2015) showed a performance increase of a factor of between $\sim$ 10 and $\sim$ 60 over the CPU model, depending on the choice of input parameters.

The modulation model used in this study is based on a finite difference numerical scheme, where the solution at each rigidity-step depends on the solution from the previous rigidity-step, which is what makes models like these difficult to parallelize. However, before each rigidity step in this model, numerous variables, parameters and coefficients have to be calculated at each of the $\sim 3 \times 10^6$ gridpoints that make up the heliosphere. Such calculations across large arrays are highly parallelizable, given that they are independent of each other, and can be performed much faster by using the CUDA API, as opposed to performing the calculations sequentially with a CPU, or even with CPU-based parallel systems like OpenMP or MPI (Message Passing Interface). This advantage that CUDA offers has been exploited in the modulation model from this work in order to perform all of the time-expensive array-based calculations up to before the ADI numerical scheme commences, resulting in a runtime performance increase of a factor of between $\sim$ 10 and $\sim$ 20. Even though CUDA is capable of achieving significant performance increases for calculations that can be performed independently, the application of this technology to traditional finite difference numerical schemes remains a challenge. The best approach for improving runtime performance in such models in the future will be to use a combination of CPU and GPU computing resources.

3.6 Summary

In this chapter the Parker TPE was given and discussed in light of the various modulation and transport mechanisms that it contains. The modulation mechanisms that are of importance to this study are: gradient, curvature and current sheet drifts in the global HMF, outward convection due to the expanding SW, diffusion that is caused by the irregular and turbulent HMF and adiabatic deceleration (see Equation 3.1). The TPE forms the central equation for modulation studies, since it determines the transport and modulation of CRs within the heliosphere. It was shown how the differential intensity j can be calculated at any point in the heliosphere from the CR distribution function f in the TPE.

In Section 3.2.3, the TPE was rewritten in spherical coordinates. The transformed version of the TPE was given in Equation 3.27, where the terms were grouped according to the modulation processes they describe.

Contained within the TPE is the diffusion tensor $\mathbf{K}$, which describes the diffusion and drifts of CRs in terms of the DCs $\kappa_{\parallel}$, $\kappa_{\perp r}$ and $\kappa_{\perp\theta}$, and the drift coefficient κ_A. The diffusion of CRs was discussed in Section 3.3. Distinction was made between diffusion parallel and perpendicular to the HMF lines, where the latter was again divided into perpendicular diffusion in the radial and polar directions.

The diffusion approach used in this study resembles that of QLT (first introduced by *Jokipii*, 1966). An expression for $\kappa_{\parallel}$ was given by Equation 3.30, where the rigidity dependence had the form of a double power law. Upper and lower limits of the rigidity dependence for the parallel MFPs for protons, electrons and positrons, as was found from this study after reproducing PAMELA energy spectra, were shown in Figure 3.2 and compared to two popular turbulence models, namely turbulence with slab and 2D geometries. These turbulence models illustrate the large variance that can occur for diffusion and the resulting MFPs, depending on the assumed turbulence model. The parallel MFPs from this study were shown to be more concise while still being in good agreement with turbulence theory.

Another well known turbulence theory that is used to calculate perpendicular diffusion is NLGC theory, which was first proposed by *Matthaeus et al.* (2003). A key aspect implied by this theory is that $\lambda_{\perp}$ is scaled with a weaker rigidity dependence compared to $\lambda_{\parallel}$, which is particularly evident at rigidities above $\sim 10\,\mathrm{GV}$ (e.g. *Bieber et al.*, 2004). This qualitative feature was accounted for in the diffusion approach used in this study, where both $\lambda_{\perp r}$ and $\lambda_{\perp\theta}$ were scaled with a weaker dependence than $\lambda_{\parallel}$ above P_k. Furthermore, $\kappa_{\perp r}$ and $\kappa_{\perp\theta}$ were scaled by $2\,\%$ and $1\,\%$ of $\kappa_{\parallel}$ below P_k, respectively, where $\kappa_{\perp\theta}$ was also enhanced toward the polar regions (e.g. *Ferreira et al.*, 2000).

Drifts were discussed in detail in Section 3.4 and an expression for the average drift velocity was given in Equation 3.44. In the modulation model, drifts are determined

by the drift coefficient κ_A, with a corresponding drift scale λ_A that is akin to the MFP for diffusion. In its simplest form, the drift coefficient is proportional to P – the weak-scattering limit – where it is assumed that drifts are unaffected by scattering as a result of turbulence (e.g. *Rossi and Olbert*, 1970). However, it was shown that particle scattering suppresses drifts at low rigidities, but the exact details of this suppression is still being studied (e.g. *Ngobeni*, 2015). For the current study, it is assumed that drifts are suppressed below $P_{A0} = 0.55\,\mathrm{GV}$, which is a reasonable assumption and comparable to e.g. *Burger et al.* (2008).

In Section 3.5, a brief overview of various modulation models was given, followed by an explanation of the numerical scheme used to solve the TPE, namely the ADI method. This method is used to solve the TPE in three (spherical) spatial dimensions and rigidity, so that a full CR energy spectrum can be obtained at any point in the heliosphere. In solving the TPE at each rigidity step, a large number of variables and coefficients have to be calculated across a grid containing $\sim 3 \times 10^6$ gridpoints. In order to increase runtime performance, the model was redesigned to take advantage of the parallel computing capability of the GPU via the CUDA API. Even though the ADI scheme itself, which is a finite difference method, cannot be parallelized efficiently, all of the time-expensive array-based calculations that take place before the numerical scheme starts, were performed using the the GPU, which resulted in exceptional runtime performance increases. A detailed discussion of the CUDA API and the implementation of GPU computing in the modulation model was given in Section 3.5.3.

Chapter 4

Heliospheric Modulation of Protons

4.1 Introduction

With the availability of accurate proton energy spectra measured by PAMELA during the widely recognized atypical minimum of 2009, this unusual solar minimum event and the time leading up to it can be studied in detail with regard to how the proton energy spectrum developed over time. Since the Ulysses mission overlapped with the PAMELA mission during most of this minimum period, proton count rates are provided by the Kiel Electron Telescope across a range of latitudes, which, when combined with simultaneous PAMELA measurements, facilitates a comprehensive study of global gradients. Voyager 1 also entered the very LISM since August 2012, measuring low-energy GCRs from this region. By combining the latter with PAMELA measurements at higher energies, uncertainties in the proton LIS can be eliminated.

All of the above topics are studied and discussed in this chapter through numerical modelling, with the aim of gaining insight into the modulation mechanisms that governed the 2009 solar minimum, and validating the empirical approach used in reproducing PAMELA observations. This procedure also attempts to narrow the scope of the parameter space and essentially extends and improves upon the research of *Vos* (2012), *Vos et al.* (2013a) and *Potgieter et al.* (2014a).

4.2 The Local Interstellar Proton Spectrum

Being one of the most abundant particle species in the Galaxy, protons, together with helium, serve as the primary measure of the GCR energy density in the ISM. Consequently, a proper knowledge of the exact shape of the proton energy spectrum in the very LISM is of particular importance when studying heliospheric modulation, since it serves as the primary input spectrum.

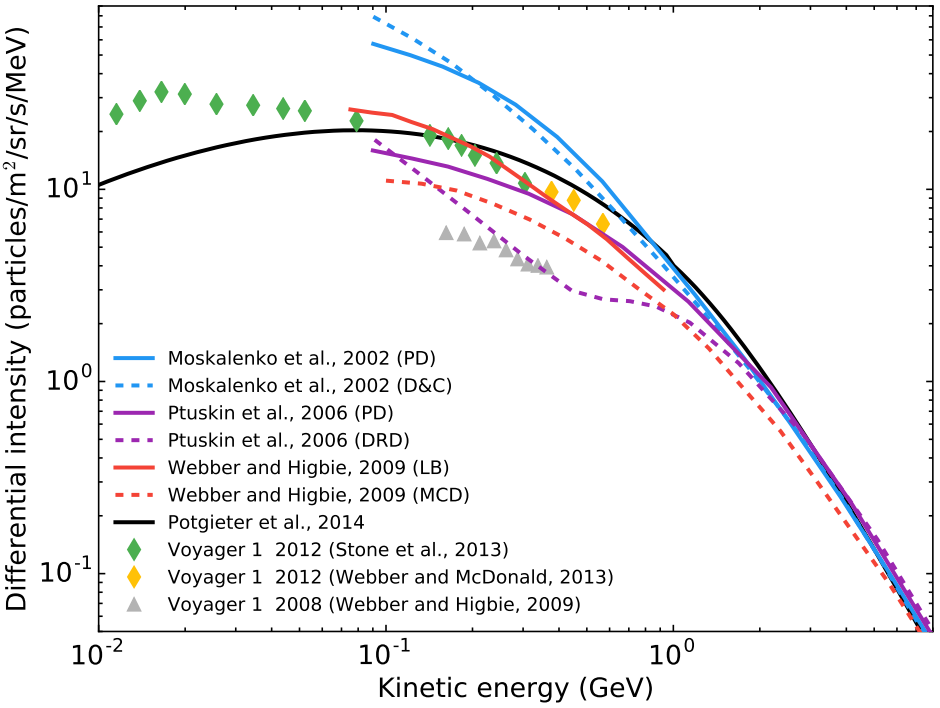

Figure 4.1: A collection of calculated interstellar proton spectra proposed by various authors (solid and dashed lines) are compared to Voyager 1 measurements at ~ 122 AU (green and orange diamonds from *Stone et al.*, 2013, and *Webber and McDonald*, 2013, respectively), and at ~ 105 AU (grey triangles from *Webber and Higbie*, 2009). *Moskalenko et al.* (2002) and *Ptuskin et al.* (2006) produced spectra based on plain diffusion (PD), diffusion and convection (D&C) and diffusive reacceleration with damping (DRD) theories used in the GALPROP code. *Webber and Higbie* (2009) used Leaky Box (LB) and Monte Carlo diffusion (MCD) models, while *Potgieter et al.* (2014a) based their LIS on solar modulation results and PAMELA measurements.

Over the years, many attempts have been made to obtain reliable LIS estimates for various GCR species, including that of protons. *Gralewicz et al.* (1997), for example, made use of cosmic gamma ray measurements from EGRET to infer the proton spectral shape in the ISM. *Moskalenko et al.* (2002) used the galactic propagation code GALPROP to study different interstellar propagation scenarios. The latter authors were able to verify their resulting interstellar spectra by simultaneously comparing the modulated B/C ratio at Earth to other GCR measurements, as well as the secondary antiprotons produced by interactions between protons and interstellar gas. In all these attempts, a simple force field model was used for modulation studies (*Gleeson and Axford*, 1968; see also *Caballero-Lopez and Moraal*, 2004).

Shown in Figure 4.1 by the solid and dashed blue lines, respectively, are the plain diffusion (PD) and the diffusion and convection (D&C) models from *Moskalenko et al.* (2002). These spectra, particularly the D&C model, yielded the most self-consistent results with regard to the B/C ratio and the primary and secondary spectra. However, when compared to the recent Voyager 1 measurements at ~ 122 AU (green diamonds), both the PD and D&C spectra are overestimated below 1 GeV. The solid purple line

gives the PD spectrum proposed by *Ptuskin et al.* (2006), which was also obtained using GALPROP. These authors additionally accounted for the scattering of GCRs caused by the damping of MHD waves through resonant interactions with the GCRs themselves, which resulted in a diffusive reacceleration model with damping (DRD) given by the dashed purple line. Even though the PD spectrum from *Ptuskin et al.* (2006) is slightly below the recent Voyager 1 measurements in the 500 MeV range, the effects of damping from the DRD model are overestimated, resulting in a spectrum that is significantly lower than the actual intensities with a spectral index that is inconsistent with measurements below 500 MeV.

Webber and Higbie (2009) reverted to using a Leaky Box model (LB) and a Monte Carlo diffusion model (MCD), respectively given by the solid and dashed red lines in Figure 4.1, while taking the latest Voyager 1 measurements at that time as the lower limit (green triangles). The spectral shape of their MCD model seems reasonable, but the absolute value is too low by a factor of ~ 2. The LB model reproduces the latest Voyager 1 measurements down to 100 MeV. The grey line in Figure 4.1 represents the LIS used by *Potgieter et al.* (2014a), who based their spectrum on a combination of solar modulation results and PAMELA measurements.

The need for a proton LIS is undoubtedly apparent, yet, in spite of the many attempts to obtain such a spectrum, neither the absolute flux nor the exact spectral shape have been determined to adequate precision across the energy range where solar modulation plays an important role. This picture has however changed since August of 2012, when Voyager 1 became the first spacecraft to cross the heliopause and enter into the very LISM to take *in situ* measurements of GCR intensities below ~ 600 MeV (*Stone et al.*, 2013; see also *Webber and McDonald*, 2013). As a result, it is now possible to determine the shape and absolute value of the proton spectrum in the very LISM below ~ 1 GeV. By also taking into account GCR measurements from experiments such as PAMELA (*Adriani et al.*, 2013a) and AMS-02 (*Aguilar et al.*, 2013), the proton LIS can be settled at energies above ~ 30 GeV, where solar modulation has little to no effect on GCRs (see e.g. *Strauss and Potgieter*, 2014a). By combining these observations at either end of the spectrum and using the GALPROP model as a reference for interpolating between 600 MeV and 30 GeV, it is possible to confine the proton LIS to a single spectrum.

This is illustrated in Figure 4.2, which shows GCR measurements from Voyager 1, PAMELA and AMS-02 (given by the coloured circles and diamonds). The latter two sets are used to normalize the computed LIS (black line) and to set the spectral index (shown in the top panel) for energies between 30 GeV and 100 GeV (shaded region). From the top panel, the spectral index of the LIS remains at -2.78 across this energy range and corresponds to what is required by measurements. Below 10 MeV the spectral index becomes fairly constant with a value of 0.12, which is in agreement with the lower limit set by Voyager 1 for the very LISM. In the bottom panel of Figure 4.2, the

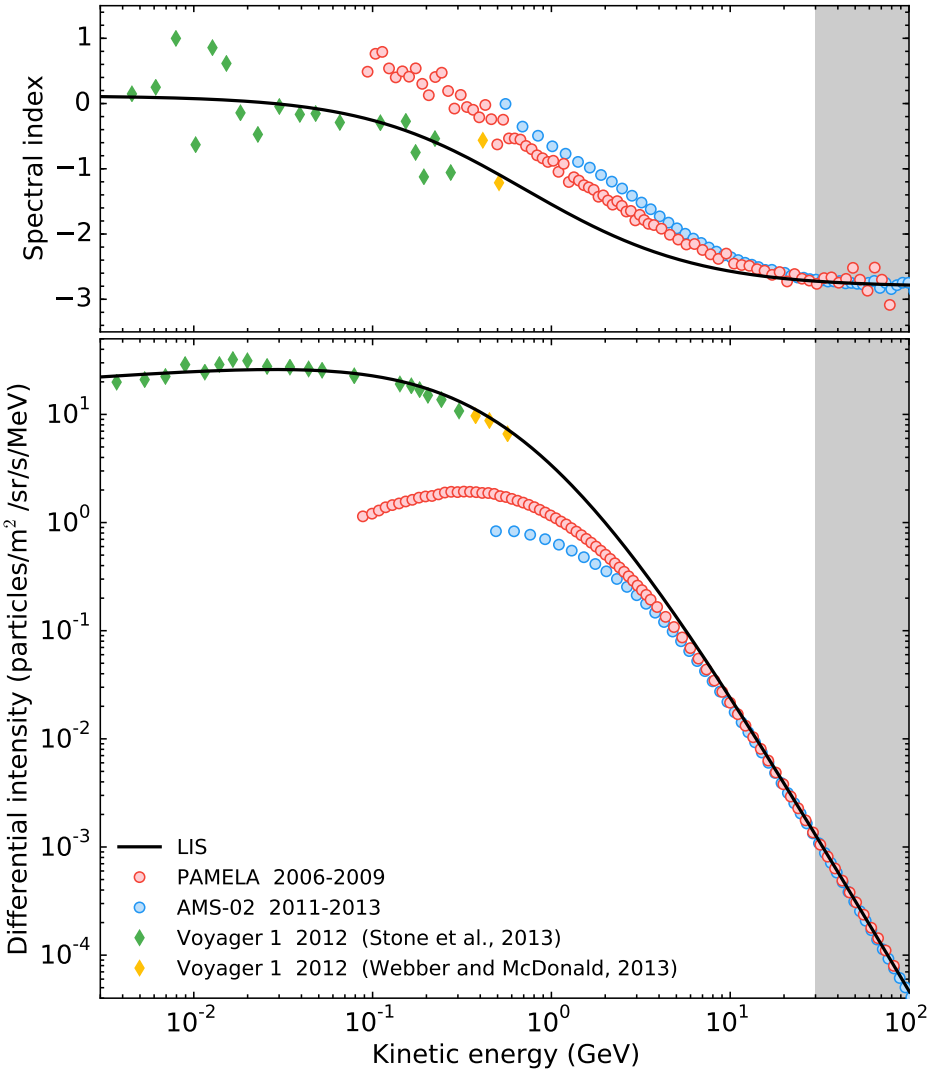

Figure 4.2: The proton very LIS used in this study (black line) is obtained by combining PAMELA, AMS-02 and Voyager 1 measurements (coloured circles and diamonds). The PAMELA (*Adriani et al.*, 2013a) and AMS-02 (*Aguilar et al.*, 2015) measurements are used to normalize the LIS at energies above 30 GeV (shaded region), while Voyager 1 measurements below 600 MeV at $\sim$ 122 AU (*Stone et al.*, 2013; see also *Webber and McDonald*, 2013) are used as a lower limit for intensities in the very LISM. The top and bottom panels give the spectral index and energy spectra respectively.

difference between the LIS and the PAMELA and AMS-02 observations below 30 GeV is indicative of solar modulation. It will be shown in Section 4.4 that measurements from other experiments also support PAMELA and AMS-02 measurements at Earth, in particular with regard to normalization.

The constructed LIS in Figure 4.2, which is used in this study, is considered as the most reliable LIS, since it adheres to all the conditions imposed on GCR intensities, especially the measurements from Voyager 1 beyond the HP. This LIS is given by

$$j_{LIS,p} = 2.70 \, \frac{E^{1.12}}{\beta^2} \left(\frac{E + 0.67}{1.67} \right)^{-3.93} , \tag{4.1}$$

where E is the kinetic energy in GeV, β the ratio of CR particle speed relative to the speed of light, and $j_{LIS,p} = P^2 f$ is the differential intensity given in units of particles/m^2/s/sr/MeV, with P the rigidity in GV and f the GCR distribution function. This very LIS is different from what was used by *Vos* (2012), *Vos et al.* (2013a) and *Potgieter et al.* (2014a). A summary of the spectral indices between 1 MeV and 100 GeV is given in Table 4.1.

Table 4.1: The spectral index of the very LIS of protons constructed in Figure 4.2 between 1 MeV and 100 GeV.

Kinetic energy (GeV)	0.001	0.01	0.1	1.0	10.0	100.0
Spectral index	0.12	0.07	−0.27	−1.54	−2.57	−2.78

Scherer et al. (2011), *Strauss and Potgieter* (2014a) and *Luo et al.* (2015) argued that the modulation of GCRs might start well beyond the HP, in a region between the HP and the BS that is suspected to be slightly more turbulent than the ISM. Since this effect is relatively small, with a $\sim 25\%$ decrease at 100 MeV for protons, this controversial issue is not yet settled and is therefore not considered in this thesis.

4.3 The PAMELA Proton Spectra

The PAMELA satellite entered into orbit just as solar cycle 23 approached its final phase, from around 2006, a time during which heliospheric conditions relaxed for the onset of solar minimum. GCR intensities measured by PAMELA during this period enable us to study the recent solar minimum to a greater degree of accuracy than what was possible before. By comparing PAMELA observations to HCS tilt angles and HMF measurements, as well as subsequent modulation modelling, it is possible to obtain a better understanding of the heliospheric conditions that led to the recent solar minimum.

The top panel of Figure 4.3 gives an overview of the PAMELA proton measurements averaged over Carrington rotations, from July 2006 to the end of 2009 (*Adriani et al.*, 2013a). With such a fine resolution in time, the development of the proton energy spectrum, due to time-dependent changes in solar modulation conditions, is evident and can be seen in the spread of the colour-coded spectra, varying from blue in 2006, to red in 2009. The increase in intensity is quantified in the bottom panel, which gives the ratio of consecutive spectra relative to July 2006. As expected, the lowest energy GCRs, being the most responsive to changes in modulation conditions, have experienced the largest increase throughout this minimum period – by a factor of ~ 3 around 100 MeV. At higher energies, this increase becomes less pronounced, with intensity variations below 10% for GCRs above 10 GeV.

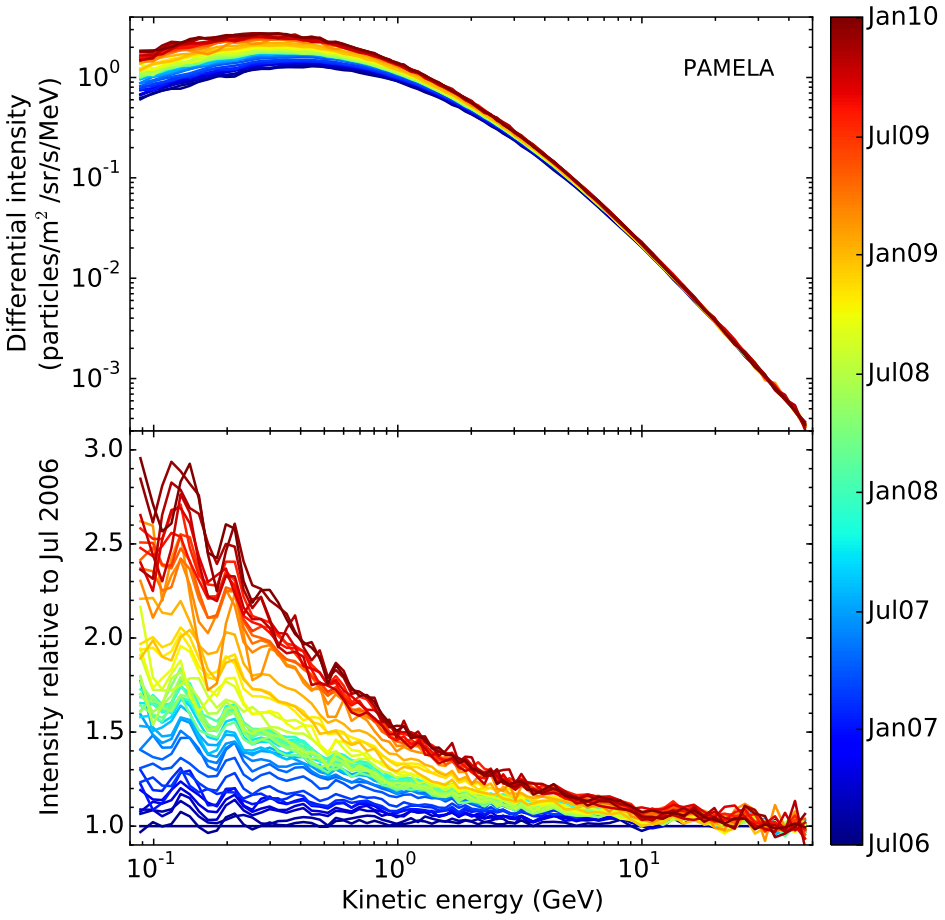

Figure 4.3: *Top panel:* The 27-Day averaged proton energy spectra from PAMELA (*Adriani et al.*, 2013a), observed between July 2006 (blue) and January 2010 (red). *Bottom panel:* Consecutive ratios of the PAMELA energy spectra shown in the top panel, relative to July 2006. The spread between the blue and red spectra represents modulation-dependent changes over the considered time period. Note how the spectra became progressively softer from 2006 to 2009.

An important observation from the bottom panel of Figure 4.3 is the range over which GCRs transition to modulation-free energies. Apart from relative large fluctuations in the 2009 spectra, the majority of the ratios show very little to no observable modulation above 30 GeV. The energy range between 30 GeV and 50 GeV is therefore regarded as the region where modulation becomes negligible (see also *Strauss and Potgieter*, 2014a).

A notable feature of the spectra is the smooth transition from an $E^{-2.78}$ power law above $\sim$ 10 GeV to the familiar adiabatic slope below $\sim$ 100 MeV. Furthermore, starting in July 2006, the peak of the spectrum shifted from $\sim$ 440 MeV down to $\sim$ 280 MeV in December of 2009, with an accompanying increase of more than 120% as the solar cycle approached the period of minimum modulation. Globally, the spectra became progressively softer over this time period.

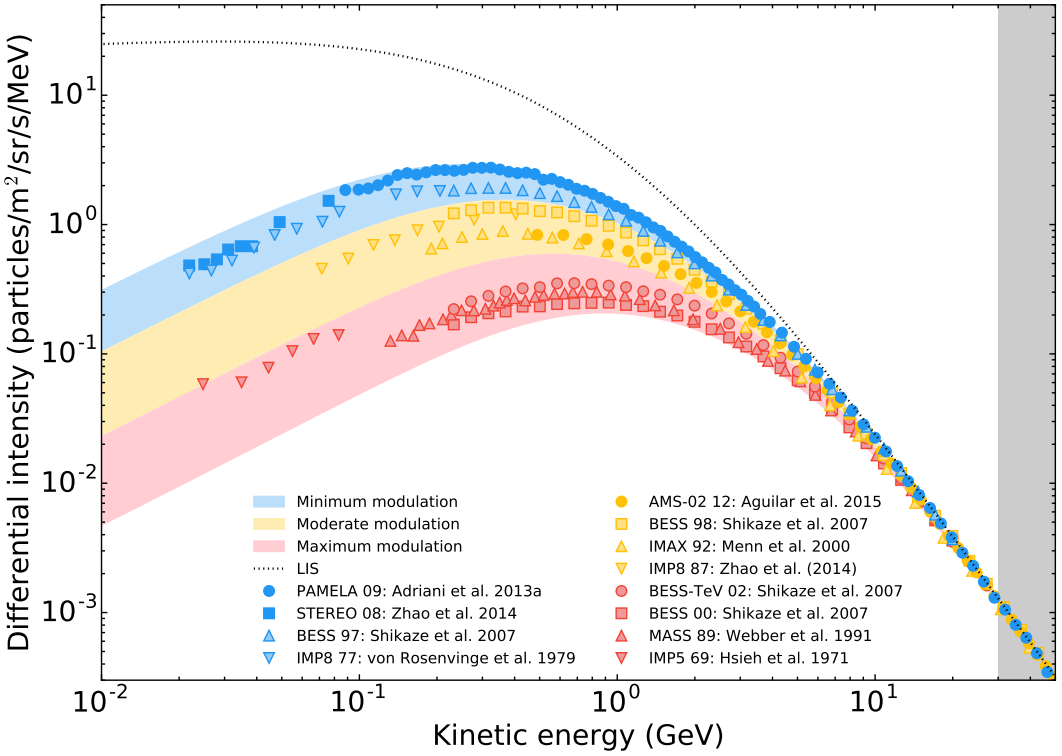

Figure 4.4: The proton spectrum measured by PAMELA at the end of 2009 is shown by the solid blue circles and is recognized as being the highest CR spectrum ever recorded at Earth. This spectrum is compared to spectra from other experiments at different times in the solar cycle. The blue, orange and red bands show approximate regimes for minimum, moderate and maximum heliospheric modulation respectively. As a reference, the LIS from Figure 4.2 is given by the dashed line, with the shaded region above 30 GeV representing the normalization region.

4.4 The Highest GCR Spectrum Recorded at Earth

For the current study, special attention is given to PAMELA measurements taken during the minimum period between 2006 and 2009. The reason for this is because heliospheric modulation conditions reached extremely low levels of activity in 2009, unlike any solar minimum that has been observed thus far. Such conditions are favourable for efficient gradient, curvature and current sheet drifts, making the 2009 minimum ideal to study charge-sign dependent modulation, which directly follows from drifts.

The uniqueness of the 2009 minimum is highlighted in Figure 4.4, which gives a comparison between PAMELA's highest proton spectrum (solid blue circles) and observations from other experiments, categorized according to what is considered as minimum, moderate and maximum modulation regimes (blue, orange and red bands, respectively). Minimum modulation of GCRs usually occur during a narrow time period when the current sheet has small tilt angle values (below $\sim 15°$). Such periods are preceded and followed by moderate modulation periods characterized by larger tilt angles, while maximum modulation is present during the largest tilt angles ($>\sim 40°$ for example).

It is clear from Figure 4.4 that the 2009 proton spectrum measured by PAMELA,

and extended to energies as low as 20 MeV by STEREO observations taken in 2008 (solid blue squares), exceeds all other spectra, which include observations from both $A < 0$ and $A > 0$ cycles. This spectrum, measured by PAMELA at the end of 2009, is widely recognized as being the highest spectrum ever recorded at Earth, and is a direct consequence of the prolonged 2009 solar minimum (see also *Strauss and Potgieter*, 2014b).

The AMS-02 proton spectrum (filled orange circles), observed between 2011 and 2012, serves as a benchmark with regard to how intensities decreased from the 2009 minimum levels to moderate modulation levels (*Aguilar et al.*, 2015). Within a time period of $\sim$ 3 years following 2009, intensities at 500 MeV decreased by a factor of ~ 3 as modulation increased, according to the combined AMS-02 spectrum. Measurements from other experiments also indicate how the peak of the spectrum moves to higher energies during times of moderate and maximum modulation, which effectively illustrates the dynamic nature of the GCR proton spectrum. PAMELA and AMS-02 are also in a clear consensus with other experiments with regard to the normalization of spectra above 30 GeV (given by the grey band).

4.5 Modelling the PAMELA Proton Spectra

4.5.1 A Selection of PAMELA Spectra

In order to understand the recent solar minimum in detail, as well as GCR modulation and the phenomenon of charge-sign dependent modulation in general, it is necessary to study the energy spectrum, spatial dependence and time evolution of intensities for a variety of these GCR particles. In this chapter, which focuses on proton modulation, the spectra measured by PAMELA between mid-2006 and the end of 2009 are considered to be the most reliable spectra for such a study.

The primary objective, therefore, is to reproduce intermittent PAMELA proton spectra measured during this time period using an attentively bench-marked 3D modulation model and utilizing what is known about modulation conditions in the heliosphere. This is done by considering a representative selection of seven 27-day averaged PAMELA proton spectra taken at the end of each semester for each year, from 2006 to 2009. These spectra were published by *Adriani et al.* (2013a) and are shown in Figure 4.5. The time periods for these spectra are given in the legend, and are from hereon simply referred to as the 2006e, 2007m, 2007e, 2008m, 2008e, 2009m and 2009e spectra, where the "m" and "e" suffixes denote the middle and end of each year, respectively.

Results from this study were published by *Vos and Potgieter* (2015) and follows on the work of *Vos*, 2012, *Vos et al.*, 2013a and *Potgieter et al.*, 2014a.

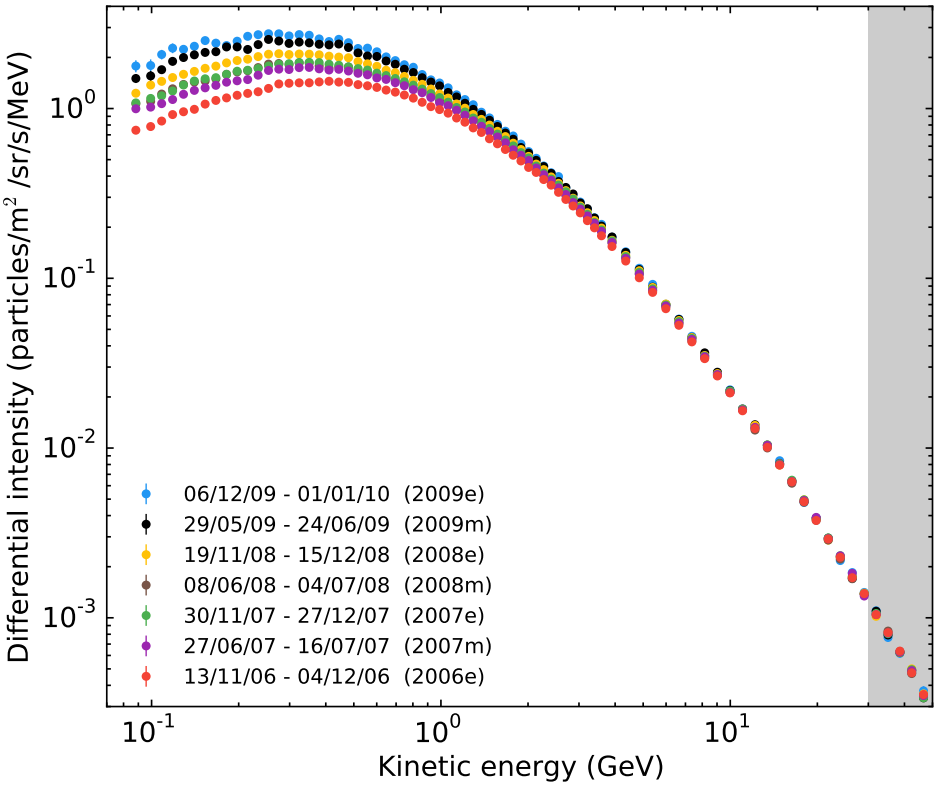

Figure 4.5: A selection of seven 27-day averaged proton spectra measured by PAMELA. These spectra, taken at the end of each semester from July 2006 to December 2009, serve as a representative sample of how the proton spectrum changed over time. Statistical errors are given by the error bars, but are mostly contained within the size of the symbols. Data taken from *Adriani et al.* (2013a).

4.5.2 Setting the Intrinsic Modulation Parameters

When working with a steady-state modulation model, it is often a challenge to determine representative values for time-varying modulation parameters. Over a four-year period prior to 2009, the HCS tilt angle and the HMF at Earth changed pronouncedly, both of which are very good proxies of solar activity. These time-dependent changes are accounted for by setting up realistic modulation conditions in the model which coincides with the sampled 27-day spectra given in Figure 4.5. This requires calculating average values for the tilt angle and the HMF at Earth which should yield approximate values that reflect the actual preceding heliospheric conditions. Even though these parameters show significant variation over the timescales considered here, it is assumed that the SW maintains a well-structured solar minimum speed profile over this time.

The calculation of these average values is based on the time it takes for the tilt angles and the frozen-in HMF to travel from the Sun to the HP taken at 122 AU, as they are carried outward by the SW. These propagation times serve as a window over which preceding averages can then be calculated. The HCS is mostly confined to the ecliptic region during solar minimum (within a $\sim 30^\circ$ latitudinal extent) and always

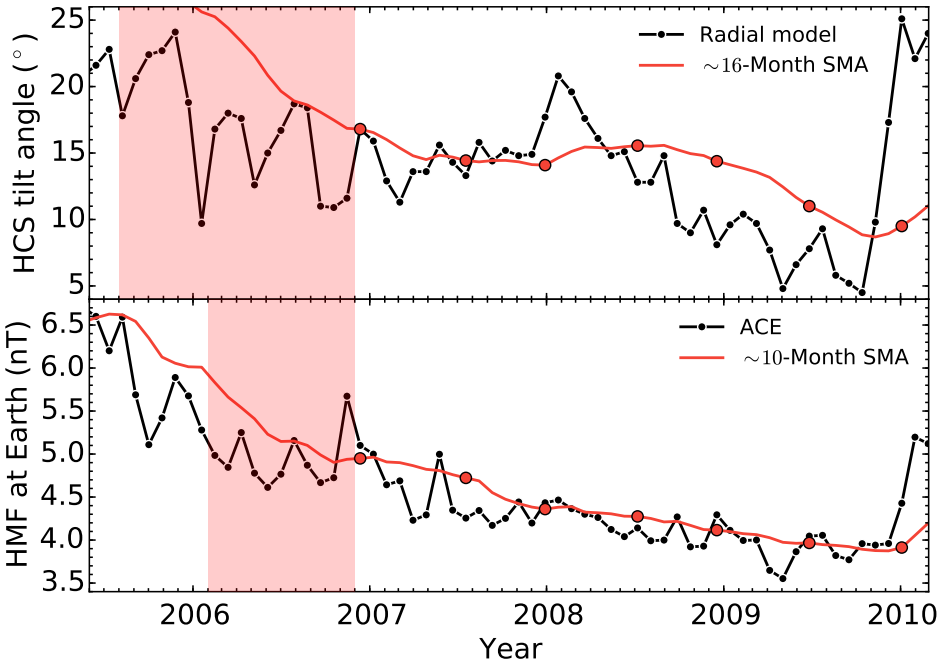

Figure 4.6: *Top panel:* Tilt angle values from the radial HCS model (black line; taken from http://wso.stanford.edu), along with a $\sim$ 16-month simple moving average (red line). *Bottom panel:* Similar to the top panel, but for the HMF at Earth measured by ACE (taken from http://omniweb.gsfc.nasa.gov), with a $\sim$ 10-month moving average. The $\sim$ 16-month and $\sim$ 10-month averaging windows used for 2006e are shown by the reddish shaded regions in both panels for illustrative purposes. The average tilt angles and HMF values that coincide with the sampled PAMELA spectra are given by the red circles.

Table 4.2: A summary of the intrinsic modulation parameters used in reproducing the PAMELA spectra. Here α, B_e and r_{TS} refer to the HCS tilt angle, the HMF at Earth and the assumed radial distance at which the TS is located in the model, respectively.

Parameter	**2006e**	**2007m**	**2007e**	**2008m**	**2008e**	**2009m**	**2009e**
α (°)	16.80	14.43	14.08	15.56	14.38	11.01	9.50
B_e (nT)	4.95	4.72	4.36	4.27	4.11	3.97	3.91
r_{TS} (AU)	88.0	87.0	86.0	85.0	84.0	82.0	80.0

remains in the slow SW region. Knowing the averaged SW speed in the slow SW region ($\sim$ 430 km/s), the propagation time for the tilt angle is calculated to be about 16 months. For the HMF, both the slow and fast (750 km/s) SW regions are taken into account by means of a weighted average, where the weights are determined by the volume occupied by the different SW regions. Following this approach, the HMF propagation time calculates to about 10 months.

Figure 4.6 shows the HCS tilt angles (top panel) and the HMF at Earth (bottom panel) over time for each Carrington rotation (black lines), along with the corresponding simple moving averages (red lines). The average tilt angles and HMF values taken for each sample spectrum are indicated by the red symbols. For illustrative purposes, the

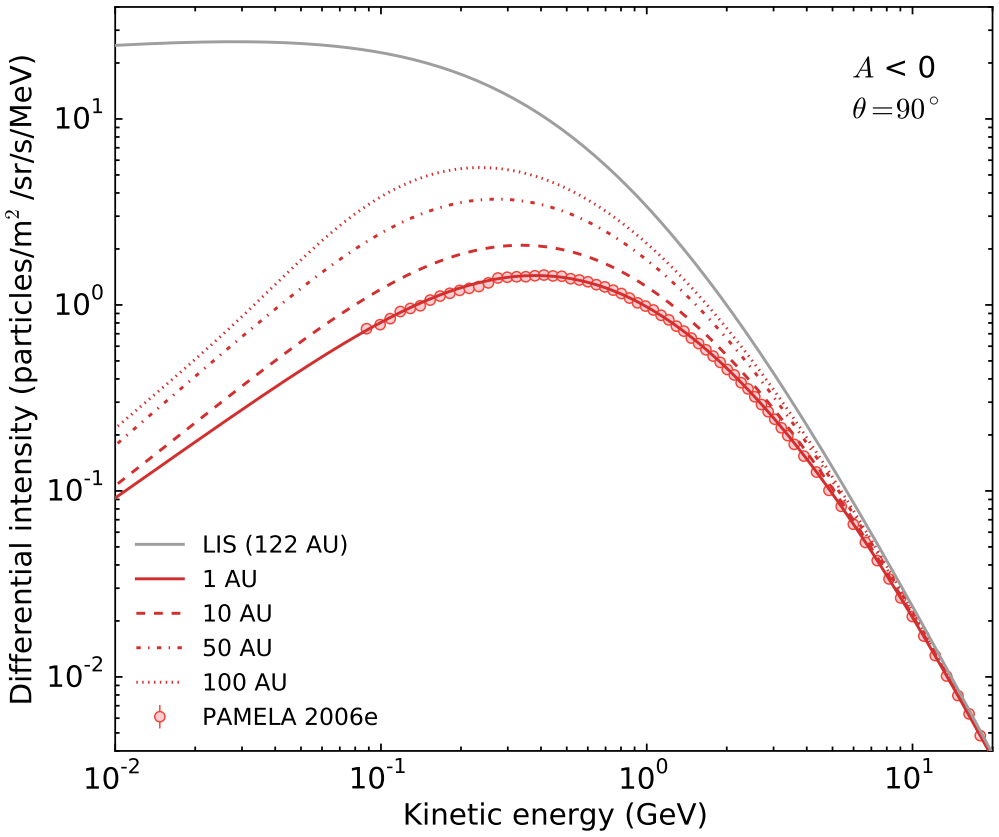

Figure 4.7: The 2006 November proton energy spectrum from PAMELA is shown by the red circles (from *Adriani et al.*,2013a). Statistical errors are mostly contained within the size of the symbols. Modulated spectra are given by the red lines at Earth (solid), 10 AU (dashed), 50 AU (dashed-dotted) and 100 AU (dotted) for 90° colatitude, i.e. the equatorial plane. The proton LIS specified at 122 AU is given by the grey line.

$\sim$ 16 and $\sim$ 10-month averaging windows are given by the reddish shaded regions which, as an example, graphically highlight the values used in calculating the 2006e tilt angle and magnetic field averages.

In addition to these solar activity variables, the position of the TS also varies with time due to the dynamic nature of the heliosphere (*Webber and Intriligator*, 2011), which affects modulation intensities even at Earth (see e.g. *Manuel et al.*, 2014). All of the above-mentioned intrinsic parameters have been accounted for in model simulations and are summarized in Table 4.2.

4.5.3 The Numerically Reproduced PAMELA Spectra

After incorporating the necessary intrinsic parameters into the modulation model, the DCs were carefully adjusted with the aim of reproducing each PAMELA sample spectrum. This was done while sufficiently adhering to conditions imposed on particle MFPs through a diffusion approach based on QLT (as discussed in Chapter 3). In addition to these constraints, the radial and latitudinal gradients between PAMELA and Ulysses

were carefully taken into account as well as the radial intensities measured by Voyager 1. These results are discussed in later sections.

The numerically reproduced PAMELA spectra are shown in Figures 4.7 and 4.8. The LIS and $A < 0$ modulated spectra are given by the grey and coloured lines respectively, where the latter are shown at Earth (solid), 10 AU (dashed), 50 AU (dashed-dotted) and 100 AU (dotted) in the equatorial plane (i.e. 90° colatitude). The PAMELA spectra at the end of each semester are given by the coloured circles. In Figure 4.8 the measured 2006e spectrum is shown by the grey circles as a reference.

It is clear from these figures that the PAMELA spectra are reproduced across all energies. The model reproduces the behaviour of GCRs above 30 GeV, where they become unaffected by heliospheric modulation. Below $\sim$ 100 MeV the modulated spectra bend into the characteristic E^1 slope as a result of adiabatic deceleration caused by the expanding SW (see e.g. *Heber and Potgieter*, 2006, 2000, and *Strauss et al.*, 2011b). For protons, the effect of adiabatic deceleration becomes dominant at non-relativistic energies (below $\sim$ 200 MeV). This is evident from the shapes of all the modulated spectra, where GCRs below these energies experience a noticeable amount of modulation, even at large radial distances, illustrating the effectiveness of this modulation process.

From Figure 4.7 it follows that the proton spectrum at Earth had a peak intensity of 1.4 particles/m^2/s/sr/MeV at 400 MeV. The model shows how this peak shifts to lower energies when moving further out into the heliosphere – a phenomenon that is determined by the shape of the LIS and through the process of energy-losses (see e.g. *Gleeson and Urch*, 1971, *Moraal and Potgieter*, 1982, and *Potgieter*, 1984). Over the course of this minimum, the proton spectrum became progressively softer, reaching an intensity of 2.7 particles/m^2/s/sr/MeV at the end of 2009, with an accompanying shift of the peak down to 270 MeV, as shown in Figure 4.8. Through modelling, predictions of intensity levels can be made for energies below 80 MeV, where PAMELA measurements are unavailable. At 10 MeV, 2006e intensities are estimated to have been $\sim$0.09 particles/m^2/s/sr/MeV, and have increased to $\sim$0.3 particles/m^2/s/sr/MeV at the end of 2009.

4.5.4 Total Modulation

The reproduced spectra from the previous section are combined and summarized in Figure 4.9. The sudden increase in tilt angle during 2008 temporarily suppressed intensities, resulting in almost identical spectra for 2007e (green) and 2008m (brown). Since the magnetic field continued to decrease during 2008 (from the bottom panel of Figure 4.6), this transient effect experienced by GCRs can be directly linked to current sheet drifts and supports the presence of this modulation mechanism in the heliosphere during the recent solar minimum.

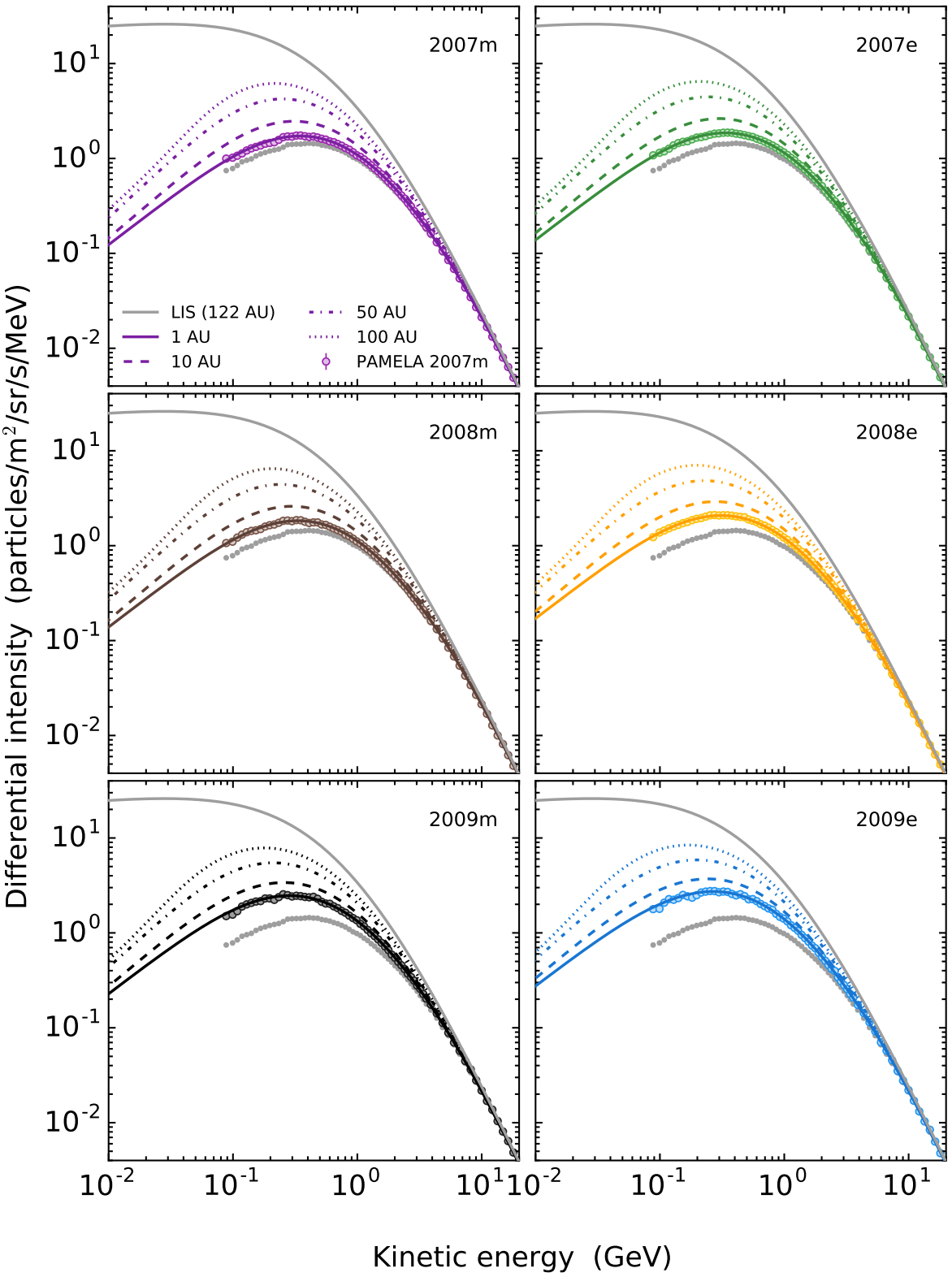

Figure 4.8: Similar to Figure 4.7 but for the measured and computed spectra of 2007m, 2007e, 2008m, 2008e, 2009m and 2009e. For comparison, the grey symbols represent the 2006e PAMELA spectrum.

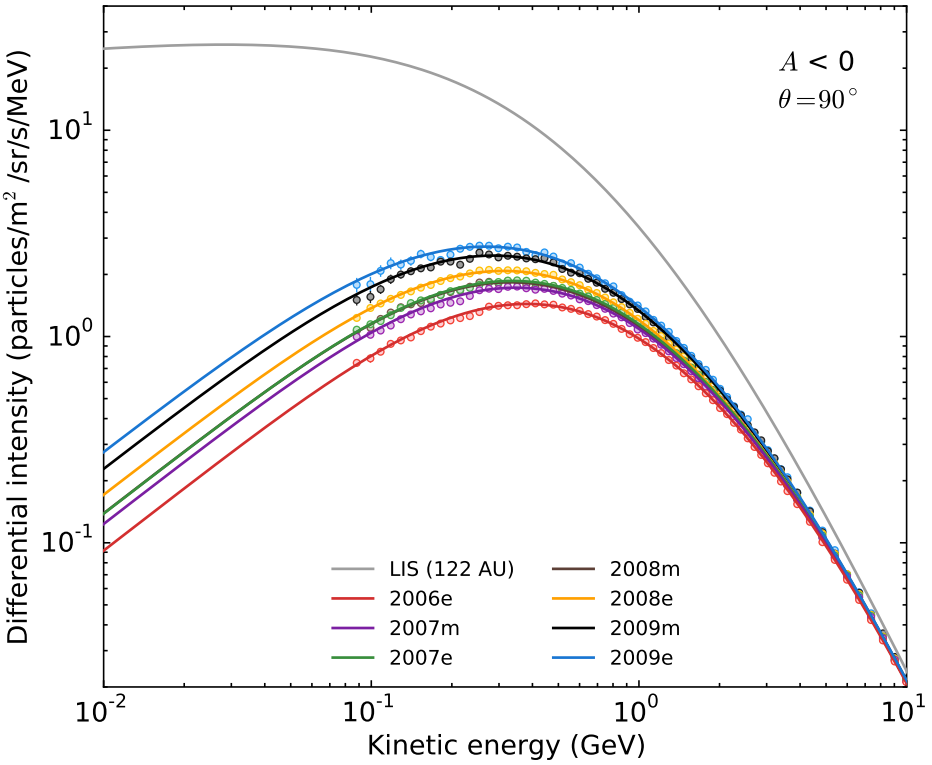

Figure 4.9: The seven computed spectra at Earth (coloured lines) with respect to the LIS at 122 AU, and the PAMELA spectra (coloured circles) from Figure 4.5 are combined.

For a quantitative measure of the total variability of the proton spectrum between 2006e and 2009e, the top panel of Figure 4.10 gives the ratio of consecutive spectra relative to the 2006e spectrum, while the bottom panel shows the modulation factor (MF) taken relative to the LIS. This figure quantifies the semesterly increase in intensity leading up to 2009e, as well as the total amount of modulation experienced by protons between the HP and Earth. The quality of the modelled spectra can also be evaluated from the ratios, which agree well within the statistical errors from PAMELA. At 10 MeV, where PAMELA data is unavailable, it is estimated that intensities in 2009e increased by a factor of 3 relative to 2006e. The largest semesterly increase of $\sim$ 65% occurred between 2008e and 2009m, likely due to the recovery of GCRs following the transient decrease during the first semester of 2008.

From the bottom panel of Figure 4.10 it follows that GCR protons experienced less than $\sim$ 10% solar modulation above 30 GeV, similar to what was found by *Strauss and Potgieter* (2014a). Measurements above these energies should therefore reflect astrophysical processes. Below 30 GeV solar modulation effects become increasingly dominant. At the lower end of the observable spectrum (around 100 MeV), solar modulation is already at $\sim$ 0.03. At these energies, local heliospheric sources of energetic particles can become important, as well as the so-called ACR component which dominates in the outer heliosphere (see e.g. *Potgieter*, 2008, 2013b; *Stone et al.*, 2013).

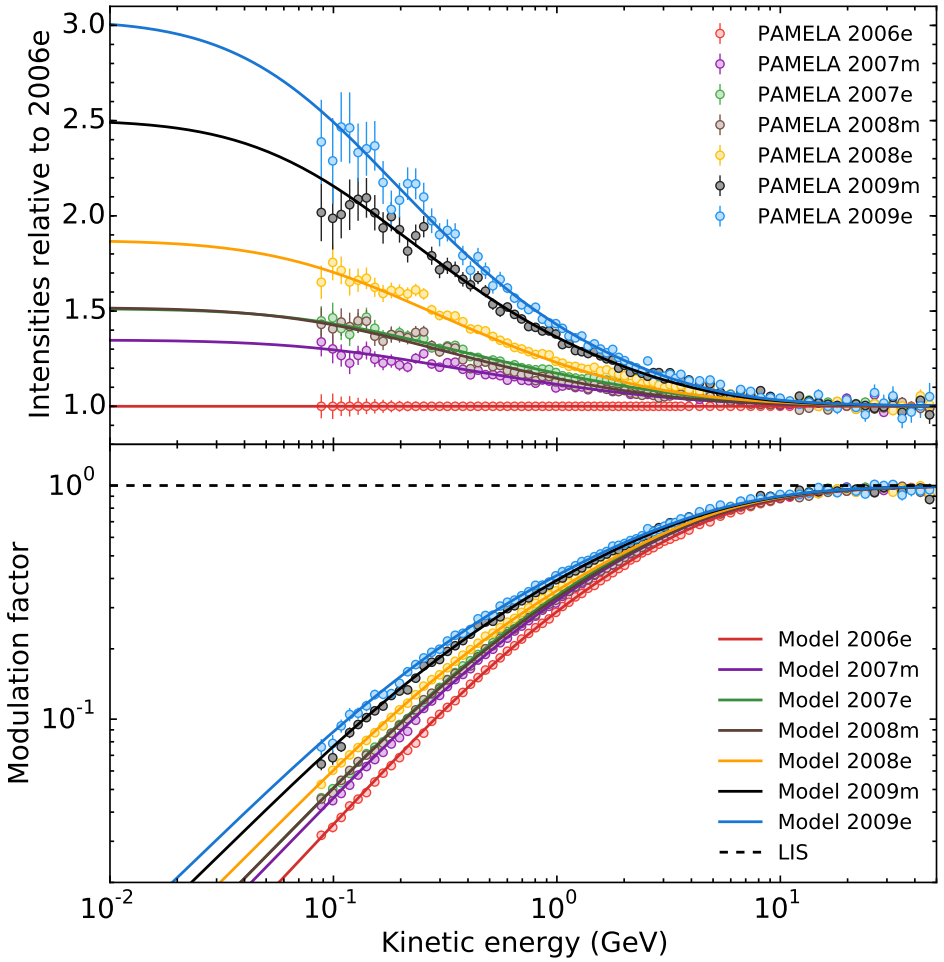

Figure 4.10: *Top panel:* Ratios of consecutive computed (lines) and measured (symbols) proton spectra from Figures 4.7 and 4.8, relative to the 2006e spectrum. *Bottom panel:* The modulation factor for the same spectra shown in the top panel, calculated by taking the ratio of the modulated spectra to the appropriate LIS value. Statistical errors are given by the error bars.

Figure 4.11 shows the MF for the year-end computed spectra from Figure 4.9 over an extended energy range. At high energies, the MF approaches unity, indicating that the amount of modulation decreases with increasing energy. This behaviour of the modulation model is in line with the variability observed in PAMELA measurements. Above ∼17 GeV, GCRs had a MF of 0.9, while MFs of 0.5 and 0.1 were observed at ∼2.3 GeV

Table 4.3: The MF for each year-end computed spectrum from Figure 4.11 at different energies between 1 MeV and 50 GeV.

Kinetic energy (GeV)	0.001	0.01	0.1	1.0	10.0	50.0
MF for 2006e	0.00046	0.0037	0.035	0.287	0.871	0.988
MF for 2007e	0.00070	0.0056	0.050	0.336	0.886	0.990
MF for 2008e	0.00086	0.0070	0.060	0.353	0.890	0.990
MF for 2009e	0.00140	0.0112	0.087	0.410	0.899	0.991

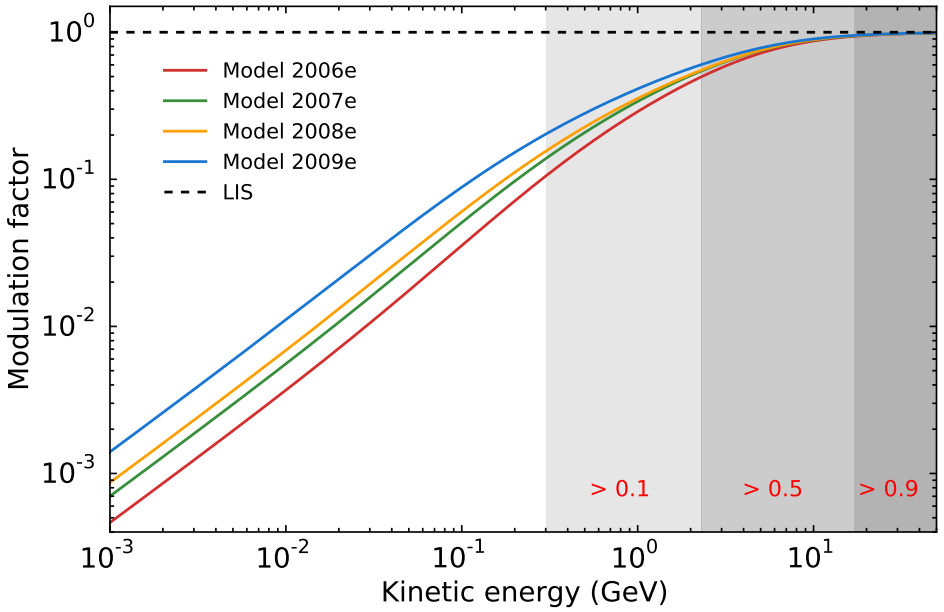

Figure 4.11: Similar to the MF in the bottom panel of Figure 4.10, but for the computed year-end spectra over an extended energy range. The grey bands indicate the energy ranges over which the MF is larger than 0.9, 0.5 and 0.1.

and ∼0.3 GeV. These limits are given by the grey bands in Figure 4.11. Similar results were found by *Strauss and Potgieter* (2014a), who used an SDE modulation model in an independent study. Table 4.3 gives a summary of the MF at different energies for the year-end spectra.

4.6 Voyager Measurements and the Radial Dependence of Proton Intensities

With the PAMELA energy spectra successfully reproduced at Earth, a study of the spatial distribution of proton intensities can further validate the accuracy and underlying assumptions of the model, as well as shed light on the behaviour of GCR protons throughout the heliosphere. This was done by comparing the radial intensity profiles from the model in the previous section to Voyager 1 and 2 measurements.

Figure 4.12 gives the computed radial intensity profiles for the 2006e, 2007e, 2008e and 2009e spectra, at energies of 142 MeV, 182 MeV and 215 MeV (from the top to bottom panel), where the TS positions are indicated by the short vertical black lines. Voyager 1 proton measurements in the form of radial intensities from *Webber et al.* (2013) are given by the grey diamonds and correspond to the above-mentioned energies for each panel. The coloured circles at 1 AU represent PAMELA measurements.

During the peak of the previous solar minimum, Voyager 1 was at 72 AU and measured intensities of ∼3.5 particles/m^2/s/sr/MeV at 142 MeV. According to the model,

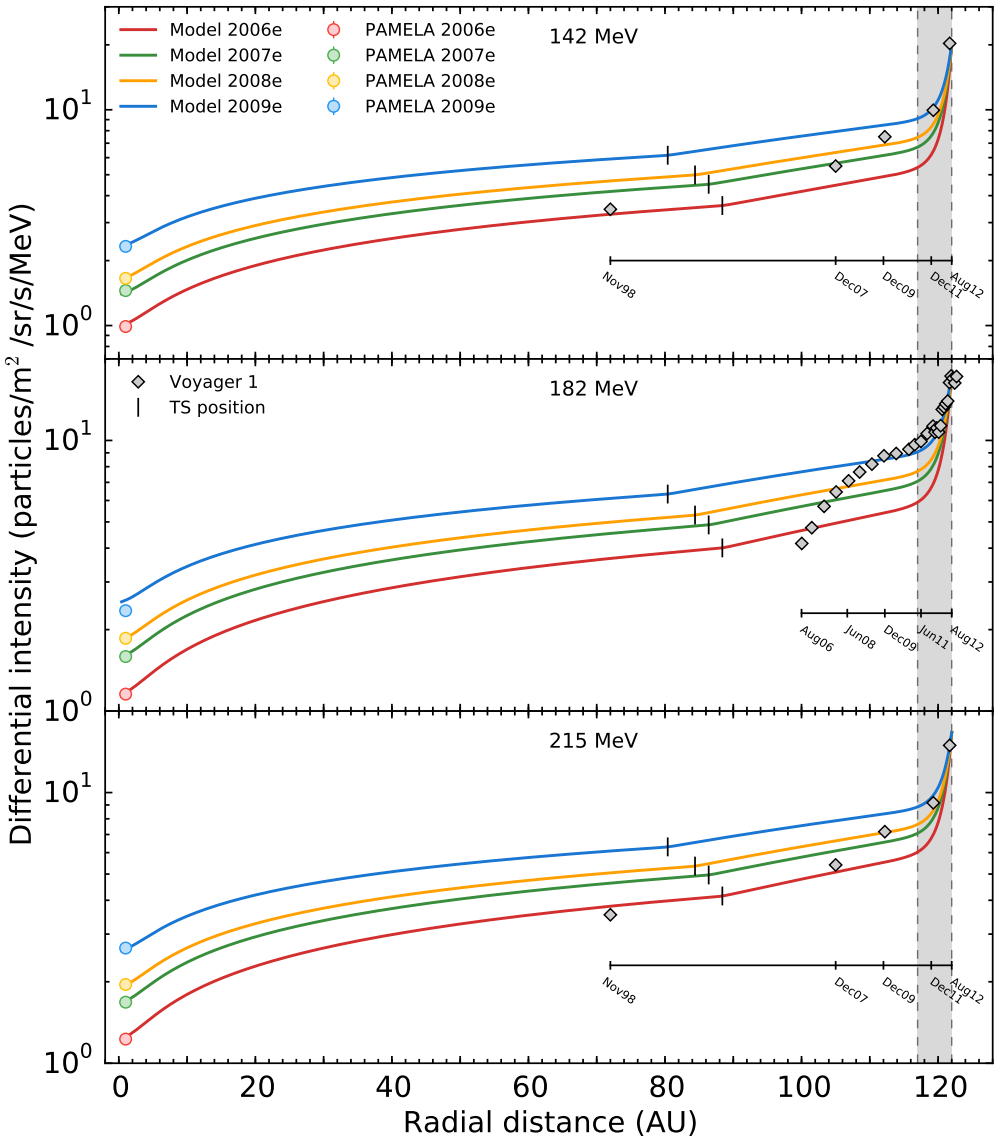

Figure 4.12: Modelled proton radial intensities at 56° colatitude between 2006e (red line) and 2009e (blue line) at energies between 142 MeV and 215 MeV (from top to bottom panel) are compared to Voyager 1 measurements (diamonds; from *Webber et al.*, 2011 and *Webber et al.*, 2013). Each panel's legend also applies to other panels. The TS positions are indicated by the short vertical black lines. The PAMELA measurements at 1 AU are given by the coloured circles. The time-scale for Voyager 1's position is included in each panel. The significance of the shaded region beyond 116 AU is discussed in the text.

such intensities are expected to have existed already at the beginning of the recent solar minimum, as shown by the red line for 2006e. The same is true for 215 MeV protons in the third panel. Observations during December 2007, at 105 AU, and December 2009, at 112 AU, in the top and bottom panels are somewhat lower than the computed intensities. This, however, is in agreement with what is expected, since Voyager 1, at this distance, essentially measured intensities related to earlier modulation conditions at the Sun. Measurements of 182 MeV protons beyond 100 AU (middle panel) support modelling results and clearly show how intensities increase up to the HP at ∼122 AU.

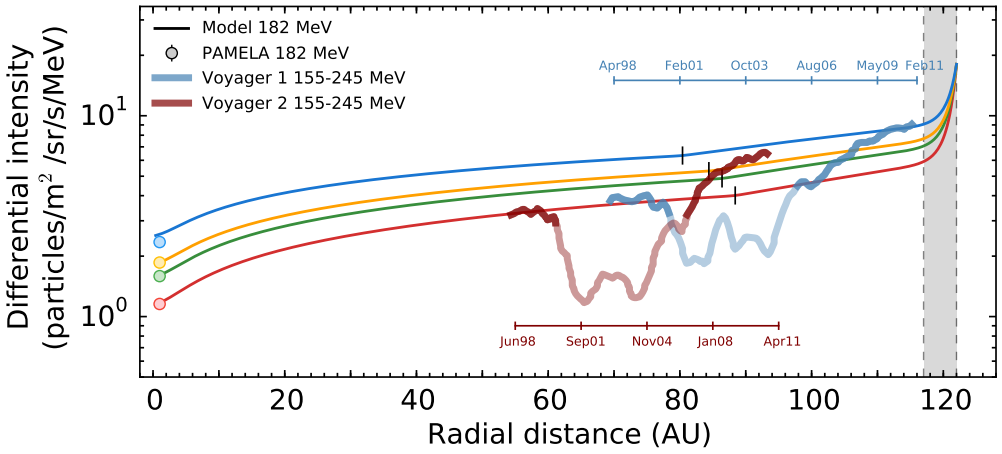

Figure 4.13: Modelled 182 MeV proton radial intensities at 56° colatitude between 2006e (red line) and 2009e (blue line) are compared to Voyager 1 and 2 observations (thick blue and maroon lines, respectively). PAMELA measurements are given by the coloured circles at 1 AU. The TS positions are indicated by the short vertical black lines. A time-scale for each Voyager spacecraft is included. The significance of the shaded region beyond 116 AU is discussed in the text. Voyager measurements were taken from *Webber et al.* (2011) and *Webber et al.* (2013).

Over a ∼5 AU region in front of the HP (indicated by the shaded region), Voyager 1 measured a pronounced increase in intensities as a precursor to entering the so-called heliosheath depletion region, now recognized as the HP region, and finally the very LISM in 2012 (e.g. *Krimigis et al.*, 2013, *Gurnett et al.*, 2013, and *Burlaga et al.*, 2013). This increase is interpreted as a barrier-region over which the SW begins to interact directly with the very LISM (e.g. *Luo et al.*, 2015). This effect has been accounted for in the model by exponentially decreasing particle MFPs in this region to reproduce the observed increase at these energies (diamond symbols). Speculation exists on how MFPs should scale in this region. Obviously, the smaller DCs must increase sharply across the HP to match the very local interstellar values as shown by *Luo et al.* (2015). The radial dependence of the DCs is discussed in Section 4.9.

Additional Voyager 1 and 2 measurements for 155 MeV to 245 MeV protons are also shown for the 1997 and 2009 minima in Figure 4.13. Since measurements between 1997 and 2000 were taken during an $A > 0$ polarity cycle, they are expected to be lower than intensities from an $A < 0$ cycle, which is the case when comparing the computed radial profiles with Voyager 1 and 2 measurements at radial distances of 53 AU to 61 AU and 68 AU to 78 AU respectively (light-blue and maroon line segments). The development of proton intensities during the maximum of solar cycle 23 can be followed by the opaque segments of these lines. Solar minimum measurements from the $A < 0$ polarity cycle between 2006 and 2011 are shown at distances of 97 AU to 115 AU and 81 AU to 93 AU for Voyagers 1 and 2 respectively. From the shape of the computed radial profiles in Figure 4.13, larger global radial gradients are expected beyond the TS and up to the HP, compared to the upstream TS region.

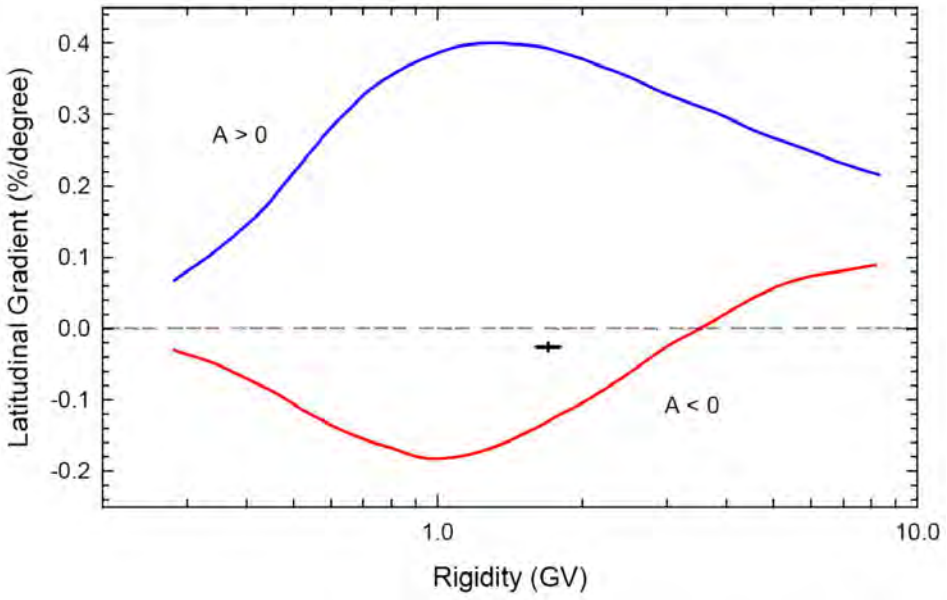

Figure 4.14: The different global latitudinal gradients predicted for protons during an $A > 0$ (blue) and an $A < 0$ (red) HMF polarity cycle (from *Potgieter et al.*, 2001a), highlighting a direct consequence of drifts. The black cross-shaped marker shows the latitudinal gradient calculated by *De Simone et al.* (2011) using PAMELA and Ulysses measurements during the solar minimum of cycle 23/24.

Evidently, the measurements discussed above agree remarkably well with the computed profiles that are based on the PAMELA observations at Earth, regarding the absolute value and the overall increase. This serves to illustrate that this global model can reproduce the modulation and the corresponding radial gradients as observed by the Voyager mission (*Vos and Potgieter*, 2015, 2016). For an in depth modelling study of GCR intensities along the Voyager trajectories, see e.g. *Manuel et al.* (2011a, 2011b, 2014).

4.7 Spatial Gradients in the Inner Heliosphere

GCRs undergo a range of modulation processes that alter their intensities over time and throughout space. Among these are the gradient and curvature drifts, which are recognized as the pre-eminent driving force behind the 22-year solar cycle. The effects that drifts have on GCRs during different polarity epochs can be measured in the radial (G_r) and latitudinal (G_θ) global gradients, which give distinct, but not invariant, results for each solar cycle – essentially serving as unique signatures of drift. Studying the spatial gradients of GCRs has consequently become key to studying GCR modulation itself.

Numerical models that include all the modulation processes (like the one used in

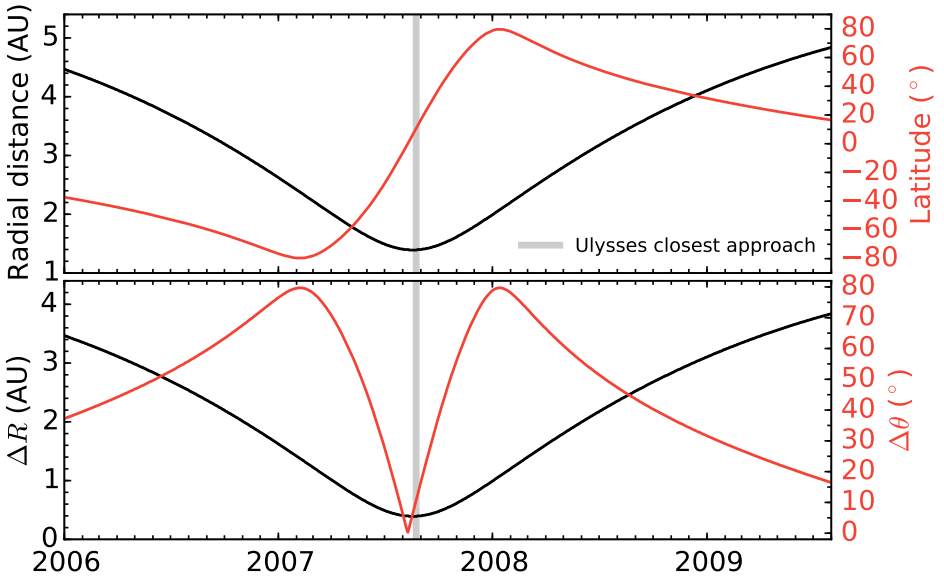

Figure 4.15: *Top panel:* The heliocentric distance (r_U) and latitude (θ_U) of Ulysses along its orbit are given by the black and red lines, respectively, between 2006 and mid-2009. *Bottom panel:* The differences in distance (Δr) and latitude ($\Delta\theta$) between the positions of Ulysses and PAMELA are given by the black and red lines respectively. The vertical grey line indicates the time of Ulysses' closest approach to Earth (see e.g. *Gieseler and Heber*, 2016).

this study) have been used to predict the radial and latitudinal gradients for differently charged GCRs. Positively charged GCRs are expected to have negative latitudinal gradients during an $A < 0$ polarity cycle for rigidities up to $\sim$3 GV, but positive latitudinal gradients during an $A > 0$ polarity cycle for all rigidities (with reversed behaviour for negatively charged GCRs). This is illustrated by the blue and red curves in Figure 4.14. These predictions were subsequently confirmed by measurements from Ulysses, Voyagers 1 and 2, IMP 8 and Pioneers 10 and 11. Positive latitudinal gradients were reported by *McKibben* (1989) during the 1975 $A > 0$ minimum, as well as during the 1995 $A > 0$ minimum by *Heber et al.* (1996a, 1996b, 1999b) and *McDonald et al.* (1997). During the 1987 $A < 0$ minimum, *Cummings et al.* (1987) reported negative latitudinal gradients, all in agreement with drift theory predictions. See also *Potgieter et al.* (1989) and *Ngobeni and Potgieter* (2010) for the definitions of spatial gradients as used in numerical modelling.

More recently, *De Simone et al.* (2011) and *Gieseler and Heber* (2016) studied the radial and latitudinal gradients of GCR protons during the $A < 0$ solar minimum of 2009, using measurements from PAMELA and the Kiel Electron Telescope on board Ulysses. For protons in the rigidity interval 1.6 GV to 1.7 GV, *De Simone et al.* (2011) reported radial and latitudinal gradients of $(2.67 \pm 0.21)\,\%/\mathrm{AU}$ and $(-0.026 \pm 0.006)\,\%/^\circ$ respectively. These gradients are much smaller than the $\sim -0.15\,\%/^\circ$ latitudinal gradients proposed by earlier drift-dominated models as shown in Figure 4.14. A likely explanation as to why such small latitudinal gradients were observed is that the 2009 solar

minimum was found to be to be diffusion-dominated. Even though the observable effects of drifts are somewhat suppressed by the excess diffusion in such a scenario, drifts still maintain a strong presence as explained by *Potgieter et al.* (2014a).

This study aims to ensure that correct global CR gradients are present in the model by comparing model results with observations from Ulysses KET and PAMELA (*Vos and Potgieter*, 2016). Instead of computing spatial gradients as defined for a heliocentric spherical coordinate system, an empirical method is used, otherwise a comparison with observationally based gradients cannot be made. For this reason the same method of analysis from *De Simone et al.* (2011) and *Gieseler and Heber* (2016) is followed here. Results from this study were published by *Vos and Potgieter* (2016).

4.7.1 An Empirical Description of Spatial Gradients

It is firstly assumed that the temporal and spatial variations of GCR intensities are separable in time and space (*McDonald et al.*, 1997). Let $J_U(R, t, r_U, \theta_U)$ be the GCR intensity at rigidity R and time t along Ulysses' orbit, with a heliocentric distance of r_U and a latitude of θ_U, averaged over one solar rotation. The intensity at PAMELA, $J_E(R, t, r_E, \theta_E)$, with r_E and θ_E the distance and latitude of Earth respectively, can be related to J_U with a function $g(R, \Delta r, \Delta\theta)$, so that

$$J_U(R, t, r_U, \theta_U) = J_E(R, t, r_E, \theta_E) \cdot g(R, \Delta r, \Delta\theta), \tag{4.2}$$

where g depends on the differences in heliocentric distance ($\Delta r = r_U - r_E$) and latitude ($\Delta\theta = |\theta_U| - |\theta_E|$) between Ulysses and PAMELA at Earth. For simplicity, the Earth's orbital inclination with respect to the solar equator is ignored so that r_E =1.0 AU and θ_E =0.0 °. Figure 4.15 gives the heliocentric distance and latitude of Ulysses between 2006 and mid-2009 (top panel), as well as the quantities Δr and $\Delta\theta$ (bottom panel). A symmetric distribution of GCRs is assumed with respect to the heliographic equator, neglecting the small asymmetries found by *Heber et al.* (1996b) and *Simpson et al.* (1996).

Assuming furthermore that radial and latitudinal variations are separable and that these variations can be approximated by an exponential law, Equation (4.2) can be rewritten as

$$J_U(R, t, r_U, \theta_U) \;=\; J_E(R, t, r_E, \theta_E)\; e^{G_r \cdot \Delta r}\; e^{G_\theta \cdot \Delta\theta}, \tag{4.3}$$

where G_r and G_θ are the respective rigidity dependent radial and latitudinal gradients. For an explanation on how corresponding rigidity channels from Ulysses KET and PAMELA are selected to ensure that data from similar rigidities are compared, see *De Simone et al.* (2011).

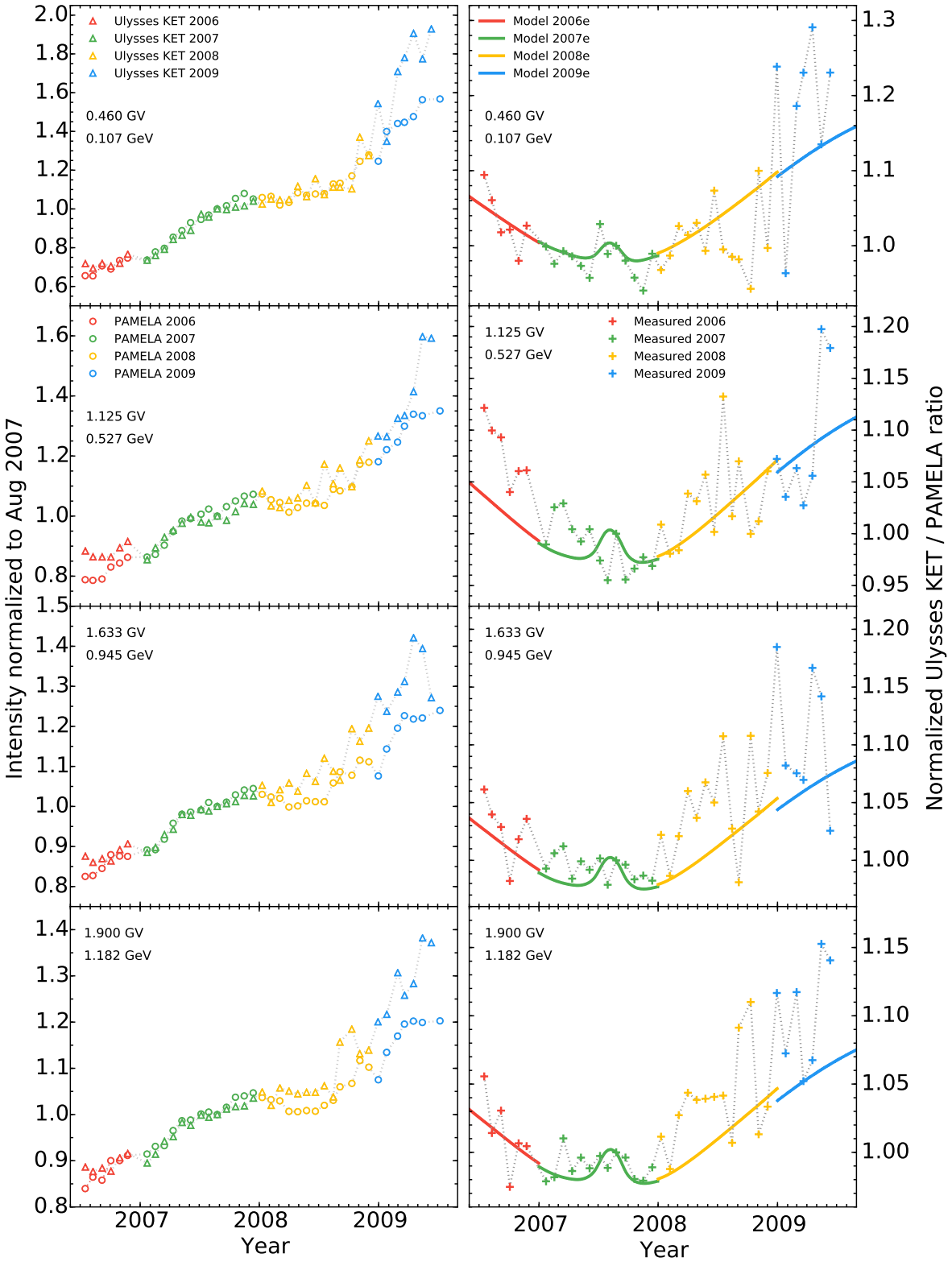

Figure 4.16: *Left panels:* The time profiles of intensities measured by Ulysses KET (triangles) and PAMELA (circles), normalized at the time of Ulysses' closest approach to Earth, in August 2007. *Right panels:* Normalized Ulysses KET to PAMELA ratios (J_u/J_E), where measured and modelled intensities are represented by the connected crosses and coloured lines respectively. From top to bottom, measured and computed intensities are shown at four rigidities between 460 MV and 1.9 GV. Only computed year-end ("e") spectra from the model were used for comparison.

4.7.2 Calculating the Spatial Gradients

In order to calculate the radial and latitudinal gradients from observed intensities, Equation (4.3) is rewritten as

$$\begin{aligned} \log\left(\frac{J_U}{J_E}\right) &= G_r \cdot \Delta r + G_\theta \cdot \Delta\theta \\ \frac{1}{\Delta r}\log\left(\frac{J_U}{J_E}\right) &= G_r + G_\theta \cdot \frac{\Delta\theta}{\Delta r}. \end{aligned} \tag{4.4}$$

Setting $X := \Delta\theta/\Delta r$ and $Y := 1/\Delta r \log(J_U/J_E)$, Equation (4.4) can be written as

$$Y = G_r + G_\theta \cdot X. \tag{4.5}$$

If it is assumed that G_r and G_θ are independent of time and space, their respective values can be obtained from the offset and slope of a straight line fitted through the graph of Y against X. Since the latter assumption is not very accurate for the time period of Ulysses' FLS, between May and December of 2007, *Gieseler and Heber* (2016) and *De Simone et al.* (2011) studied the spatial gradients during the Southern ascent, the FLS and the Northern descent phases of Ulysses' trajectory separately and combined. In the current study, however, the four year-end spectra corresponding to the PAMELA spectra from *Adriani et al.* (2013a) are used.

In determining G_r and G_θ, the intensity time profiles of Ulysses KET (Gieseler, 2014, *private communication*) and PAMELA are normalized to unity at the time of Ulysses' closest approach to Earth in August 2007 (vertical grey line in Figure 4.15). This is done as an attempt to minimize possible uncertainties in flux estimation related to determining Ulysses' geometrical factor. This is shown in the left panels of Figure 4.16, which gives four sets of measurements at rigidities between 460 MV and 1.9 GV (from top to bottom), normalized as required. Yearly intensities are once again colour-coded as indicated by the legend. Both instruments show a similar time evolution in intensities, except that Ulysses, as expected, measured higher relative intensities than PAMELA over most of its orbit. These plots also illustrate the ongoing recovery of GCRs after August 2007, even though the lowest SSN was observed in 2007 and 2008 (e.g. *Heber et al.*, 2009). The differences between PAMELA and Ulysses KET can primarily be ascribed to spatial variations.

Shown in the right panels of Figure 4.16 are the normalized Ulysses KET to PAMELA intensity ratios that appear as J_U/J_E in Equation (4.4). In these graphs, measurement ratios (crosses) are compared to the normalized and interpolated intensity ratios from the modulation model at Earth and along Ulysses' trajectory (lines) that correspond to the yearly intervals. Given the fact that continuous temporal variations are approximated by only four sets of parameters that reflect yearly variations in a steady-state model,

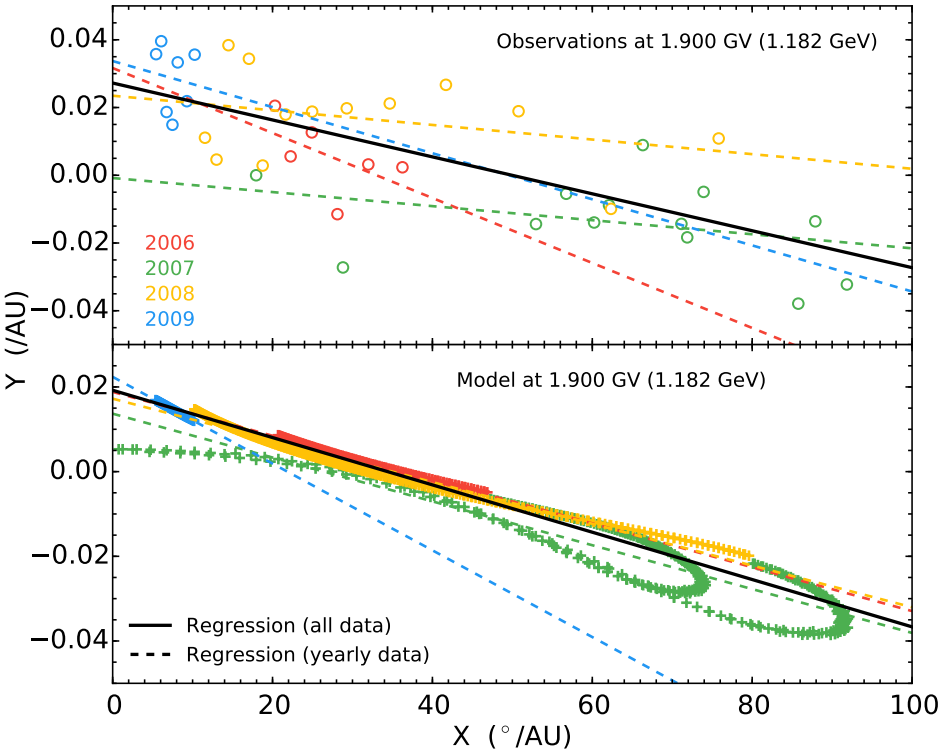

Figure 4.17: Quantities Y and X (from Equation 4.5) are plotted against each other, based on the observed 1.9 GV protons (top panel) and the modelled year-end spectra (bottom panel). Linear regression is performed to obtain a best fit to the data (solid black line), from which G_r and G_θ can in turn be obtained. Yearly fits are also shown by the coloured dashed lines.

the ratios of the computed solutions are in very good agreement with observations. At 460 MV, for example, the model reproduces the relative higher intensities at high latitudes in the inner heliosphere, as required by measurements taken during this time. However, differences between the model and measurements are noticeable at 1.125 GV during 2006 and at 1.633 GV and 1.9 GV between 2008 and 2009. The effect of drifts can also be identified from the marked increase in intensity in 2007, when Ulysses performed its FLS. This increase is caused by positive particles that drift inward mainly along the HCS during an $A < 0$ cycle, resulting in higher intensities in the equatorial regions than at higher latitudes. Observations also confirm this behaviour.

With $\Delta\theta$ and Δr known and J_U/J_E calculated as in Figure 4.16, Y can be plotted against X, which is shown in Figure 4.17 for 1.9 GV proton measurements (top panel) and modelled results (bottom panel). Linear regression is used to find a best fit to the data, from which G_r and G_θ follow from the offset and slope of the fitted line (solid black) respectively. By considering the yearly colour-coded data points separately, corresponding yearly gradients are obtained (dashed lines). However, due to the sparsity of observational data, these results give large variations in the radial and latitudinal gradients, which is evident from the dashed lines in the top panel. Consequently, all of the observational data points are used for calculating gradients between Ulysses and

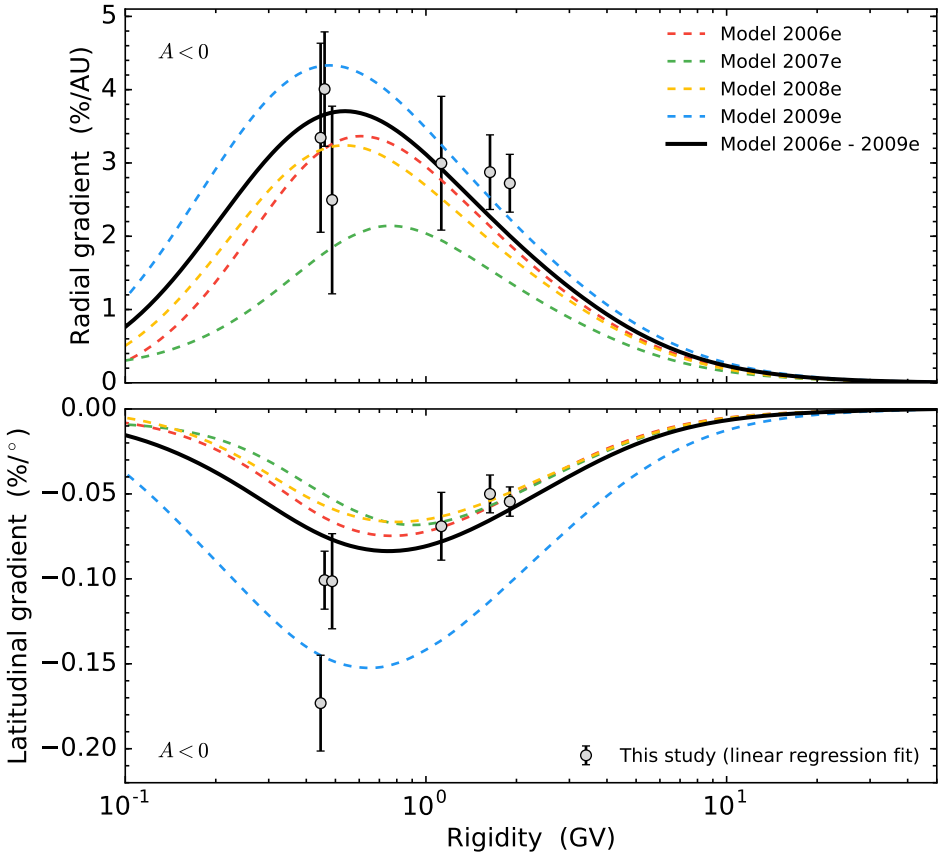

Figure 4.18: *Top panel:* Global radial gradients (G_r) calculated between the positions of PAMELA (at Earth) and along Ulysses' orbit, from July 2006 to June 2009. *Bottom panel:* Similar to the top panel but for global latitudinal gradients (G_θ). In both panels the year-end model gradients are given by the coloured dashed lines, while model gradients for the combined time period are given by the solid black line. These are compared to the gradients calculated in this study from measurements of Ulysses KET and PAMELA (symbols), for an $A < 0$ polarity cycle. Error margins represent standard deviations.

PAMELA. The yearly X and Y data that follow from modelling (bottom panel) appear more correlated, so that the gradients from these will be considered as an estimation range for temporal variation. This procedure is applied to model solutions at every rigidity step, as well as to Ulysses KET and PAMELA observations for the coinciding rigidity channels.

The resulting radial and latitudinal gradients are shown as a function of rigidity in the top and bottom panels of Figure 4.18 respectively. In addition to producing positive radial and negative latitudinal gradients, as expected from drift theory for protons in an $A < 0$ cycle, modelling results (lines) are also found to agree remarkably well with observational data (symbols), where the error bars represent standard deviation values. When considering the error bars, almost all of the observational points are within the yearly variation range (dashed lines). According to this analysis, the model predicts that the largest radial gradients occured during 2009, with a maximum of $\sim$3.75 %/AU around 500 MV, while the smallest radial gradients were predicted during 2007. The

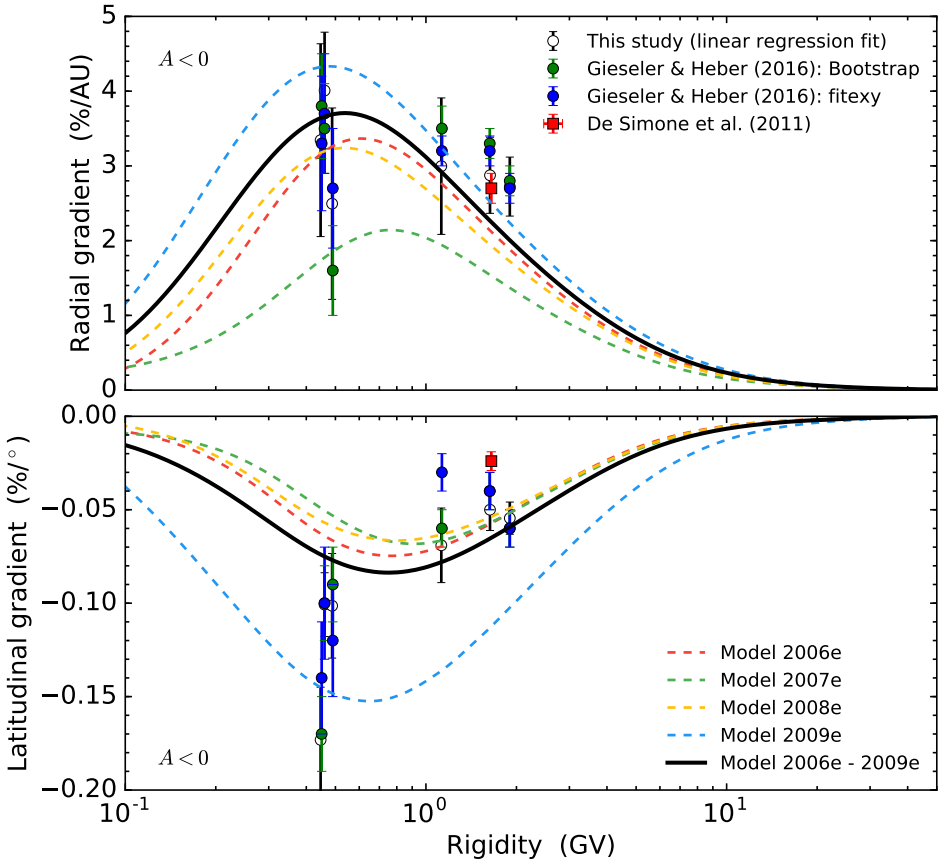

Figure 4.19: Similar to Figure 4.18, now for a comparison between the year-end computed gradients from this study (lines) to the observational-based results from other authors as indicated in the legend.

latter comes as a result of the fact that $\Delta\theta$ varied significantly during 2007, when Ulysses performed its FLS, causing the assumption that G_r and G_θ are independent of time and space to become less accurate.

For the latitudinal gradients, the largest values were also predicted for 2009, with a maximum of $\sim -0.085\,\%/^\circ$ around 800 MV, while the smallest latitudinal gradients were predicted for 2007. A characteristic feature of modelling results is that gradient magnitudes decrease significantly below $\sim$400 MV, because drifts decrease with decreasing rigidity (as shown in Figure 4.22). Table 4.4 gives the radial and latitudinal gradients calculated from PAMELA and Ulysses/KET observations in this study.

Figure 4.19 gives a comparison of modelled (lines) and observational gradients from this study (open circles), to observational gradients from other authors (filled symbols). *De Simone et al.* (2011) calculated respective radial and latitudinal gradients of $(2.67 \pm 0.21)\,\%/\mathrm{AU}$ and $(-0.026 \pm 0.006)\,\%/^\circ$ for 1.6 GV to 1.7 GV protons (red square symbols). Apart from the latitudinal gradient being noticeably lower than the $\sim -0.065\,\%/^\circ$ model prediction, which can be ascribed to differences in the analysis method and recent refinements in the PAMELA data, the gradients from these authors

Table 4.4: Radial and latitudinal gradients calculated in this study from PAMELA and Ulysses/KET observations.

Rigidity (GV)	**Radial Gradient (%/AU)**	**Latitudinal Gradient (%/°)**
0.45	3.3 ± 1.3	-0.173 ± 0.028
0.46	4.0 ± 0.8	-0.101 ± 0.017
0.49	2.5 ± 1.3	-0.101 ± 0.028
1.13	3.0 ± 0.9	-0.069 ± 0.020
1.63	2.9 ± 0.5	-0.050 ± 0.011
1.90	2.7 ± 0.4	-0.055 ± 0.009

are comparable with gradients from the model. Two different sets of gradient results from *Gieseler and Heber* (2016) are also shown by the green and blue circles, where these were calculated using observations over the full time period from mid-2006 to mid-2009, in the 1.25 GV to 1.90 GV range. The green and blue sets of gradients were obtained using two different statistical fitting procedures that were applied to the X and Y data points, hence the differences in their values (see *Gieseler and Heber*, 2016, and references therein, for more information about these statistical procedures). Compared to the model gradients, slightly larger radial and smaller latitudinal gradients were measured around ~ 1.5 GV. In general, however, observed gradients from *Gieseler and Heber* (2016) are in good agreement with model predictions, as well as with the observational gradients calculated in the current study (given by the open circles and taken from Figure 4.18).

In conclusion, it is clear from these results that the model used in this study produces radial and latitudinal gradients that are in agreement with *in situ* measurements taken during the time that the Ulysses and PAMELA missions overlapped. Through the combination of measurements from these instruments, as was done in this section, the characteristic signatures of gradient, curvature and current sheet drifts are highlighted and well reproduced through modelling (see Section 4.9 for a discussion of the DCs used to obtain the computed results).

4.8 Proton Intensities Over Time

The time-dependent evolution of GCRs forms an important study with regard to temporal changes in modulation. The effect of gradient, curvature and current sheet drifts are particularly more prevalent over a long-term modulation cycle, such as the 11-year and 22-year cycles. *Potgieter et al.* (1993) and *le Roux and Potgieter* (1995) showed that a complete 22-year modulation cycle can be simulated to a first-order by combining drifts and GMIRs in a time-dependent modulation model, concluding that drifts were

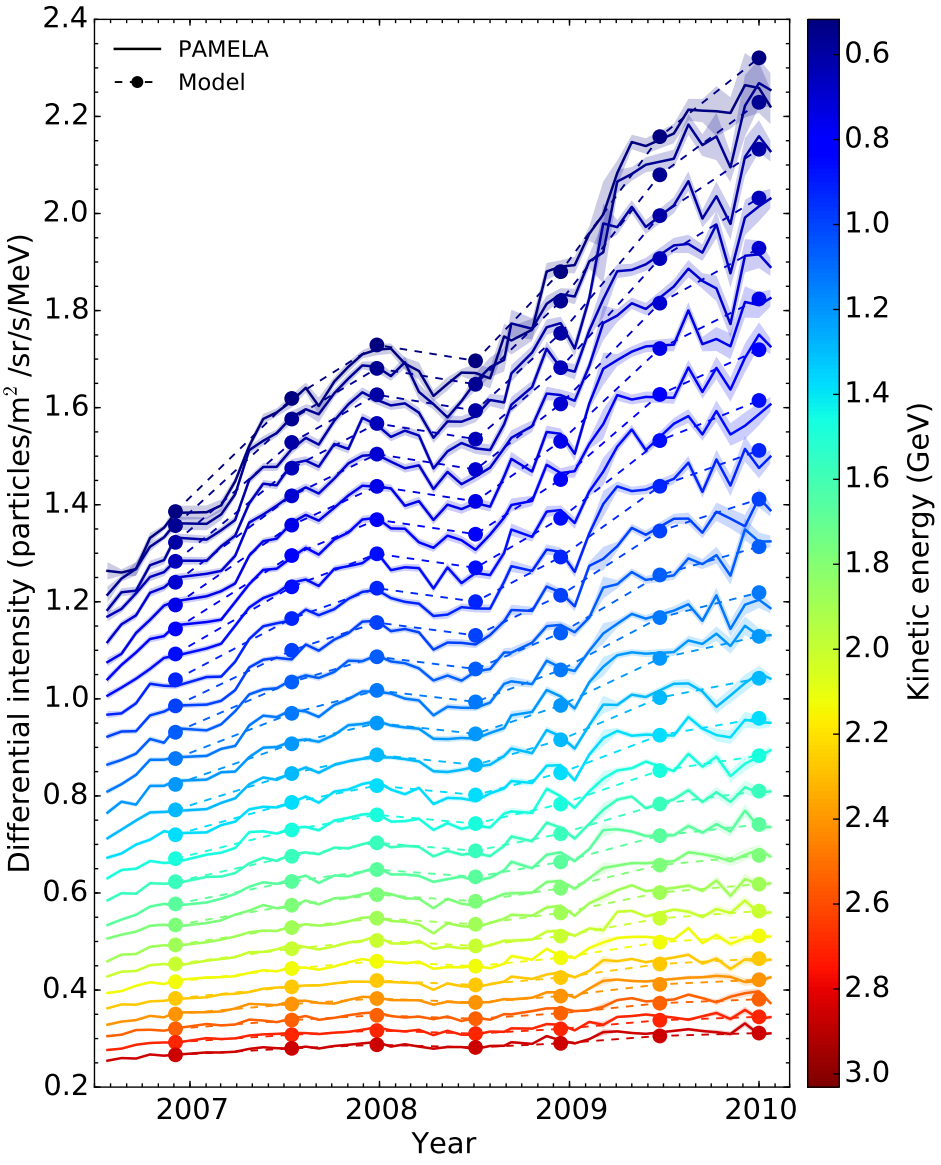

Figure 4.20: PAMELA proton intensities (solid lines), along with statistical errors (shaded bands) are compared to modelled intensities (dashed lines and filled circles) over time. Different energies are represented by the range of colours according to the colorbar.

primarily responsilbe for time-dependent modulation during moderate to minimum solar conditions, whereas during maximum solar activity drifts became less dominant (see also *Potgieter*, 1993, 1997). A compound model was introduced by *Ferreira and Potgieter* (2004) in which all transport parameters are scaled over time by HMF values observed at Earth. Various authors have shown that this approach gives results that are in good agreement with observations from Voyager 1 and 2, Ulysses and IMP 8 (*Ndiitwani et al.*, 2005; *Ferreira and Scherer*, 2006; *Manuel et al.*, 2011a, 2011b, 2014).

By studying the time-evolution of measured proton intensities, in comparison with the numerically reproduced spectra, quantitative and qualitative insights can be gained of how intensities developed during the recent solar minimum period. Figure 4.20 shows

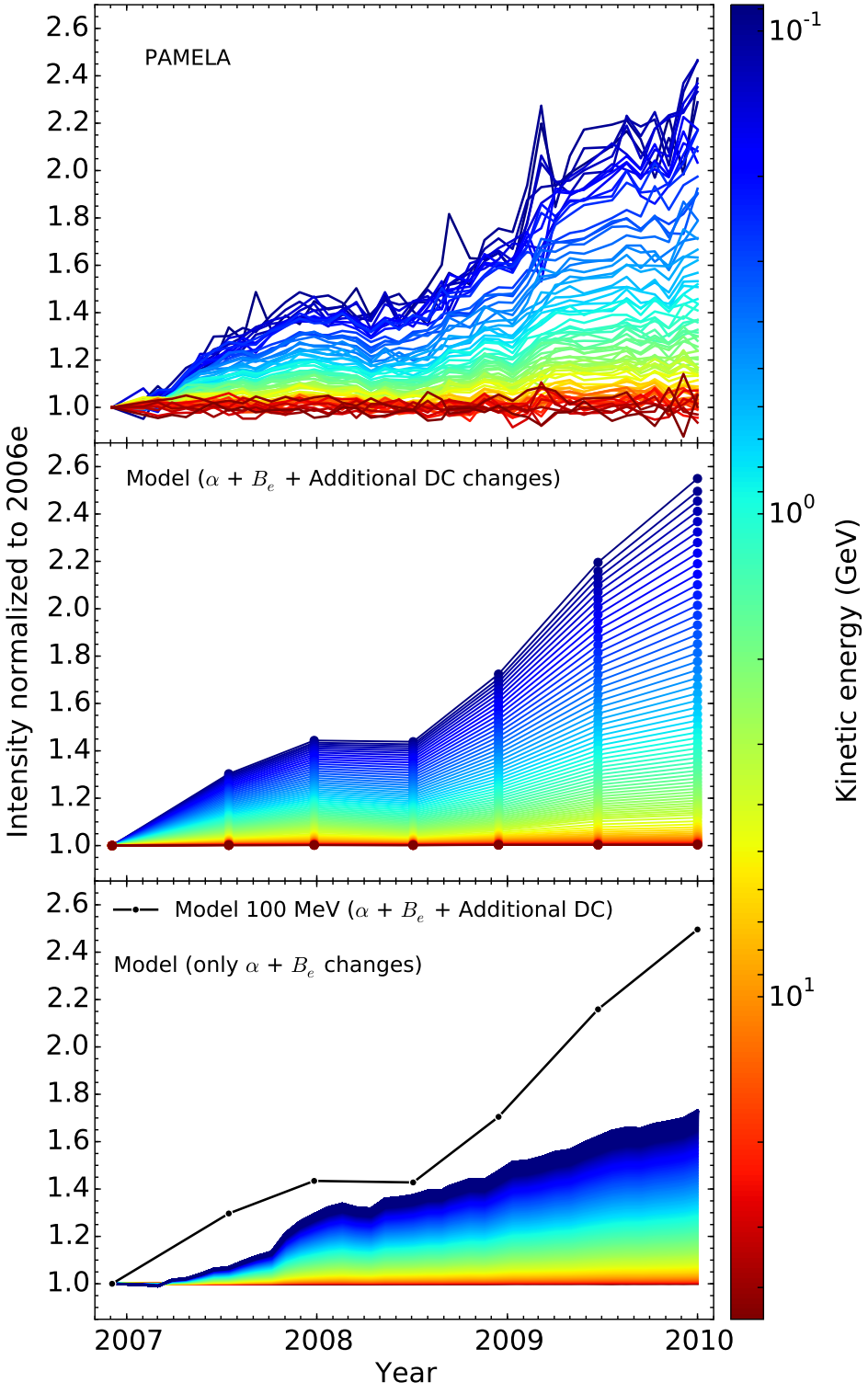

Figure 4.21: *Top panel:* PAMELA proton intensities between 90 MeV and 50 GeV, normalized to 2006e, as a function of time. Energy values are colour-coded according to the colorbar. *Middle panel:* Similar to the top panel, but for the computed intensities. Changes in α and B_e were considered here, as well as additional DC changes. *Bottom panel:* Similar to the middle panel, but only considering changes in α and B_e. For comparison, the black line represents ∼100 MeV computed intensities from the middle panel.

the observed PAMELA intensities with statistical errors in the 500 MeV to 3.0 GeV energy range from mid-2006 to the end of 2009 (solid lines and shaded bands), along with the model intensities at the same energies (dashed lines and symbols), with the different energy ranges colour-coded according to the colorbar. Less time-dependent modulation is evident from the smaller intensity increases at higher energies. During 2007, intensities increased gradually, with fluctuations observable only at lower energies. In 2008, however, as a result of the sudden increase in the HCS tilt angle, proton intensities decreased across all energies, and recovered by the end of 2008. During 2009, intensities increased more rapidly than during the previous two years, due to the continued decrease in solar activity. Even though the proton spectrum changed dynamically over time, modelled intensities are consistent with how the proton spectrum evolved at these energies.

Figure 4.21 gives a quantitative measure of the normalized intensity increase relative to November 2006. Shown in the top panel are PAMELA measurements, while the middle panel gives computed intensities that include changes in α and B_e, as shown in Figure 4.6, as well as additional DC changes that will be described in Figure 4.22. The bottom panel gives the computed intensities for which the above-mentioned DC changes are neglected. At the lowest energy ($\sim$100 MeV), measured proton intensities increased by a factor of 1.4 during 2007, followed by a 1.3 factor increase in 2008. During 2009 an increase by a factor of $\sim$ 1.4 was observed.

Through modelling, these observed increases were reproduced, as shown in the middle panel of Figure 4.21. Apart from changing α and B_e (as discussed in Section 4.5.2), additional increases in the DCs were also required, i.e. on top of the corresponding DC changes caused by using a time varying HMF. Neglecting these lead to intensities that are $\sim$ 75% smaller compared to PAMELA measurements (at an average energy of 100 MeV). This is illustrated in the bottom panel of Figure 4.21, where the black line represents normalized 100 MeV computed intensities from the middle panel, and the coloured region represents the computed intensities where only averaged α and B_e values for each Carrington rotation were changed. The difference between the dark blue region and the black line essentially represents the contribution from these additional increases in DCs. The rigidity and spatial dependencies of the DCs are further discussed in more detail in the next section.

4.9 Rigidity and Spatial Dependence of the Modulation Coefficients

As the heliosphere approached solar minimum conditions, it can be inferred that the HMF became more structured in the years leading up to 2009 (e.g. *McComas et al.*,

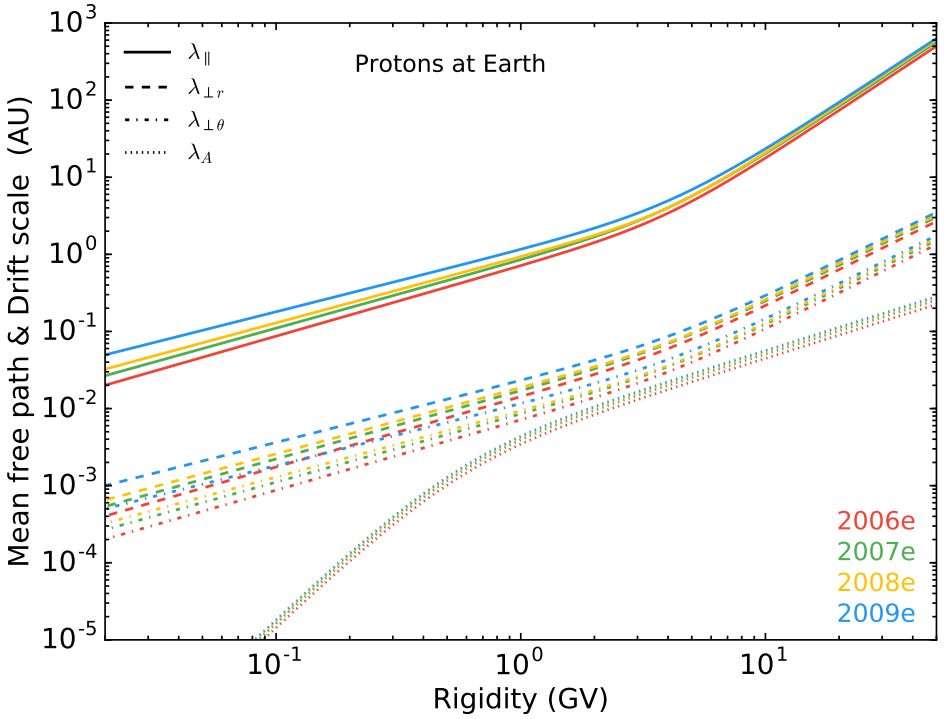

Figure 4.22: The time development of the rigidity dependence of the proton MFPs and drift scale for diffusion parallel and perpendicular to the magnetic field lines at Earth. Parallel MFPs ($\lambda_\parallel$) are given by the solid lines, while perpendicular MFPs in the radial ($\lambda_{\perp r}$) and polar ($\lambda_{\perp\theta}$) directions are given by the dashed and dashed-dotted lines respectively. The drift scale (λ_A) is given by the dotted lines.

2008), which effectively reduced the amount of turbulence in the heliosphere and increasing particle MFPs. These increases, combinded with drifts, are expected to be directly responsible for the intensity increase observed across the greater part of the proton spectrum between 2006 and 2009. The numerical solutions given in Figures 4.7 and 4.8 were obtained by using an intuitive diffusion approach that approximates QLT (e.g *Jokipii*, 1966) while still adhering to certain constraints from turbulence theory. This approach also aims to improve on similar approaches used by *Vos* (2012), *Vos et al.* (2013a) and *Potgieter et al.* (2014a).

Figure 4.22 shows the rigidity dependence of the parallel ($\lambda_\parallel$) and perpendicular ($\lambda_\perp$) MFPs, as well as the drift scale (λ_A), for the reproduced 2006 to 2009 year-end spectra (see Equations 3.28 and 3.43 for the corresponding coefficients). As mentioned in the previous section, it follows from this study that, apart from the self-consistent changes caused by the yearly weakening average HMF strength, additional increases in proton MFPs below ~3.0 GV were required in order to reproduce subsequent PAMELA spectra. This resulted in a change in slope of the rigidity dependence from $P^{0.9}$ in 2006, to $P^{0.8}$ in 2009, consistent with what is expected from the non-linear intensity increase that can be seen toward lower energies in the bottom panel of Figure 4.3. Above ~3.0 GV the rigidity slope gradually steepens to $P^{2.1}$, similar to the P^2 dependence found by *Pei*

et al. (2010a) following their QLT-based analysis of $\lambda_{\parallel}$.

For diffusion perpendicular to the magnetic field lines, a rigidity dependence similar to that of $\lambda_{\parallel}$ is assumed below 4 GV, while a slightly weaker dependence of $P^{1.58}$ is assumed above 4 GV. Distinction is made between the radial ($\lambda_{\perp r}$) and polar ($\lambda_{\perp\theta}$) diffusion directions, where the former and latter are scaled by 2% ($\kappa^0_{\perp r} = 0.02$) and 1% ($\kappa^0_{\perp\theta} = 0.01$) of the parallel diffusion respectively. This differs from what *Vos* (2012) and *Potgieter et al.* (2014a) used and is more in line with what is required from turbulence theory (see e.g. *Burger et al.*, 2000; *Bieber et al.*, 2004; *Strauss et al.*, 2013).

Due to the non-axisymmetry found in turbulence and the background HMF (e.g *Matthaeus et al.*, 2003), *Zhao et al.* (2014) followed a similar approach for perpendicular diffusion and also proceeded to reproduce the PAMELA proton spectra from 2007, 2008 and 2009, from which they reported perpendicular scaling factors of $\kappa^0_{\perp r} = 0.02$ and $\kappa^0_{\perp\theta} = 0.01$. These authors additionaly reproduced IMP 8 measurements from the $A > 0$ minimum of solar cycle 22/23 and the $A < 0$ minimum of solar cycle 21/22, using values of $\kappa^0_{\perp r} = 0.03$ and $\kappa^0_{\perp\theta} = 0.02$ in both cases. Furthermore, optimal parameters of $\kappa^0_{\perp r} = 0.014$ and $\kappa^0_{\perp\theta} = 0.01$ were obtained by *Manuel et al.* (2014) for measurements in the inner and outer heliosphere from Voyager 1, IMP 8 and Ulysses. These results favour larger MFPs, suggesting the possibility of more efficient radial diffusion in times of weak turbulence found during solar minima (see also *Effenberger et al.*, 2012).

In an independent study, *Raath* (2014) applied a SDE-based model to reproduce PAMELA proton spectra between 2006 and 2009, using the same very LIS, HMF modification and diffusion approach that was assumed for this study. This author found that a $\lambda_{\parallel}$ rigidity dependence of between $P^{0.85}$ and $P^{0.73}$ was required to reproduce the

Table 4.5: A summary of the parameters used to reproduce the sampled PAMELA spectra in Figures 4.7 and 4.8. See Chapter 3 for discussions of these variables and the equations containing them.

Parameter	**2006e**	**2007m**	**2007e**	**2008m**	**2008e**	**2009m**	**2009e**
$\lambda_{\parallel}$ (AU) *	0.715	0.812	0.855	0.850	0.937	1.068	1.162
$\kappa_{A\,0}$	1.00	1.00	1.00	1.00	1.00	1.00	1.00
$P_{A\,0}$ (GV)	0.55	0.55	0.55	0.55	0.55	0.55	0.55
$\kappa^0_{\perp r}$	0.02	0.02	0.02	0.02	0.02	0.02	0.02
$\kappa^0_{\perp\theta}$	0.01	0.01	0.01	0.01	0.01	0.01	0.01
c_1	0.91	0.89	0.88	0.87	0.86	0.83	0.80
$c_{2\,\parallel}$	2.10	2.10	2.10	2.10	2.10	2.10	2.10
$c_{2\,\perp}$	1.58	1.58	1.58	1.58	1.58	1.58	1.58
c_3	2.60	2.60	2.40	2.70	3.00	2.20	2.20
P_k (GV)	4.00	4.05	4.05	4.05	4.08	4.30	4.30
$d_{\perp\theta}$	2.00	2.00	2.00	2.00	2.00	2.00	2.00

* For 1.0 GeV at Earth

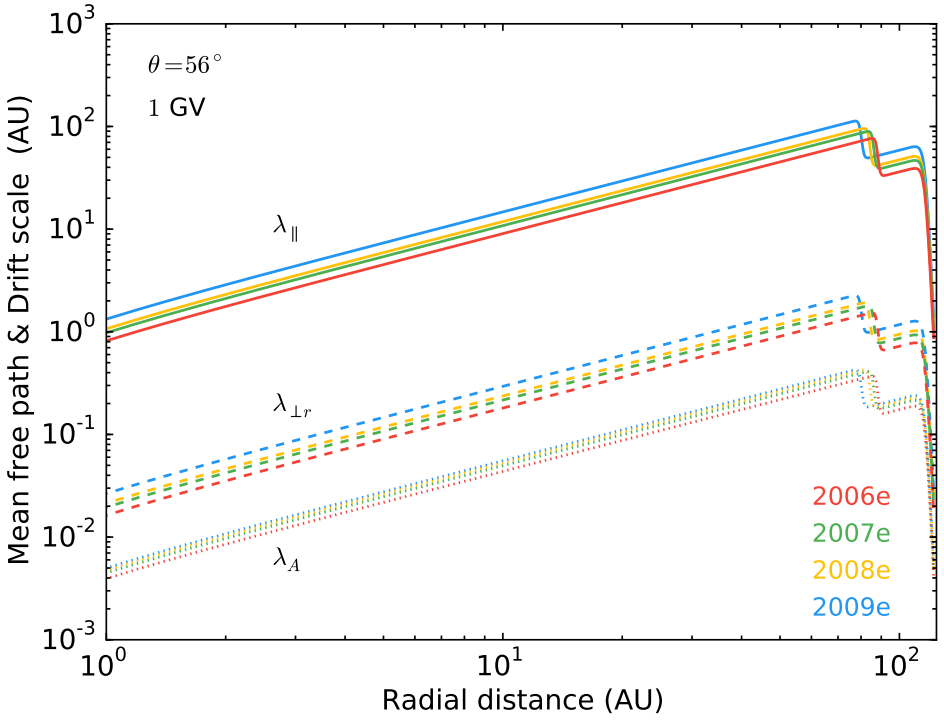

Figure 4.23: MFPs and drift scale for 1 GV protons for 2006e, 2007e, 2008e and 2009e, as a function of radial distance at a polar angle of $\theta = 56°$. The TS was moved outward during this period as discussed in Section 4.5.2 (see Table 4.2).

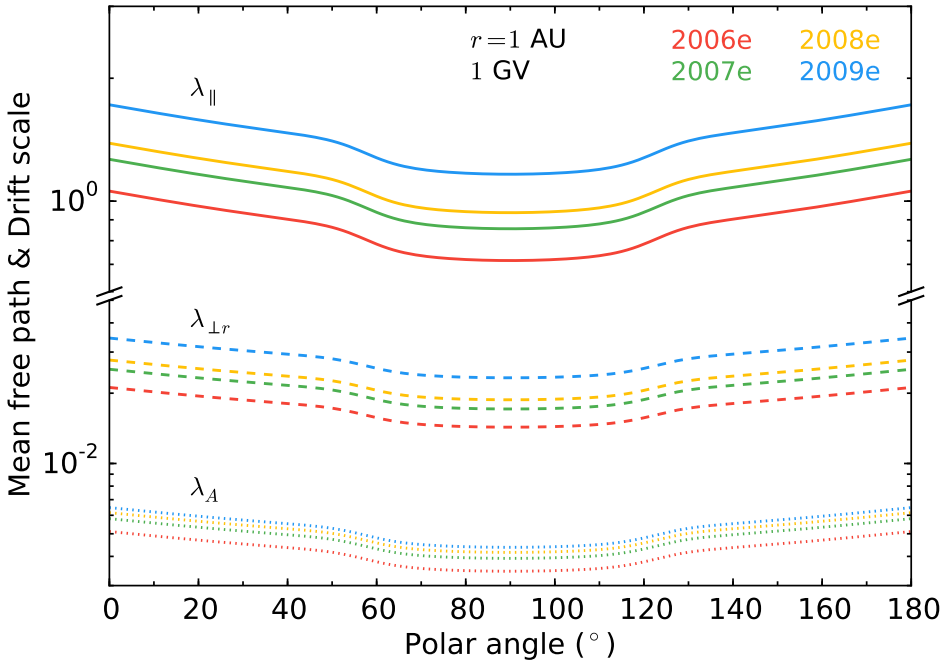

Figure 4.24: Similar to Figure 4.23, but as a function of polar angle at a radial distance of r =1 AU.

PAMELA spectra. In general, the results from *Raath* (2014) are qualitatively similar to the results from this study, where any quantitative differences can be ascribed to the different numerical techniques.

The radial and polar angle dependencies for the MFPs and drift scales of 1 GV protons are given in Figures 4.23 and 4.24. These quantities increase like r^1 with distance for $\theta = 56°$, but undergo a sudden decrease at the TS between 80 AU and 90 AU. MFPs and drifts are scaled down exponentially about 5 AU ahead of the HP as modulation processes become less dominant and the SW start to interact with the very LISM (e.g. *Luo et al.*, 2015). This reproduces the steep increase in proton intensities observed by Voyager 1 (see Figure 4.12). From Figure 4.24 it is clear that smaller MFPs and drift scales are present in the slow SW region (between 60° and 120° polar angle), relative to the fast SW regions. This follows from the $1/B$ spatial dependence found in diffusion and drifts, and the fact that the HMF magnitude is larger in the slow SW region.

Table 4.5 gives a summary of the important diffusion-related variables used to reproduce the sampled PAMELA spectra. The values of these variables are different than those found by *Vos* (2012), *Vos et al.* (2013a) and *Potgieter et al.* (2014a), primarily because the Smith-Bieber HMF modification is used in this study, as well as the updated LIS and the slightly different assumptions made with regard to diffusion that are more compatable with turbulence theory. Smaller $\kappa_{\parallel 0}$ values were required for this study, while DCs below 4 GV had a stronger rigidity dependence compared to previous studies.

It is apparent from proton measurements, as well as from modelling results, that increasingly more low-energy particles reached the Earth during the ~ 4 years leading up to 2009. Even though diffusion remained a dominant modulation mechanism during this time, it will be shown throughout this work that the presence of drifts still had a significant contribution to the record-high intensities measured by PAMELA at the peak of the 2009.

4.10 Summary

Various aspects pertaining to GCR proton modulation during the recent 2009 solar minimum were discussed in this chapter. A new observationally based proton very LIS was constructed using PAMELA measurements at Earth above 30 GeV, where the effects of modulation become negligible, and Voyager 1 measurements beyond the HP for energies below 600 MeV. The expression for this very LIS is given by Equation (4.1).

Using this very LIS, and the modulation model discussed in Chapter 3, a selection of seven PAMELA proton spectra at semesterly intervals were reproduced for the time between mid-2006 and the end of 2009. This was done using a diffusion approach based on QLT (similar to previous studies from *Vos*, 2012, *Vos et al.*, 2013a, and

Potgieter et al., 2014a) and by setting up appropriate modulation conditions in the model with HCS tilt angle and HMF averages. The above-mentioned averages were calculated by taking respective ∼16-month and ∼10-month simple moving averages of Carrington rotation tilt angle and HMF measurements, and are given in Table 4.2. These averages show that α decreased from 16.8° in 2006e, to 9.5° in 2009e, while B_e decreased from 4.95 nT to 3.91 nT over the same time period. In addition to an updated very LIS, a Smith-Bieber HMF modification was used in this study for reasons discussed in Chapter 3. The reproduced PAMELA spectra were shown in Figures 4.7 and 4.8.

Special emphasis was placed on PAMELA measurements taken during the 2009 solar minimum, since this minimum proved to be extraordinary in the sense that minimum conditions lasted longer than expected, making it ideal to study charge-sign dependent modulation. PAMELA consequently measured a factor of ~ 3 increase in 100 MeV protons during this minimum, with respect to June 2006, resulting in the highest spectrum ever recorded at Earth at the end of 2009.

In Section 4.6, the radial dependence of proton intensities was also investigated and compared with Voyager 1 and 2 measurements at different energies. In order to reproduce the sharp increase measured by Voyager 1 ahead of the HP, DCs and drifts were scaled down exponentially starting at 116 AU. Overall, good agreement was found between computed intensities and Voyager measurements (see Figure 4.12).

With the overlapping of the Ulysses and PAMELA missions between mid-2006 and mid-2009, when Ulysses also performed its final FLS, a detailed study of the global radial and latitudinal gradients was conducted in Section 4.7. This was done by calculating the gradients of CR intensities between the positions of PAMELA and Ulysses in the inner heliosphere, and comparing these to similar calculated gradients from the model (following the analysis of *De Simone et al.*, 2011, and *Gieseler and Heber*, 2016). Figures 4.18 and 4.19 give comparisons between the model gradients, observational gradients calculated in this study from Ulysses KET and PAMELA measurements and observational gradients from other authors. Good agreement was found in all cases, especially when considering the statistical error bars on observations, and how the model predicts gradients to vary between years. These global gradients also show distinct signatures of gradient, curvature and current sheet drifts as expected from drift theory for an $A < 0$ solar cycle.

In Section 4.8, the time dependence of proton intensities was discussed. Figure 4.20 shows how the general time development of these GCRs, as measured by PAMELA, was reproduced, including the transient intensity decrease seen in 2008. Apart from self-consistently changing α and B_e for every semester, additional changes in the DCs were also required in order to reach sufficiently high intensities. The relative intensity increase observed by PAMELA could only be reproduced when all of these changes were incorporated in the model.

The resulting MFPs and drift scales were discussed in Section 4.9. In order to reproduce the PAMELA spectra, the MFPs below ∼4 GV were increased by reducing the MFP rigidity depdendence. A $P^{0.91}$ dependence was required for 2006e, while a $P^{0.8}$ was required for 2009e. For diffusion perpendicular to the HMF, $\lambda_{\perp r}$ and $\lambda_{\perp \theta}$ were scaled by factors of $\kappa^0_{\perp r} = 0.02$ and $\kappa^0_{\perp \theta} = 0.01$ relative to $\lambda_{\parallel}$ below ~ 4 GV. Figure 4.22 shows the MFPs and drift scales for the computed year-end spectra and summarizes how these quantities developed over time. Because Voyager 1 measured a sharp increase in proton intensities beyond 116 AU, as the SW starts to interact with the very LISM, the MFPs and drift scale were scaled down exponentially ∼5 AU ahead of the HP in order to increase proton intensities in accordance with observations (see Figure 4.23).

The values of important modulation-related variables are given in Table 4.5. Differences between these values and the values found by *Vos* (2012), *Vos et al.* (2013a) and *Potgieter et al.* (2014a) can be ascribed to the use of an updated very LIS, a different HMF modification and a somewhat different rigidity dependence for $\kappa_{\parallel}$ and $\kappa_{\perp}$ for this study. Similar studies performed by *Zhao et al.* (2014) and *Raath* (2014) yielded spectra and MFPs that are in good agreement with those found in this study.

Chapter 5

Heliospheric Modulation of Electrons

5.1 Introduction

Over the course of the recent solar minimum of cycle 23/24, the PAMELA mission measured electron intensities over the energy range of interest to heliospheric modulation. Drift models predict that for an $A < 0$ cycle, positively charged CRs drift toward Earth mostly along the wavy HCS, while negatively charged CRs drift mainly over the heliospheric polar regions, leading to charge-sign dependent modulation. During such polarity cycles, electrons evade the modulation impact that the HCS has on CRs.

In this chapter the model is applied to electron modulation, with the aim of reproducing seven semesterly averaged electron spectra from PAMELA. This is achieved by carefully adjusting the necessary modulation parameters in order to obtain accurate solutions that correspond to each successive measured spectrum at Earth. These results will provide valuable insight with regard to the underlying modulation processes responsible for the observed electron intensities. The combination of electrons with positively charged CRs, like protons or positrons, can be used to test drift theory and the effect of charge-sign dependent modulation.

5.2 The Local Interstellar Electron Spectrum

5.2.1 An Overview of Local Interstellar Spectra

As previously stated, a proper knowledge of the very LIS is essential for modelling the heliospheric modulation of GCRs, since it eliminates possible uncertainty in calculating the modulated spectrum at Earth. A stark difference between electrons and protons is that electrons radiate synchrotron radiation with frequencies from $\sim 0.5\,\mathrm{MHz}$ to $2.0\,\mathrm{GHz}$, which is observable in the energy range of $0.1\,\mathrm{GeV}$ to $6.0\,\mathrm{GeV}$ (e.g. *Peterson*,

1999). Electrons are therefore the only component for which the LIS can be derived directly from the shape of the galactic polar radio spectrum (e.g. *Langner*, 2004, and *Webber and Higbie*, 2008). Even though other physical processes in the ISM also produce γ-rays and radio wavelength photons with similar energies and wavelengths than that produced by CR electrons, the diffuse continuum γ-ray emission from the galactic plane at MeV energies is believed to originate primarily from bremsstrahlung interactions between CR electrons and the interstellar gas. The main γ-ray production mechanisms are known to be inverse Compton scattering, π^0 production and bremsstrahlung, where the contribution from each mechanism depends on various parameters such as interstellar electron and proton spectra, interstellar radiation and magnetic fields and gas distribution, among other (*Strong et al.*, 2000). The dominant physical process behind γ-ray production at energies above $\sim 1\,\mathrm{GeV}$ and below $\sim 30\,\mathrm{MeV}$ remains uncertain.

At energies $\leq\sim 1\,\mathrm{GeV}$, synchrotron, Compton and bremsstrahlung energy losses are relatively small, so that the galactic propagation of electrons are primarily determined by diffusion, in contrast to the nuclear components for which ionization energy loss is important at these lower energies. Apart from γ-rays and radio synchrotron photons, electron interactions in the ISM do not produce secondary particles that can be used to infer the characteristics of their propagation. Consequently, measurements of the γ-ray spectrum at low energies provide imperative constraints on electron propagation and the subsequent electron spectrum (see e.g. *Langner et al.*, 2001, and *Webber and Higbie*, 2008).

Figure 5.1 shows two versions of the electron very LIS calculated by *Bisschoff and Potgieter* (2014) using GALPROP, each of which was adjusted to reproduce a different version of Voyager 1 electron intensities (as published by *Stone et al.* 2013). The orange symbols suggest an $E^{-1.55}$ dependence for the very LIS below $\sim 200\,\mathrm{MeV}$ and represent measurements from Voyager 1 that were derived using instrument response functions based on pre-launch accelerator calibrations. Observations given by the green symbols were derived with response functions from GEANT 4 simulations and imply a notably weaker $E^{-1.35}$ dependence below $\sim 200\,\mathrm{MeV}$. At the lowest energy, the two sets of Voyager 1 observations have the same intensity, but progressively differ with increasing energy. The difference in intensity between the orange and green symbols is an indication of the systematic uncertainty in the observations, which leads to a significant difference in the LISs between 100 MeV and 1 GeV.

Bisschoff and Potgieter (2014) found that the electron LIS consists of two power laws – an $E^{-(1.45\pm0.15)}$ dependence below $\sim 100\,\mathrm{MeV}$ and an $E^{-(3.15\pm0.05)}$ dependence above $\sim 30\,\mathrm{GeV}$, with a gradual turn in the spectral shape between $2.0 \pm 0.5\,\mathrm{GeV}$ and $100\pm10\,\mathrm{MeV}$. In reproducing the two sets of Voyager 1 spectra, these authors found that an $E^{-1.35}$ spectrum was easily achievable and only required moderate changes to the power index of GALPROP's source spectrum. However, they found that reproducing

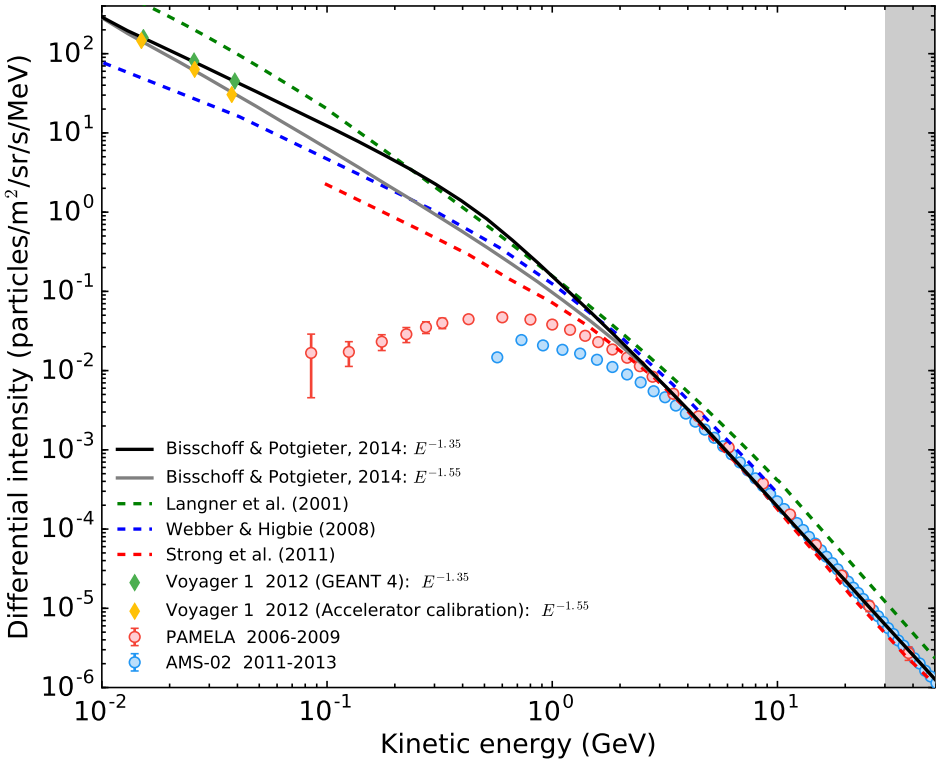

Figure 5.1: A comparison between two versions of the electron very LIS produced by *Bisschoff and Potgieter* (2014) using GALPROP (solid grey and black lines). These spectra correspond to two different power laws suggested by recent Voyager 1 measurements (*Stone et al.*, 2013) taken from beyond the HP (green and orange symbols). The reason for the difference in these measurements is explained in the text. PAMELA energy spectra from *Adriani et al.* (2015b), averaged over 2006 to 2009 (red symbols), and AMS-02 energy spectra from *Aguilar et al.* (2014a), averaged over 2011 to 2013 (blue symbols), are used to assist in normalizing the LISs above 30 GeV (grey shaded band). For comparison with other authors, the dashed green, blue and red lines represent versions of the LIS from *Langner et al.* (2001), *Webber and Higbie* (2008) and *Strong et al.* (2011) respectively.

the $E^{-1.55}$ power law spectrum was significantly more difficult and also less convincing, requiring not only adjustments in the power index of the electron source spectrum, but also varying the rigidity dependence of the DC. On this basis, as well as the fact that GEANT 4 simulations are considered accurate and reliable, the electron observations based on the GEANT 4 response functions are favoured in this study.

Figure 5.1 also shows earlier versions of the very LIS from other authors. The dashed green line shows an LIS from *Langner et al.* (2001), who based their spectrum on synchrotron data derived from polar synchrotron measurements. Above ~ 10 GeV this LIS version has a power law index comparable to the GALPROP versions of *Bisschoff and Potgieter* (2014). Below ~ 200 MeV it overestimates the Voyager 1 observations and above ~ 1 GeV it also overestimates PAMELA and AMS-02 observations. The dashed blue line gives the IS-7 spectrum from *Webber and Higbie* (2008), who used a Monte Carlo diffusion model to simulate the propagation of electrons in the Galaxy. These authors also took observations of the polar galactic nonthermal radio synchrotron spectrum

into consideration. Below $\sim 300\,\mathrm{MeV}$ this spectrum has a power law index similar to the $E^{-1.35}$ spectrum of *Bisschoff and Potgieter* (2014), but is lower in magnitude below $\sim 1\,\mathrm{GeV}$. The dashed red line represents a spectrum from *Strong et al.* (2011), who also used synchrotron radiation to constrain the electron LIS at low energies, in addition to direct electron measurements from various experiments like HEAT, BESS, *Fermi*-LAT and PAMELA, among other. However, this spectrum also significantly underestimates the spectra from *Bisschoff and Potgieter* (2014) below $\sim 2\,\mathrm{GeV}$.

Using a similar modulation model than the one from this study, *Potgieter and Nndanganeni* (2013b) investigated the modulation of electrons by reproducing Voyager 1 observations throughout the heliosphere along with the 2009 PAMELA spectrum at Earth. These authors investigated various scenarios for the LIS, including the $E^{-1.35}$ and the $E^{-1.55}$ spectra suggested by Voyager 1 data beyond the HP. They reported an LIS with an $E^{-(3.15\pm0.05)}$ dependence above $\sim 5\,\mathrm{GeV}$, a spectral break between $\sim 800\,\mathrm{MeV}$ and $\sim 2\,\mathrm{GeV}$, and an $E^{-(1.50\pm0.15)}$ dependence below the break. See also *Potgieter and Nndanganeni* (2013a) and *Nndanganeni* (2016) for extensive studies on the electron very LIS, as well as on reproducing Voyager measurements throughout the heliosphere. An approach similar to the one followed here was later reported by *Potgieter* (2014b) and *Potgieter et al.* (2014b). Preliminary reports were also published by *Vos et al.* (2013a, 2013b).

5.2.2 A New and Revised Very Local Interstellar Electron Spectrum

The electron very LIS used in this study is obtained using Voyager 1 measurements below 40 MeV, taken from beyond the HP (*Stone et al.*, 2013; *Gurnett et al.*, 2013), and PAMELA and AMS-02 measurements above 30 GeV, taken at Earth (*Aguilar et al.*, 2014a; *Adriani et al.*, 2015b). For energies between 40 MeV and 30 GeV, the $E^{-1.35}$ GALPROP spectrum from *Bisschoff and Potgieter* (2014) was used to infer the shape of the very LIS.

Electron modulation is considered to become negligent above 30 GeV (shown by the grey band), so that PAMELA and AMS-02 observations at these energies can be used to normalize the very LIS. The spectral index for the very LIS was inferred from the PAMELA and AMS-02 measurements in the normalization region. However, *Vos et al.* (2013b) pointed out that, from a modulation point of view, the double power law shape for the very LIS from GALPROP becomes problematic around 10 GeV. If a constant spectral index is assumed for the LIS above the break, as prescribed by PAMELA and AMS-02 measurements above $\sim 30\,\mathrm{GeV}$, the LIS intensity falls below the observed electron flux at Earth between $\sim 5\,\mathrm{GeV}$ and $\sim 15\,\mathrm{GeV}$, which is clear from Figure 5.1. Since modulation is expected to be significant at these energies, the modulated PAMELA

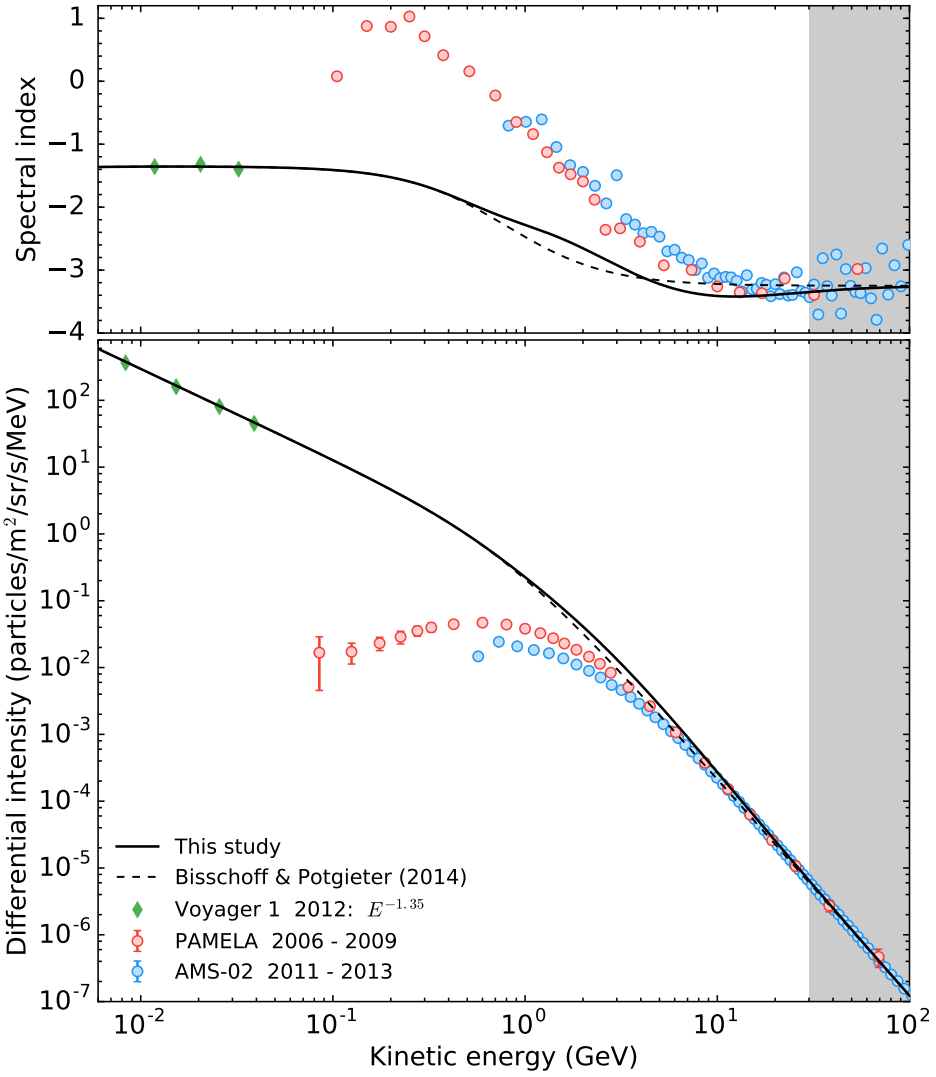

Figure 5.2: The original (dashed) and adjusted (solid) LISs for electrons are shown here. These are based on the $E^{-1.35}$ GALPROP spectrum from Figure 5.1. Also shown are PAMELA and AMS-02 measurements at Earth (filled circles), and Voyager 1 measurements (diamonds) from beyond the HP (derived using GEANT 4 response functions). The top and bottom panels give the spectral index and corresponding energy spectrum respectively.

and AMS-02 measurements at Earth are in fact expected to be below the LIS. This interesting spectral change cannot be ignored for modulation studies. As a result, the assumption of a constant power law dependence for the very LIS above ~ 1 GeV fails.

Shown in the bottom panel of Figure 5.2 (solid black line) is a modified version of the $E^{-1.35}$ GALPROP solution from *Bisschoff and Potgieter* (2014), where the spectrum between 1 GeV and 30 GeV has been adjusted by increasing the intensities over these energies, using PAMELA measurements as the benchmark for modulated spectra at Earth. Since no process in the heliosphere is able to accelerate CRs up to such high energies, it is assumed that these increased intensities can most likely be ascribed to a process or source effect in the ISM. The dashed black line represents the GALPROP

very LIS with a constant power law energy dependence above 1 GeV.

Given in the top panel of Figure 5.2 are the corresponding spectral indices for the very LIS and measurements. Below 40 MeV, the spectral shape of the adjusted spectrum shows good agreement with the $E^{-1.35}$ dependence of the GEANT 4-based Voyager 1 measurements. According to *Adriani et al.* (2011c), who conducted a study of PAMELA electron measurements between 1 GeV and 625 GeV during July 2006 to January 2010, a spectral index of $\gamma = -3.18 \pm 0.05$ is required for electrons above 30 GeV. With some margin of error, the AMS-02 observations yield a similar spectral index in the normalization region.

The adjusted very LIS in Figure 5.2 conforms to all of the constraints imposed on it by measurements, and is used as an input spectrum at the HP for electron modulation modelling throughout this study. These aspects were reported by *Vos et al.* (2013a, 2013b), *Potgieter and Nndanganeni* (2013b) and *Potgieter* (2014b). In terms of differential intensity, with units of particles/m^2/s/sr/MeV, this spectrum is given mathematically as

$$j_{LIS,e^-} = \frac{0.21\,E^{-1.35}}{\beta^2}\left(\frac{E^{1.65}+0.6920}{1.6920}\right)^{-1.1515} + J_{\text{bump}} \tag{5.1}$$

where

$$J_{\text{bump}} = 1.73\,\exp\left(4.19 - 5.40\,\log E - 8.9\,E^{-0.64}\right), \tag{5.2}$$

with E the kinetic energy in GeV and β the ratio of particle speed to the speed of light.

As previously mentioned in Chapter 4, *Scherer et al.* (2011), *Strauss and Potgieter* (2014a) and *Luo et al.* (2015) argued that the modulation of GCRs might start well beyond the HP, in a region between the HP and the BS that is suspected to be slightly more turbulent than the ISM. Since this effect is relatively small, with a $\sim 25\%$ decrease at 100 MeV for protons, this controversial issue is not yet settled and is therefore not considered in this thesis.

5.3 The PAMELA Electron Spectra

In addition to protons, PAMELA also measured high-precision electron spectra during the recent unusual solar minimum over the energy range that is of importance to heliospheric modulation. These energy spectra, which were reported by *Adriani et al.* (2015b) as averages over $\sim$ 6-monthly time periods (i.e. semesters), are shown in the top panel of Figure 5.3. The averaging period for each spectrum is indicated by the legend. From here on forward these spectra are referred to as the 2006b, 2007a, 2007b, 2008a, 2008b, 2009a and 2009b PAMELA electron spectra, where the "a" and "b" suffixes represent the first and second semesters of that year respectively. Due to extreme

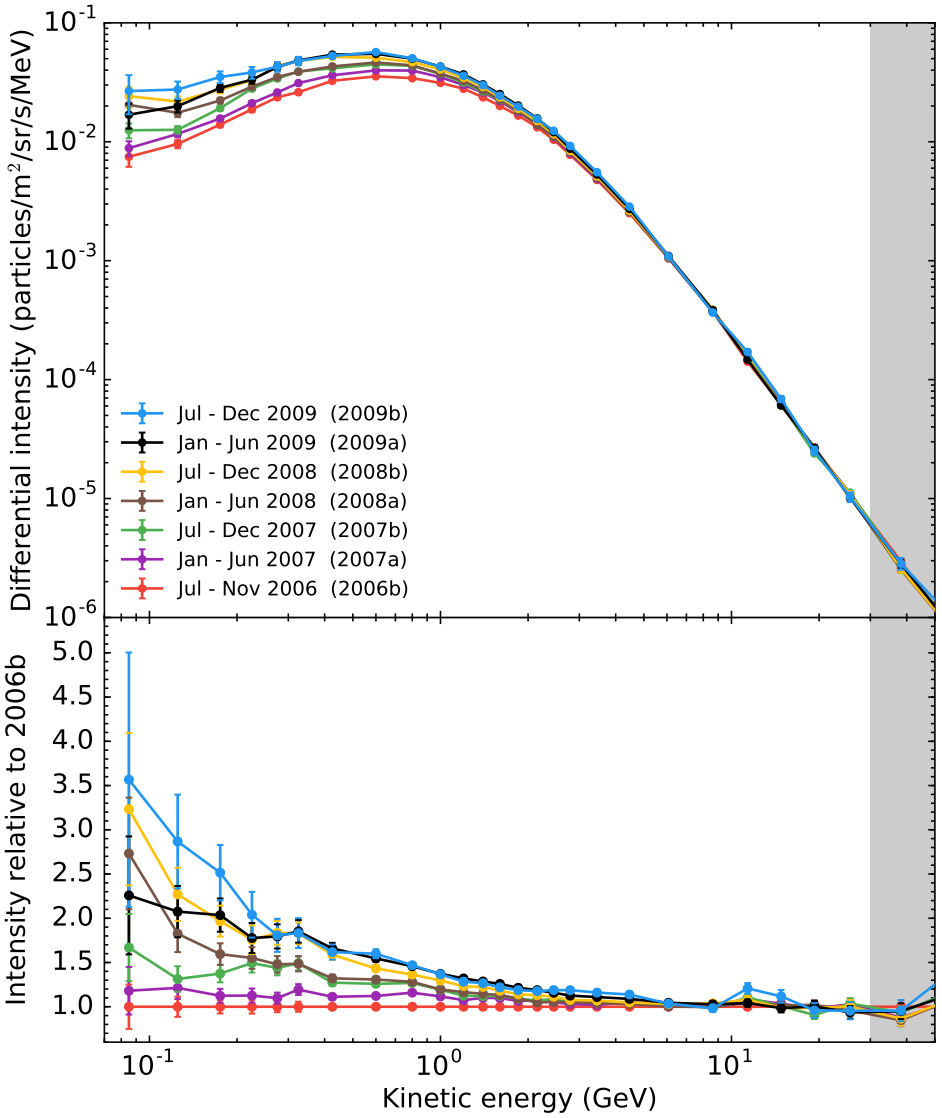

Figure 5.3: *Top panel:* Electron energy spectra measured by PAMELA in semesterly intervals, and averaged over ∼ 6-month periods, from July 2006 to December 2009. *Bottom panel:* Corresponding intensity ratios relative to the 2006b PAMELA spectrum. The grey band indicates the region where heliospheric modulation becomes negligible above 30 GeV.

solar activity that resulted in a Forbush-type decrease, the month of December 2006 was not included in deriving the 2006b spectrum (*Adriani et al.*, 2011c).

In a previous extensive study of electron modulation, *Vos* (2012) used PAMELA spectra that were available at Carrington Rotation intervals between July 2006 and December 2010 from *Di Felice* (2010). Even though these spectra were only available for energies from ∼ 300 MeV and higher, the high time resolution provided much needed insight into how the electron spectrum developed over time. The finalized electron spectra published by *Adriani et al.* (2015b), given in the top panel of Figure 5.3, were extended down to 80 MeV, which is essential for studying the so-called upturn region of the electron spectrum. Signs of this characteristic feature can be seen at the lowest

energies, where the electron spectrum starts to flatten off. From January 2010 onward, solar activity started to increase which resulted in a decrease in intensities, so that observations after December 2009 are excluded in this study.

The bottom panel of Figure 5.3 shows the consecutive energy spectra relative to the 2006b spectrum, quantifying the amount by which the electron spectrum increased on average in semesterly intervals. Over a timespan of 3.5 years, starting at 2006b, intensities around 1 GeV increased by a factor of ~ 1.5, while 80 MeV intensities increased by a factor of ~ 3.5. Similar to what was seen for protons, higher energies show very little change in intensity over time, apart from minor fluctuations smaller than 20%.

5.4 Modelling the PAMELA Electron Spectra

5.4.1 Setting the Intrinsic Modulation Parameters

The primary aim of this chapter is to reproduce the seven semesterly averaged PAMELA electron spectra shown in Figure 5.3. This was done by solving the TPE for a heliosphere that best represents the modulation conditions prior to each of the measured semesterly averaged spectra. Section 4.5.2 explained in detail how values for the HCS tilt angle (α) and the HMF at Earth (B_e) were derived for modelling, in order to obtain modulation conditions that are representative of each measured spectrum. This approach was followed for reproducing proton spectra averaged over Carrington Rotations in Chapter 4 and will also be applied for semesterly averaged electron spectra.

5.4.2 The Numerically Reproduced PAMELA Spectra

Figure 5.4 shows the measured 2006b spectrum (red symbols), overlaid by the computed model spectra at 1 AU, 10 AU, 50 AU and 100 AU (solid, dashed, dashed-dotted and dotted red lines, respectively) in the equatorial plane for an $A < 0$ polarity cycle. By using averaged values for α and B_e as described above and by adjusting the DCs, the 2006b spectrum was accurately reproduced. The very LIS from Figure 5.2 is given by the grey line. The 2006b spectrum will serve as a reference spectrum for illustrating how electron intensities developed over the course of the solar minimum of cycle 23/24.

Figure 5.5 is similar to Figure 5.4, but gives the reproduced spectra from 2007a to 2009b. The 2006b PAMELA spectrum is given by the grey symbols for comparison. It is clear that the model is capable of reproducing the observed electron spectra from each semester, with only minor deviation around $\sim$ 100MeV in 2009a. Important features exhibited by the measured spectra and reproduced by the model, are as follow: From 2006b to 2009b, the local maximum at the peak of the spectrum shifted to lower energies, from $\sim$ 700 MeV in 2006b, to $\sim$ 500 MeV in 2009b, due

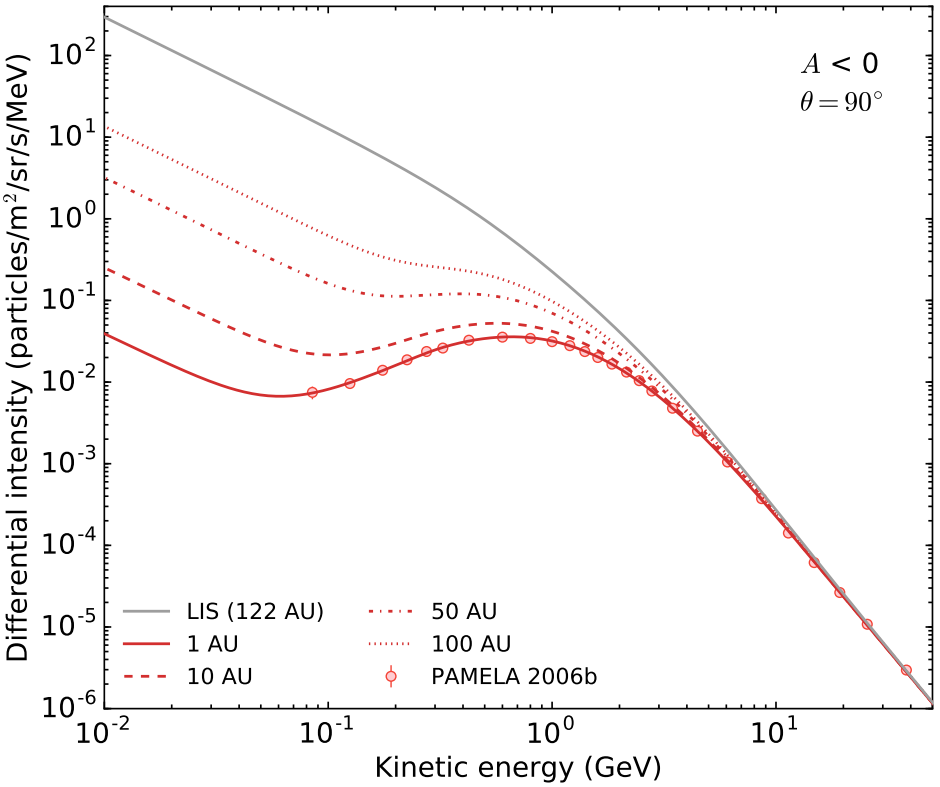

Figure 5.4: The 2006b electron energy spectrum measured by PAMELA (red symbols), overlaid by the computed energy spectrum at radial distances of 1 AU, 10 AU, 50 AU and 100 AU (as indicated by the legend) in the equatorial plane (i.e. $\theta = 90°$) for an $A < 0$ polarity cycle. The very LIS, specified at 122 AU, is given by the grey line.

to changes in the interplay between drifts and diffusion. In 2006b, the observed spectrum had a peak intensity of $\sim 3.8 \times 10^{-2}$ particles/m^2/s/sr/MeV, which increased to $\sim 6.0 \times 10^{-2}$ particles/m^2/s/sr/MeV. In the region where the spectrum turns upward, the position of the local minimum gradually shifts from ~ 60 MeV up to ~ 100 MeV as the spectrum flattens toward 2009b. This occurs because drift processes start to fade out and modulation becomes dominated by diffusion. Below ~ 50 MeV the modulated spectra computed at Earth take on the same spectral shape as the very LIS, since electrons don't undergo adiabatic deceleration caused by the SW. This happens for all radial distances at the lower end of the energy spectrum.

Through modelling it becomes possible to extend the electron spectrum to energies below the observable range of PAMELA. Since computed intensities above 80 MeV are based on PAMELA measurements and those below 80 MeV are subject to constraints imposed on it by the LIS with regard to the spectral shape, the computed spectra over the entire energy range are considered to be very reliable.

Figure 5.6 quantifies how the electron spectrum unfolded between 2006b and 2009b, by showing intensity ratios of the measured (symbols) and computed spectra (solid lines) relative to 2006b. Statistical and systematic errors for PAMELA measurements

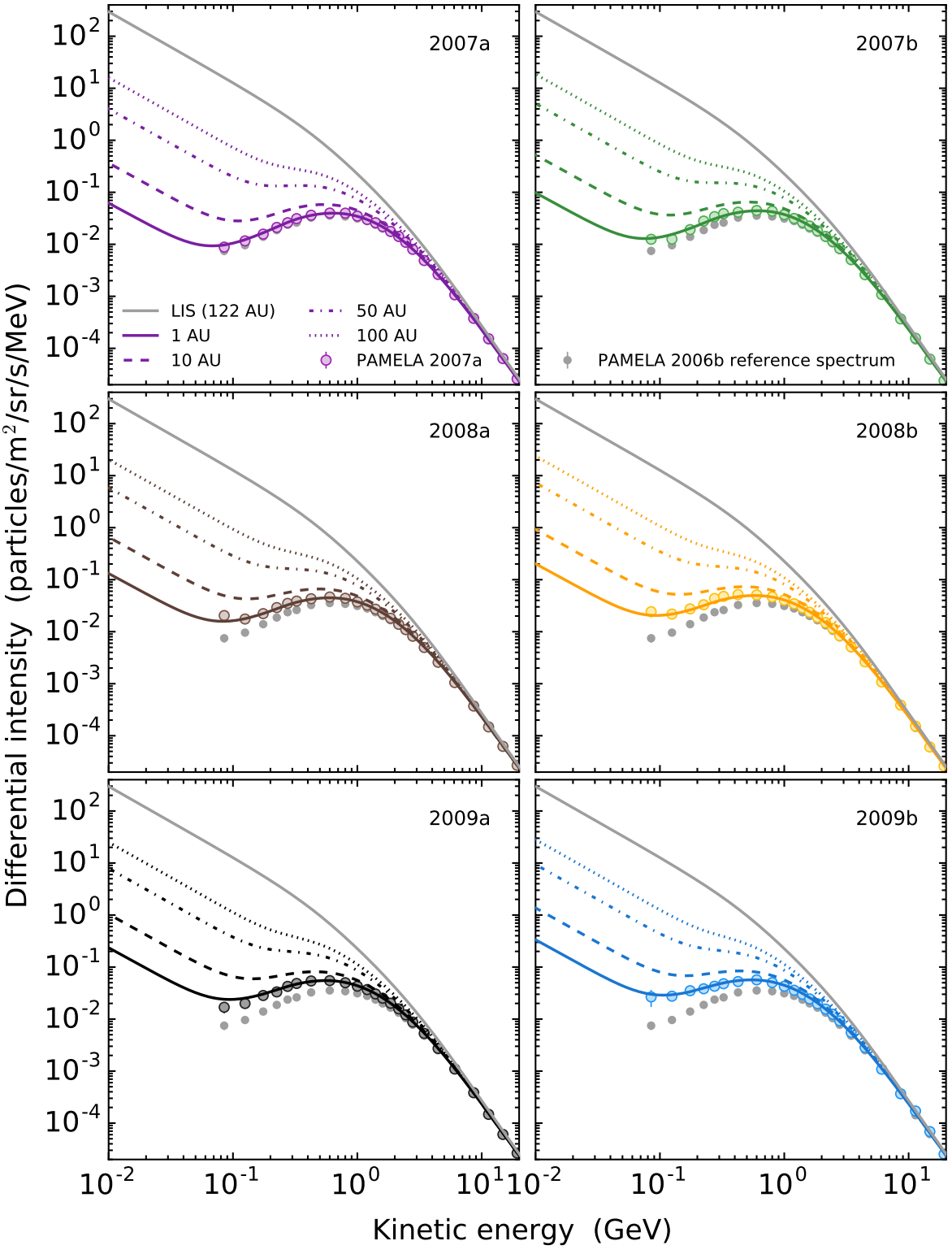

Figure 5.5: Similar to Figure 5.4, but for the measured and computed spectra of 2007a, 2007b, 2008a, 2008b, 2009a and 2009b. The 2006b PAMELA spectrum, shown by the grey symbols in each panel, is given as a reference.

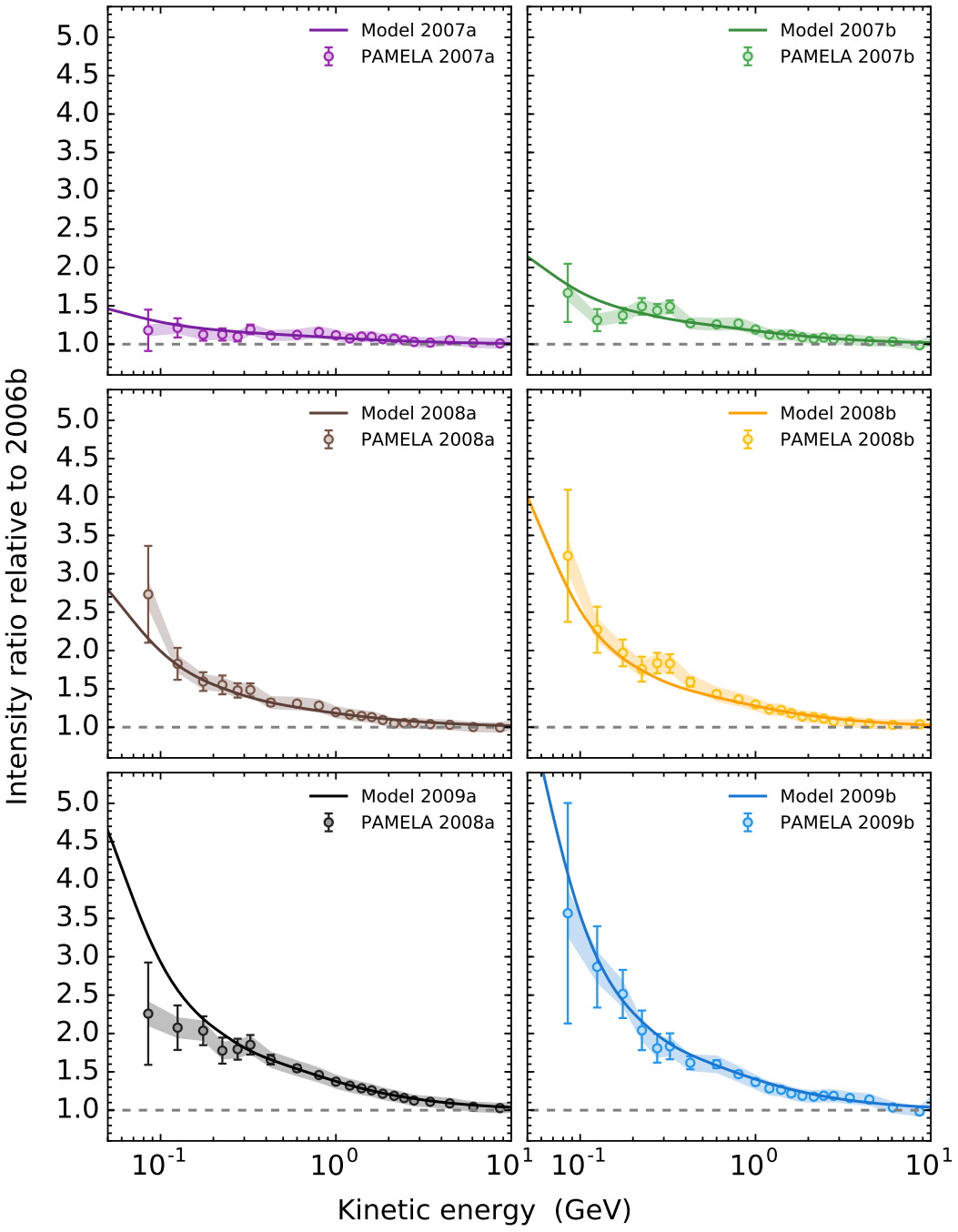

Figure 5.6: Electron intensity ratios of spectra between 2007a to 2009b, relative to the 2006b reference spectrum. PAMELA observations are given by the symbols, along with statistical errors (error-bars) and systematic errors (shaded bands). Computed spectra are given by the solid lines.

are shown by the error-bars and shaded bands respectively. Care was taken to reproduce the measured 2006b spectrum, since it serves as a reference for semesters 2007a through 2009b. The same procedure was followed for each semesterly averaged spectrum.

From Figure 5.6, the general trend of how the electron spectrum increased, was reproduced with the model by updating α and B_e and by adjusting the DC's, as was done for protons. The largest relative increase occurred at the lowest energies around

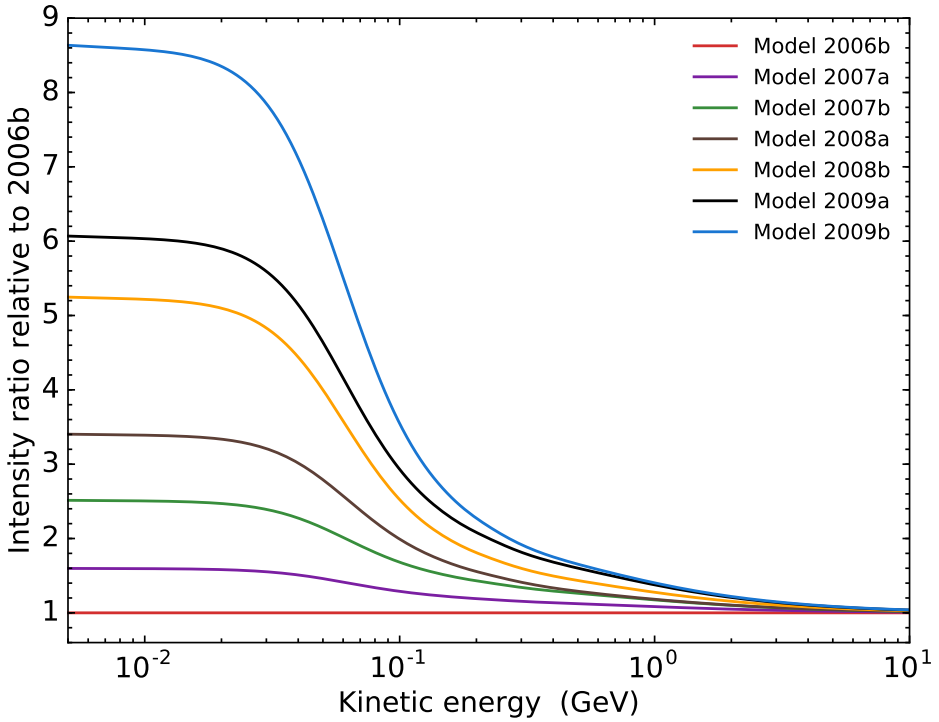

Figure 5.7: Similar to Figure 5.6, but for the computed spectra only and over an energy range of between 5 MeV and 10 GeV.

100 MeV, while smaller increases occurred at higher energies as the effects of modulation fade out. Electron intensities around 1 GeV increased by a factor of ~ 1.4 from 2006b to 2009b, while intensities at 80 MeV increased by a factor of ~ 3.6, which is less than what was found for protons over the same time period (*Potgieter et al.*, 2014a). Even though deviations between the computed and measured intensities are present below $\sim$ 200 MeV, most of the modeled spectra are within the measured error margins. In general, the overall trends observed by PAMELA are well reproduced with this modelling approach.

Since electron fluxes at the lowest energies could not be determined with the same accuracy as those at higher energies, statistical and systematic errors increase toward the lower end of the energy spectrum. Furthermore, as a result of the decrease in efficiency of PAMELA's tracking system, the above errors also increase over time.

Figure 5.7 is similar to Figure 5.6, but shows only the computed spectra over a wider energy range. By using the model to infer what intensities should be at energies below 80 MeV, where PAMELA measurements are not available, the relative increase between 2006b and 2009b can be calculated. It follows from Figure 5.7 that differential intensities at 10 MeV are expected to have increased by a factor of ~ 8.6.

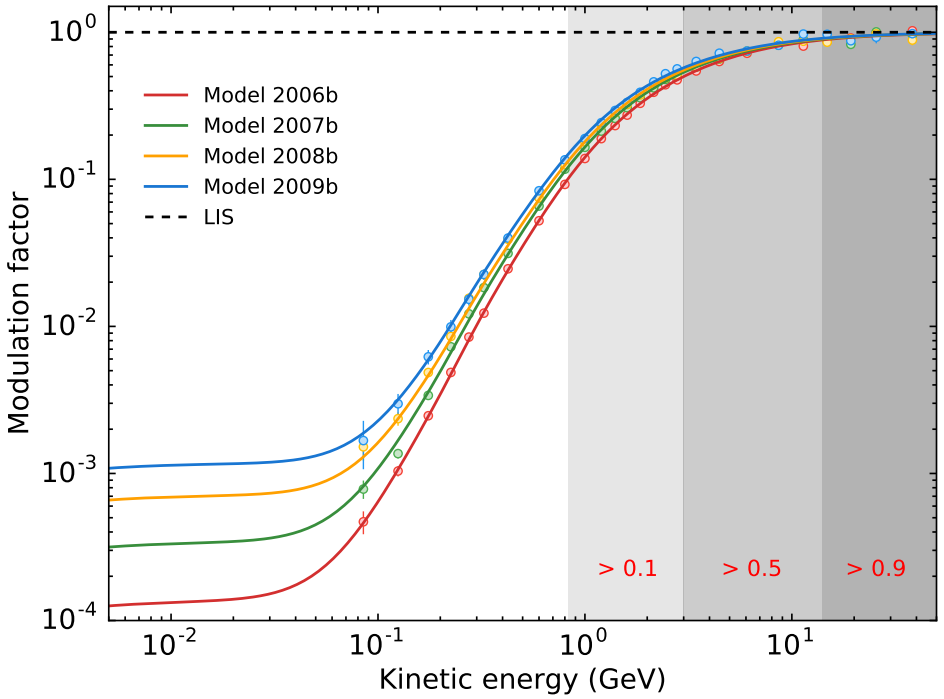

Figure 5.8: The MF for electrons, calculated by taking the ratio of the very LIS to the modulated spectrum at Earth. The solid lines and symbols represent model solutions and PAMELA observations, respectively, for the "b" semesters.

5.4.3 Total Modulation

For a long time the concept of total modulation has been an issue for heliospheric modulation studies. Up to now, the total modulation between Earth and the HP couldn't be determined with accuracy over all relevant energies. However, since Voyager 1 was able to determine the position of the HP as well as the very LIS at low energies, this question can now be answered with more confidence.

The MF is calculated as the ratio of the LIS at the HP over the modulated spectrum at Earth, as shown in Figure 5.8 for the "b" semesters. The MF is clearly very small at high energies, but rather significant at low energies. Below $\sim 50\,\mathrm{MeV}$, the MF for electrons will remain constant, as long as the DCs are kept constant (or independent of rigidity) at these low energies (see also *Potgieter*, 1996; *Nndanganeni*, 2016). The MF for protons will be different, since protons experience much larger adiabatic energy losses in the inner heliosphere, so that the shapes of modulated proton spectra are determined by these instead of the rigidity dependence of the DCs. Table 5.1 gives the MF values for the "b" semesters at various energies. These MF values can be useful to serve as a gauge for the reported Force-Field parameter used by many experimental groups (see e.g. *Usoskin et al.*, 2015).

In the following chapters, this increase in electron intensities is compared to similar semesterly increases in protons and positrons. From drift theory it is expected that electrons should experience a smaller relative increase than protons and positrons –

a phenomenon indicative of charge-sign dependent modulation. Furthermore, when considering simultaneous electron and positron measurements, the inclusion of the latter will provide an added constrain to the DCs for when either of these observations are reproduced.

5.5 Rigidity Dependence of the Diffusion Coefficients

In order to reproduce the seven semesterly averaged PAMELA electron spectra, changes in α and B_e, as well as the diffusion and drift coefficients, were taken into account. Over the $\sim$ 3.5-year time period between 2006b and 2009b, α changed from 16.8° to 9.5°, accompanied by a change in B_e from 4.95 nT to 3.91 nT. Both of these time-dependent modulation parameters are considered as very good proxies for solar activity and section 5.4.1 discussed how average representative values for these parameters are calculated.

The approach followed for adjusting the DCs is similar to that used to reproduce the proton spectra in Chapter 4. Based on our assumptions for diffusion and drifts, as discussed in Chapter 3, changes in B_e directly affect these modulation processes, since the expressions for these coefficients depend on the HMF. In addition to the changes caused by changing B_e, the DCs were further adjusted, in particular with regard to the absolute value, to obtain good agreement with observations.

Over the years, many predictions have been made about the DC rigidity dependence at Earth using turbulence theory. For electrons it was found that diffusion becomes energy independent below $\sim$ 500 MeV, with a possible increase below $\sim$ 20 MeV, depending on the assumptions made for turbulence; see e.g. *Bieber et al.* (1994), *Potgieter* (1996, 2000), *Burger et al.* (2000), and *Teufel and Schlickeiser* (2002).

Figure 5.9 shows the MFP rigidity dependence for the "b" semesters of the resulting DCs. Solid and dashed lines represent the parallel ($\lambda_\parallel$) and perpendicular ($\lambda_\perp$) MFPs, while the dotted lines represent the drift scale (λ_A). Below $\sim$ 200 MV, the diffusion of electrons is considered to be independent of rigidity, where $\lambda_\perp$ in the radial and polar directions are scaled by 2% of $\lambda_\parallel$. Above $\sim$ 500 MV, $\lambda_\parallel \propto P^{1.55}$ while $\lambda_\perp \propto P^{1.24}$, so that the ratio of parallel diffusion to perpendicular diffusion doesn't remain constant. For drifts, the weak-scattering approach was required to be modified below 1.0 GV, as

Table 5.1: The MF for each computed "b"-semester spectrum from Figure 5.8 at different energies between 1 MeV and 50 GeV.

Kinetic energy (GeV)	0.01	0.1	1.0	10.0	50.0
MF for 2006b	0.00013	0.00062	0.143	0.831	0.977
MF for 2007b	0.00033	0.0011	0.168	0.847	0.979
MF for 2008b	0.00069	0.0016	0.182	0.855	0.981
MF for 2009b	0.00113	0.0022	0.201	0.864	0.982

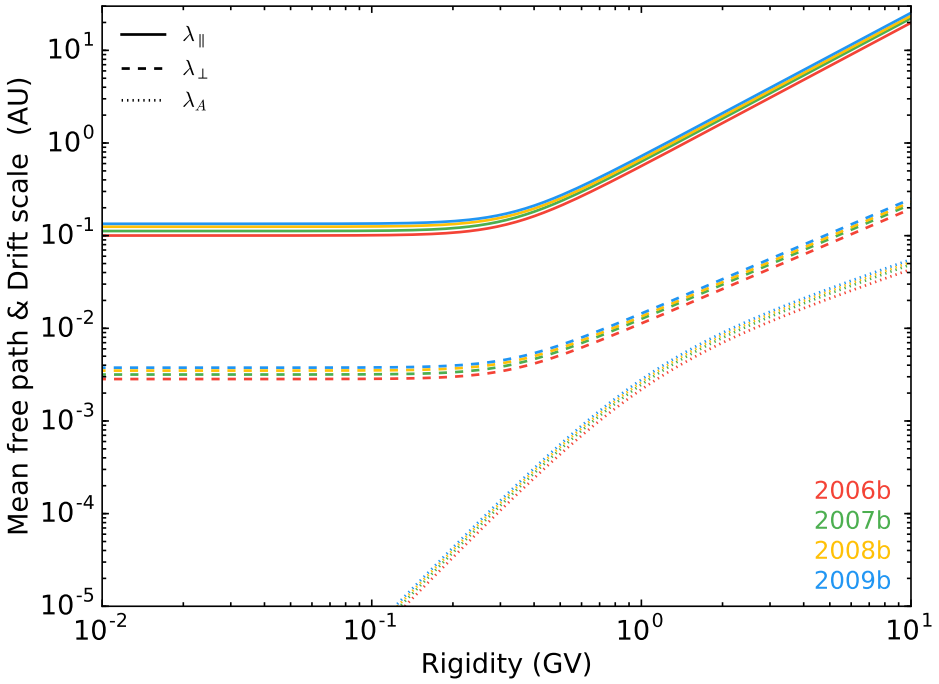

Figure 5.9: The rigidity dependence of the parallel ($\lambda_\parallel$) and perpendicular ($\lambda_\perp$) MFPs are shown here, along with the drift scale (λ_A). For this modelling approach, the MFPs in the radial and polar directions, perpendicular to the average background HMF, are scaled in a similar fashion, i.e. $\lambda_\perp \equiv \lambda_{\perp r} \equiv \lambda_{\perp\theta}$).

Table 5.2: A summary of the modulation parameters obtained after reproducing the 2006b to 2009b PAMELA electron spectra is given here. See Chapter 3 for discussions of these variables and the equations containing them.

Parameter	**2006e**	**2007m**	**2007e**	**2008m**	**2008e**	**2009m**	**2009e**
$\lambda_\parallel$ (AU) *	0.564	0.597	0.631	0.635	0.672	0.712	0.722
a	0.02	0.02	0.02	0.02	0.02	0.02	0.02
b	0.02	0.02	0.02	0.02	0.02	0.02	0.02
c_1	0.00	0.00	0.00	0.00	0.00	0.00	0.00
$c_{2\,\parallel}$	1.55	1.55	1.55	1.55	1.55	1.55	1.55
$c_{2\,\perp}$	1.55	1.55	1.55	1.55	1.55	1.55	1.55
c_3	3.50	3.50	3.50	3.30	3.50	3.50	3.50
P_k (GV)	0.33	0.33	0.33	0.34	0.34	0.33	0.34
$d_{\perp\theta}$	1.20	1.20	1.20	1.20	1.20	1.20	1.20
$\kappa_{A\,0}$	1.00	1.00	1.00	1.00	1.00	1.00	1.00
$P_{A\,0}$ (GV)	1.00	1.00	1.00	1.00	1.00	1.00	1.00

* For 1.0 GeV at Earth

shown by the dotted lines in Figure 5.9 (see also *Ngobeni and Potgieter*, 2015). The spatial dependencies of all the coefficients are of the form B^{-1}.

These predictions of the diffusion and drift coefficients are presented as the outcome of the comparison between our modulation model and PAMELA electron measurements.

Below $\sim$ 300 MeV the ratio between these coefficients remain unchanged. It was still required to include a small polar-dependent enhancement in the perpendicular diffusion in the polar direction, given that the HMF has also been modified in the polar regions with the Smith-Bieber modification. In a separate study *Potgieter and Nndanganeni* (2013a) used a similar modulation model and a similar approach to diffusion and drift to reproduce Voyager 1 observations in the outer heliosphere.

The modelling results presented in this chapter were published by *Vos et al.* (2013b) and *Potgieter et al.* (2015), along with a publication by *Adriani et al.* (2015b) containing the PAMELA measurements and experimental results. Table 5.2 gives a summary of the relevant modulation parameters obtained after reproducing the measured PAMELA spectra. Even though good agreement was found between the model and measurements, the robustness of the modulation parameters and the resulting spectra can be further refined by including simultaneous positron measurements. This is discussed in the following chapter.

5.6 Summary

During the 2006 to 2009 solar minimum period, PAMELA measured seven semesterly averaged electron spectra over energies where CRs experience significant heliospheric modulation. Even though electrons don't experience the same diffusion as protons, the addition of measurements of negatively charged particles is important for a study of drifts and charge-sign dependent modulation.

The primary goal of this chapter was to reproduce the seven semesterly averaged PAMELA electron spectra given in Figure 5.3, using the modulation model. In doing this, the first step was to obtain a reliable electron very LIS to be used as an input spectrum for modelling (as discussed in Section 5.2). The GALPROP modulation code was able to provide two possible LIS spectra that are based on Voyager 1 electron measurements from beyond the HP. By making use of response functions from pre-launch accelerator calibrations, the measurements derived from Voyager 1 suggest an $E^{-1.55}$ energy dependence. For response functions derived from GEANT 4 simulations, the measurements indicate a weaker dependence of $E^{-1.35}$. The latter dependence was chosen for this study.

Figure 5.2 shows how the GALPROP code was used in combination with Voyager 1 measurements below 40 MeV, and PAMELA and AMS-02 measurements above 30 GeV. The resulting LIS spectrum, which has a double power law shape, had to be adjusted by increasing the spectrum in the energy range between 1 GeV and 30 GeV in order to account for modulation predicted by the model at these energies. It has therefore became clear that the shape of the very LIS above $\sim$ 1GeV is most probably not a constant power law.

The seven reproduced semesterly spectra were presented in Figures 5.4 and 5.5. The approach followed for calculating average values for the time-varying modulation parameters α and B_e, corresponding to each semester, was similar to what was followed for reproducing the PAMELA proton spectra in Chapter 4. At the lowest observed energy of $\sim 80\,\text{MeV}$, PAMELA measured an increase in the differential electron intensity of a factor of ~ 3.5 between semesters 2006b and 2009b. At this energy, clear evidence of the expected upturn in the electron spectrum was observed. The electron spectrum was extended through modelling to energies below PAMELA's observable range, making it possible to study characteristic features of this spectrum at low energies.

In 2006b, PAMELA measured a peak electron intensity of $\sim 3.8\times10^{-2}$ particles/m^2/s/sr/MeV at 700 MeV, which increased to $\sim 6.0\times10^{-2}$ particles/m^2/s/sr/MeV in 2009b, accompanied by a shift in energy down to $\sim 500\,\text{MeV}$. From the computed spectra, the expected position of the local minimum in the upturn region could be determined, which occurred at $\sim 60\,\text{MeV}$ in 2006b and shifted toward $\sim 100\,\text{MeV}$ in 2009b. At energies below $\sim 50\,\text{MeV}$ it was seen that the modulated spectra at Earth (and at other radial distances) had the same shape as the very LIS. This is know to happen, since electrons don't experience large adiabatic deceleration from the outward blowing SW (see e.g. *Moraal and Potgieter*, 1982; *Strauss et al.*, 2011b).

It also followed that the assumptions made with regard to diffusion and drifts were able to correctly reproduce the observed spectra. Even though relatively small changes were made to the DCs, in addition to all the self-consistent changes that resulted from changing α and B_e, the combined effect of these changes have proved to be sufficient for the purpose of reproducing modulated electron measurements at Earth. Preliminary modelling results were published by *Vos et al.* (2013a, 2013b) and final results by *Potgieter et al.* (2015).

In the following chapter, the positron GCR component is introduced with the aim of combining electron and positron measurements, together with modelling, for a comprehensive study of drifts.

Chapter 6

Combined Heliospheric Modulation of Electrons and Positrons

6.1 Introduction

In the previous chapter, the heliospheric modulation of electrons was studied using PAMELA measurements taken during the solar minimum of cycle 23/24 and a modulation model capable of reproducing these measurements. The addition of the precisely measured negative electron component by PAMELA is extremely valuable for charge-sign dependent modulation studies. Even though electrons can be compared to protons of the same rigidity for such a study, the diffusion experienced by these CRs are different, due to the difference in their respective rest masses.

Fortunately, the primary scientific goal of the PAMELA mission is in fact to study the antiparticle CR component (antiprotons, positrons and antihelium), as well as the heliospheric modulation of CRs. PAMELA therefore also measured positron intensities down to energies of $\sim$ 80 MeV over the same time period that it measured protons and electrons. Since electrons and positrons only differ in the charge they carry, they undergo the same diffusion, but experience drift in opposite directions. From a modelling perspective, this provides a unique opportunity to further constrain the modulation parameters, while studying the charge-sign dependent modulation of these particles.

A new very LIS for positrons is presented in this chapter and used for modelling the modulation of positrons. The DCs from the previous chapter are re-evaluated in order to obtain a set of coefficients that can reproduce simultaneous electron and positron measurements at the Earth from PAMELA. The results of this study are presented and discussed here.

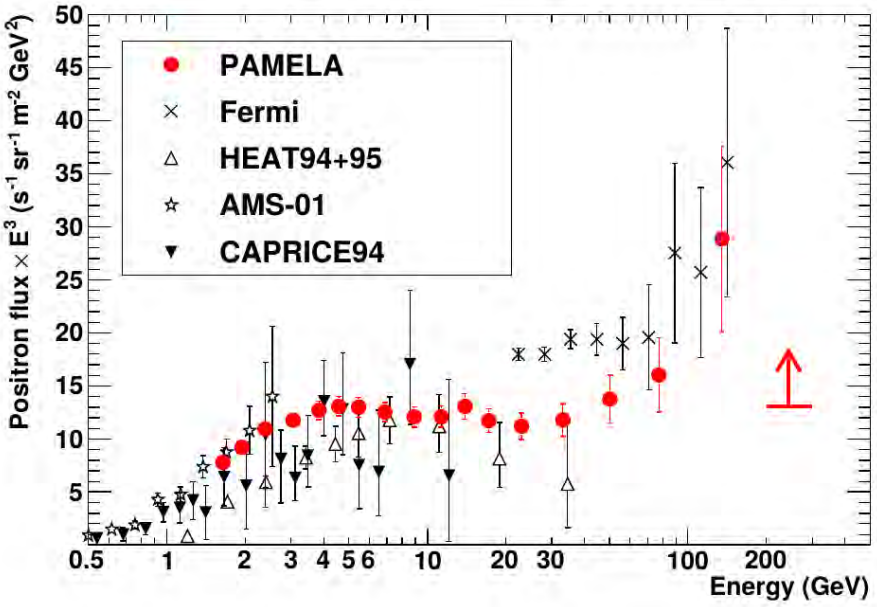

Figure 6.1: The PAMELA positron spectrum, averaged over July 2006 to December 2009, is shown by the red symbols, where the error-bars include statistical and systematic errors. Also shown are measurements from CAPRICE94 (*Boezio et al.*, 2000), AMS-01 (*Alcaraz et al.*, 2000a), HEAT94+95 (*DuVernois et al.*, 2001) and Fermi (*Ackermann et al.*, 2012). Above 200 GeV the lower limit of PAMELA is given as a 90% confidence level. Figure taken from *Adriani et al.* (2013b).

6.2 Positron Measurements From PAMELA

It is well known that proton and helium nuclei dominate the positive charge spectrum, along with a very small amount of heavier nuclei. Electrons, which account for a mere $\sim 1\,\%$ of the total CR count, dominate the negative charge spectrum, while CR antiparticles like positrons and antiprotons are even more rare. These particles make up a small fraction of secondary CRs, which are produced in collisions of primary CRs with the ISM. Even though positrons and antiprotons can therefore not be considered as direct indicators for the existence of antimatter domains, they serve as a probe for astrophysical scenarios (e.g. *Casolino et al.*, 2008, and *Boezio et al.*, 2009). Local astrophysical sources like nearby and young pulsars, for example, would appear as a distortion in the secondary electron and positron fluxes. Antiparticles could also come from other unusual sources, like the annihilation of heavy supersymmetric dark matter particles within the galactic halo, which could lead to positrons and antiprotons with distinct energy signatures (see e.g. *Menn et al.*, 2013).

The PAMELA detector is capable of measuring positrons and antiprotons with unprecidented statistics across a range of energies that hasn't been explored up to now. PAMELA's energy range of acceptance for positrons is 50 MeV to 270 GeV, while for antiprotons it is 80 MeV to 190 GeV. Obtaining accurate spectra for positrons, however, require careful analysis of the measurements due to the possibility of misidentifying

protons as positrons (see e.g. *Adriani et al.*, 2010).

Figure 6.1 compares the positron energy spectrum (multiplied by E^3), as measured by PAMELA between July 2006 and December 2009 (*Adriani et al.*, 2013b), with a selected few other space-borne and balloon-borne experiments (*Boezio et al.*, 2000; *Alcaraz et al.*, 2000a; *DuVernois et al.*, 2001; *Ackermann et al.*, 2012). This figure serves to illustrate how PAMELA improved the accuracy of positron measurements. Below $\sim 30\,\mathrm{GeV}$ the spectrum is significantly affected by heliospheric modulation, which will reflect in temporal changes when shown at a higher time resolution. Between 200 GeV and 300 GeV, a lower limit at the 90% level of confidence is shown for positron intensities. Many astrophysical models have attempted to explain the strong increase in positron intensities above 30 GeV. *Atoyan et al.* (1995), for example, suggested that the decay of synchrotron gamma rays can possibly contribute to the high-energy electron and positron CR components. *Finkbeiner et al.* (2011) calculated the intensity of secondary positrons and added the expected primary contribution from the annihilation of dark matter particles as an attempt to explain the positron excess at higher energies. *Büsching et al.* (2008) investigated two nearby pulsars, namely Geminga and B0656+14, and found that leptonic particles accelerated by these pulsars and released into the ISM upon breakup of the pulsar wind nebulae, contribute non-negligible amounts to the local CR positron spectrum above several GeV. See also e.g. *Venter et al.* (2015) for a recent study on the contribution of positrons from millisecond pulsars.

Since the focus of this study is on the lower energy range of the spectrum, the observed positron excess, which starts at $\sim 10\,\mathrm{GeV}$, only influences certain energies that are important to heliospheric modulation. Furthermore, the effects of charge-sign dependent modulation are investigated using semesterly averaged PAMELA electron measurements from *Adriani et al.* (2013a) and preliminary PAMELA positron measurements at the same intervals (~ 6 months), obtained via *private communication* (R. Munini, 2015). This is the first time that such accurate simultaneous electron and positron measurements have become available and evidently also coincides with the very quiet solar minimum of cycle 23/24.

The PAMELA positron energy spectra are shown in Figure 6.2 (top panel), along with the intensity ratios for consecutive spectra relative to semester 2006b (bottom panel). The semesterly time periods are indicated in the legend and the corresponding spectra will be referred to as the 2006b, 2007a, 2007b, 2008a, 2008b, 2009a and 2009b spectra, similar to the convention used for electrons in Chapter 5. Measurements below $\sim 200\,\mathrm{MeV}$ are still under review and are therefore not accounted for as strictly as measurements at higher energies when attempting to reproduce the spectra (these are shown by the slightly opaque lines and symbols).

The shape of the positron spectrum for this energy range looks similar to that of electrons, with a local maximum peak below 1 GeV and an upturn in the spectrum

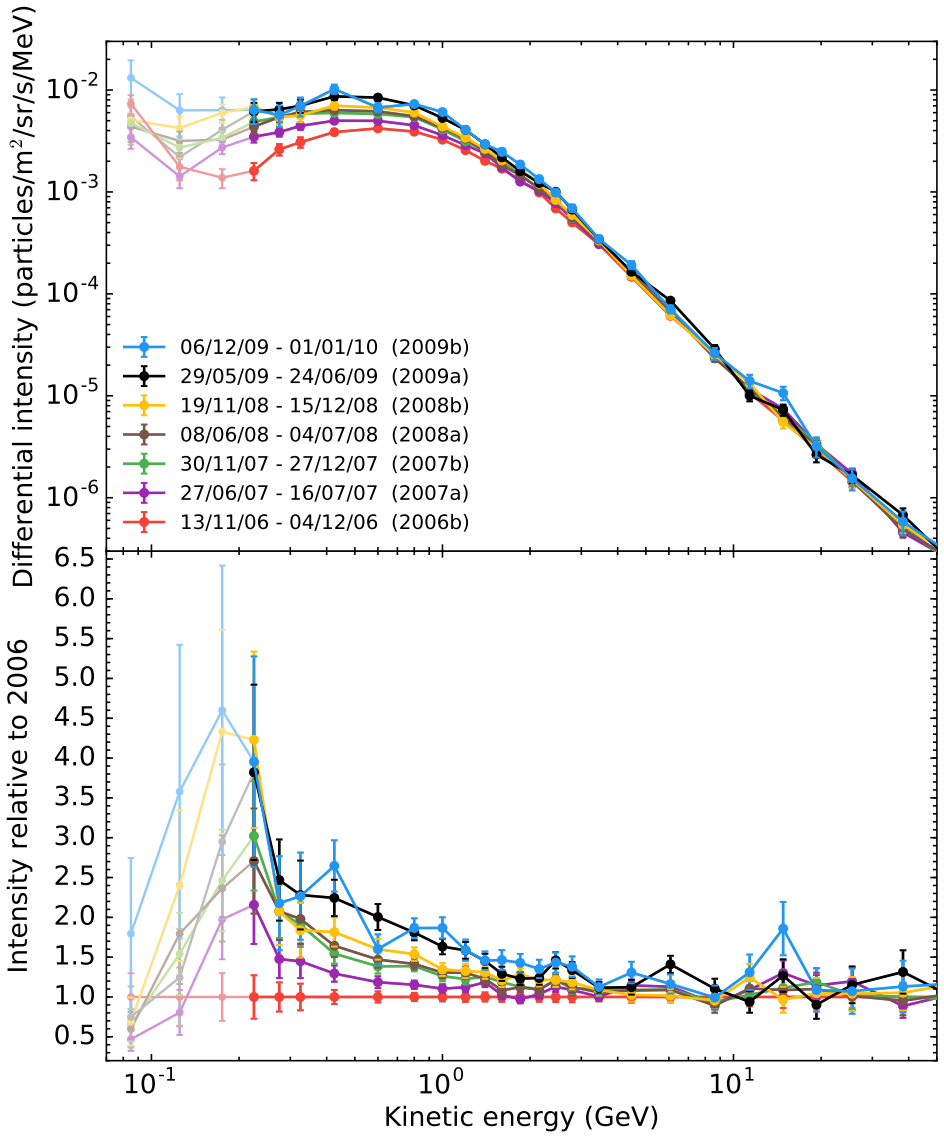

Figure 6.2: *Top panel:* Preliminary positron energy spectra measured by PAMELA between July 2006 and December 2009 and averaged over ∼ 6-month semesterly intervals (obtained via *private communication* from R. Munini, 2015). *Bottom panel:* Corresponding intensity ratios for consecutive spectra from the top panel, relative to the 2006b spectrum.

at lower energies. It follows from the preliminary measurements that the upturn for positrons occurs between 100 MeV and 200 MeV, whereas for electrons it occurs well below 100 MeV. This will be further investigated with the modulation model. In 2006b, the positron spectrum had a local peak intensity of 4.0×10^{-3} particles/m^2/s/sr/MeV at ∼ 600 MeV, which shifted down to ∼ 420 MeV in 2009b with an increase in intensity up to 1.0×10^{-2} particles/m^2/s/sr/MeV. From the bottom panel of Figure 6.2, positron intensities at ∼ 220 MeV increased by a factor of ∼ 4 over a period of 3.5 years from 2006b to 2009b. At higher energies, the relative increase in intensity decreases as modulation diminishes toward 50 GeV.

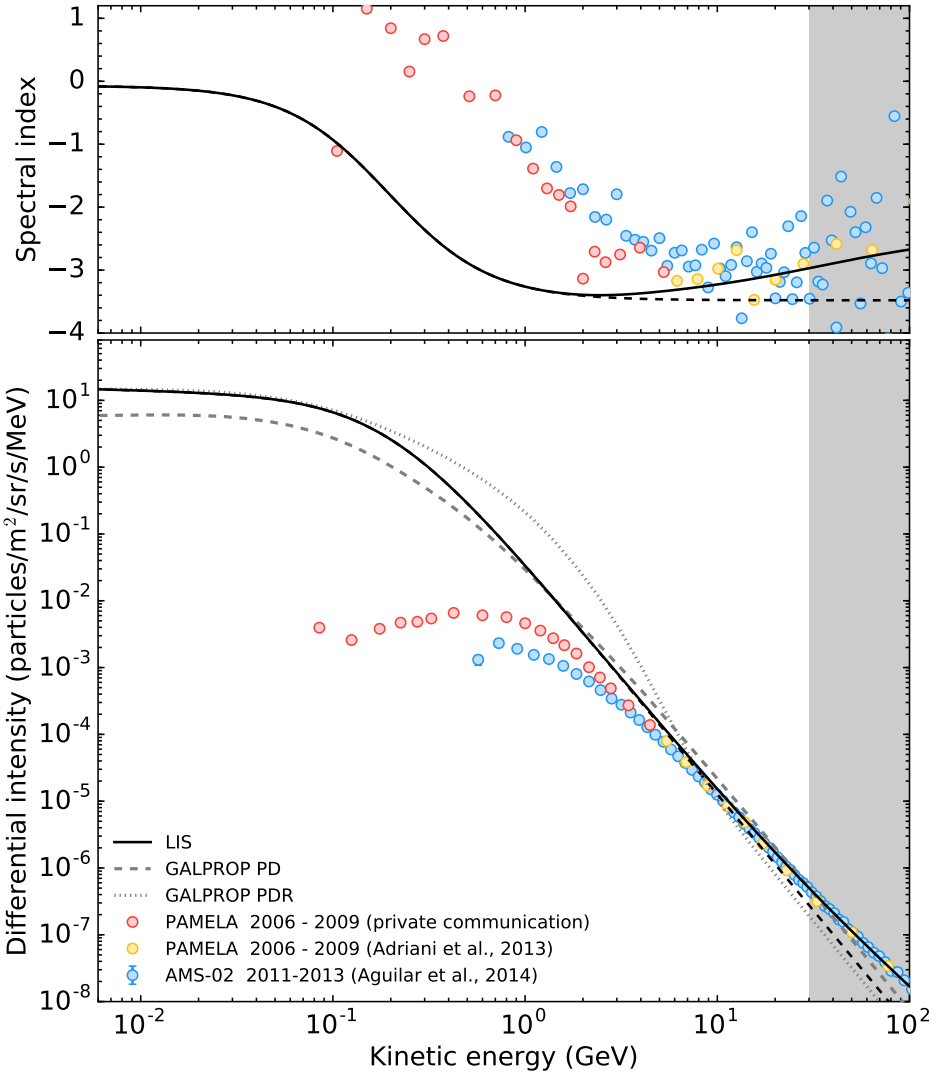

Figure 6.3: The newly constructed positron very LIS used in this study (solid black line), along with preliminary positron measurements from PAMELA below 5 GeV (red symbols), PAMELA positron measurements published by *Adriani et al.* (2013b) above 5 GeV (orange symbols) and AMS-02 measurements (blue symbols) published by *Aguilar et al.* (2014a). The top panel gives the spectral index for the various measurements as well as the constructed positron LIS, while the bottom panel shows the energy spectra. In both panels the dashed black line serves as an $E^{-3.5}$ reference line. The dashed and dotted grey lines in the bottom panel represent the plain diffusion and plain diffusion with reacceleration propagation regimes used with GALPROP, respectively (described further in the text).

6.3 The Local Interstellar Positron Spectrum

To obtain an estimate of the very LIS for positrons, the PAMELA measurements published by *Adriani et al.* (2013b) are used to normalize the LIS between 30 GeV and 50 GeV. These are also in agreement with AMS-02 measurements from *Aguilar et al.* (2014a). The bottom panel of Figure 6.3 shows the PAMELA positron energy spectrum from *Adriani et al.* (2013b) for energies above 5 GeV (orange symbols). This spectrum is extended to lower energies with an average spectrum calculated from the seven

semesterly spectra given in Figure 6.2 (red symbols). The blue symbols represent an average AMS-02 spectrum for measurements taken between May 2011 and November 2013. Both PAMELA and AMS-02 are in good agreement in the normalization region where modulation is negligible (shaded band).

Since Voyager 1 electron measurements include intensities of both electrons and positrons, no *in situ* low-energy measurements of positrons are available from beyond the HP. We consequently have to rely on GALPROP spectra to obtain an approximation of the LIS for positrons below $\sim 10\,\mathrm{GeV}$. The GALPROP code for galactic propagation was initially developed by *Strong and Moskalenko* (1998) and further extended by *Strong et al.* (2000), who included a new evaluation of the interstellar radiation field and presented six different models to illustrate the effects of different assumptions on the resulting galactic spectra.

As an attempt to account for uncertainties related to CR propagation, we consider two galactic propagation regimes for GALPROP, namely plain diffusion (PD) and plain diffusion with reacceleration (PDR). The resulting spectra served as constraints for the range of possible intensities of the positron very LIS. The PD spectrum is given by the dashed grey line in Figure 6.3, while the PDR spectrum is given by the dotted grey line.

The solid black line in the bottom panel of Figure 6.3 represents the positron very LIS constructed as described above by using GALPROP PD and PDR solutions below $\sim 10\,\mathrm{GeV}$ as lower and upper limits and PAMELA and AMS-02 measurements above 30 GeV for normalization. Shown in the top panel are the corresponding spectral indices for the newly constructed positron LIS and the measurements. The dashed black line serves as a reference for a constant power law of $E^{-3.5}$. Both PAMELA and AMS-02 measurements show a decrease in the spectral index up to $\sim 10\,\mathrm{GeV}$, after which it starts to increase toward higher energies. This illustrates that the positron excess contributes to measured intensities from energies of $\sim 10\,\mathrm{GeV}$ and higher.

Above $\sim 10\,\mathrm{GeV}$, the PDR spectrum from GALPROP is much steeper than what PAMELA and AMS-02 measurements require and is therefore unable to reproduce neither the spectral index, nor the absolute value of these measurements. This is also the case for the GALPROP PD spectrum above $\sim 30\,\mathrm{GeV}$. The reason for this difference is that the GALPROP model is not yet able to account for the observed positron excess above $\sim 10\,\mathrm{GeV}$. Therefore, only PAMELA and AMS-02 measurements can be relied on for normalization. The newly constructed positron very LIS was adjusted to reproduce these measurements accordingly. Below $\sim 5\,\mathrm{GeV}$, the PD spectrum increases significantly above the PDR spectrum. However, down to $\sim 1\,\mathrm{GeV}$, the model produce modulated spectra that better corresponds to measurements at Earth when using a lower LIS, similar to the PD spectrum. Conversely, below $\sim 200\,\mathrm{MeV}$, low-energy measurements at Earth favour a higher LIS like the PDR spectrum. The resulting very LIS for positrons therefore adhere to the chosen constraints, while also leading to

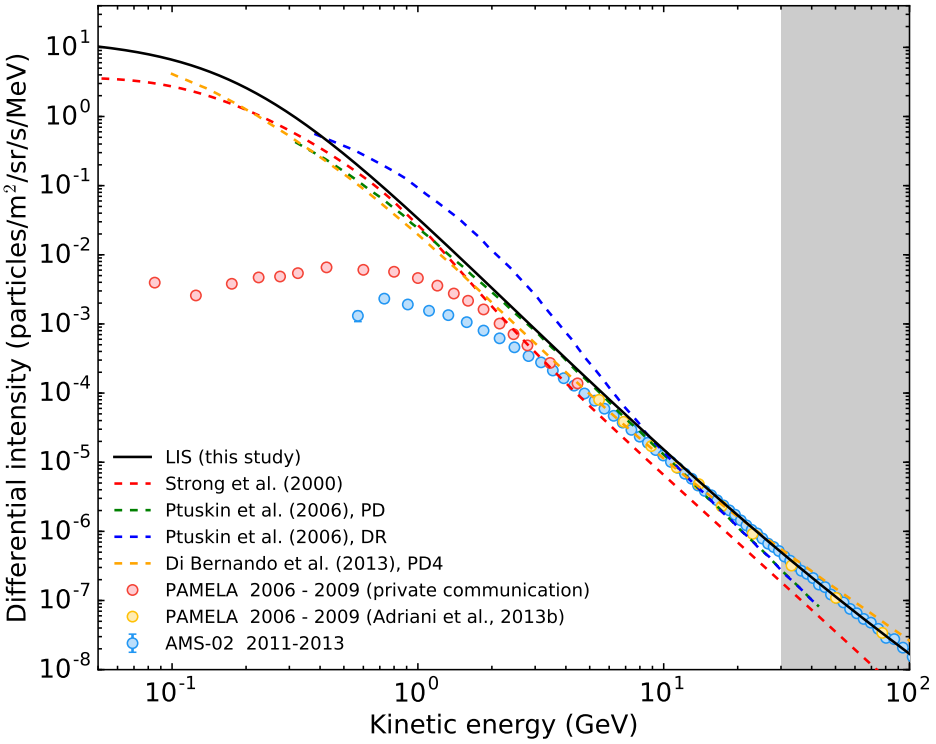

Figure 6.4: The positron very LIS used in this study (solid black line) is compared to versions of the LIS suggested by other authors. The LIS from *Strong et al.* (2000) is given by the dashed red line, while two versions from *Ptuskin et al.* (2006), namely plain diffusion (PD) and diffusion with reacceleration (DR), are given by the dashed green and blue lines respectively, all of which were obtained from GALPROP. The dashed orange line represents the PD4 spectrum from *Di Bernardo et al.* (2013), who used the DRAGON code for galactic propagation, which is similar to the GALPROP model. The PAMELA and AMS-02 measurements (coloured symbols) are the same as in Figure 6.3.

modulated spectra that best reproduce measurements. See also *Bisschoff and Potgieter* (2014, 2016) for related LIS studies.

Figure 6.4 gives a comparison of the newly constructed positron very LIS from this study (solid black line) to different versions of the LIS from other authors (coloured dashed lines). The dashed red line shows the model C positron LIS from *Strong et al.* (2000), where the corresponding electron spectrum from this model was adjusted to satisfy the synchrotron spectral index constraints, while also matching local electron and proton observations at that time. This spectrum was used extensively in earlier modulation studies (e.g. *Langner*, 2004; *Langner and Potgieter*, 2004). However, when compared to PAMELA and AMS-02 measurements it falls well below what the LIS is expected to be above ~ 3 GeV.

The dashed blue and green lines in Figure 6.4 are the PD and DR spectra from *Ptuskin et al.* (2006) respectively. The PD spectrum slightly improves on the spectrum from *Strong et al.* (2000) between 1 GeV and 10 GeV, but is unable to accommodate for the positron excess above 10 GeV. By including reacceleration, the DR model shows an

excessive intensity increase between 400 MeV and 7 GeV. The corresponding modulated spectra of the DR model will be difficult to reconcile with measurements.

The PD4 spectrum from *Di Bernardo et al.* (2013) is given by the dashed orange line in Figure 6.4. Using the DRAGON code, these authors included a new $e^{\pm}$ (electron + positron) extra component in their modelling, which is still of unknown origin, as an attempt to account for the observed positron excess toward higher energies. They furthermore used the force-field model to obtain modulated spectra at Earth, and compared these to PAMELA measurements in order to validate the galactic propagation models and the resulting interstellar spectra. Even though the addition of the $e^{\pm}$ extra component improves on previous galactic propagation models, the use of the force-field model for the purpose of heliospheric modulation is less convincing. The 3D modulation model used in this study, which includes all of the important modulation mechanisms, is able to significantly improve on the force-field model. The PD4 spectrum overestimates the PAMELA and AMS-02 measurements above ~ 30 GeV and underestimates intensities between ~ 2 GeV and ~ 10 GeV, which can be verified through modelling by comparing the amount of modulation expected at these energies and the intensity level of the LIS in relation to measurements.

6.4 Reproducing the PAMELA Spectra

In the previous chapter, electron measurements from PAMELA were reproduced independently, i.e. without considering what the modulated spectra for the positively charged positrons look like. Since electrons and positrons both have the same rest mass, they will experience the exact same diffusion. Simultaneously observed electrons and positrons from the same detector, measured over a relatively long time period, can consequently be studied and reproduced, thereby adding additional constraints to diffusion and drifts.

By using the DCs from Figure 5.9, along with the positron very LIS from Figure 6.3, the modulation of positrons is modelled by reversing only the drift directions of electrons. The measured and modelled "b"-semester spectra are shown in Figure 6.5 (open symbols represent preliminary measurements below 200 MeV that are still under review). The model clearly doesn't reproduce positron measurements as accurate as it does the electron measurements in Figures 5.4 and 5.5. This motivates a revision of the DCs used for modelling electrons, in order to find a set of coefficients that can improve the calculated positron spectra in Figure 6.5, while still accurately reproducing electron measurements. However, more emphasis will be given to reproducing the finalized PAMELA electron spectra from *Adriani et al.* (2015b), since PAMELA positron measurements are still preliminary and the significantly lower statistics for these particles inevitably lead to larger uncertainties.

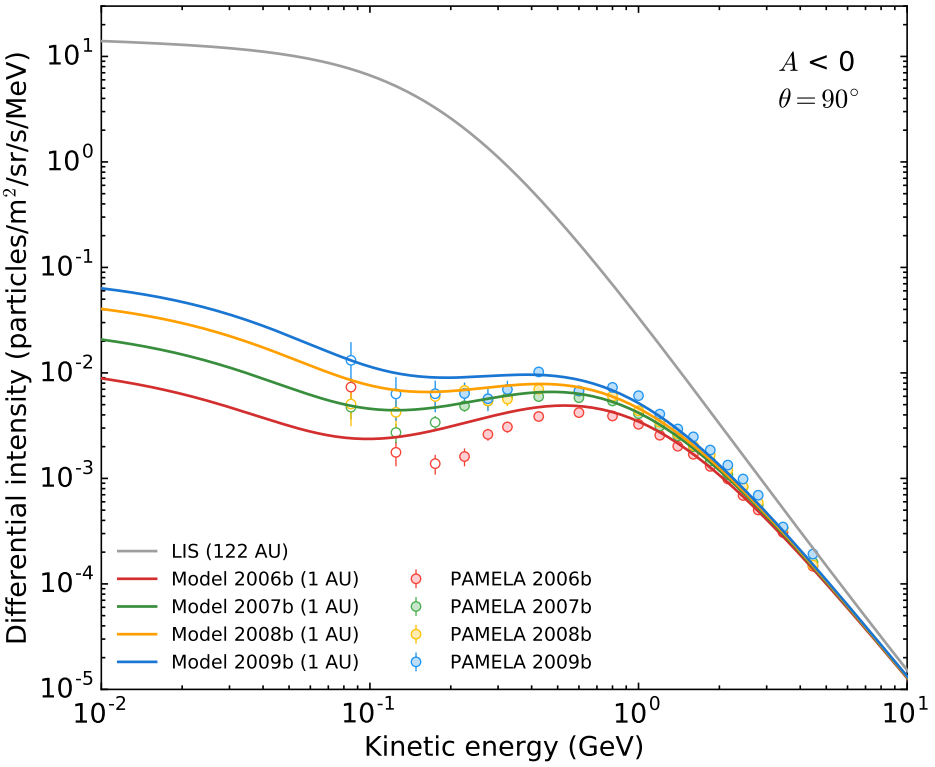

Figure 6.5: Modelled (coloured lines) and measured (coloured symbols) positron spectra at Earth, using DCs from Figure 5.9 and the newly constructed positron very LIS from Figure 6.3.

In the upcoming sections a more general set of DCs is proposed to account for simultaneous electron and positron measurements. Obtaining exact reproduced spectra for each semesterly period for both electrons and positrons has proven to be a difficult feat, since many transient perturbations in the turbulence significantly affect measurements at Earth. This does, however, provide a way to establish the impact of drifts on heliospheric modulation and also helps to prove the robustness of this modelling approach with regard to diffusion and drifts.

6.4.1 Constrained Diffusion Coefficients for Simultaneous Electron and Positron Measurements

The primary goal of this chapter is to show that, by using a QLT approach for turbulence as discussed in Chapter 3, along with the necessary modifications, simultaneous electron and positron measurements can be reproduced reasonably accurate. After revising the DCs reported in Figure 5.9 and making adjustments to the rigidity dependence, a more generally applicable set of coefficients was obtained that accounted for the modulation of both electrons and positrons. The rigidity dependence of these coefficients are shown in Figure 6.6.

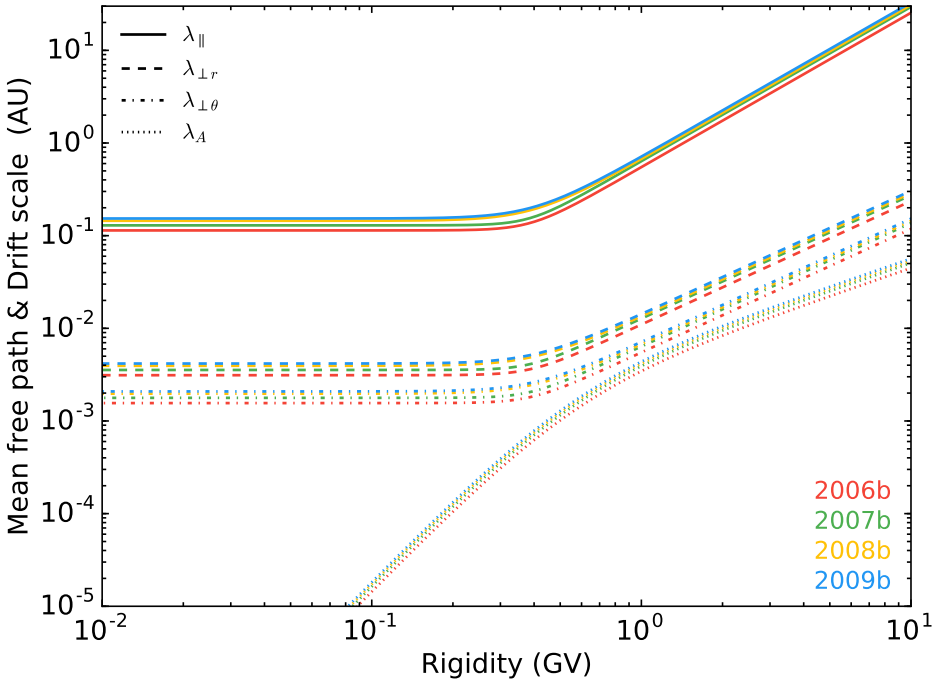

Figure 6.6: Rigidity dependence of the MFPs and drift scale for the "b" semesters of electrons and positrons. Parallel MFPs ($\lambda_\parallel$) are given by the solid lines, while perpendicular MFPs in the radial ($\lambda_{\perp r}$) and polar ($\lambda_{\perp\theta}$) directions are given by the dashed and dashed-dotted lines respectively. The drift scale (λ_A) is given by the dotted lines.

The approach to diffusion used here is very similar to that used when only electrons were considered in Chapter 5. The most significant change that was made, was for diffusion perpendicular to the average background HMF in the polar direction ($\lambda_{\perp\theta}$). In the previous chapter both $\lambda_{\perp\theta}$ and $\lambda_{\perp r}$ were scaled to 2 % of $\lambda_\parallel$ (*Giacalone and Jokipii*, 1999), an assumption that has been used in many modulation studies (e.g. *Ndiitwani et al.*, 2005; *Potgieter and Nndanganeni*, 2013a; *Potgieter et al.*, 2015) and sufficed in reproducing the electron measurements. For reproducing simultaneous PAMELA electron and positron measurements, $\lambda_{\perp\theta}$ had to be scaled to 1 % of $\lambda_\parallel$ below the bend, while keeping $\lambda_{\perp r}$ scaled at 2 %. This approach of modifying the scaling factor of $\lambda_{\perp\theta}$ to be smaller than $\lambda_{\perp r}$ has been successfully applied in recent proton modulation studies (*Zhao et al.*, 2014; *Manuel et al.*, 2014; *Vos and Potgieter*, 2015), and is extended here to electrons and positrons also.

It is clear that the rigidity dependence shape of the DCs in Figure 6.6 is very similar to those in Figure 5.9. However, minor adjustments were made to the rigidity dependence in order to obtain best agreement to electron and positron measurements. The bend, which is located around 330 MeV in Figure 5.9, is shifted to $\sim$ 400 MeV, along with a 14 % increase in MFPs below the bend where DCs become independent of rigidity. Above the bend, the $P^{1.55}$ power law dependence for $\lambda_\parallel$ is increased to $P^{1.67}$, while the power law dependence for $\lambda_\perp$ is increased from $P^{1.24}$ to $P^{1.33}$. A summary of the

modulation parameters, as they relate to the diffusion and drift equations in Chapter 3, is given in Table 6.1.

6.4.2 Modelling the Modulation of Simultaneous Electron and Positron Measurements

Using the DCs presented in Figure 6.6, an updated set of energy spectra was computed for electrons and positrons. Figure 6.7 gives the newly computed 2006b electron energy spectrum at various distances indicated by the legend, along with the previously calculated energy spectrum at Earth (in Figure 5.4) where DCs from Figure 5.9 were used (dashed grey line). Figure 6.8 shows the same spectra for semesters 2007a through 2009b. PAMELA measurements from *Adriani et al.* (2015b) are given by the coloured symbols for each semester. As a reference, the 2006b PAMELA spectrum is shown by the grey symbols in Figure 6.8.

The changes made to the DCs still produce modulated spectra at Earth that are in agreement with electron measurements. For 2006b, the local maximum at the peak of the spectrum is at $\sim 700\,\mathrm{MeV}$ and shifts down to $\sim 500\,\mathrm{MeV}$ toward 2009b. When comparing the solid red and dashed grey lines, the local minimum for the newly computed 2006b spectrum in the upturn region is located at $\sim 70\,\mathrm{MeV}$, which now occurs at a higher energy than the previously computed spectrum. This can also be seen in the spectra from other semesters, as shown in Figure 6.8. The new set of DCs predicts that the modulated spectra generally turn upward at slightly higher energies, which is in agreement with what measurements indicate around 100 MeV. The shift of the local minimum at the upturn region to higher energies over time is evident when comparing

Table 6.1: A summary of the modulation parameters used to reproduce the simultaneous electron and positron measurements from PAMELA. See Chapter 3 for discussions of these variables and the equations containing them.

Parameter	**2006b**	**2007a**	**2007b**	**2008a**	**2008b**	**2009a**	**2009b**
$\lambda_{\parallel}$ (AU) *	0.555	0.589	0.644	0.657	0.684	0.707	0.723
$\kappa_{A\,0}$	1.00	1.00	1.00	1.00	1.00	1.00	1.00
$P_{A\,0}$ (GV)	0.55	0.55	0.55	0.55	0.55	0.55	0.55
$\kappa^0_{\perp r}$	0.02	0.02	0.02	0.02	0.02	0.02	0.02
$\kappa^0_{\perp\theta}$	0.01	0.01	0.01	0.01	0.01	0.01	0.01
c_1	0.00	0.00	0.00	0.00	0.00	0.00	0.00
$c_{2\,\parallel}$	1.67	1.67	1.67	1.67	1.67	1.67	1.67
$c_{2\,\perp}$	1.34	1.34	1.34	1.34	1.34	1.34	1.34
c_3	6.00	6.50	6.50	6.00	4.00	4.00	4.00
P_k (GV)	0.39	0.39	0.39	0.40	0.40	0.40	0.40
$d_{\perp\theta}$	1.50	1.50	1.50	1.50	1.50	1.50	1.50

* For 1.0 GeV at Earth

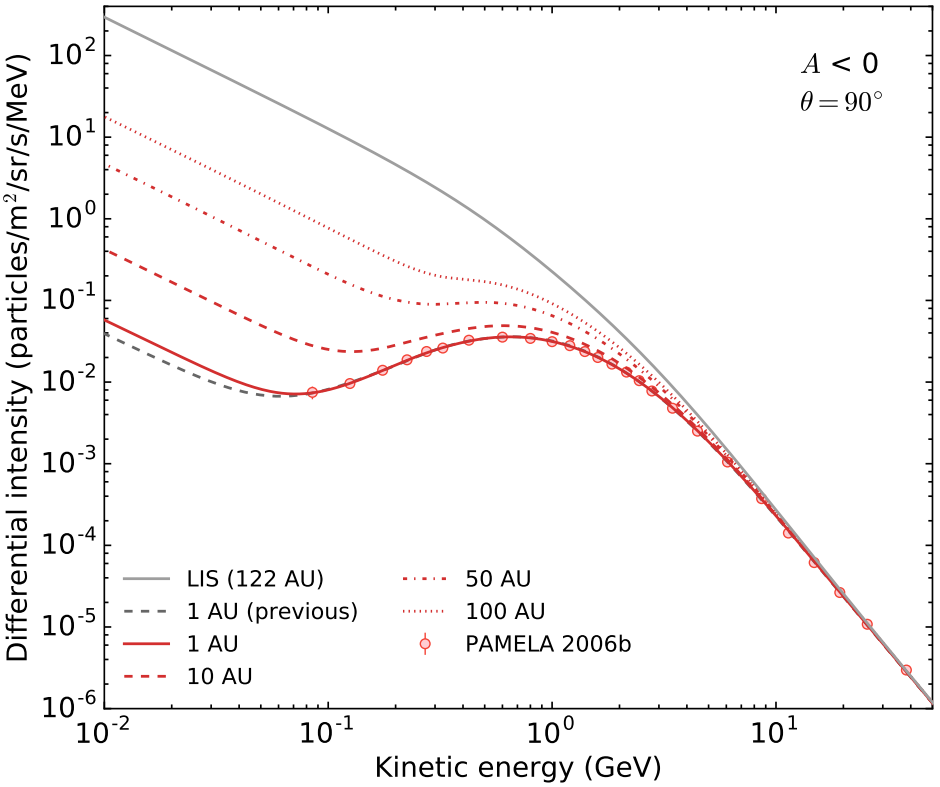

Figure 6.7: The 2006b electron energy spectra calculated by using DCs from Figure 6.6 at radial distances of 1 AU, 10 AU, 50 AU and 100 AU (as indicated by the legend). Also shown is the previous modulated spectrum from the model at 1 AU, calculated using DCs from the previous chapter in Figure 5.9 (dashed grey line). All modelled spectra are shown for an $A < 0$ polarity cycle in the equatorial region (i.e. $\theta = 90°$). The very LIS from Figure 5.2 has been used (solid grey line). PAMELA 2006b measurements are given by the red symbols.

the 2006b reference spectrum to the successive measured spectra. For 2006b, the measured spectrum continues to decrease toward the lowest energy, while the spectra for 2007b and later show how intensities begin to turn upward around 80 MeV.

Figure 6.9 shows the corresponding intensity ratios for the electron spectra between 2007a and 2009b relative to 2006b. Apart from small quantitative changes, these ratios don't show any qualitative differences when compared to the previous ratios from Figure 5.6. The observed ratios are generally better reproduced by the model, indicating that the model correctly estimates the quantitative changes in electron intensities over the course of the recent solar minimum.

By reversing the drift directions and using the very LIS from Figure 6.3, modulated positron spectra were calculated and are shown in Figures 6.10 and 6.11, along with preliminary PAMELA measurements. The 2006b spectrum in Figure 6.10 serves as a reference for how intensities developed throughout the 2006 to 2009 solar minimum. Computed intensities are given by the red lines at various distances (as indicated by the legend), with the very LIS given by the solid grey line (at 122 AU). The dashed grey line represents the previously calculated spectrum at 1 AU which corresponds to

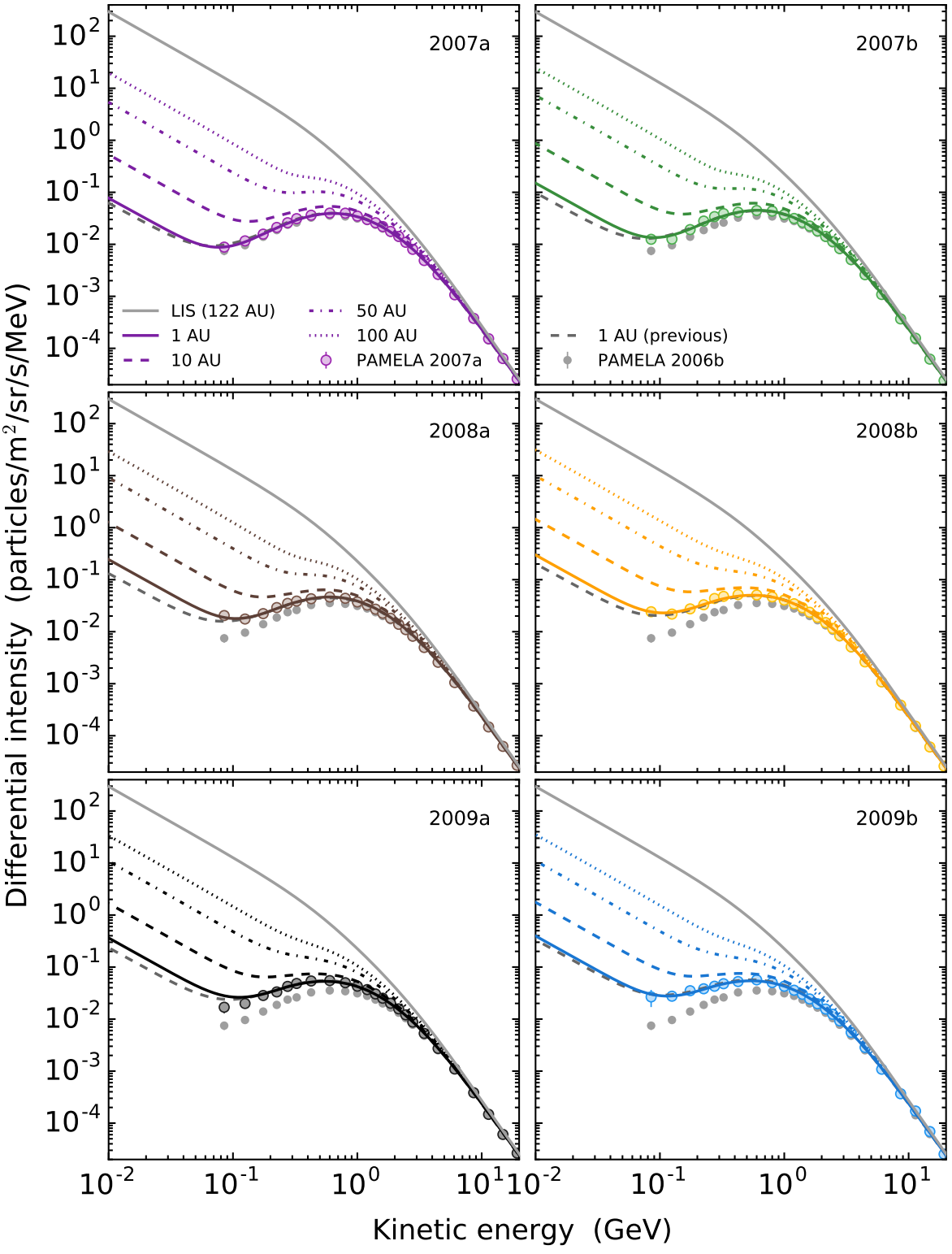

Figure 6.8: Similar to Figure 6.7, but for the measured and computed spectra of semesters 2007a through 2009b. The 2006b PAMELA spectrum, shown by the grey symbols in each panel, is given as a reference.

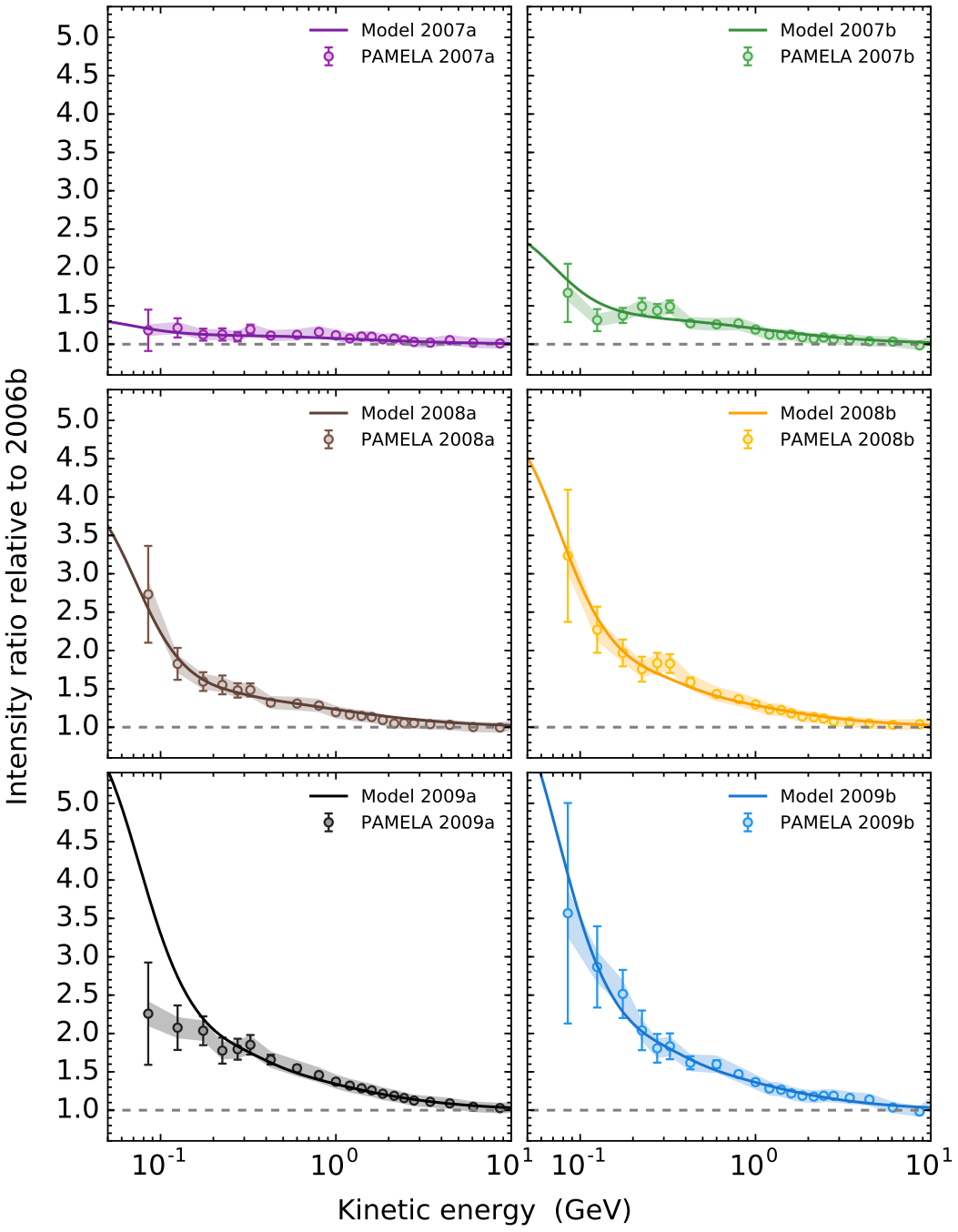

Figure 6.9: Electron intensity ratios for the spectra between 2007a and 2009b, relative to the 2006b reference spectrum. These ratios were calculated from the updated spectra from Figures 6.7 and 6.8. PAMELA measurements are given by the symbols, along with statistical errors (error-bars) and systematic errors (shaded bands). Computed spectra are given by the solid lines.

DCs from Figure 5.9. PAMELA measurements below 5 GeV are still preliminary, with measurements below 200 MeV still under review. Measurements above 5 GeV represent intensities averaged between 2006 and 2009, as published by *Adriani et al.* (2013b).

In reproducing the preliminary PAMELA positron measurements, care was taken to still obtain modulated electron spectra that reproduce electron measurements for the

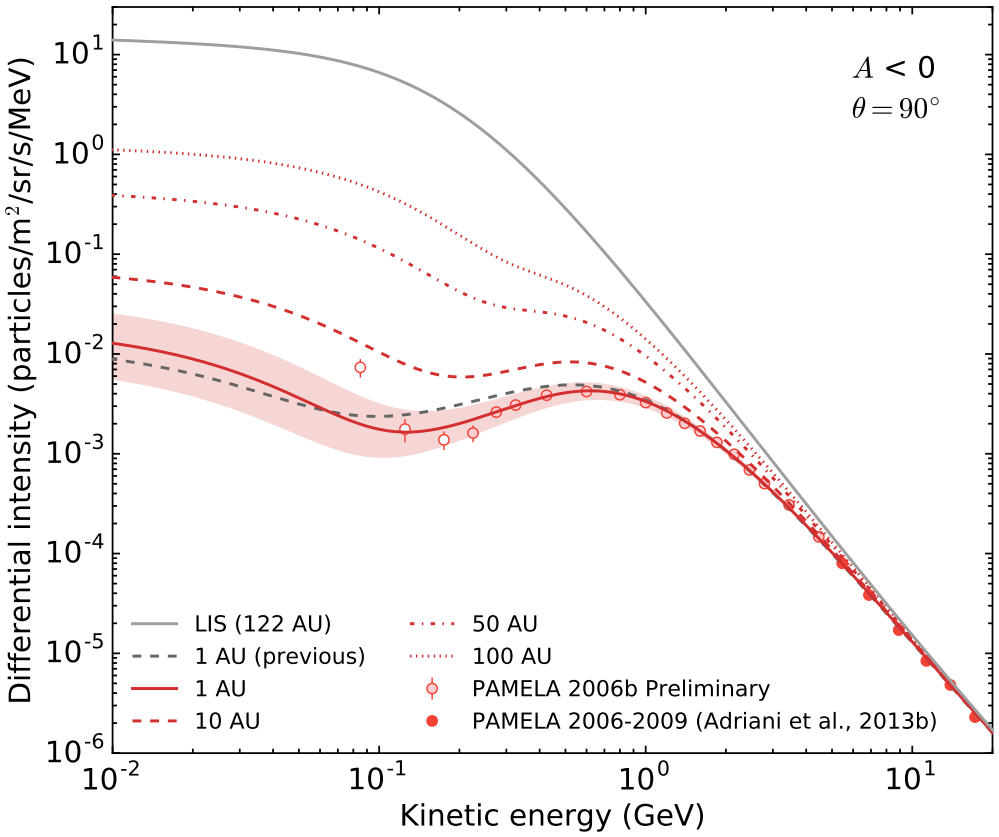

Figure 6.10: The 2006b positron energy spectra calculated by using DCs from Figure 6.6 at radial distances of 1 AU, 10 AU, 50 AU and 100 AU (as indicated by the legend). Also shown is the previous modulated spectrum from the model at 1 AU, calculated using DCs from Figure 5.9 (dashed grey line). All modelled spectra are shown for an $A < 0$ polarity cycle in the equatorial region (i.e. $\theta = 90°$). The very LIS from Figure 6.3 has been used (solid grey line). See the text for an explanation and purpose of the red shaded band. PAMELA measurements below 5 GeV are preliminary (light-red filled symbols), with measurements below 200 MeV regarded as work in progress and subject to possible changes (open symbols). Measurements above 5 GeV represent intensities averaged between 2006 and 2009 (solid red symbols), as published by *Adriani et al.* (2013b).

opposite drift cycle. The solid red line in Figure 6.10 represents the computed spectrum at Earth, which is in good agreement with measurements down to $\sim$ 250 MeV. Below this energy, intensities decrease significantly, followed by a sharp increase toward lower energies. This behaviour of the positron energy spectrum below $\sim$ 250 MeV was not possible to reproduce with the model without sacrificing the good agreement between model solutions and measurements for electrons. Consequently, an alternative approach was taken wherein the effect of a 10 % variation in the DCs was considered. This lead to a range of possible intensity values that can be obtained through modelling while still adhering to the required shape of the spectrum and is shown by the red shaded band in Figure 6.10. With this approach, the majority of PAMELA measurements can be contained within the upper and lower limits achievable by the model assuming a 10 % variance in the DCs.

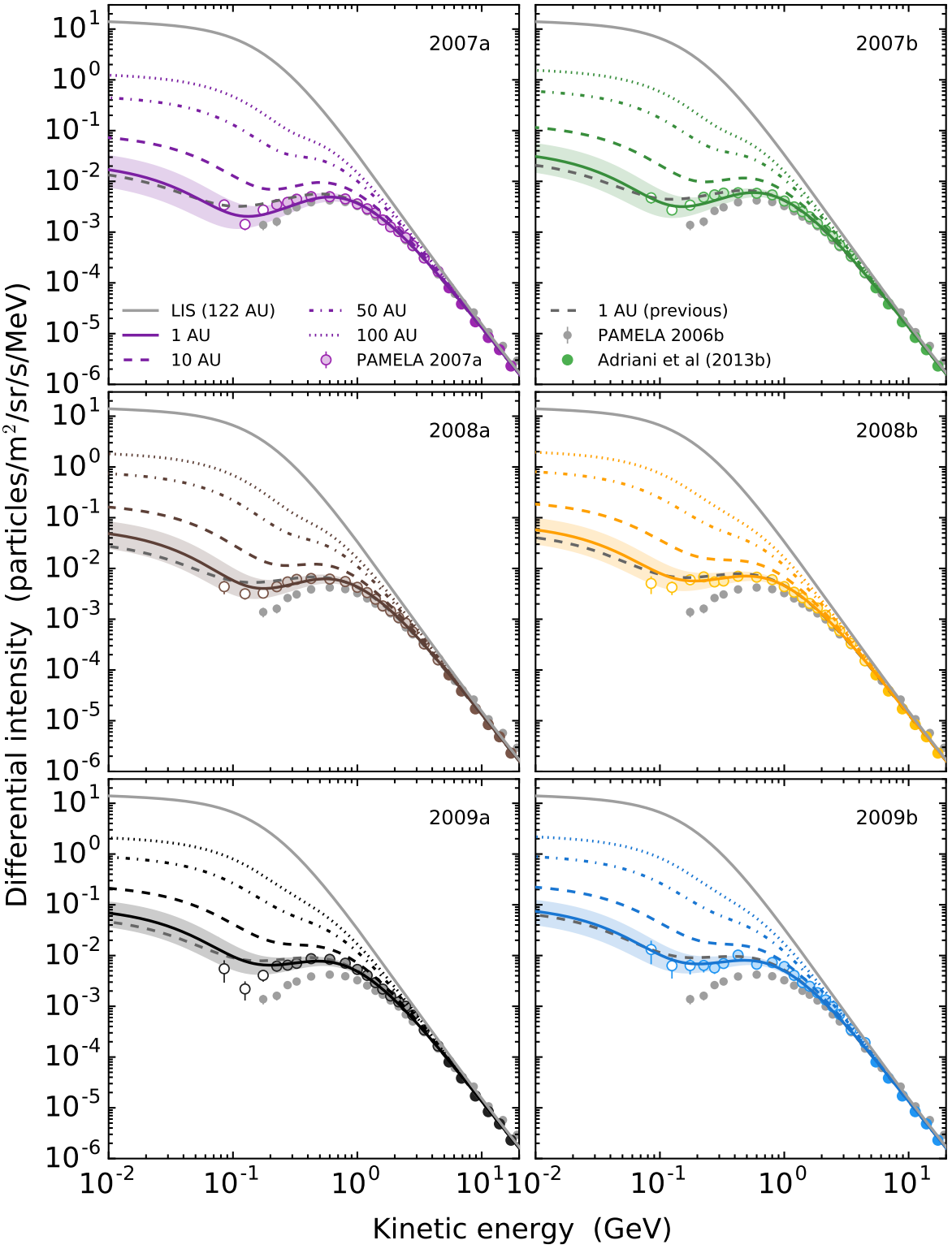

Figure 6.11: Similar to Figure 6.10, but for computed and measured spectra for semesters 2007a to 2009b.

Modulated positron spectra from the model have similar qualitative features than electrons. A local maximum occurs at the peak of the spectrum which is situated at $\sim$ 600 MeV for semester 2006b, and shifts down to $\sim$ 450 MeV toward semester 2009b as the spectrum becomes softer. Accompanying this downward shift of the local peak is an increase in intensity from $\sim 4.5 \times 10^{-3}$ particles/m^2/s/sr/MeV to $\sim 9.0 \times 10^{-3}$ particles/m^2/s/sr/MeV over the same time period. The local minimum at the upturn region occurs at $\sim$ 120 MeV in 2006b, but shifts to $\sim$ 200 MeV toward 2009b. The general shape of the modulated spectra below the upturn is still determined by the very LIS due to negligible amounts of adiabatic energy losses from the SW for electrons and positrons.

Overall, the model is able to reasonably reproduce the measured positron spectra at Earth for all semesters over most energies. The shaded bands in Figures 6.10 and 6.11 contain all the measurements except for 2006b, where measurements increase very steeply at the lowest energy around $\sim$ 80 MeV, and for 2009a, where measurements decrease to very low intensity levels in the range of 80 MeV to 200 MeV. However, since measurements below 200 MeV are considered to be work in progress, model spectra at these energies will be further refined when measurements are finalized.

When comparing the previously modulated positron spectra from the model (dashed grey lines) to the most recent model solutions at Earth, it is clear that for 2006b the previously calculated spectrum significantly overestimated measured intensities below $\sim$ 1 GeV. The previous spectra also seem to predict that the upturn region is located at a noticeably lower energy than what is suggested by preliminary PAMELA measurements.

The intensity ratios given in Figure 6.12 are taken relative to semester 2006b and quantify how the positron spectrum increased over time. The dashed lines represent the corresponding ratios of the upper and lower limits of the shaded bands in Figure 6.11. It is clear from the solid coloured lines that the model ratios are qualitatively similar to the measured ratios, with the largest ratios occuring at lower energies, which indicates that CR positrons at lower energies experienced larger intensity increases as solar activity decreased – similar to electrons and protons. When considering the 10 % variation in DCs, most of the measured ratios can also be contained within the ranges given by the dashed lines. Most importantly, since the 2006b positron spectrum was accurately reproduced down to $\sim$ 300 MeV, the good agreement between modelling and measurements for semester 2009b (bottom right panel in Figure 6.11) essentially shows that the model is able to reproduce the overall observed increase in positron intensities, in addition to electrons, when using the DCs from Figure 6.6.

The computed ratios can be extended to lower energies, as shown in Figure 6.13 and 6.14 for electrons and positrons respectively. It is clear that positrons experienced maximum intensity increases between 50 MeV and 80 MeV, relative to 2006b. Below these energies, drifts fade away and diffusion begins to dominate, resulting in a flattening

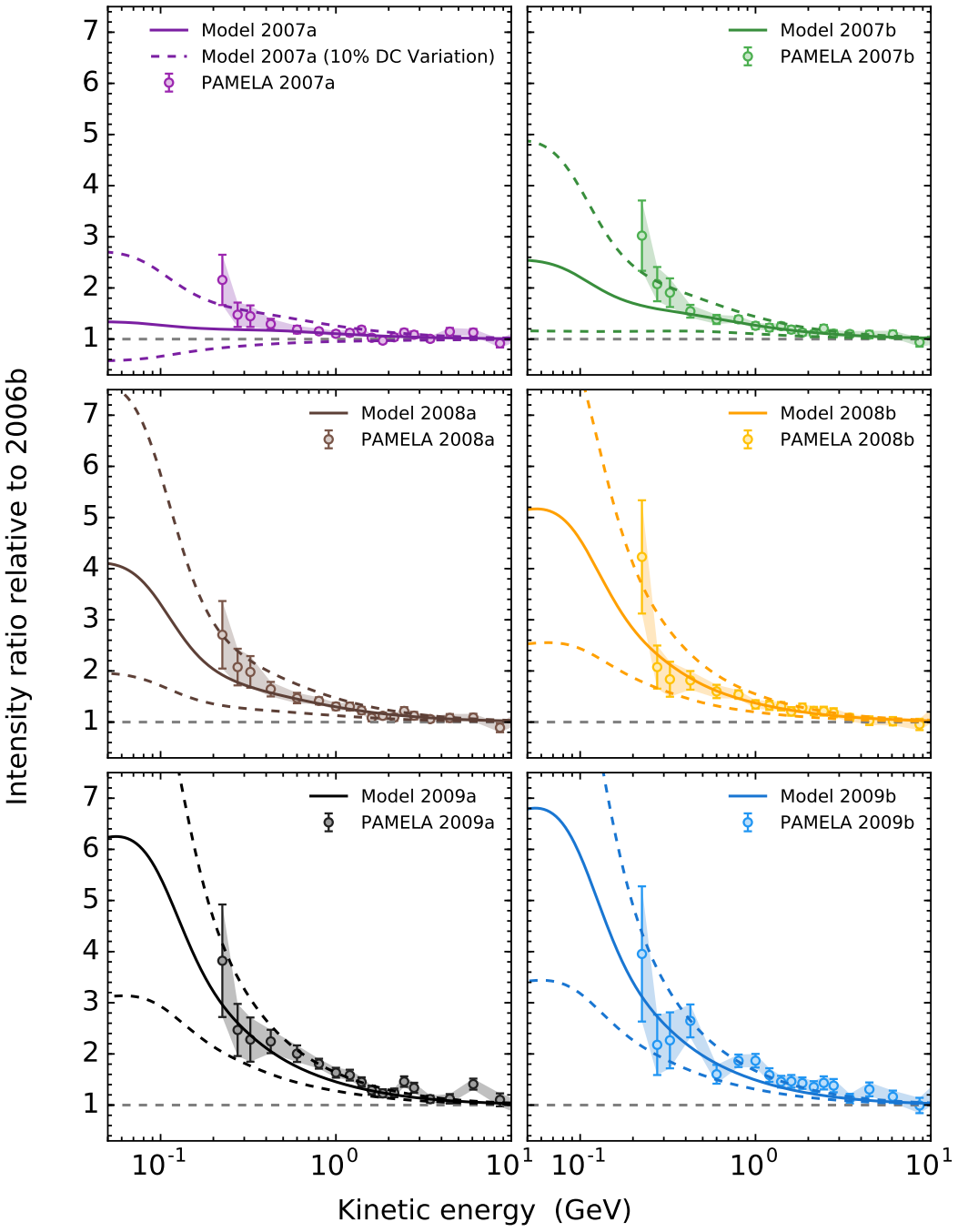

Figure 6.12: Positron intensity ratios for the spectra between 2007a and 2009b, relative to the 2006b reference spectrum. These ratios were calculated from the spectra from Figures 6.10 and 6.11. Preliminary PAMELA measurements are given by the symbols down to $\sim 200\,\mathrm{MeV}$, along with statistical errors (error-bars and shaded bands). Computed spectra are given by the solid coloured lines, while the dashed lines represent the limits for when the DCs are varied by 10 %.

of the intensity ratios as the modulated spectrum at Earth takes on the shape of the very LIS. The differences in the shapes of the relative ratios for electrons and positrons can be ascribed to drifts. Even though these features are not directly measured, due to the limited observable energy range of CR experiments, the model can be used to infer

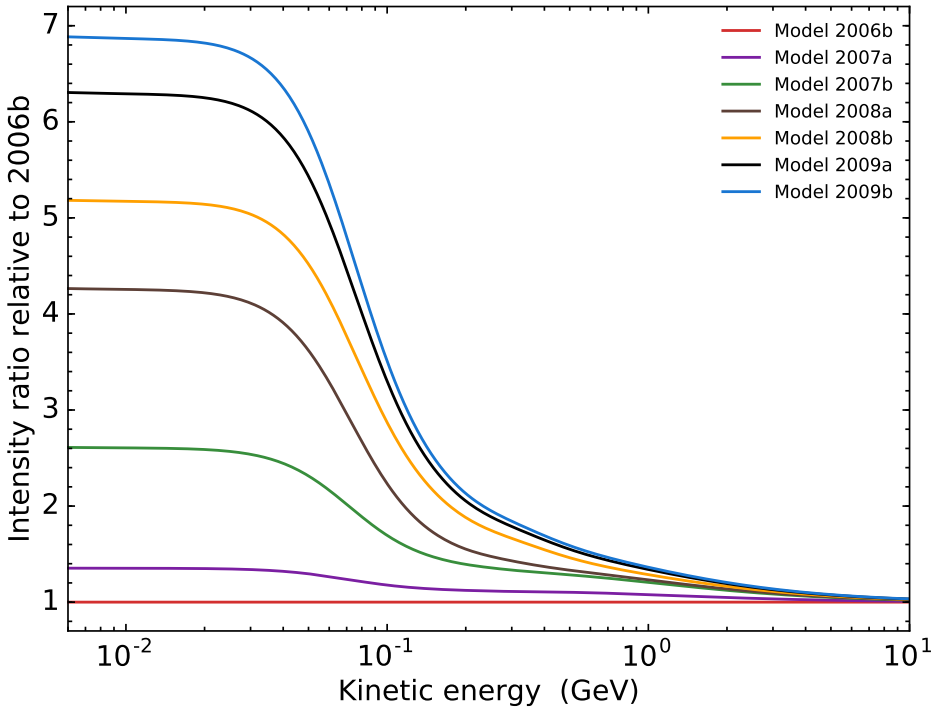

Figure 6.13: Similar to Figure 6.9, but for the computed spectra only, and over an energy range of 3 MeV to 10 GeV.

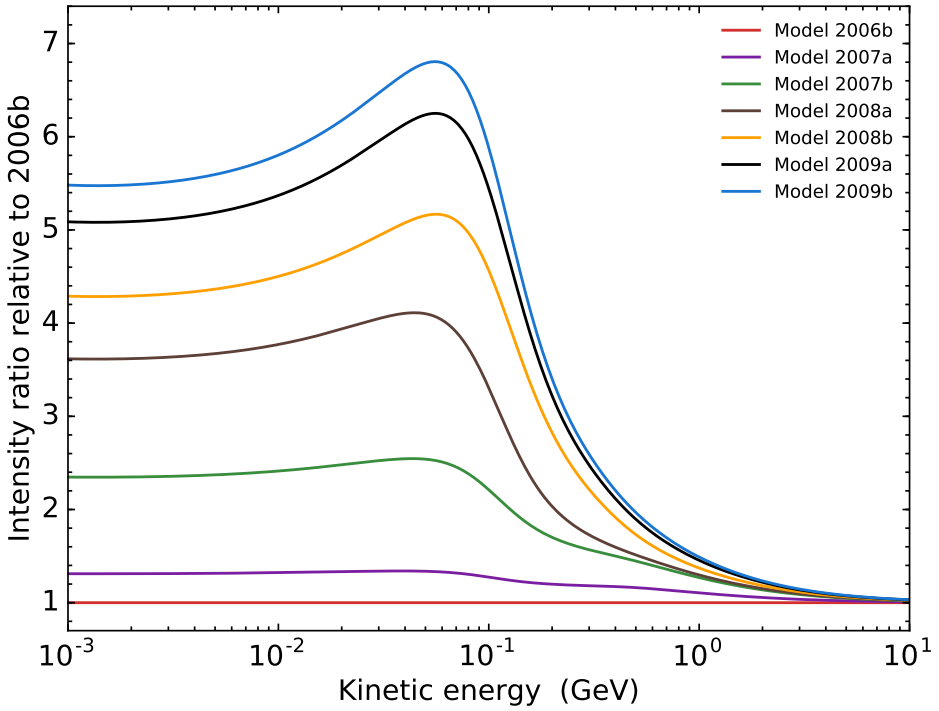

Figure 6.14: Similar to Figure 6.13, but for positrons.

and make predictions of such features, as illustrated in this study.

See *Adriani et al.* (2016) for a study of electrons and positrons measured by PAMELA from 2006 to 2015.

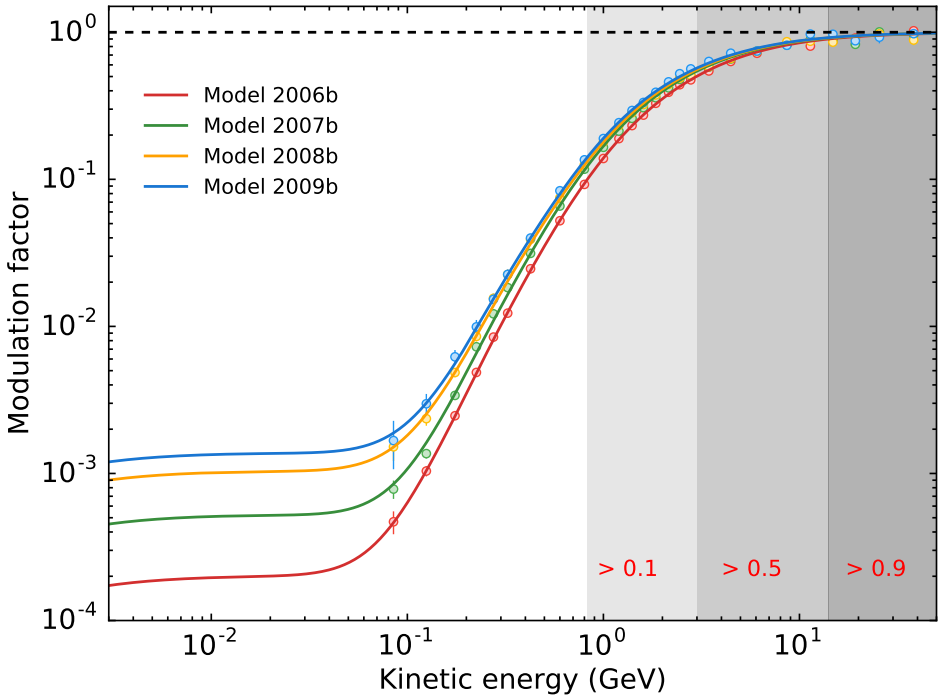

Figure 6.15: The MF for electrons, calculated by taking the ratio of the very LIS to the modulated spectra at Earth. The solid lines and symbols represent the model solutions and PAMELA observations, respectively, for the "b" semesters. The latest electron spectra from Figures 6.7 and 6.8 were used for calculating these MFs.

6.4.3 Total Modulation

The concept of total modulation and the importance of the MF were discussed in Section 5.4.3 of the previous chapter. With an accurate estimate of the electron very LIS at 122 AU and modulated spectra at Earth as verified by PAMELA, it is possible to calculate the total modulation between the HP and Earth. Even though no measurements of positrons are available from beyond the HP, it follows from the good agreement between modelling and measurements of electrons and positrons at Earth, that the newly constructed positron LIS from Figure 6.3 can be considered reliable with regard to shape and absolute value.

Figure 6.15 gives the MF for electrons using the new modulated spectra from this chapter. Apart from slightly larger values for the MF below $\sim$ 100 MeV, these MFs are qualitative similar to those shown in Figure 5.8. The MFs of positrons for the "b" semesters are shown in Figure 6.16. When compared to electrons, the MFs for positrons are very similar at higher energies, with a value of 0.5 at 3 GeV, decreasing with increasing energies. Drifts begin to influence modulation toward lower energies, resulting in larger intensities for positrons compared to electrons of the same energy. Maximum modulation for positrons occurs around $\sim$ 100 MeV, which is in the region where the spectrum at Earth has a local minimum before turning upward. As modulated spectra for both electrons and positrons take on the shape of the LIS, the MF for these

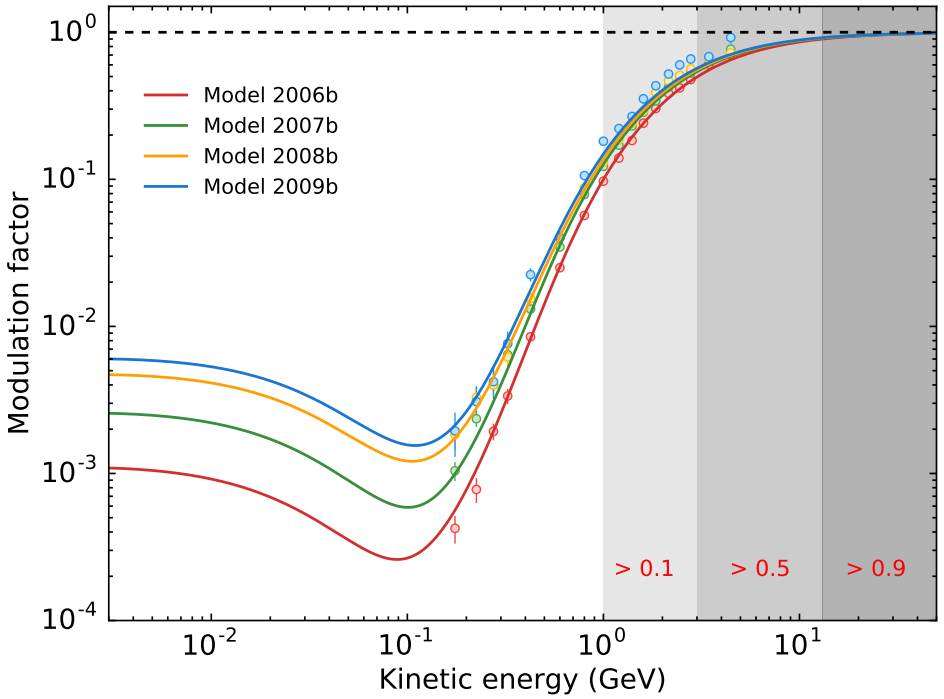

Figure 6.16: Similar to Figure 6.15, but for positrons.

particles begin to flatten below $\sim 100\,\mathrm{MeV}$. The weak rigidity dependence of the positron LIS below $\sim 100\,\mathrm{MeV}$, in contrast to the strong power law shape of the electron LIS, lead to notable differences in the MF for these particles. The MF values for electrons and positrons are given at various energies in Table 6.2.

6.5 Summary

Preliminary, semesterly averaged positron measurements from PAMELA were made available for this study via *private communication* (R. Munini, 2015), along with simultaneous PAMELA electron measurements at similar time intervals, as published by *Adriani et al.* (2013a). This presented a unique opportunity to find a set of DCs that are able to reproduce the spectra of both of these particles over time, which is only possible because electrons and positrons experience the same diffusion, but drift in opposite directions as a result of the opposite charge they carry.

Firstly, the very LIS for positrons was revisited, and a newly constructed LIS was presented in Figure 6.3. This LIS was modified to account for the positron excess above $\sim 10\,\mathrm{GeV}$. Published PAMELA and AMS-02 positron measurements were used to normalize the new positron LIS at energies above 30 GeV. Since no Voyager 1 positron measurements are available from beyond the HP, GALPROP spectra had to be relied on, where the plain diffusion and diffusion with reacceleration regimes were used as limits for a range of possible values for the LIS. In addition, since the electron LIS was

Table 6.2: The MF for each of the "b"-semester computed spectrum for electrons and positrons from Figures 6.15 and 6.16, at different energies between 1 MeV and 50 GeV.

Electrons					
Kinetic energy (GeV)	0.01	0.1	1.0	10.0	50.0
MF for 2006b	0.00019	0.00064	0.141	0.849	0.982
MF for 2007b	0.00051	0.0011	0.170	0.867	0.984
MF for 2008b	0.00101	0.0018	0.182	0.872	0.985
MF for 2009b	0.00134	0.0022	0.192	0.877	0.985
Positrons					
Kinetic energy (GeV)	0.01	0.1	1.0	10.0	50.0
MF for 2006b	0.00095	0.00027	0.102	0.860	0.983
MF for 2007b	0.00221	0.00059	0.129	0.877	0.986
MF for 2008b	0.00412	0.00121	0.139	0.882	0.986
MF for 2009b	0.00531	0.00160	0.151	0.887	0.987

accurately determined, adjustments to the positron LIS could be made in order for the modulated spectra at Earth to best reproduce the PAMELA measurements.

Figure 6.5 showed how the computed electron spectra at Earth differ from PAMELA measurements when using the same DCs from Chapter 5. Since the aim of this Chapter was to find a set of DCs that is able to reproduce the simultaneous electron and positron measurements from PAMELA, the electron DCs had to be revised. Apart from minor adjustments made to the shape of the DCs' rigidity dependence, it was necessary to scale $\lambda_{\perp\theta}$ by 1 % of $\lambda_{\parallel}$ instead of 2 %. A similar approach was followed for protons in Chapter 4 (see also *Vos and Potgieter*, 2015; *Zhao et al.*, 2014). As the DCs were adjusted, care was taken to firstly reproduce the seven $\sim$ 6-monthly averaged PAMELA electron spectra from *Adriani et al.* (2015b), followed by preliminary positron measurements. These revised DCs were given in Figure 6.6.

The updated electron spectra and corresponding ratios were shown in Figures 6.7 to 6.9. When compared with the previous solutions from Chapter 5, the new spectra have slightly larger intensities below the upturn region, but still reproduces the PAMELA measurements with the correct amount of semesterly increases over time relative to 2006b, as required by the measurements. Figures 6.10 to 6.12 showed the computed and measured positron spectra and ratios, where most semesterly spectra were successfully reproduced down to $\sim$ 200 MeV. Measurements below $\sim$ 200 MeV are still under review. As an illustration of what is possible with the modulation model, the DCs were varied by a relative amount of 10 %, resulting in a range of intensities that were able to include the majority of the positron measurements.

Most importantly, though, over the course of the recent minimum, from 2006 to 2009, the exact amount of intensity increase for electrons, at all observable energies,

were reproduced with the model. In addition, from the positron figures it followed that the total increase observed in positron intensities was also correctly reproduced with the same set of DCs as used for electrons. This stands to prove that the approach for diffusion followed in this study is fairly robust, and that by using drift theory, as included in the model, it became possible to reproduce the energy spectra of oppositely charged CR lepton particles.

In the next chapter, charge-sign dependent modulation will be studied in detail by combining and comparing the measurements and computed results of protons, electrons and positrons from the previous chapters.

Chapter 7

Charge-Sign Dependent Modulation and Drifts During the Solar Minimum of Cycle 23/24

7.1 Introduction

The primary focus of this chapter is to further uncover and highlight charge-sign dependent modulation during the 2009 solar minimum period by combining PAMELA measurements and model results from the previous chapters. Doing so will provide evidence that gradient, curvature and current sheet drifts played a role during the recent solar minimum.

According to drift theory, the intensity of positively charged CRs during an $A < 0$ polarity cycle is expected to show a more rapid increase compared to negatively charged CRs. To test this, the modulation of electrons is compared to that of protons and positrons at the same rigidities. To self-consistently compare electrons and protons, a new set of 6-monthly averaged proton spectra is calculated and reproduced with the modulation model. The intervals of these new proton spectra correspond to those of electrons and positrons.

The intensity-time profiles of all of these particles are shown, from which clear differences between the development of intensities of negatively charged CRs and positively charged CRs are expected over time. In addition, the electron to proton (e^-/p) and electron to positron (e^-/e^+) ratios are also calculated. These ratios provide a comprehensive picture of charge-sign dependent modulation and drifts, especially with the addition of model solutions at rigidities where measurements are unavailable.

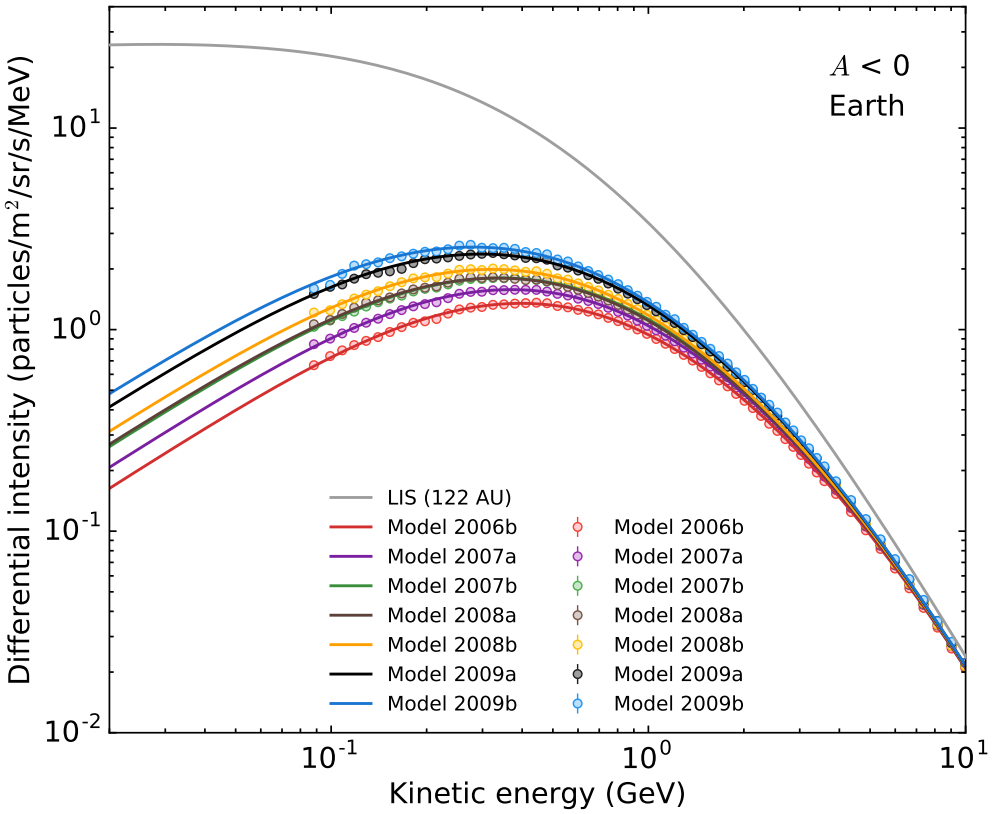

Figure 7.1: Semesterly averaged proton energy spectra from PAMELA (coloured symbols), calculated using Carrington Rotation spectra from *Adriani et al.* (2013a), and overlaid by the reproduced model spectra (coloured lines).

7.2 Reproducing Semesterly Averaged Proton Spectra

In order to compare the modulation of protons and electrons, as well as to calculate their ratios, the observational time periods and respective rigidities for these particles must coincide. Semesterly averaged proton spectra were calculated over time periods that correspond to those of electrons by using measurements at Carrington Rotation intervals from *Adriani et al.* (2013a). Since these semesterly averaged PAMELA spectra are different than those at Carrington Rotation intervals reproduced in Chapter 4 at the middle and end of each year, it is necessary to adjust the model parameters to account for these averages. The exact time periods over which measured proton averages are calculated are given in Figure 5.3.

Figure 7.1 shows a graph of the newly calculated semesterly averaged proton spectra from PAMELA overlaid by the model spectra. Measurements and computed spectra for semesters 2007b and 2008a overlap almost completely. Since the semesterly averaged time periods for protons also contain the time periods considered in Chapter 4, similar values for α and B_e were used to reproduce the new averaged PAMELA proton spectra.

Minor adjustments were made to the DCs in order to account for a slight decrease in measured intensities as a result of averaging. These DCs now represent an average estimate of the diffusion over 6-monthly intervals, similar to the coefficients of electrons and positrons from Chapters 5 and 6. The measured and computed semesterly proton spectra, from hereon referred to as semesters 2006b, 2007a, 2007b, 2008a, 2008b, 2009a and 2009b, are used for comparison with electrons and positrons throughout this chapter.

7.3 Modulation of Electrons and Protons

7.3.1 Intensity-Time Profiles

Adriani et al. (2013a) and *Potgieter et al.* (2014a) reported on the time development of GCR protons during the 2009 solar minimum period in detail. From a modelling perspective, it was found that, even though the recent solar minimum appeared to have been more diffusion-dominated than previous solar minima, drifts still contributed to $\sim 50\,\%$ of the total increase in intensity, while changes in diffusion were responsible for the other $\sim 50\,\%$. *Potgieter et al.* (2014a) therefore concluded that all modulation processes contributed to the observed changes in the proton energy spectra. Similar conclusions were made by *Potgieter et al.* (2015) and *Adriani et al.* (2015b), who investigated the time development of GCR electrons during the 2009 solar minimum. These results have been confirmed in Chapters 4 through 6 of this study. See *Vos* (2012) for a detailed discussion about the relative contributions of the various modulation processes during the 2009 solar minimum. See also *Adriani et al.* (2016) for an investigation of the electron and positron time dependence from PAMELA between July 2006 and December 2015.

Figure 7.2 shows a comparison of the time development of electrons (blue lines and symbols) and protons (red lines and symbols) at the same rigidities, relative to semester 2006b. Solid lines and filled circles represent PAMELA measurements, while dashed lines and open circles represent computed intensities from the model. Both the measured and computed intensities represent 6-monthly averages.

From Figure 7.2, it follows that 426 MV electron intensities increased by a factor of ~ 1.6, while proton intensities at the same rigidity increased by a factor of ~ 2.4. This apparent difference in the relative increase is correctly reproduced through modelling, and is a consequence of the different drift patterns that oppositely charged CR particles experience. During an $A < 0$ polarity cycle, negatively charged particles (like electrons and antiprotons) drift into the heliosphere mainly over the polar regions, and thereby gaining quick access to Earth's position. Positively charged particles (like protons and positrons) generally drift into the heliosphere along the HCS and equatorial regions, and are additionally affected by the waviness of the current sheet. As a result, the intensities of protons and positrons increase more rapidly when compared to electrons

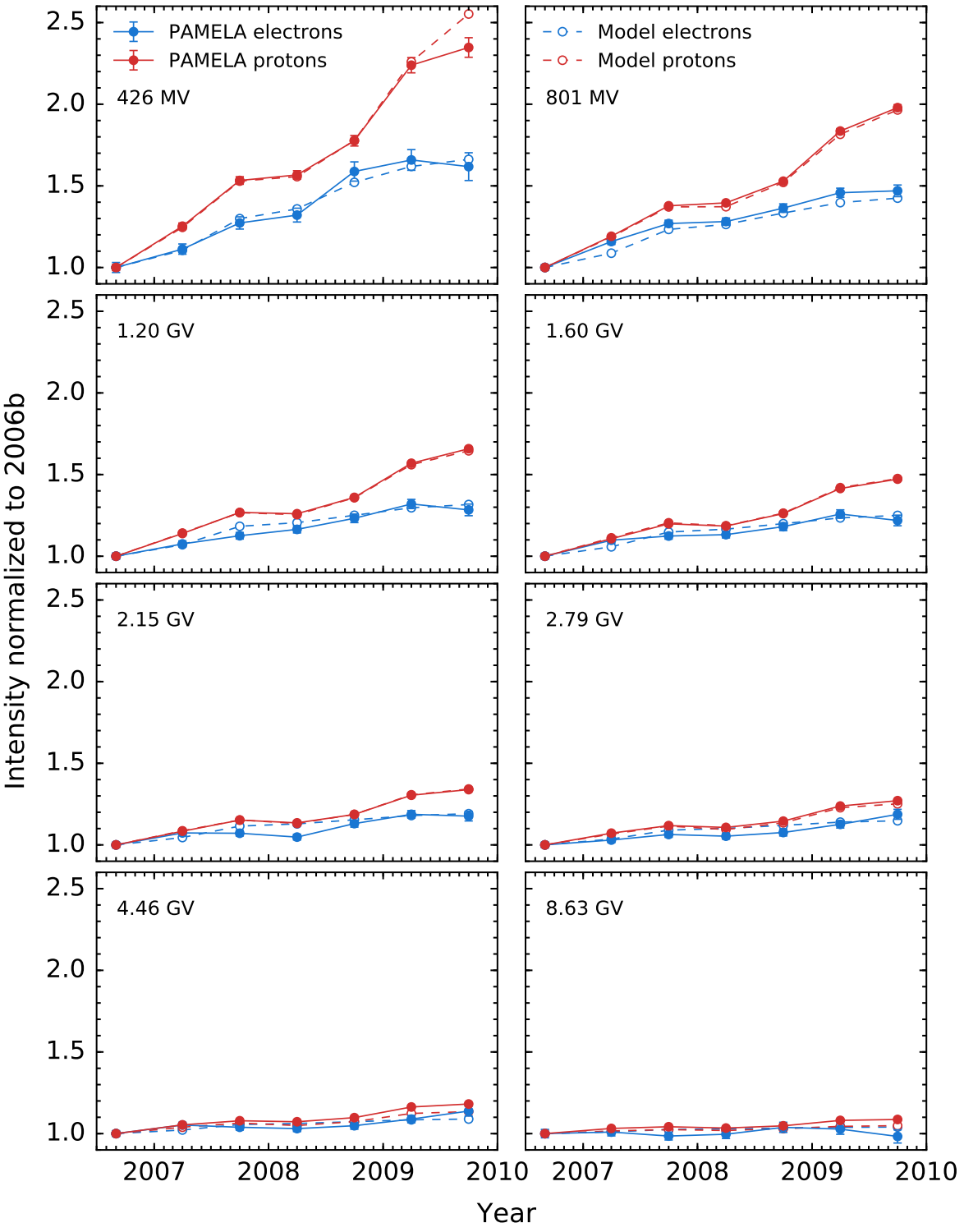

Figure 7.2: Normalized intensities of protons (red) and electrons (blue) relative to semester 2006b over time at various rigidities between 426 MV and 8.63 GV. PAMELA measurements are given by the solid circles and lines, while model results are given by the open symbols and dashed lines.

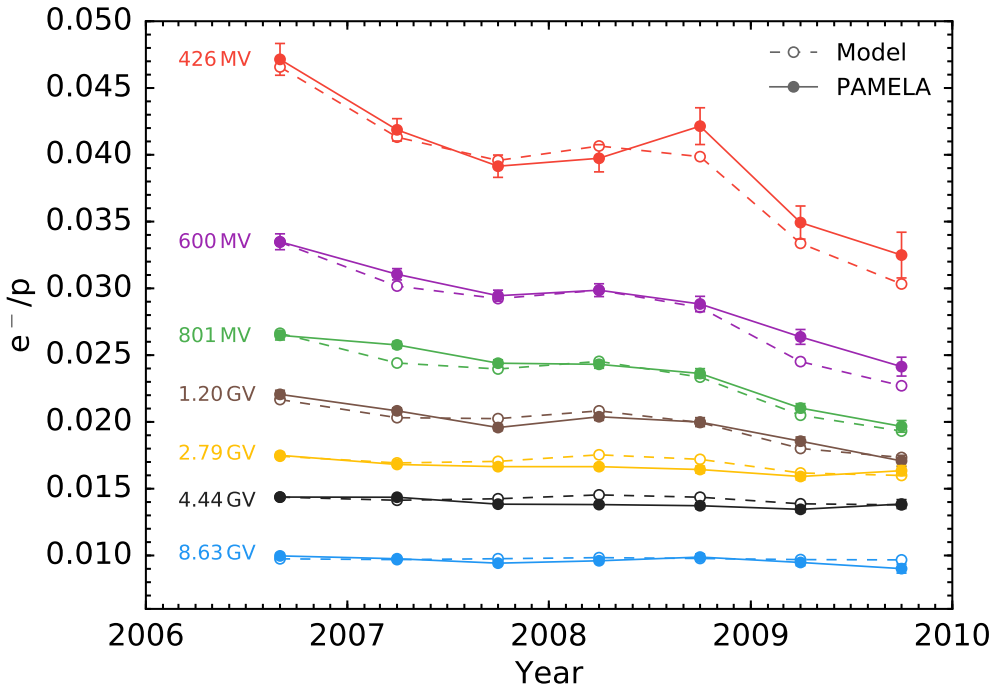

Figure 7.3: Electron to proton ratios at various rigidities between 426 MV and 8.63 GV as a function of time. Ratios measured by PAMELA are given by the solid lines and filled circles, and computed ratios from the model are given by the dashed lines and open circles.

or antiprotons, since progressively more of these particles arrive at Earth over time as the HCS become less wavy.

It follows from Figure 7.2 that relatively more protons reached the Earth by 2009b with respect to 2006b, than did electrons. Moving up in rigidity, the magnitude of the relative intensity increases of both electrons and protons become smaller as modulation fades out, where the relative increase is below 10 % for 8.63 GV particles. The shapes of the proton time profiles have a more prominent peak in 2009 compared to the flatter peak of electrons, indicating that the rate of increase of electron intensities might have reached a limit, while the rate of change of proton intensities might have continued to increase, had minimum modulation conditions persisted beyond 2009.

7.3.2 e^-/p Ratios Over Time

Shown in Figure 7.3 are the measured and computed electron to proton ratios as a function of time at different rigidities. The strongest decrease in the e^-/p ratio between 2006b and 2009b is seen at 426 MV, which is the lowest matching rigidity for PAMELA electrons and protons. At this rigidity the ratio decreased by a factor of ~ 1.5 from 0.047 down to 0.033. Even though the electron spectra increased between 2006b and 2009b, increasingly more protons were observed at Earth relative to electrons.

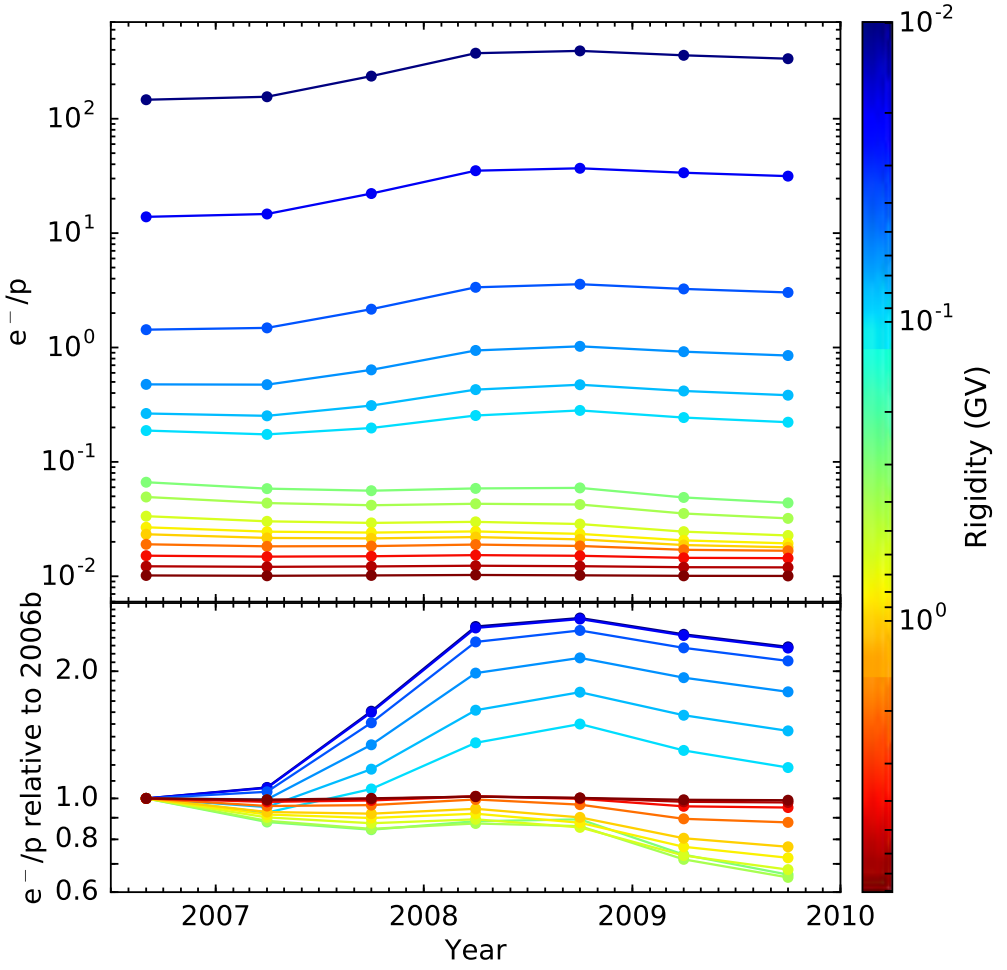

Figure 7.4: *Top panel:* Computed e^{-}/p ratios from the modulation model, as a function of time at different rigidities between 10 MV and 8 GV (according to the colorbar). *Bottom panel:* Similar to the e^{-}/p ratios in the top panel, but normalized with respect to semester 2006b.

Below $\sim$ 400 MV, electron MFPs become independent of rigidity and drifts are decreased with respect to the weak scattering limit (see Figure 6.6). It is at these rigidities that diffusion becomes the dominant modulation process as drifts begin to fade out. At higher rigidities all modulation processes compete equally (see *Potgieter et al.*, 2014a, 2015).

Furthermore, from the interplay between drifts and diffusion, *Vos* (2012) found that gradient, curvature and current sheet drifts are expected to have a maximum effect between $\sim$ 300 MV and $\sim$ 800 MV. The factor of $\sim$ 1.5 decrease in the e^{-}/p ratio at 426 MV from 2006b to 2009b can therefore be considered a good approximation of the maximum change in this ratio as a result of drifts, as well as the rigidity at which electrons and protons experienced the largest combined drift effects. At higher rigidities, the decrease in the ratio becomes less steep as CRs experience less modulation. This behaviour of the e^{-}/p ratio for rigidities between 426 MV and 8.63 GV was reproduced with the modulation model (dashed lines and open circles). Highlighting the effect of

charge-sign dependent modulation, *Potgieter et al.* (2001a) showed that the largest e^-/p ratio is expected during an $A < 0$ cycle, which is also supported by observations made over a span of 22 years (e.g. *Heber and Marsden*, 2001).

Additionally, computed energy spectra allow for an investigation of how the e^-/p ratio changed at lower rigidities where observations are unavailable. The top panel of Figure 7.4 shows the computed e^-/p ratios over time for energies ranging from 10 MV up to 8 GV, while the bottom panel shows the same ratios normalized relative to semester 2006b. Overall, the e^-/p ratio increased from 2006b to 2009b for rigidities between 10 MV and 100 MV, where the largest increase occurred between 2007a and 2008a. Between 2008a and 2009b the ratio decreased by a small amount. In this rigidity range, the parallel and perpendicular diffusion of electrons are independent of rigidity. From the bottom panel of Figure 7.4 it follows that the e^-/p ratio increased by a factor of ~ 2.3 at the lowest rigidity of 10 MV, while at 100 MV the increase was only a factor of ~ 1.2. The upward trend in the e^-/p ratio between 2006b to 2008b implies that electron intensities increased more than protons. At these low rigidities protons are subject to adiabatic deceleration, contributing to the decrease in proton intensities below ~ 1 GV, whereas electrons remain largely unaffected by this modulation process, taking on the shape of the LIS below $\sim$ 80 MV. The decrease observed in the e^-/p ratio between 2008b and 2009b indicates that proton intensities increased more than electrons, since electrons most likely reached maximum intensity levels under solar minimum conditions by the end of 2008, while proton intensities continued to increase throughout 2009. This was also foreseen by *Heber et al.* (2009), who used COSPIN/KET electron and proton count rates, taken along Ulysses' orbit, which have been corrected to obtain count rates equivalent to 1 AU.

For rigidities above 200 MV, the e^-/p ratio decreased, as shown by the set of lines from light-green to red in both panels of Figure 7.4. The reason for this is because the effect of drifts on CR modulation becomes more observable at these rigidities, resulting in relatively more protons reaching Earth compared to electrons. Above $\sim$ 400 MV electron MFPs are no longer independent of rigidity, but start to increase with increasing rigidity. See *Vos* (2012) and *Potgieter et al.* (2014a) for an in-depth study of the interplay between the various modulation mechanisms.

This behaviour of the e^-/p ratio is indicative of the interplay between drifts and other modulation mechanisms with varying rigidity. In a previous study, based on a first generation drift-dominated model, *Burger and Potgieter* (1999) investigated the tilt angle dependence of CR e^-/p ratios at Earth for various rigidities, the results of which are shown in Figure 7.5. During an $A > 0$ cycle the ratios have a "w" shape, and are less responsive to tilt angle changes, while during an $A < 0$ cycle the ratios have an "m" shape, changing rapidly with tilt angle. It is also evident that changes in the ratios become larger with decreasing rigidity. The shaded region gives an approximate

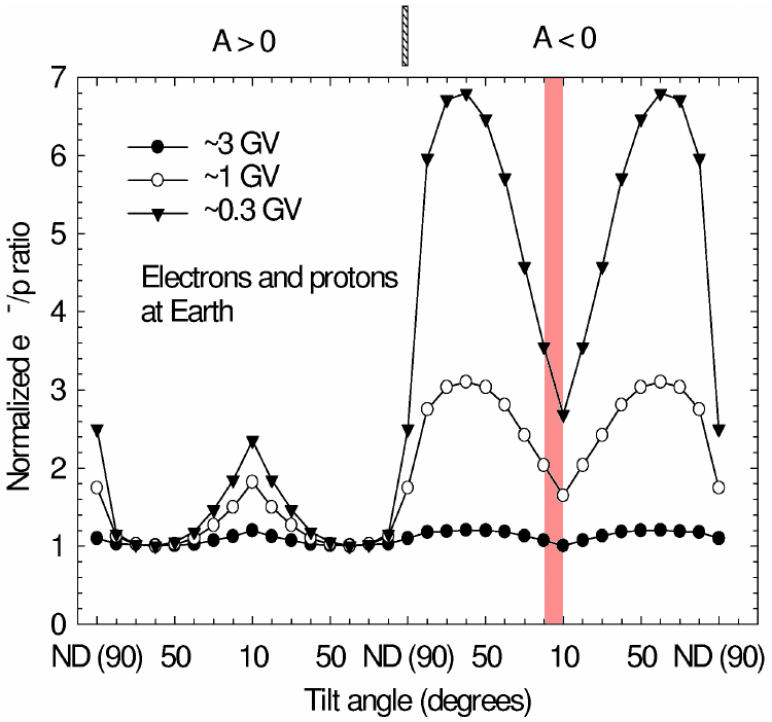

Figure 7.5: Tilt angle and solar polarity-sign dependence of the e^-/p ratio at Earth for rigidities of $\sim 3\,GV$, $\sim 1\,GV$ and $\sim 0.3\,GV$, as indicated by the legend. The shaded region is analogous of the time period between 2006b and 2009b. Figure taken from *Burger and Potgieter* (1999). See also *Potgieter et al.* (2001a).

indication of where the solar minimum period between 2006 and 2009 would fit. By comparison, the measured and computed e^-/p ratios from Figures 7.3 and 7.4 show the same qualitative features.

See also e.g. *Potgieter et al.* (2001a) for an in depth theoretical study of CR modulation and the various modulation mechanisms, in particular drifts, during solar minimum and solar maximum conditions, as well as *Heber et al.* (2009) for a study on the modulation of simultaneously observed GCR protons and electrons during the solar minimum of cycle 23/24. Long-term studies of the e^-/p ratios were also made by e.g. *Ferreira et al.* (2003), *Heber et al.* (2003) and *Ndiitwani et al.* (2005).

7.3.3 Rigidity Dependence of the e^-/p Ratios

Figure 7.6 gives a complete picture of the rigidity dependence of the e^-/p ratio for the "b" semesters from 2006 to 2009. Below $\sim 20\,GV$ both the modulated and LIS ratios deviate from a constant slope to form a slight bulge between $\sim 2\,GV$ and $\sim 20\,GV$, as a result of the region of enhanced LIS intensities over the same rigidity range (see Equation 5.1). For all semesters, the ratio of modulated spectra are very similar to the LIS ratio down to rigidities between $\sim 1\,GV$ and $\sim 2\,GV$. At lower rigidities the modulated ratios measured by PAMELA begin to fall below the LIS ratios. Overall, the

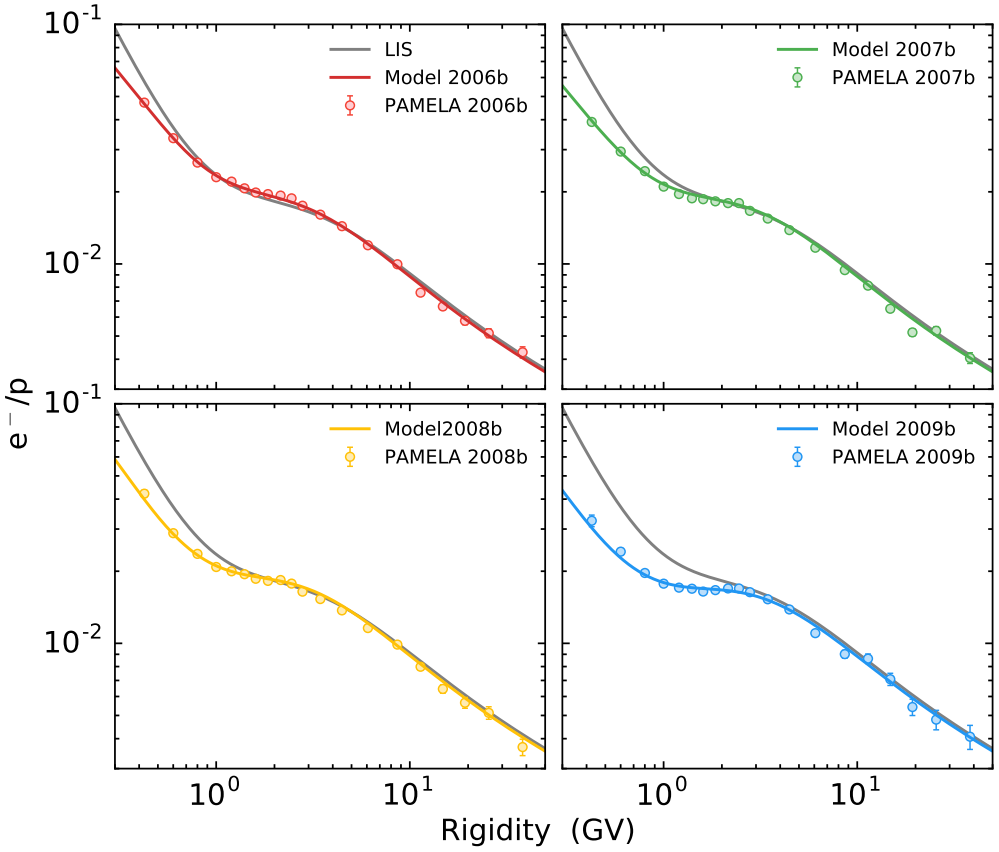

Figure 7.6: The e^-/p ratios as a function of rigidity for the 2006 to 2009 "b" semesters. Computed and measured ratios are represented by the coloured lines and symbols, respectively. The LIS ratio is given by the grey line.

computed ratios give a good representation of the measured ratios in terms of absolute value and shape.

Figure 7.7 is similar to Figure 7.6, but only shows the computed and LIS ratios over a wider rigidity range. Below $\sim$ 50 MV the e^-/p ratio, for both the modulated and LIS spectra, increase above unity, which means that electron intensity exceeds the proton intensity at these rigidities. The opposite is true for rigidities above $\sim$ 50 MV. Modulated proton spectra take on the characteristic adiabatic slope below $\sim$ 1 GV, while modulated electrons take on the same slope as the very LIS. This causes the modulated e^-/p ratio to have a constant slope below $\sim$ 100 MV that is steeper than the slope of the LIS ratio.

The modulated ratio for semester 2006b is the lowest of all the modulated ratios below $\sim$ 100 MV, which indicates that electron intensities increased relatively more than that of protons during the consecutive semesters. This is because the electron DCs are independent of rigidity, so that diffusion dominates electron intensities at these low rigidities while the proton intensities are dominated by adiabatic energy losses. As drifts come into play above $\sim$ 100 MV, the 2006b ratio becomes the highest of the modulated ratios, indicating that proton intensities increased more than electrons over time, which

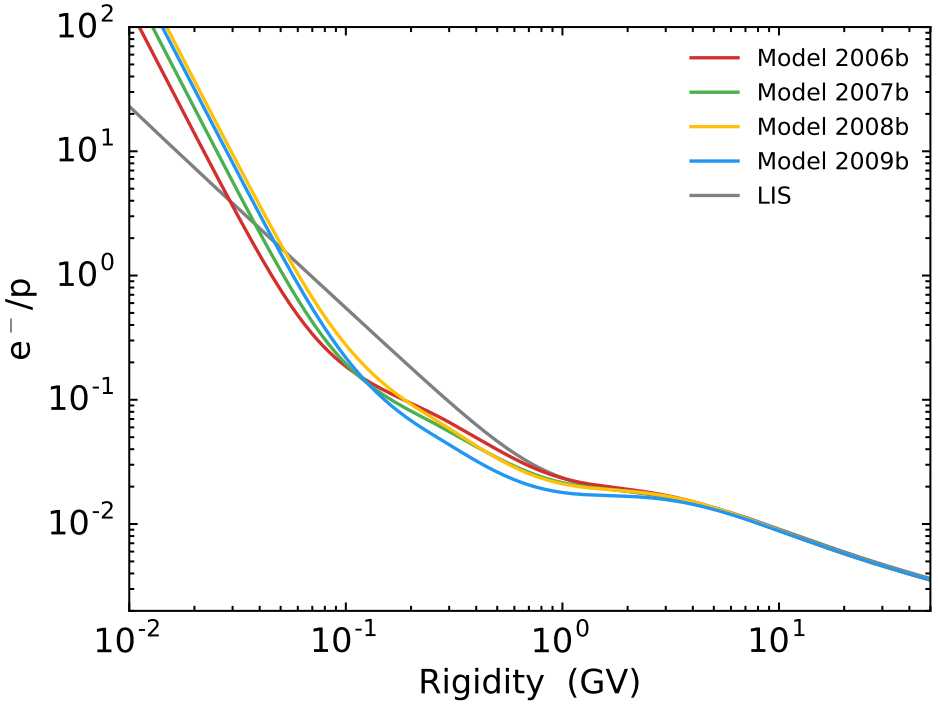

Figure 7.7: Similar to Figure 7.6, but combining only the computed e^-/p ratios into a single plot and over a wider rigidity range from 10 MV to 50 GV.

is in line with predictions from drift theory (*Ferreira and Potgieter*, 2004; *Potgieter*, 2014a).

Langner and Potgieter (2004) and *Potgieter and Langner* (2004) also studied the charge-sign dependence of electron and proton modulation. The focus of their study was on the effects that the TS has on the modulation of CRs. These authors used a 2D drift model with diffusive shock acceleration and assumed the proton LIS from *Moskalenko et al.* (2001) and the electron LIS from *Langner et al.* (2001). See *Langner et al.* (2004) for a detailed description of the modulation model and parameters. Figure 7.8 shows the proton (left) and electron (right) energy spectra from their modelling, respectively, calculated for an $A < 0$ polarity cycle during solar minimum conditions ($\alpha = 10°$). These LISs and the modulated spectra at Earth were used to calculate corresponding e^-/p ratios, shown as function of rigidity in Figure 7.9. The LIS ratio from this figure (solid line) has some quantitative differences when compared to the one in Figure 7.7, due to the recent improvements that have been made to the proton and electron LISs. At 100 MV, the LIS ratio from this study is a factor of ~ 0.5, while the LIS ratio from Figure 7.9 is a factor of ~ 2. Above ~ 2 GV, the latter ratio flattens off and begins to increase, suggesting a stronger rigidity dependence for the proton LIS compared to that of electrons. In Figure 7.7, the rigidity dependence of the LIS ratio weakens between 1 GV and 4 GV, but continues to increase. Quantitative differences in the $A < 0$ modulated energy spectra and e^-/p ratios can be ascribed to the addition

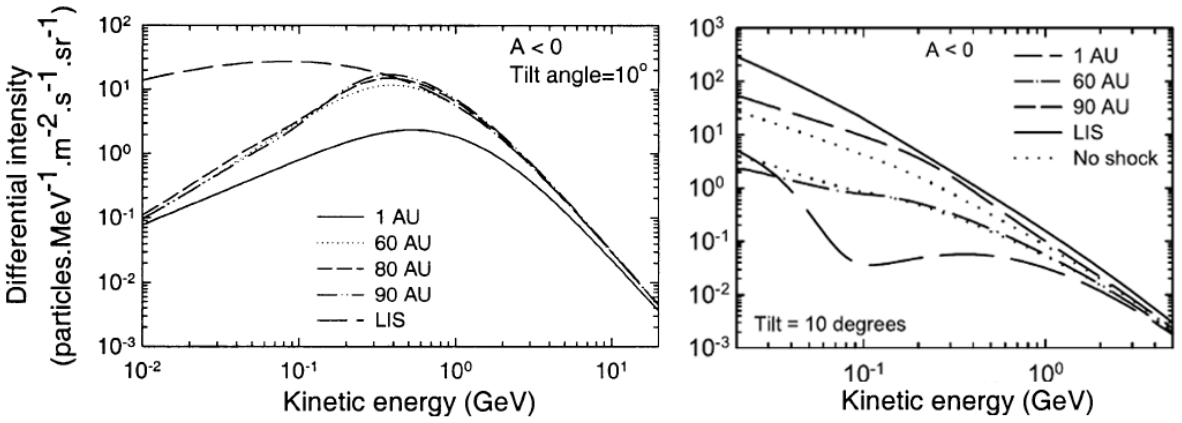

Figure 7.8: Computed proton (left) and electron (right) energy spectra from *Langner and Potgieter* (2004) and *Potgieter and Langner* (2004), respectively, for an $A < 0$ polarity cycle, at radial distances of 1 AU, 60 AU, 80 AU and 90 AU as shown by the legend. These spectra were calculated for a tilt angle of 10°. The LISs were taken at 120 AU and are given by the dashed line for protons, and the solid line for electrons. Solutions without shock acceleration are given by the dotted lines for electrons in the panel on the right.

of shock acceleration in the model used by *Potgieter and Langner* (2004), which has a large effect on electrons between 100 MeV and 1 GeV.

Important qualitative similarities exist between the results from this study and that of *Potgieter and Langner* (2004). For example, from Figure 7.8, protons experience large adiabatic energy losses at low energies, while electrons do not, resulting in an increasing e^-/p ratio toward lower rigidities where electron intensities begin to exceed proton intensities below ~ 100 MV. Electron modulation becomes progressively independent of

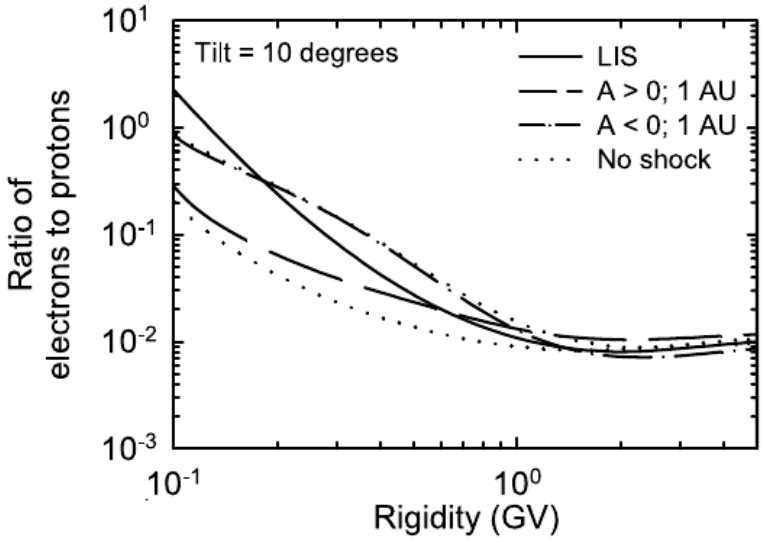

Figure 7.9: The e^-/p intensity ratios from *Potgieter and Langner* (2004) as a function of rigidity at 1 AU for solar minimum conditions ($\alpha = 10°$). The dashed and dashed-dotted lines represent the $A > 0$ and $A < 0$ polarity cycles, respectively, where the dotted line gives the no-shock solutions. As a reference, the LIS ratio (at 120 AU) is given by the solid line.

drifts with decreasing rigidity, which explains why the $A > 0$ and $A < 0$ spectra in Figure 7.8 start to converge at lower rigidities.

7.4 Modulation of Electrons and Positrons

Having discussed the modulation of electrons and protons, and the consequent ratios of these particles, the investigation of charge-sign dependent modulation and drifts is continued by combining electrons and positrons. The advantage of this comparison over that of electrons and protons is that differences in diffusion can be eliminated, because electrons and positrons experience the exact same diffusion. Furthermore, since electrons and positrons only differ in the charge they carry and their respective LISs, differences in how these particles modulate indicate charge-sign dependent modulation and is a direct consequence of the gradient, curvature and current sheet drift mechanism behind this phenomenon. See also *Ferreira and Potgieter* (2004) for a long-term study of CR modulation in light of charge-sign dependent modulation and *Ndiitwani et al.* (2005) for a similar modelling study. Since electrons and positrons are relativistic particles, the energies considered here (in GeV) have almost identical corresponding rigidity values.

7.4.1 Intensity-Time Profiles

Positrons, similar to protons, drift inward into the heliosphere primarily through the equatorial regions during an $A < 0$ polarity cycle, encountering the wavy HCS along the way. Qualitatively similar results can therefore be expected than what were found for the previous comparison of electrons and protons.

Figure 7.10 is similar to Figure 7.2, but shows the time development of electrons (blue lines and symbols) and positrons (red lines and symbols) over the rigidity (or kinetic energy) ranges indicated by the legend in each panel, all taken relative to semester 2006b. This approach of using average values over rigidity ranges was used to minimize fluctuations in positron observations. Solid lines and filled circles give PAMELA measurements, while computed intensities are given by the dashed lines and open circles, all of which represent semesterly spectra from Figures 6.7, 6.8 and 7.1.

From the time profiles in Figure 7.10 it is evident that positrons increased relatively more than electrons. The largest relative increase observed by PAMELA was for the lowest rigidity range of 226 MV to 326 MV (where PAMELA positron measurements below 200 MV were excluded on the premise of still being under revision). Positrons in this rigidity range increased by a factor of ~ 3 between 2006b and 2009b, while electrons increased by a factor of ~ 2. As before, these relative increases diminish toward higher rigidities. For the 3.45 GV to 6.07 GV range, intensities of both electrons and positrons increased by less than 20 %. The total intensity increase from 2006b to

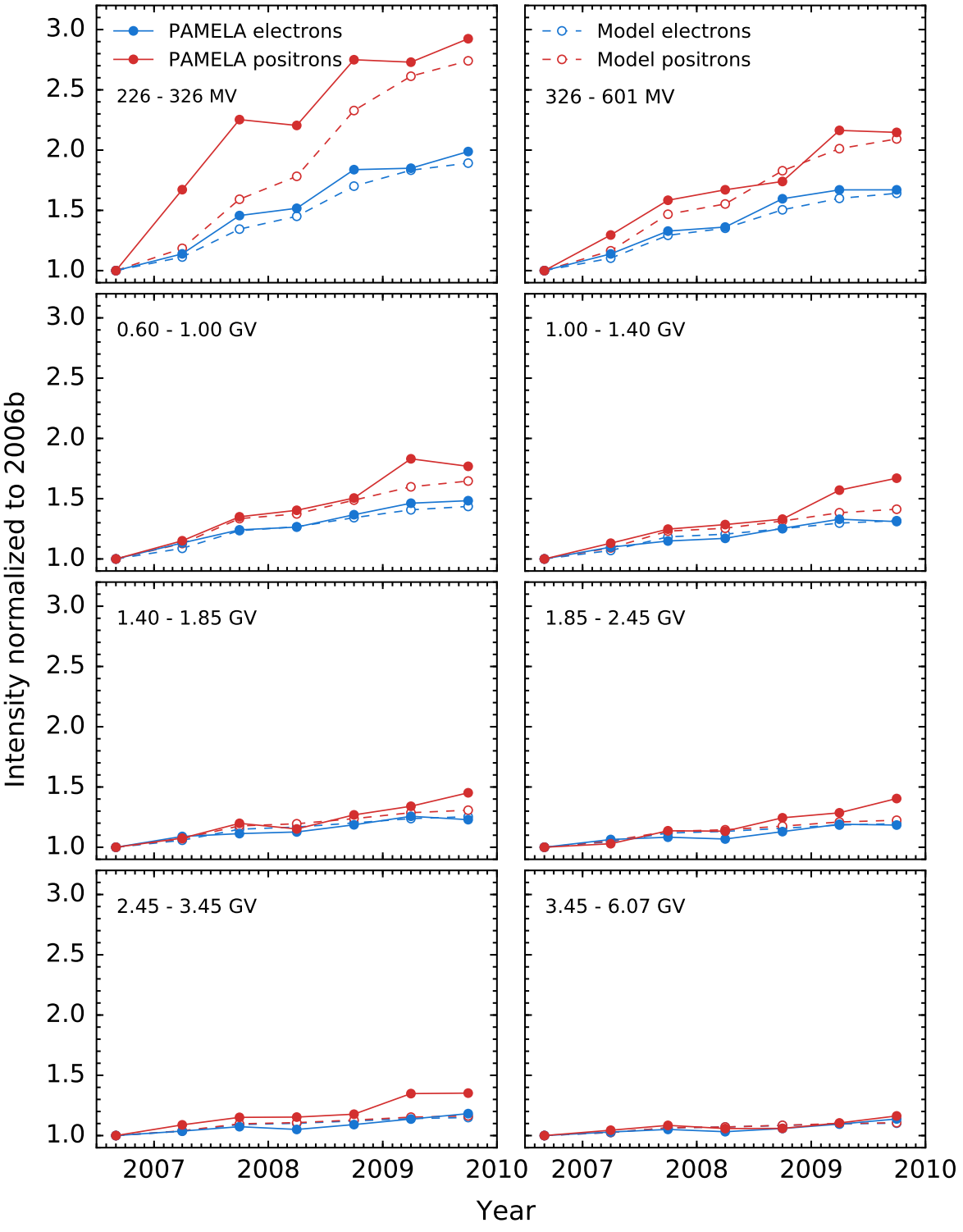

Figure 7.10: Normalized intensities of positrons (red) and electrons (blue) relative to semester 2006b over time. Average intensity values were calculated for various rigidity (or kinetic energy) ranges between 226 MV and 6.07 GV, as shown by the legend in each panel. PAMELA measurements are given by the solid circles and lines, while model results are given by the open symbols and dashed lines.

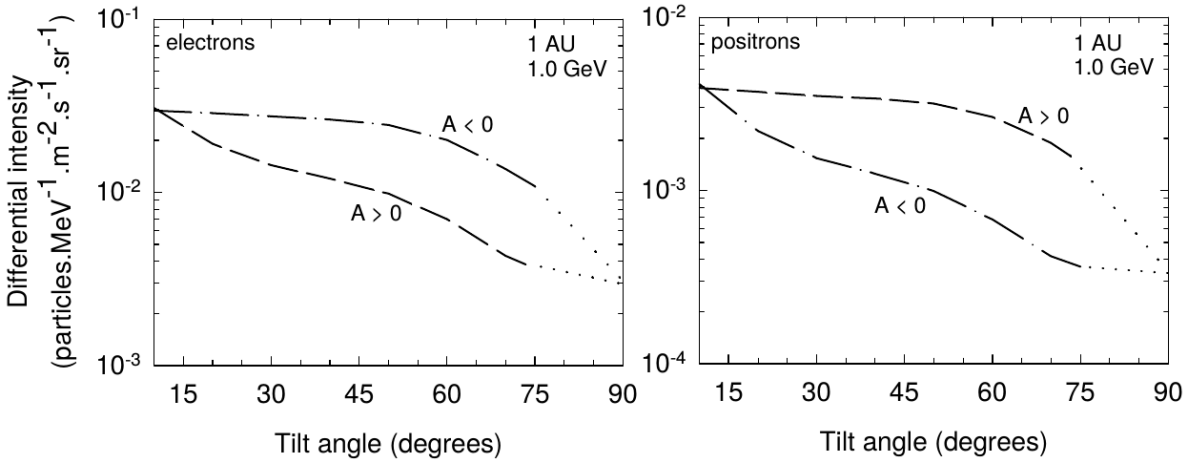

Figure 7.11: Differential intensities of 1 GeV electrons and positrons as a function of tilt angle at the Earth, for $A > 0$ (dashed) and $A < 0$ (dashed-dotted) solar polarity cycles. Figures taken from *Langner* (2004).

2009b are correctly reproduced by the model for each rigidity range. However, model solutions for positrons in the 226 MV to 326 MV range between semesters 2007a and 2008b is lower than what measurements indicate. Any attempt to reproduce these measurements would influence computed electron intensities.

Langner (2004) demonstrated the general trends of charge-sign dependent modulation as caused by drifts, by calculating the tilt angle dependence for electrons and positrons for both solar polarity cycles. The results are shown in Figure 7.11. The model used by this author predicts a gradual decrease with tilt angle for electrons during an $A > 0$ cycle, which is in contrast with earlier drift models that predicted an almost parabolic tilt angle dependence for electrons in an $A > 0$ cycle and a weak tilt angle dependence during an $A < 0$ cycle (e.g. *Burger and Potgieter*, 1989; *Potgieter and Burger*, 1990). Up to $\sim 50°$, electron intensities in Figure 7.11 remain almost constant before decreasing toward larger tilt angles. The reason why these results differ from earlier studies is because, in the model used by *Langner* (2004), drifts are reduced with increasing tilt angles, causing electron and positron intensities for both polarity cycles to converge as solar activity increases.

In terms of the time development of a solar cycle, the tilt angle dependence between 10° and 20° in Figure 7.11 is comparable to the 2006 to 2009 solar minimum time period considered in this study. Apart from the intensity being a factor of ~ 7.5 lower, the tilt angle dependence for positrons during an $A > 0$ (dashed line) and an $A < 0$ (dashed-dotted line) cycle is exactly opposite to that of electrons. These characteristic features of charge-sign dependent modulation are also evident in the results from this study, providing further support for the presence of drifts during the solar minimum of cycle 23/24. Although Figure 7.11 also shows the electron and positron intensities expected for very large tilt angles – which is typical of solar maximum periods – these conditions

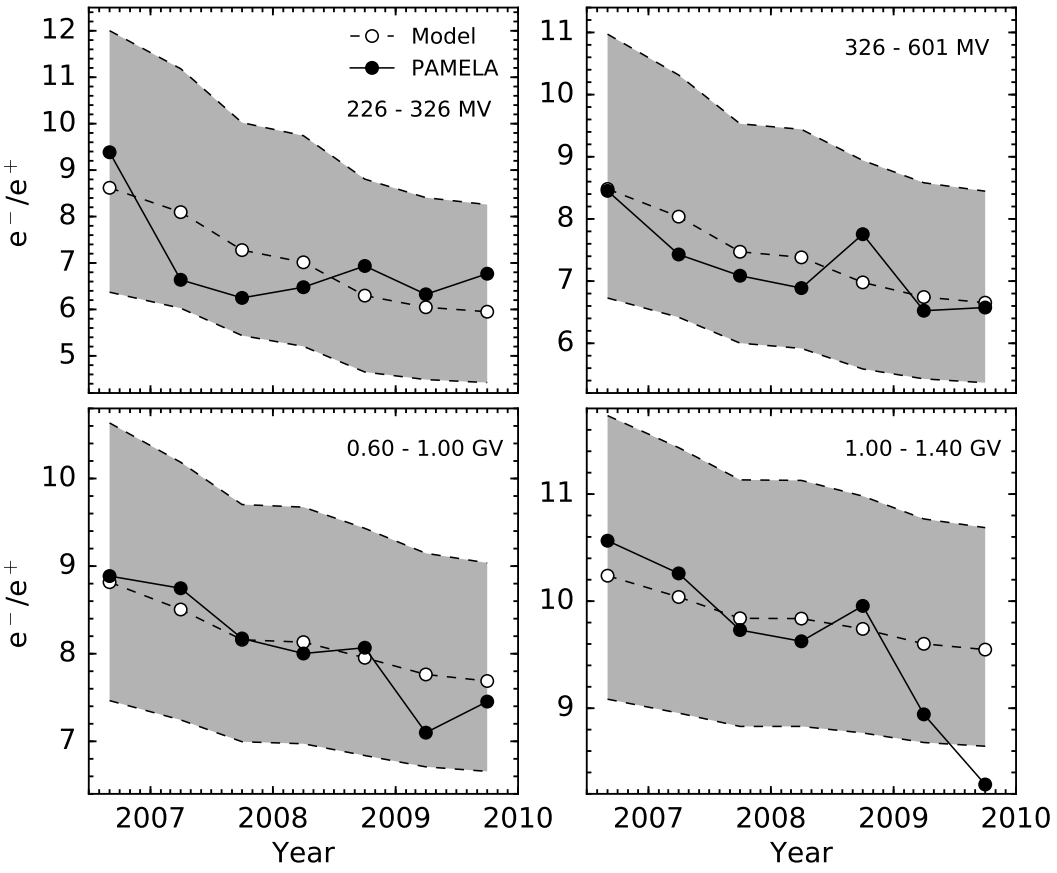

Figure 7.12: Electron to positron ratios at various rigidity ranges between 226 MV and 1.4 GV as a function of time. Ratios measured by PAMELA are given by the solid lines and filled circles, and computed ratios from the model are given by the dashed lines and open circles. The shaded bands represent the range of possible intensities obtainable by the model for a 10 % variation in diffusion.

are not considered here. See *Adriani et al.* (2016) for recently reported PAMELA e^-/e^+ observations from 2006 up to 2015.

7.4.2 e^-/e^+ Ratios Over Time

The effect of drifts can be further isolated by taking the ratio of electrons to positrons. Figure 7.12 shows how the e^-/e^+ ratios at various rigidity ranges between 226 MV and 1.4 GV developed as a function of time. The solid lines and filled circles represent PAMELA measurements, while the dashed lines and open circles represent computed intensities. The grey band represents the range of possible values obtainable when assuming a 10 % variation in the DCs (as illustrated for positrons in Chapter 6).

Even though the model does not precisely reproduce the time development of the measured e^-/e^+ ratios, the model describes the overall decreasing trend observed by PAMELA. In terms of the absolute value, the computed ratios are also in good agreement with observations. When a 10 % variation in diffusion is considered, the resulting grey

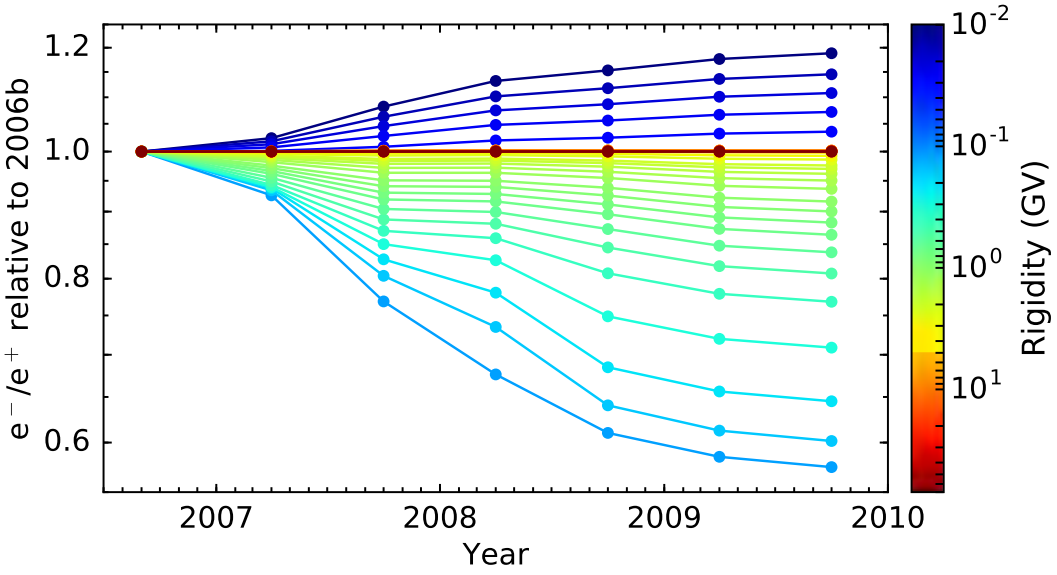

Figure 7.13: Computed e^-/e^+ ratios from the modulation model, as a function of time at different rigidities between 10 MV and 30 MV (dark-blue lines) and between 120 MV and 70 GV (light-blue to red lines), according to the colorbar. All ratios are normalized with respect to semester 2006b.

band is obtained which includes all of the measured ratios, except for the 2009b semester in the 1.0 GV to 1.4 GV range.

Since increasingly more positrons arrive at Earth during an $A < 0$ polarity cycle compared to electrons, a decrease in the e^-/e^+ ratios over time, as shown in Figure 7.12, is typically expected from drift theory. Even though PAMELA electron and positron measurements are available down to sufficiently low rigidities to observe these drift effects, the modulation model is able to provide predicted intensities down to much lower rigidities. This allows for an investigation of the behaviour of the e^-/e^+ ratio at rigidities where diffusion is expected to dominate, as well as at rigidities where drifts have a measureable influence.

Figure 7.13 shows the e^-/e^+ time development, normalized to 2006b, for two rigidity ranges. The dark-blue lines above unity show an increase in the ratio and represent electrons and positrons for rigidities between 10 MV and 30 MV. At the lowest rigidity of 10 MV, the ratio is expected to have increased by $\sim 20\,\%$, according to the model. It is at these rigidities (and lower) that electrons and positrons are less affected by drifts. The range of light-blue to red coloured lines below unity represent ratios over a rigidity range between 120 MV and 70 GV. Since these relative ratios are decreasing – by as much as $\sim 43\,\%$ at 120 MV – drifts are considered an important modulation process, with a maximum effect in the region of 120 MV. The e^-/e^+ ratio for rigidities between 30 MV and 120 MV are not shown in Figure 7.13, but also decrease from 2006b to 2009b.

Similar qualitative results were found by *Langner and Potgieter* (2004), *Potgieter and Langner* (2004) and *Langner* (2004), who also investigated the modulation of electrons

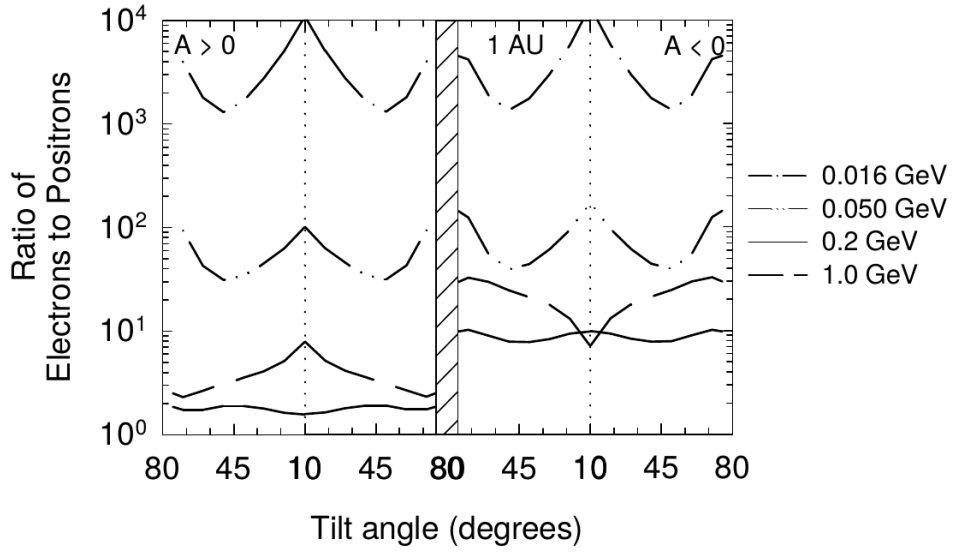

Figure 7.14: Tilt angle dependence of the e^-/e^+ ratios for an $A > 0$ (left) and an $A < 0$ (right) polarity cycle, at the position of Earth. The different linestyles correspond to the energies given by the legend. The tilt angles between $\sim 20°$ and $\sim 10°$ for the $A < 0$ cycle are representative of the solar minimum period between 2006 and 2009 considered in this study. Figure taken from *Langner* (2004).

and positrons. Figure 7.14 shows the tilt angle dependence for the e^-/e^+ ratios at Earth during $A > 0$ (left) and $A < 0$ (right) polarity cycles. Various energies between 16 MeV and 1.0 GeV are given by the different linestyles. In the right-hand panel, the intensity ratio at 1.0 GeV has a characteristic "V" shape around solar minimum (when α is small), which is indicative of drifts. This feature changes to an "Λ" shape for energies above ~ 500 MeV, as drifts fade out. Due to the absence of drifts, the shapes of the ratios for both polarity cycles at energies below ~ 100 MeV become approximately the same.

7.4.3 Rigidity Dependence of the e^-/e^+ Ratios

The e^-/e^+ ratios are shown as a function of rigidity in Figures 7.15 and 7.16. Computed ratios (coloured lines) are compared to ratios obtained from PAMELA (coloured symbols) in Figure 7.15, while Figure 7.16 shows all of the computed ratios over a wider rigidity range. The grey line represents the LIS ratio.

It follows from Figure 7.15 that the ratios of the modulated spectra start to deviate from the LIS ratio at about 2 GV, as indicated by measurements. Furthermore, from Figure 7.16, the modulated ratios of the various semesters also begin to diverge from each other around 2 GV, toward lower rigidities. With electrons and positrons experiencing the same diffusion, this indicates that drift effects become evident below ~ 2 GV. In general, the model ratios are in good agreement with measurements.

An important result from Figure 7.16, is that the ratios of the modulated spectra take on the same slope as the LIS ratio below ~ 20 MV. This happens because adiabatic

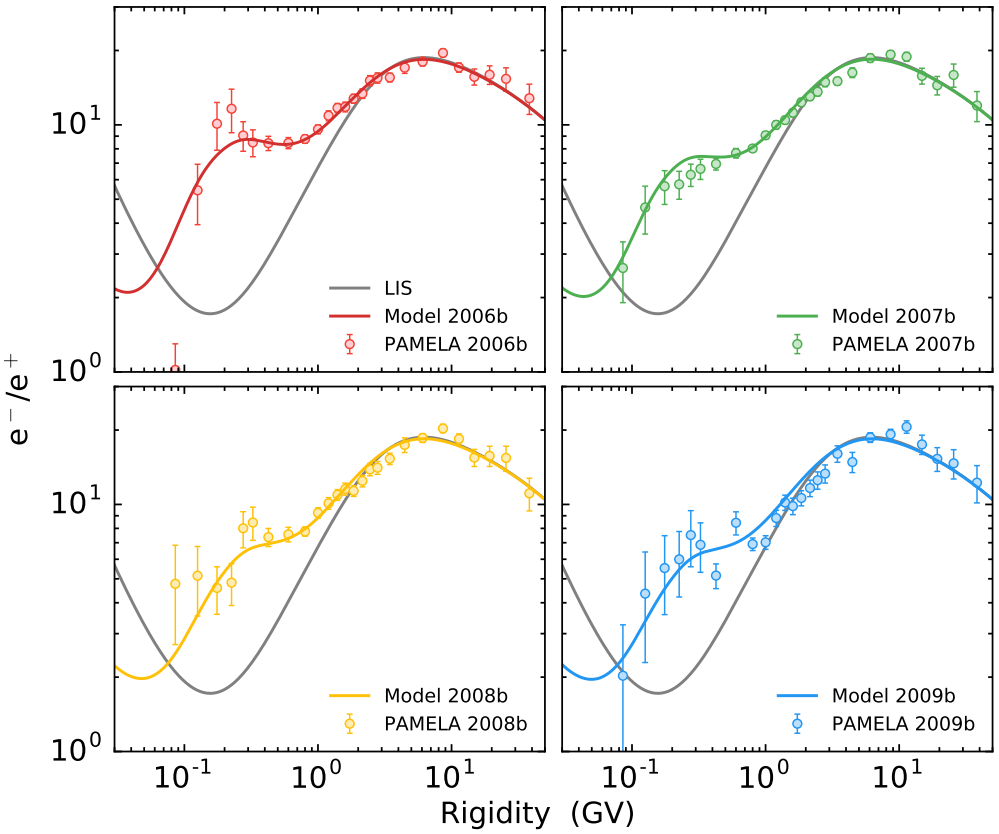

Figure 7.15: The e^-/e^+ ratios as a function of rigidity for the "b" semesters of each year from 2006 to 2009. Computed and measured ratios are represented by the coloured lines and symbols, respectively. The LIS ratio is given by the grey line.

energy losses are insignificant for both electrons and positrons at these rigidities and because the DCs become independent of rigidity. The ratios from the different semesters also converge at ~ 30 MV. It is therefore clear, from the spread in the coloured lines, that drifts play an evident role at rigidities between ~ 30 MV and ~ 2 GV. Since the LIS and modulated ratios in Figure 7.16 remain above unity, electron intensities exceed the positron intensities across all rigidities shown in Figure 7.16. At 150 MV the LIS has the lowest ratio of a factor 1.7, while the ratio at Earth reaches a minimum of ~ 2 between 35 MV and 50 MV. This is in contrast to the e^-/p ratios, where the proton intensities exceed the electron intensities above ~ 60 GV (see Figure 7.7).

Figure 7.17 shows the e^-/e^+ ratios calculated by *Potgieter and Langner* (2004) at Earth during $A > 0$ (dashed line) and $A < 0$ (dashed-dotted line) polarity cycles, with the LIS ratio and no-shock (i.e. without diffusive shock acceleration at the TS) solutions given by the solid and dotted lines, respectively. The LIS ratio is similar in shape than the one used in the current study (from Figure 7.16), however, in terms of absolute value the former is significantly higher than the latter. Modulated $A > 0$ and $A < 0$ ratios in Figure 7.17 follow the trends in the LIS ratio down to ~ 1 GeV before deviating from the LIS and from each other. As electron and positron modulation becomes progressively

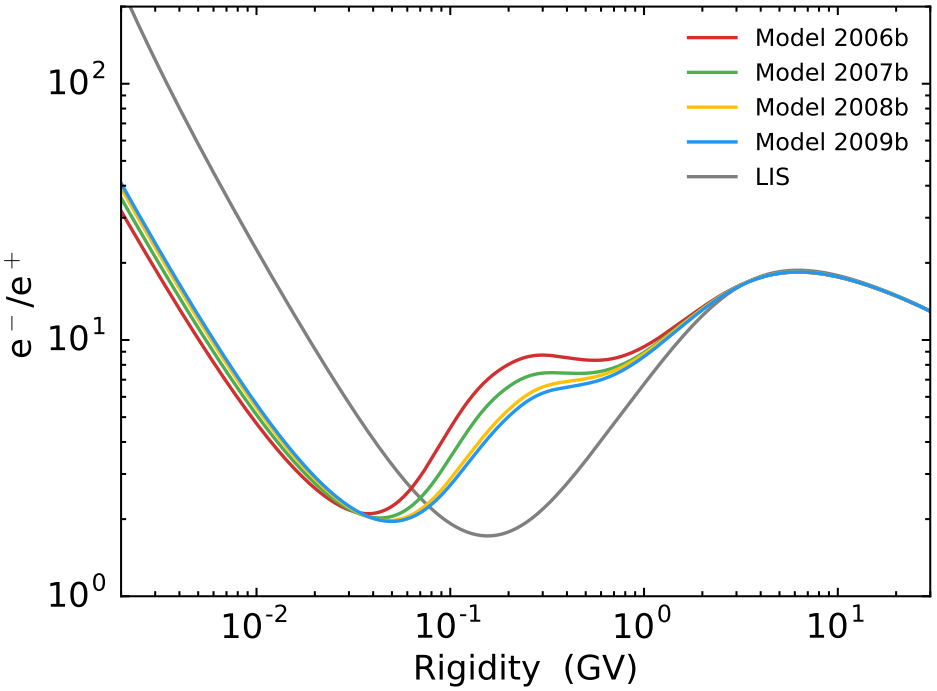

Figure 7.16: Similar to Figure 7.15, but combining only the computed e^-/e^+ ratios into a single plot and over a wider rigidity range from 2 MV up to 30 GV.

independent of drifts, the modulated ratios begin to converge from $\sim$ 70 MeV toward lower energies. This implies that drifts, due to the difference in the $A > 0$ and $A < 0$ spectra, are evident between $\sim$ 70 MeV and $\sim$ 1 GeV – similar to the rigidity range identified in Figure 7.16. As a result of the addition of a Jovian source by *Potgieter and Langner* (2004), the $A < 0$ modulated ratio remains above the LIS ratio and is much higher than the ratios from the current study where Jovain electrons are excluded. For a comprehensive modelling study of Jovian and galactic electron modulation, see *Nndanganeni* (2016).

Knowing that modulated electron and positron spectra at Earth take on the same shape and slope as their respective LISs below $\sim$ 40 MeV (e.g. *Potgieter et al.*, 2001b), the slope of the LIS ratio can be inferred using modulated spectra at these energies. With Voyager 1 electron measurements available below 40 MeV from beyond the HP, and measurements of the e^-/e^+ ratio available at Earth, the slope of the positron very LIS can be determined. Combining this result with interstellar CR propagation models will ultimately lead to a robust estimate of the positron very LIS.

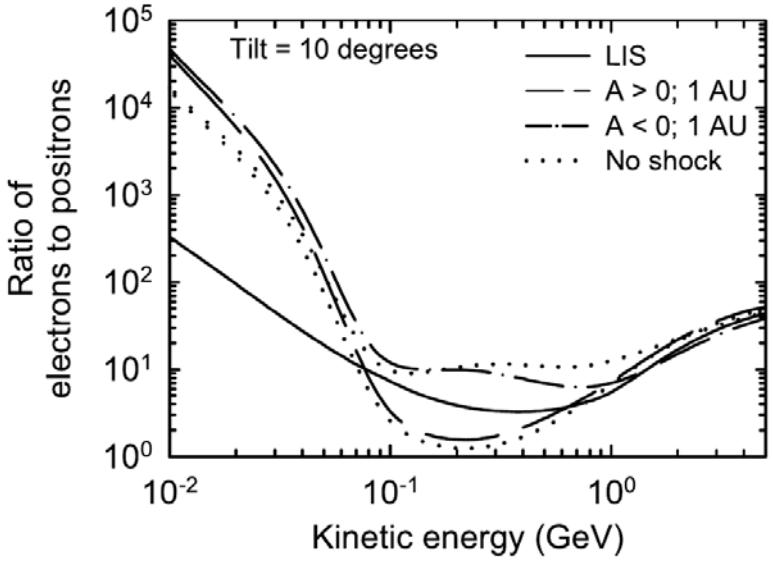

Figure 7.17: The computed e^-/e^+ intensity ratios from *Potgieter and Langner* (2004) as a function of kinetic energy (or rigidity) at the Earth (1 AU) for solar minimum conditions ($\alpha = 10°$). The dashed and dashed-dotted lines represent the $A > 0$ and $A < 0$ polarity cycles, respectively, with the dotted line showing the no-shock solutions (i.e. without diffusive shock acceleration at the TS). As a reference, the LIS ratio (at 120 AU) is given by the solid line.

7.5 An Overview of the Combined Modulation of Protons, Electrons and Positrons

In the previous sections, the charge-sign dependent nature of CR modulation was emphasized by comparing electron results to proton and positron results separately and at various rigidities. Figure 7.18 combines the time-profiles of PAMELA electron, proton and positron intensities relative to 2006b at various rigidities. This figure serves to emphasize that proton and positron intensities both increase relatively more than electron intensities at almost all rigidities. It also follows from Figure 7.18 that proton and positron intensities increase by almost equal amounts, by a factor of ~ 2 at 800 MV over a period of 3.5 years, while electrons increased by a factor of only 1.5.

Figure 7.19 gives a comprehensive summary of the measured (left panels) and computed (right panels) intensities for protons (top), electrons (middle) and positrons (bottom) between 2006b and 2009b. Low rigidities are represented by the blue coloured lines and symbols, while higher rigidities are represented by red coloured lines and symbols. At the lowest rigidity of ~ 600 MV, proton and positron intensities increased by factors of ~ 2.2 and ~ 1.8 respectively, while electrons only increased by a factor of ~ 1.5. A comparison of intensities at other rigidities will yield similar qualitative results.

In conclusion, it follows from the measurements of oppositely charged CRs that clear evidence of charge-sign dependent modulation were observed and subsequently confirmed through modelling. Even though the solar minimum of cycle 23/24 has been

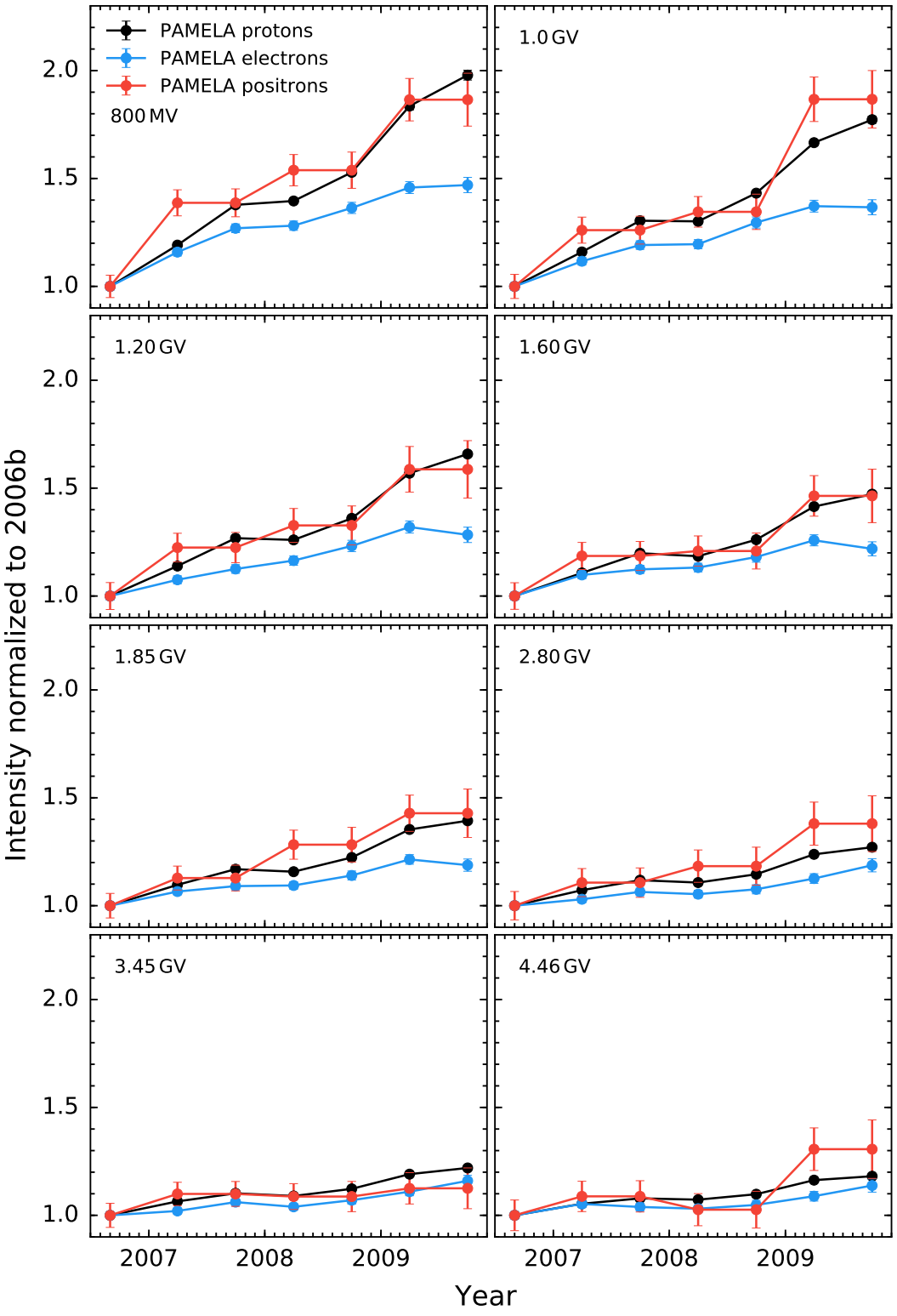

Figure 7.18: PAMELA measurements of protons (black), electrons (blue) and positrons (red), relative to 2006b, at different rigidities between 800 MV and 4.46 GV.

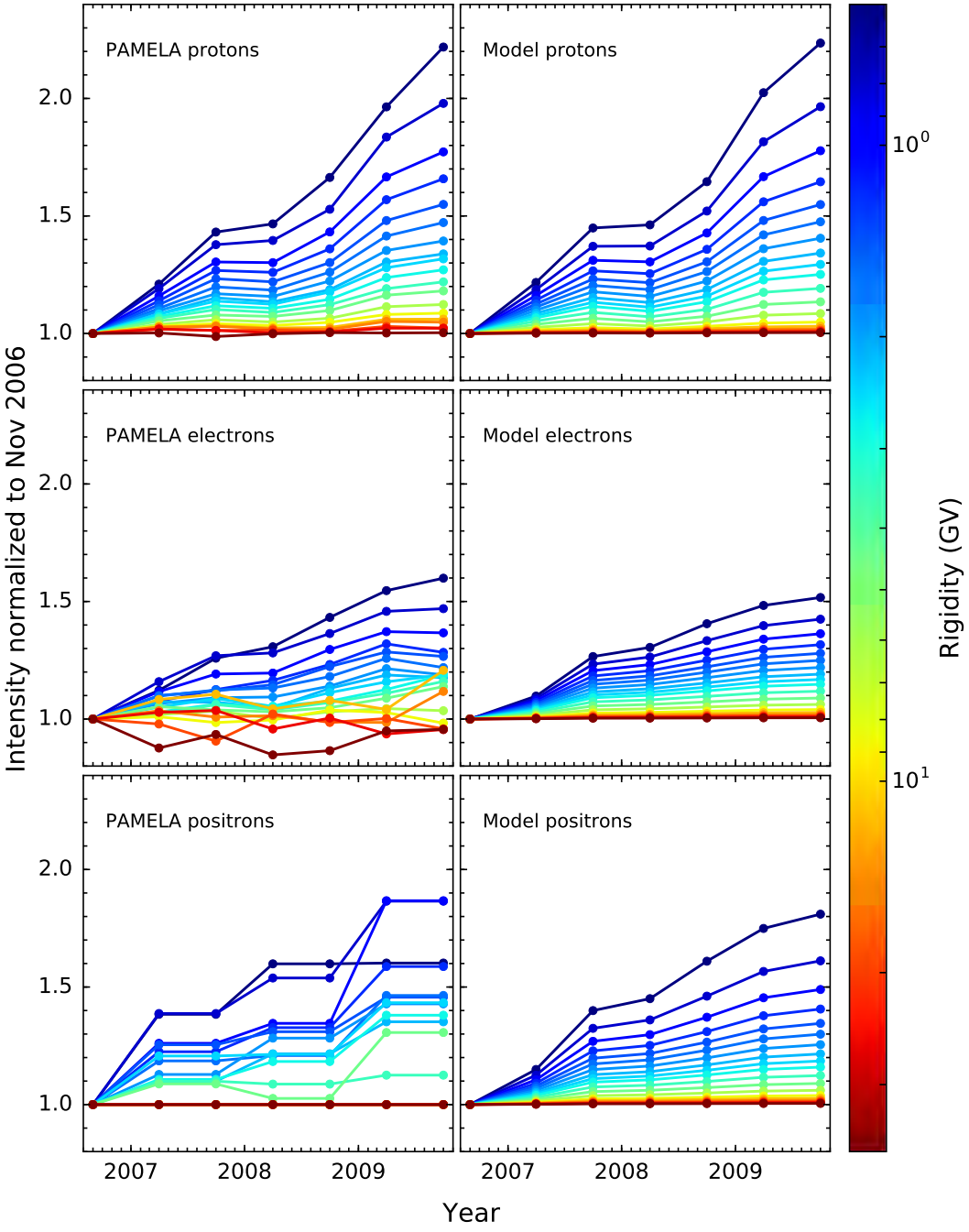

Figure 7.19: A summary of the intensity-time profiles, relative to 2006b, for PAMELA measurements (left panels) and computed model solutions (right panels). The top, middle and bottom panels represent protons, electrons and positrons, respectively. The intensities at different rigidity values are given by the coloured lines according to the colorbar.

described as more diffusion-dominated (e.g. *Potgieter et al.*, 2014a), drifts still played an important and measureable role. For more on the charge-sign dependence of CR modulation, see *Potgieter* (2014a). For detailed studies on the proton, electron and positron measurements taken by PAMELA during the solar minimum of cycle 23/24, see *Di Felice* (2010), *De Simone* (2011), *Munini* (2015), *Adriani et al.* (2016) and *Di Felice et al.* (2016).

7.6 Summary

In chapters 5 and 6, the modulation model was used to reproduce PAMELA electron and positron measurements at 6-monthly intervals, while proton measurements were reproduced at Carrington Rotation intervals in Chapter 4 (see *Potgieter et al.*, 2014a; *Vos and Potgieter*, 2015). In order to self-consistently compare electrons, protons and positrons, semesterly averaged proton spectra were calculated from PAMELA Carrington Rotation measurements and reproduced with the modulation model (Figure 7.1).

Section 7.3 focused on the modulation of electrons compared to protons. It follows from the intensity-time profiles in Figure 7.2 that proton intensities increased more than electrons between 2006b and 2009b at all energies. The largest increase observed by PAMELA was at 426 MV, where electrons increased by $\sim 60\,\%$ and protons increased by $\sim 140\,\%$. This behaviour of oppositely charged CRs, which is indicative of the charge-sign dependent modulation that occur during an $A < 0$ magnetic polarity cycle, can only be reproduced through modelling by including drifts.

To further quantify the difference in modulation between electrons and protons, the e^-/p ratios were calculated at selected rigidities and are shown as a function of time in Figure 7.3. These measured and computed ratios decreased over time, where larger decreases occured at rigidities below ~ 1.2 GV.

Using modelled spectra, it was possible to calculate e^-/p ratios at low rigidities where observations are unavailable. This is shown in Figure 7.4 as a function of time and in Figures 7.6 and 7.7 as a function of rigidity. For rigidities below ~ 100 MV, where diffusion dominates, the e^-/p ratio increased over time, while for rigidities above ~ 200 MV drifts become more evident, resulting in a decrease of the ratio. Similar results of the interplay between drifts and diffusion were modelled and illustrated by *Potgieter* (1996, 2000), *Potgieter and Langner* (2004) and *Langner and Potgieter* (2004).

Even though the comparison of electrons and protons showed clear charge-sign dependent modulation that stems from drifts, the diffusion experienced by these particles were different, which lead to a complicated interplay between drifts and diffusion. Fortunately, by comparing electrons with positrons, this indifference in diffusion can be eliminated, since both electrons and positrons undergo the same diffusion.

In Section 7.4, the modulation of electrons and positrons was discussed and compared. The intensity-time profiles of electrons and positrons, given in Figure 7.10 for various rigidity ranges are qualitatively similar to that of electrons and protons. Intensities of positrons, which mainly drift into the heliosphere in the equatorial regions and along the HCS, increased relatively more than electrons, which mainly drift towards the Earth over the polar regions. In the 226 MV to 326 MV rigidity range, positrons increased by $\sim 200\%$ relative to 2006b, while electrons increased by $\sim 100\,\%$. This difference in the intensity increase of electrons and positrons becomes smaller toward higher energies as drifts and modulation in general, decline.

The e^-/e^+ ratios are given as a function of time in Figure 7.12. It is shown in this figure that the model is able to reproduce the decreasing trend in the ratios as measured by PAMELA, but were unable to reproduce all of the short-term variations. However, when assuming a 10 % variance in the diffusion for positrons, almost all of the measured ratios could be contained within the resulting range of intensities.

The time-dependent changes of the computed ratios, relative to 2006b, are shown in Figure 7.13. These were extended to low energies where PAMELA measurements are unavailable. It was found that the e^-/e^+ ratios above $\sim$ 30 MV decreased by variable amounts, depending on rigidity, where the largest decrease of $\sim 43\,\%$ occurred at $\sim$ 120 MV. Below $\sim$ 30 MV, the ratios showed an increase as drifts began to fade out. The range over which drifts play an evident role was further highlighted in Figures 7.15 and 7.16, which gives the rigidity dependence of the e^-/e^+ ratios. The variation between the different ratios corresponding to different semesters in Figure 7.16, is an indication of drifts. Drifts were found to contribute significantly toward modulation in the rigidity range between $\sim$ 30 MV and $\sim$ 2 GV. A comprehensive summary of measured and modelled results were given in Figures 7.18 and 7.19.

Chapter 8

Summary

The heliospheric modulation of GCRs during the unusual solar minimum of cycle 23/24 formed the focus of this study, where the primary goal was to investigate the features and signatures of gradient, curvature and current sheet drifts. This was achieved by combining the numerical modelling of heliospheric modulation with *in situ* measurements from PAMELA, Ulysses, AMS-02 and the Voyager spacecraft. In particular, this study has set out to identify the effects of charge-sign dependent modulation in observations and to subsequently reproduce these effects through modelling. In what follows, a concise summary of each of the preceding chapters is given to highlight the important theory, results and possible conclusions that can be drawn from this study.

A brief introduction and layout of this work was given in **Chapter 1**, followed by a general framework of the various concepts and theory related to heliospheric physics and CR modulation in **Chapter 2**. This included brief discussions of CR populations, the structure of the heliosphere and the $\sim$ 11-year solar activity cycle. The SW, HMF and HCS were discussed in detail. Expressions for the radial and polar angle dependencies of the SW speed were given, as well as a expressions for the Parker HMF and the various HMF modifications. The Smith-Bieber modification was chosen for this study on the basis that it achieves the desired reduction in drifts by explicitly altering the HMF geometry over the polar regions. The role that drifts and the HCS play in producing the $\sim$ 22-year cycle seen in NM counts was explained and illustrated.

The numerical modulation model used in this study was discussed in **Chapter 3**, along with the Parker TPE, the ADI numerical scheme used in solving the TPE and the elements of the diffusion tensor. The TPE was shown to take into account all of the modulation processes, of which diffusion and drifts formed an important part of this chapter. The general expression for $\kappa_{\parallel}$ was given in Equation 3.30, from which it follows that $\kappa_{\parallel}$ has a B^{-1} spatial dependence and a double power law rigidity dependence. Key features of turbulence theory were incorporated in the diffusion approach followed here. It was also assumed that drifts are suppressed at low rigidities through scattering caused

by turbulence. Drifts were consequently scaled down below 0.55 GV with respect to the weak-scattering limit.

The basic concept of GPU computing with the CUDA API was also discussed. This parallel computing technology was implemented in the model to perform time-intensive calculations, which resulted in significant improvements in runtime performance.

In **Chapter 4** the model was used to reproduce seven proton energy spectra from PAMELA taken between July 2006 and December 2009 (*Adriani et al.*, 2013a; *Potgieter et al.*, 2014a; *Vos and Potgieter*, 2015). In doing so, a new proton very LIS was constructed by combining PAMELA measurements at Earth and Voyager 1 measurements beyond the HP. This newly constructed LIS has a spectral index of −2.78 at 100 GeV, which changes to a nearly flat index of 0.07 at 10 MeV and is regarded as the most reliable proton LIS constructed yet.

In order to reproduce the PAMELA 2006e spectrum, a rigidity dependence of $P^{0.91}$ was required for the DCs below ~ 4 GV, while for 2009e a $P^{0.8}$ dependence was needed. It therefore follows that proton MFPs below ~ 4 GV are expected to have increased from 2006e to 2009e, where larger increases occurred at lower rigidities. Since low-energy CRs are more responsive to changes in modulation conditions, this effect is in line with what is expected for the time between 2006 and 2009, which saw a significant decrease in modulation. PAMELA measurements also indicated a factor of ~ 3 increase in intensities at 100 MeV (~ 440 MV), compared to a factor increase of ~ 0.1 at 10 GeV.

As a result of the unusual low modulation conditions in 2009, the energy spectrum measured at the end of 2009 was shown to be the highest CR spectrum ever measured at Earth and it is possible that intensities for the next $A > 0$ minimum (around 2020) might even be higher. The reproduced PAMELA proton spectra serve to prove that the assumptions that were made for diffusion and drifts are robust and reliable.

Following the analysis of *Gieseler and Heber* (2016), PAMELA spectra were combined with Ulysses KET measurements in order to calculate the global radial and latitudinal proton gradients in the inner heliosphere for the time between mid-2006 and mid-2009. Small negative latitudinal gradients were found, which is in agreement with what drift theory predicts for positively charged particles during an $A < 0$ polarity cycle; for 1.63 GV protons, $G_\theta = (-0.05 \pm 0.01)\,\%/^\circ$ and $G_r = (2.87 \pm 0.51)\,\%/\mathrm{AU}$. These observed gradients were reproduced with the model, all of which give concrete evidence that drifts played a measureable role during the 2009 solar minimum period (*Vos and Potgieter*, 2016). The modulation model used here also improves on the large latitudinal gradients produced by earlier drift dominated models.

In **Chapter 5** the model was applied to electron modulation. Seven semesterly averaged PAMELA electron spectra, observed between mid-2006 and the end of 2009, were reproduced through modelling (*Potgieter et al.*, 2015; *Adriani et al.*, 2015b). A new very LIS for electrons was constructed using measurements from PAMELA and

Voyager 1. Below the LIS break (at $\sim 700\,\mathrm{MeV}$), the $E^{-1.35}$ GALPROP spectrum from *Bisschoff and Potgieter* (2014) was used, which corresponds to Voyager 1 measurements derived from GEANT 4 response functions. It was also shown with the model that, for energies above $\sim 1\,\mathrm{GV}$, the electron LIS does not maintain a constant spectral index.

PAMELA measurements showed that electron intensities at $\sim 80\,\mathrm{MeV}$ (or MV) increased by a factor of ~ 3.5 as the electron spectrum softened from semester 2006b to semester 2009b, while smaller relative increases were observed at higher energies. Since electrons are not affected by large adiabatic deceleration from the SW, the power law index of the modulated electron spectra at Earth are expected to be similar to that of the LIS below $\sim 50\,\mathrm{MeV}$. All of these features were correctly reproduced with the model. This study was extended by considering simultaneously observed electrons and positrons.

The modulation of simultaneously observed positrons and electrons were investigated in **Chapter 6**. Since electrons and positrons undergo the same diffusion, the combination of these simultaneous measurements facilitate a comprehensive study of drifts and charge-sign dependent modulation (e.g. *Adriani et al.*, 2016). The aim of this chapter was to reproduce preliminary semesterly averaged positron energy spectra measured by PAMELA between semesters 2006b and 2009b, while also reproducing the PAMELA electron spectra from Chapter 5 with the same set of DCs.

Using GALPROP spectra, as well as PAMELA and AMS-02 measurements, a new positron very LIS was constructed, where the peculiar positron excess above $\sim 10\,\mathrm{GeV}$ was accounted for. The DCs obtained from the model in Chapter 5 were applied to positrons but yielded unsatisfactory modulation, prompting a revision of these coefficients that take into account the simultaneous measurements of both electrons and positrons. The MFPs of the new set of DCs were found to be independent of rigidity below $\sim 400\,\mathrm{MeV}$, with $\lambda_{\perp} r$ and $\lambda_{\perp\theta}$ scaled by 2 % and 1 % of $\lambda_{\parallel}$, respectively. Above $\sim 400\,\mathrm{MeV}$, $\lambda_{\parallel} \propto P^{1.67}$, with $\lambda_{\perp r} \propto \lambda_{\perp\theta} \propto P^{1.33}$.

This modelling approach reproduced the seven simultaneously observed PAMELA electron and positron spectra from 2006b to 2009b, concluding that the DCs found from this approach are robust and reliable. Moreover, since the model was also able to reproduce energy spectra from both positive and negatively charged CRs – where each of these were drifting in opposite directions – it follows that the assumptions made with regard to drifts in this modelling approach are reasonable and capable of correctly simulating charge-sign dependent modulation. The drift-related assumptions made here include 100 % drift effects and the downscaling of drifts below $\sim 0.55\,\mathrm{GV}$ with respect to the weak-scattering limit.

The focus of **Chapter 7** was to uncover and highlight the effects of charge-sign dependent modulation in PAMELA observations (*Adriani et al.*, 2016; *Di Felice et al.*, 2016), as well as the computed model spectra. This was done by combining the proton,

electron and positron results from the previous chapters to perform a comparative study. For a self-consistent comparison, a new set of semesterly averaged proton spectra were calculated and reproduced with the model, so that all CR spectra used in this study represented $\sim$ 6-monthly averages at semesterly intervals.

A comparison of the intensity-time profiles of electrons and protons showed that the proton intensities increased more rapidly between semesters 2006b and 2009b than electrons did, indicating that increasingly more protons arrived at Earth toward the end of 2009 compared to electrons. At 426 MV, protons increased by a factor of $\sim$ 2.4, while electrons of the same rigidity increased by a factor of $\sim$ 1.6.

The comparison of electron and positron intensities yielded similar results – in the 226 MV to 326 MV range, positron intensities increased by a factor of $\sim$ 3 from 2006b to 2009b, while electron intensities increased by a factor of $\sim$ 2. All of these effects are characteristic features of charge-sign dependent modulation and confirms what drift theory predicts for oppositely charged particles during an $A < 0$ polarity cycle. By applying the above-mentioned diffusion and drift approaches, these features could be reproduced through modelling.

The e^-/p and e^-/e^+ ratios were investigated as a function of time and rigidity. Modelling showed that the e^-/p ratio increased over time for rigidities between 10 MV and 100 MV, contrary to drift predictions, but decreased for rigidities above 200 MV. This behaviour illustrates the complicated interplay between drifts and diffusion that exist for electrons and protons. Drifts were scaled down below $\sim$ 0.55 GV while diffusion remained rigidity independent, which allowed diffusion to dominate at these rigidities and thereby obscuring the effects of drifts. Above 200 MV, the effect of drifts became observable.

The e^-/e^+ ratios provide an even better handle on drifts, since these particles only differ in the charge they carry. For rigidities between 10 MV and 30 MV, the e^-/e^+ ratios increased over time, but decreased for rigidities above $\sim$ 30 MV. This result proves that measurable effects of charge-sign dependent modulation already occurred at rigidities as low as $\sim$ 30 MV, illustrating that drifts are important across a wide range of rigidities. Perhaps the most conclusive evidence of this was seen when the e^-/e^+ ratios were plotted as a function of rigidity. Drifts were found to contribute significantly toward CR modulation for rigidities between $\sim$ 30 MV and $\sim$ 1 GV, from 2006b to 2009b.

Considerations for future research include:

- Applying a time-dependent SDE-based modulation model to reproduce and investigate measurements from PAMELA and AMS-02 after 2009.
- Investigating the modulation of CR helium and antiprotons as part of a study of drifts.
- Calculating the global radial and latitudinal gradients in the inner heliosphere for electrons, using PAMELA and Ulysses electron measurements.

References

Accardo, L., et al., High statistics measurement of the positron fraction in primary cosmic rays of 0.5 – 500 GeV with the Alpha Magnetic Spectrometer on the International Space Station, *Physical Review Letters*, *113*, 121101, 2014.

Ackermann, M., et al., Measurement of separate cosmic-ray electron and positron spectra with the Fermi Large Area Telescope, *Physical Review Letters*, *108*, 011103, 2012.

Adriani, O., et al., New measurement of the antiproton-to-proton flux ratio up to 100 GeV in the cosmic radiation, *Physical Review Letters*, *102*, 05101, 2009a.

Adriani, O., et al., The PAMELA space mission, *Nuclear Physics B Proceedings Supplements*, *188*, 296–298, 2009b.

Adriani, O., et al., An anomalous positron abundance in cosmic rays with energies 1.5 – 100GeV, *Nature*, *458*, 607–609, 2009c.

Adriani, O., et al., A statistical procedure for the identification of positrons in the PAMELA experiment, *Astroparticle Physics*, *34*, 1–11, 2010.

Adriani, O., et al., PAMELA measurements of cosmic-ray proton and helium spectra, *Science*, *332*, 69–72, 2011a.

Adriani, O., et al., Cosmic-ray electron flux measured by the PAMELA experiment between 1 and 625 GeV, *Physical Review Letters*, *106*, 201101, 2011b.

Adriani, O., et al., Observations of the December 13 and 14, 2006, solar particle events in the 80 MeV/n – 3 GeV/n range from space with PAMELA detector, *Astrophysical Journal*, *742*, 102, 2011c.

Adriani, O., et al., Time dependence of the proton flux measured by PAMELA during the 2006 July – 2009 December solar minimum, *Astrophysical Journal*, *765*, 91, 2013a.

Adriani, O., et al., Cosmic-ray positron energy spectrum measured by PAMELA, *Physical Review Letters*, *111*, 081102, 2013b.

Adriani, O., et al., The PAMELA mission: Heralding a new era in precision cosmic ray physics, *Physics Reports*, *544*, 323–370, 2014.

Adriani, O., et al., PAMELA's measurements of magnetospheric effects on high energy solar particles, *Astrophysical Journal Letters*, *801*, L3, 2015a.

Adriani, O., et al., Time dependence of the e^- measured by PAMELA during the 2006 July – 2009 December solar minimum, *Astrophysical Journal*, *810*, 142, 2015b.

Adriani, O., et al., Time dependence of the electron and positron components of the cosmic radiation measured by the PAMELA experiment between July 2006 and December 2015, *Physical Review Letters*, *116*, 241105, 2016.

Aguilar, M., et al., First result from the Alpha Magnetic Spectrometer on the International Space Station: Precision measurement of the positron fraction in primary cosmic rays of

0.5 – 350 GeV, *Physical Review Letters*, *110*, 141102, 2013.

Aguilar, M., et al., Electron and positron fluxes in primary cosmic rays measured with the Alpha Magnetic Spectrometer on the International Space Station, *Physical Review Letters*, *113*, 121102, 2014a.

Aguilar, M., et al., Precision measurement of the (e^++e^-) flux in primary cosmic rays from 0.5 GeV to 1 TeV with the Alpha Magnetic Spectrometer on the International Space Station, *Physical Review Letters*, *113*, 221102, 2014b.

Aguilar, M., et al., Precision measurement of the proton flux in primary cosmic rays from rigidity 1 GV to 1.8 TV with the Alpha Magnetic Spectrometer on the International Space Station, *Physical Review Letters*, *114*, 171103, 2015.

Alcaraz, J., et al., Protons in near Earth orbit, *Physics Letters B*, *472*, 215–226, 2000a.

Alcaraz, J., et al., Leptons in near Earth orbit, *Physics Letters B*, *484*, 10–22, 2000b.

Alfven, H., Electric currents in cosmic plasmas, *Reviews of Geophysics and Space Physics*, *15*, 271–284, 1977.

Ashbourn, J. M. A., and L. C. Woods, Accelerating the solar wind, *Astrophysical Journal*, *623*, 511–518, 2005.

Atoyan, A. M., F. A. Aharonian, and H. J. Völk, Electrons and positrons in the galactic cosmic rays, *Physical Review D*, *52*, 3265–3275, 1995.

Babcock, H. W., The topology of the Sun's magnetic field and the 22-year cycle, *Astrophysical Journal*, *133*, 572–587, 1961.

Balogh, A., E. J. Smith, B. T. Tsurutani, D. J. Southwood, R. J. Forsyth, and T. S. Horbury, The heliospheric magnetic field over the south polar region of the Sun, *Science*, *268*, 1007–1010, 1995.

Balogh, A. B., L. J. Lanzerotti, and S. T. Suess (Eds.), The heliosphere through the solar activity cycle, Springer-Praxis, Chichester, UK, 2008.

Bartusiak, M., Sounds of the Sun, *American Scientist*, *82*, 61–68, 1994.

Behannon, K. W., M. H. Acuna, L. F. Burlaga, R. P. Lepping, N. F. Ness, and F. M. Neubauer, Magnetic field experiment for Voyagers 1 and 2, *Space Science Reviews*, *21*, 235–257, 1977.

Bieber, J. W., and W. H. Matthaeus, Cosmic ray pitch angle scattering in dynamical magnetic turbulence, in *Proceedings of the International Cosmic Ray Conference, 3,* 248-251, 1991.

Bieber, J. W., W. H. Matthaeus, C. W. Smith, W. Wanner, M. B. Kallenrode, and G. Wibberenz, Proton and electron mean free paths: The Palmer consensus revisited, *Astrophysical Journal*, *420*, 294–306, 1994.

Bieber, J. W., W. H. Matthaeus, A. Shalchi, and G. Qin, Nonlinear guiding center theory of perpendicular diffusion: General properties and comparison with observation, *Geophysical Research Letters*, *31*, L10805, 2004.

Biermann, L., The solar wind and the interplanetary media, in *Space Astrophysics*, edited by Liller, W., McGraw-Hill, New York, USA, 1961.

Bisschoff, D., and M. S. Potgieter, Implications of Voyager 1 observations beyond the heliopause for the local interstellar electron spectrum, *Astrophysical Journal*, *794*, 166, 2014.

Bisschoff, D., and M. S. Potgieter, New local interstellar spectra for protons, helium and carbon derived from PAMELA and Voyager 1 observations, *Astrophysics and Space Science*, *361*, 48, 2016.

Boezio, M., et al., The cosmic-ray electron and positron spectra measured at 1 AU during solar minimum activity, *Astrophysical Journal*, *532*, 653–669, 2000.

Boezio, M., et al., PAMELA and indirect dark matter searches, *New Journal of Physics*, *11*, 105023, 2009.

Bridge, H. S., J. W. Belcher, R. J. Butler, A. J. Lazarus, A. M. Mavretic, J. D. Sullivan, G. L. Siscoe, and V. M. Vasyliunas, The plasma experiment on the 1977 Voyager mission, *Space Science Reviews*, *21*, 259–287, 1977.

Burger, R. A., On the theory and application of drift motion of charged particles in inhomogeneous magnetic fields, Ph.D. thesis, Potchefstroom University for CHE, South Africa, 1987.

Burger, R. A., and M. Hattingh, Effect of Fisk-type heliospheric magnetic fields on the latitudinal transport of cosmic rays, in *Proceedings of the International Cosmic Ray Conference, 9,* 3698-3701, 2001.

Burger, R. A., and M. Hitge, The effect of a Fisk-type heliospheric magnetic field on cosmic-ray modulation, *Astrophysical Journal Letters*, *617*, L73–L76, 2004.

Burger, R. A., and M. S. Potgieter, The calculation of neutral sheet drift in two-dimensional cosmic-ray modulation models, *Astrophysical Journal*, *339*, 501–511, 1989.

Burger, R. A., and M. S. Potgieter, The effect of large heliospheric current sheet tilt angles in numerical modulation models: A theoretical assessment, in *Proceedings of the International Cosmic Ray Conference, 7,* 13-16, 1999.

Burger, R. A., and D. J. Visser, Reduction of drift effects due to solar wind turbulence, *Astrophysical Journal*, *725*, 1366–1372, 2010.

Burger, R. A., H. Moraal, and G. M. Webb, Drift theory of charged particles in electric and magnetic fields, *Astrophysics and Space Science*, *116*, 107–129, 1985.

Burger, R. A., M. S. Potgieter, and B. Heber, Rigidity dependence of cosmic ray proton latitudinal gradients measured by the Ulysses spacecraft: Implications for the diffusion tensor, *Journal of Geophysical Research*, *105*, 27447–27456, 2000.

Burger, R. A., T. P. J. Krüger, M. Hitge, and N. E. Engelbrecht, A Fisk-Parker hybrid heliospheric magnetic field with a solar-cycle dependence, *Astrophysical Journal*, *674*, 511–519, 2008.

Burlaga, L. F., N. F. Ness, and E. C. Stone, Magnetic field observations as Voyager 1 entered the heliosheath depletion region, *Science*, *341*, 147–150, 2013.

Büsching, I., and M. S. Potgieter, The variability of the proton cosmic ray flux on the Sun's way around the galactic center, *Advances in Space Research*, *42*, 504–509, 2008.

Büsching, I., O. C. de Jager, M. S. Potgieter, and C. Venter, A cosmic-ray positron anisotropy due to two middle-aged, nearby pulsars?, *Astrophysical Journal Letters*, *678*, L39–L42, 2008.

Caballero-Lopez, R. A., and H. Moraal, Limitations of the force field equation to describe cosmic ray modulation, *Journal of Geophysical Research (Space Physics)*, *109*, A01101, 2004.

Casolino, M., et al., Launch of the space experiment PAMELA, *Advances in Space Research*, *42*, 455–466, 2008.

Casolino, M., et al., The PAMELA experiment: A space-borne observatory for heliospheric phenomena, *Advances in Space Research*, *41*, 2043–2049, 2008b.

Chenette, D. L., T. F. Conlon, and J. A. Simpson, Burst of relativistic electrons from Jupiter observed in interplanetary space with the time variation of the planetary rotation period, *Journal of Geophysical Research*, *79*, 3551–3558, 1974.

Clem, J., P. Evenson, and B. Heber, Cosmic electron gradients in the inner heliosphere, *Geophysical Research Letters*, *29*, 11, 2002.

Cliver, E. W., Solar energetic particles: Acceleration and transport, in *Proceedings of the International Cosmic Ray Conference, 516,* 103-119, 2000.

Cranmer, S. R., Coronal Holes, *Living Reviews in Solar Physics*, *6*, 2009.

Cummings, A. C., E. C. Stone, and W. R. Webber, Latitudinal and radial gradients of anomalous and galactic cosmic rays in the outer heliosphere, *Geophysical Research Letters*, *14*, 174–177, 1987.

De Simone, N., Galactic and solar proton flux measurements in the energy range 80 MeV – 1.2 TeV with the PAMELA space experiment, Ph.D. thesis, University of Rome Tor Vergata, Italy, 2011.

De Simone, N., V. di Felice, J. Gieseler, M. Boezio, M. Casolino, P. Picozza, B. Heber, and the PAMELA Collaboration, Latitudinal and radial gradients of galactic cosmic ray protons in the inner heliosphere – PAMELA and Ulysses observations, *Astrophysics and Space Sciences Transactions*, *7*, 425–434, 2011.

Decker, R. B., S. M. Krimigis, E. C. Roelof, M. E. Hill, T. P. Armstrong, G. Gloeckler, D. C. Hamilton, and L. J. Lanzerotti, Voyager 1 in the foreshock, termination shock, and heliosheath, *Science*, *309*, 2020–2024, 2005.

Di Bernardo, G., C. Evoli, D. Gaggero, D. Grasso, and L. Maccione, Cosmic ray electrons, positrons and the synchrotron emission of the Galaxy: Consistent analysis and implications, *Journal of Cosmology and Astroparticle Physics*, *3*, 036, 2013.

Di Felice, V., Low energy electron and positron measurements in space with the PAMELA experiment, Ph.D. thesis, University of Rome Tor Vergata, Italy, 2010.

Di Felice, V., R. Munini, M. S. Potgieter, and E. E. Vos, New evidence for charge-sign dependent modulation during the solar minimum of 2006 to 2009, *Astrophysical Journal*, Submitted, 2016.

Douglas, J., On the numerical integration $\frac{\partial^2 u}{\partial x^2} + \frac{\partial^2 u}{\partial y^2} = \frac{\partial u}{\partial t}$ by implicit methods, *Journal of the Society for Industrial and Applied Mathematics*, *3*, 42–65, 1955.

Douglas, J., Alternating direction methods for three space variables, *Numerische Mathematik*, *4*, 41–63, 1962.

Dresing, N., C. M. S. Cohen, R. Gómez-Herrero, B. Heber, A. Klassen, R. A. Leske, G. M. Mason, R. A. Mewaldt, and T. T. von Rosenvinge, Approaching solar maximum 24 with STEREO – multipoint observations of solar energetic particle events, *Brazilian Journal of Physics*, *44*, 504–511, 2014.

Dunzlaff, P., A. Kopp, and B. Heber, Propagation of Jovian electron jets in heliospheric flux tube structures, *Journal of Geophysical Research (Space Physics)*, *115*, A10106, 2010.

Dunzlaff, P., R. D. Strauss, and M. S. Potgieter, Solving Parker's transport equation with stochastic differential equations on GPUs, *Computer Physics Communications*, *192*, 156–165, 2015.

DuVernois, M. A., et al., Cosmic-ray electrons and positrons from 1 to 100 GeV: Measurements with HEAT and their interpretation, *Astrophysical Journal*, *559*, 296–303, 2001.

Earl, J. A., The diffusive idealization of charged-particle transport in random magnetic fields, *Astrophysical Journal*, *193*, 231–242, 1974.

Effenberger, F., H. Fichtner, K. Scherer, S. Barra, J. Kleimann, and R. D. Strauss, A generalized diffusion tensor for fully anisotropic diffusion of energetic particles in the heliospheric magnetic field, *Astrophysical Journal*, *750*, 108, 2012.

Engelbrecht, N. E., On the heliospheric diffusion tensor and its effect on 26-day recurrent cosmic ray variations, Master's thesis, North-West University, South Africa, 2008.

Engelbrecht, N. E., On the development and applications of a three-dimensional *ab initio* cosmic-ray modulation model, Ph.D. thesis, North-West University, South Africa, 2013.

Engelbrecht, N. E., and R. A. Burger, An ab initio model for cosmic-ray modulation, *Astrophysical Journal*, *772*, 46, 2013.

Feldman, U., E. Landi, and N. A. Schwadron, On the sources of fast and slow solar wind, *Journal of Geophysical Research (Space Physics)*, *110*, A07109, 2005.

Ferreira, R., The heliospheric transport of galactic cosmic rays and jovian electrons, Ph.D. thesis, Potchefstroom University for CHE, South Africa, 2002.

Ferreira, S. E. S., A study of the modulation of cosmic ray electrons in the heliosphere, Master's thesis, Potchefstroom University for CHE, South Africa, 1998.

Ferreira, S. E. S., The transport of galactic and jovian cosmic ray electrons in the heliosphere, *Advances in Space Research*, *35*, 586–596, 2005.

Ferreira, S. E. S., and M. S. Potgieter, Long-term cosmic-ray modulation in the heliosphere, *Astrophysical Journal*, *603*, 744–752, 2004.

Ferreira, S. E. S., and K. Scherer, Time evolution of galactic and anomalous cosmic-ray spectra in a dynamic heliosphere, *Astrophysical Journal*, *642*, 1256–1266, 2006.

Ferreira, S. E. S., M. S. Potgieter, R. A. Burger, and B. Heber, Modulation effects of anisotropic perpendicular diffusion on cosmic ray electron intensities in the heliosphere, *Journal of Geophysical Research*, *105*, 18305–18314, 2000.

Ferreira, S. E. S., M. S. Potgieter, R. A. Burger, B. Heber, and H. Fichtner, Modulation of Jovian and galactic electrons in the heliosphere: 1. Latitudinal transport of a few MeV electrons, *Journal of Geophysical Research*, *106*, 24979–24988, 2001a.

Ferreira, S. E. S., M. S. Potgieter, R. A. Burger, B. Heber, H. Fichtner, and C. Lopate, Modulation of Jovian and galactic electrons in the heliosphere: 2. Radial transport of a few MeV electrons, *Journal of Geophysical Research*, *106*, 29313–29322, 2001b.

Ferreira, S. E. S., M. S. Potgieter, B. Heber, and H. Fichtner, Charge-sign dependent modulation in the heliosphere over a 22-year cycle, *Annales Geophysicae*, *21*, 1359–1366, 2003.

Fichtner, H., Anomalous cosmic rays: Messengers from the outer heliosphere, *Space Science Reviews*, *95*, 639–754, 2001.

Fichtner, H., M. Potgieter, S. Ferreira, and A. Burger, On the propagation of Jovian electrons in the heliosphere: Transport modelling in 4-D phase space, *Geophysical Research Letters*, *27*, 1611–1614, 2000.

Fichtner, H., M. S. Potgieter, S. E. S. Ferreira, B. Heber, and R. A. Burger, Time-dependent 3-D modelling of the heliospheric propagation of few-MeV electrons, in *Proceedings of the International Cosmic Ray Conference, 9,* 3666-3669, 2001.

Finkbeiner, D. P., L. Goodenough, T. R. Slatyer, M. Vogelsberger, and N. Weiner, Consistent scenarios for cosmic-ray excesses from Sommerfeld-enhanced dark matter annihilation, *Journal of Cosmology and Astroparticle Physics*, *5*, 002, 2011.

Fisk, L. A., Solar modulation of galactic cosmic rays 2, *Journal of Geophysical Research*, *76*, 221–226, 1971.

Fisk, L. A., Possible evidence for latitude-dependent cosmic-ray modulation, in *Proceedings of the International Cosmic Ray Conference, 3,* 905-909, 1975.

Fisk, L. A., Solar modulation of galactic cosmic rays. IV - Latitude-dependent modulation, *Journal of Geophysical Research*, *81*, 4646–4650, 1976.

Fisk, L. A., Motion of the footpoints of heliospheric magnetic field lines at the Sun: Implications for recurrent energetic particle events at high heliographic latitudes, *Journal of Geophysical Research*, *101*, 15547–15554, 1996.

Fisk, L. A., An overview of the transport of galactic and anomalous cosmic rays in the heliosphere: Theory, *Advances in Space Research*, *23*, 415–423, 1999.

Fisk, L. A., and G. Gloeckler, Acceleration of galactic cosmic rays in the interstellar medium, *Astrophysical Journal*, *744*, 127, 2012.

Fisk, L. A., and G. Gloeckler, On whether or not Voyager 1 has crossed the heliopause, *Astrophysical Journal*, *789*, 41, 2014.

Fisk, L. A., G. Gloeckler, and T. H. Zurbuchen, Acceleration of low-energy ions at the termination shock of the solar wind, *Astrophysical Journal*, *644*, 631–637, 2006.

Florinski, V., Pickup ion acceleration at the termination shock and in the heliosheath, *Space Science Reviews*, *143*, 111–124, 2009.

Florinski, V., and N. V. Pogorelov, Four-dimensional transport of galactic cosmic rays in the outer heliosphere and heliosheath, *Astrophysical Journal*, *701*, 642–651, 2009.

Florinski, V., G. P. Zank, and N. V. Pogorelov, Galactic cosmic ray transport in the global heliosphere, *Journal of Geophysical Research*, *108*, 1228, 2003.

Forbush, S. E., Three unusual cosmic-ray increases possibly due to charged particles from the Sun, *Physical Review*, *70*, 771–772, 1946.

Formato, V., Measurement of the nuclear and isotopic composition of galactic cosmic rays with the pamela experiment, Ph.D. thesis, University of Trieste, Italy, 2013.

Forsyth, R. J., A. Balogh, E. J. Smith, G. Erdös, and D. J. McComas, The underlying Parker spiral structure in the Ulysses magnetic field observations 1990-1994, *Journal of Geophysical Research*, *101*, 395–404, 1996.

Giacalone, J., Particle transport and acceleration at corotating interaction regions, *Advances in Space Research*, *23*, 581–590, 1999.

Giacalone, J., and J. R. Jokipii, The transport of cosmic rays across a turbulent magnetic field, *Astrophysical Journal*, *520*, 204–214, 1999.

Gieseler, J., and B. Heber, Spatial gradients of GCR protons in the inner heliosphere derived from Ulysses COSPIN/KET and PAMELA measurements, *Astronomy and Astrophysics*, *589*, A32, 2016.

Gleeson, L. J., and W. I. Axford, Cosmic rays in the interplanetary medium, *Astrophysical Journal Letters*, *149*, L115–L118, 1967.

Gleeson, L. J., and W. I. Axford, Solar modulation of galactic cosmic rays, *Astrophysical Journal*, *154*, 1011–1026, 1968.

Gleeson, L. J., and I. H. Urch, Energy losses and modulation of galactic cosmic rays, *Astrophysics and Space Science*, *11*, 288–308, 1971.

Gloeckler, G., and L. A. Fisk, More evidence that Voyager 1 is still in the heliosphere, *Astrophysical Journal Letters*, *806*, L27, 2015.

Gralewicz, P., J. Wdowczyk, A. W. Wolfendale, and L. Zhang, The energy spectrum of cosmic ray protons in the local interstellar medium, *Astronomy and Astrophysics*, *318*, 925–930, 1997.

Grechnev, V. V., et al., An extreme solar event of 20 January 2005: Properties of the flare and the origin of energetic particles, *Solar Physics*, *252*, 149–177, 2008.

Grimani, C., et al., Measurements of the absolute energy spectra of cosmic-ray positrons and electrons above 7 GeV, *Astronomy and Astrophysics*, *392*, 287–294, 2002.

Gurnett, D. A., W. S. Kurth, L. F. Burlaga, and N. F. Ness, In situ observations of interstellar plasma with voyager 1, *Science*, *341*, 1489–1492, 2013.

Haasbroek, L. J., Modulation of cosmic rays in the heliosphere: A model study of the Ulysses mission (in Afrikaans), Ph.D. thesis, Potchefstroom University for CHE, South Africa, 1993.

Haasbroek, L. J., and M. S. Potgieter, The modulation of cosmic rays in the high latitude heliosphere: A computer simulation, *Space Science Reviews*, *72*, 385–390, 1995.

Haasbroek, L. J., M. S. Potgieter, and J. A. le Roux, The time-dependent recovery after the large cosmic-ray decrease in 1991, in *Proceedings of the International Cosmic Ray Conference, 4,* 710-713, 1995.

Hale, G. E., and S. B. Nicholson, The law of Sun-spot polarity, *Astrophysical Journal*, *62*, 270–300, 1925.

Hathaway, D. H., The solar cycle, *Living Reviews in Solar Physics*, *7*, 2010.

Hattingh, M., Drift of cosmic rays at a wavy neutral sheet in the heliosphere (in Afrikaans), Master's thesis, Potchefstroom University for CHE, South Africa, 1993.

Hattingh, M., The modulation of galactic cosmic rays in a three-dimensional heliosphere, Ph.D. thesis, Potchefstroom University for CHE, South Africa, 1998.

Heber, B., Modulation of galactic and anomalous cosmic rays in the inner heliosphere, *Advances in Space Research*, *27*, 451–460, 2001.

Heber, B., Cosmic rays through the solar hale cycle, *Space Science Reviews*, *176*, 256–278, 2011.

Heber, B., and R. G. Marsden, Cosmic ray modulation over the poles at solar maximum: Observations, *Space Science Reviews*, *97*, 309–319, 2001.

Heber, B., and M. S. Potgieter, Galactic cosmic ray observations at different heliospheric latitudes, *Advances in Space Research*, *26*, 839–852, 2000.

Heber, B., and M. S. Potgieter, Cosmic rays at high heliolatitudes, *Space Science Reviews*, *127*, 117–194, 2006.

Heber, B., and M. S. Potgieter, Galactic and anomalous cosmic rays through the solar cycle: New insights from Ulysses, in *The heliosphere through the solar activity cycle*, edited by A. Balogh, L. J. Lanzerotti, and S. T. Suess, Springer-Praxis, Chichester, UK, 2008.

Heber, B., W. Dröge, H. Kunow, R. Müller-Mellin, G. Wibberenz, P. Ferrando, A. Raviart, and C. Paizis, Spatial variation of >106 Mev proton fluxes observed during the Ulysses rapid latitude scan: Ulysses COSPIN/KET results, *Geophysical Research Letters*, *23*, 1513–1516, 1996b.

Heber, B., T. R. Sanderson, and M. Zhang, Corotating interaction regions, *Advances in Space Research*, *23*, 567–579, 1999a.

Heber, B., J. M. Clem, R. Müller-Mellin, H. Kunow, S. E. S. Ferreira, and M. S. Potgieter, Evolution of the galactic cosmic ray electron to proton ratio: Ulysses COSPIN/KET observations, *Geophysical Research Letters*, *30*, 8032, 2003.

Heber, B., J. Gieseler, P. Dunzlaff, R. Gómez-Herrero, A. Klassen, R. Müller-Mellin, R. A. Mewaldt, M. S. Potgieter, and S. E. S. Ferreira, Latitudinal gradients of galactic cosmic rays during the 2007 solar minimum, *Astrophysical Journal*, *689*, 1443–1447, 2008.

Heber, B., A. Kopp, J. Gieseler, R. Müller-Mellin, H. Fichtner, K. Scherer, M. S. Potgieter, and S. E. S. Ferreira, Modulation of galactic cosmic ray protons and electrons during an unusual solar minimum, *Astrophysical Journal*, *699*, 1956–1963, 2009.

Heber, B., et al., Spatial variation of >40MeV/n nuclei fluxes observed during the ULYSSES rapid latitude scan, *Astronomy and Astrophysics*, *316*, 538–546, 1996a.

Heber, B., et al., Differences in the temporal variations of galactic cosmic ray electrons and protons: Implications from Ulysses at solar minimum, *Geophysical Research Letters*, *26*, 2133–2136, 1999b.

Heber, B., et al., 3-20 MeV electrons in the inner three-dimensional heliosphere at solar maximum: Ulysses COSPIN/KET observations, *Astrophysical Journal*, *579*, 888–894, 2002a.

Heber, B., et al., Ulysses cosmic ray and solar particle investigation/Kiel electron telescope observations: Charge sign dependence and spatial gradients during the 1990-2000 A > 0 solar magnetic cycle, *Journal of Geophysical Research (Space Physics)*, *107*, 1274, 2002b.

Hitge, M., and R. A. Burger, Cosmic ray modulation with a Fisk-type heliospheric magnetic field and a latitude-dependent solar wind speed, *Advances in Space Research*, *45*, 18–27, 2010.

Hoeksema, J. T., Large-scale structure of the heliospheric magnetic field - 1976-1991, in *Solar Wind Seven Colloquium*, edited by E. Marsch and R. Schwenn, 1992.

Hsieh, K. C., G. M. Mason, and J. A. Simpson, Cosmic-ray ^{2}H from satellite measurements 1965-1969, *Astrophysical Journal*, *166*, 221–233, 1971.

Jokipii, J. R., Cosmic-ray propagation. I. Charged particles in a random magnetic field, *Astrophysical Journal*, *146*, 480–487, 1966.

Jokipii, J. R., Particle acceleration at a termination shock. I - Application to the solar wind and the anomalous component, *Journal of Geophysical Research*, *91*, 2929–2932, 1986.

Jokipii, J. R., Latitudinal heliospheric magnetic field: Stochastic and causal components, *Journal of Geophysical Research*, *106*, 15841–15848, 2001.

Jokipii, J. R., and D. A. Kopriva, Effects of particle drift on the transport of cosmic rays. III - Numerical models of galactic cosmic-ray modulation, *Astrophysical Journal*, *234*, 384–392, 1979.

Jokipii, J. R., and J. Kóta, The polar heliospheric magnetic field, *Geophysical Research Letters*, *16*, 1–4, 1989.

Jokipii, J. R., and E. N. Parker, On the convection, diffusion, and adiabatic deceleration of cosmic rays in the solar wind, *Astrophysical Journal*, *160*, 735–744, 1970.

Jokipii, J. R., and B. Thomas, Effects of drift on the transport of cosmic rays. IV - Modulation by a wavy interplanetary current sheet, *Astrophysical Journal*, *243*, 1115–1122, 1981.

Jokipii, J. R., E. H. Levy, and W. B. Hubbard, Effects of particle drift on cosmic-ray transport. I - General properties, application to solar modulation, *Astrophysical Journal*, *213*, 861–868, 1977.

Jokipii, J. R., J. Kóta, J. Giacalone, T. S. Horbury, and E. J. Smith, Interpretation and consequences of large-scale magnetic variances observed at high heliographic latitude, *Geophysical Research Letters*, *22*, 3385–3388, 1995.

Kirk, D. B., and W. W. Hwu, Programming massively parallel processors – A hands-on approach (2nd ed), Elsevier, Amsterdam, Netherlands, 2010.

Kissmann, R., H. Fichtner, and S. E. S. Ferreira, The influence of CIRs on the energetic electron flux at 1 AU, *Astronomy and Astrophysics*, *419*, 357–363, 2004.

Kohlhase, C. E., and P. A. Penzo, Voyager mission description, *Space Science Reviews*, *21*, 77–101, 1977.

Kojima, M., A. R. Breen, K. Fujiki, K. Hayashi, T. Ohmi, and M. Tokumaru, Fast solar wind after the rapid acceleration, *Journal of Geophysical Research (Space Physics)*, *109*, A04103, 2004.

Kopp, A., I. Büsching, M. S. Potgieter, and R. D. Strauss, A stochastic approach to galactic proton propagation: Influence of the spiral arm structure, *New Astronomy*, *30*, 32–37, 2014.

Kóta, J., 3-D simulations of heliospheric transport: A comparison of models, in *Proceedings of the International Cosmic Ray Conference, 2,* 25-28, 1997.

Kóta, J., Cosmic-ray modulation and the structure of the heliospheric magnetic field, in *Proceedings of the International Cosmic Ray Conference, 7,* 9-12, 1999.

Kóta, J., and J. R. Jokipii, Effects of drift on the transport of cosmic rays. VI - A three-dimensional model including diffusion, *Astrophysical Journal*, *265*, 573–581, 1983.

Kóta, J., and J. R. Jokipii, 3-D distribution of cosmic rays in the outer heliosphere, in *Proceedings of the International Cosmic Ray Conference, 4,* 680-683, 1995.

Krimigis, S. M., C. O. Bostrom, T. P. Armstrong, W. I. Axford, C. Y. Fan, G. Gloeckler, and L. J. Lanzerotti, The Low Energy Charged Particle (LECP) experiment on the Voyager spacecraft, *Space Science Reviews*, *21*, 329–354, 1977.

Krimigis, S. M., R. B. Decker, E. C. Roelof, M. E. Hill, T. P. Armstrong, G. Gloeckler, D. C. Hamilton, and L. J. Lanzerotti, Search for the exit: Voyager 1 at heliosphere's border with the Galaxy, *Science*, *341*, 144–147, 2013.

Kunow, H., et al., High energy cosmic-ray nuclei results on Ulysses: 2. Effects of a recurrent high-speed stream from the southern polar coronal hole, *Space Science Reviews*, *72*, 397–402, 1995.

Kunow, H., et al., Corotating interaction regions at high latitudes, *Space Science Reviews*, *89*, 221–268, 1999.

Langner, U. W., Effects of termination shock acceleration on cosmic rays in the heliosphere, Ph.D. thesis, Potchefstroom University for CHE, South Africa, 2004.

Langner, U. W., and M. S. Potgieter, Effects of the solar wind termination shock on charge-sign dependent cosmic ray modulation, *Advances in Space Research*, *34*, 144–149, 2004.

Langner, U. W., O. C. de Jager, and M. S. Potgieter, On the local interstellar spectrum for cosmic ray electrons, *Advances in Space Research*, *27*, 517–522, 2001.

Langner, U. W., M. S. Potgieter, and W. R. Webber, Modelling of 'barrier' modulation for cosmic ray protons in the outer heliosphere, *Advances in Space Research*, *34*, 138–143, 2004.

Lapidus, L., and G. Pinder, Numerical solution of partial differential equations in science and engineering, Wiley-Interscience, New York, USA, 1982.

Lave, K. A., et al., Galactic cosmic-ray energy spectra and composition during the 2009–2010 solar minimum period, *Astrophysical Journal*, *770*, 117, 2013.

le Roux, J. A., The solar modulation of galactic cosmic rays as described by a time-dependent drift model, Ph.D. thesis, Potchefstroom University for CHE, South Africa, 1990.

le Roux, J. A., and M. S. Potgieter, The simulation of complete 11 and 12 year modulation cycles for cosmic rays in the heliosphere using a drift model with global merged interaction regions, *Astrophysical Journal*, *442*, 847–851, 1995.

le Roux, J. A., M. S. Potgieter, and V. S. Ptuskin, A transport model for the diffusive shock acceleration and modulation of anomalous cosmic rays in the heliosphere, *Journal of Geophysical Research*, *101*, 4791–4804, 1996.

Leighton, R. B., A magneto-kinematic model of the solar cycle, *Astrophysical Journal*, *156*, 1–26, 1969.

Levy, E. H., The interplanetary magnetic field structure, *Nature*, *261*, 394–395, 1976.

Li, H., C. Wang, and J. D. Richardson, Properties of the termination shock observed by Voyager 2, *Geophysical Research Letters*, *351*, L19107, 2008.

Lockwood, M., and R. Stamper, Long-term drift of the coronal source magnetic flux and the total solar irradiance, *Geophysical Research Letters*, *26*, 2461–2464, 1999.

Luo, X., M. Zhang, H. K. Rassoul, N. V. Pogorelov, and J. Heerikhuisen, Galactic cosmic-ray modulation in a realistic global magnetohydrodynamic heliosphere, *Astrophysical Journal*, *764*, 85, 2013.

Luo, X., M. Zhang, M. Potgieter, X. Feng, and N. V. Pogorelov, A numerical simulation of cosmic-ray modulation near the heliopause, *Astrophysical Journal*, *808*, 82, 2015.

Manoharan, P. K., Three-dimensional evolution of solar wind during solar cycles 22-24, *Astrophysical Journal*, *751*, 128, 2012.

Manuel, R., Time-dependent modulation of cosmic rays in the outer heliosphere, Ph.D. thesis, North-West University, South Africa, 2013.

Manuel, R., S. E. S. Ferreira, and M. S. Potgieter, Cosmic ray modulation in the outer heliosphere: Predictions for cosmic ray intensities up to the heliopause along Voyager 1 and 2 trajectories, *Advances in Space Research*, *48*, 874–883, 2011a.

Manuel, R., S. E. S. Ferreira, M. S. Potgieter, R. D. Strauss, and N. E. Engelbrecht, Time-dependent cosmic ray modulation, *Advances in Space Research*, *47*, 1529–1537, 2011b.

Manuel, R., S. E. S. Ferreira, and M. S. Potgieter, Time-dependent modulation of cosmic rays in the heliosphere, *Solar Physics*, *289*, 2207–2231, 2014.

Manuel, R., S. E. S. Ferreira, and M. S. Potgieter, The effect of a dynamic inner heliosheath thickness on cosmic-ray modulation, *Astrophysical Journal*, *799*, 223, 2015.

Marsch, E., W. I. Axford, and J. F. McKenzie, Solar wind, in *Dynamic Sun*, edited by Dwivedi, B. N., Cambridge University Press, Cambridge, UK, 2003.

Marsden, R. G., The heliosphere after Ulysses, *Astrophysics and Space Science*, *277*, 337–347, 2001.

Matthaeus, W. H., G. Qin, J. W. Bieber, and G. P. Zank, Nonlinear collisionless perpendicular diffusion of charged particles, *Astrophysical Journal Letters*, *590*, L53–L56, 2003.

McComas, D. J., R. W. Ebert, H. A. Elliott, B. E. Goldstein, J. T. Gosling, N. A. Schwadron, and R. M. Skoug, Weaker solar wind from the polar coronal holes and the whole Sun, *Geophysical Research Letters*, *35*, L18103, 2008.

McDonald, F. B., P. Ferrando, B. Heber, H. Kunow, R. McGuire, R. Müller-Mellin, C. Paizis, A. Raviart, and G. Wibberenz, A comparative study of cosmic ray radial and latitudinal gradients in the inner and outer heliosphere, *Journal of Geophysical Research*, *102*, 4643–4652, 1997.

McKibben, R. B., Reanalysis and confirmation of positive latitude gradients for anomalous helium and galactic cosmic rays measured in 1975-1976 with Pioneer II, *Journal of Geophysical Research*, *94*, 17021–17033, 1989.

McKibben, R. B., Cosmic-ray diffusion in the inner heliosphere, *Advances in Space Research*, *35*, 518–531, 2005.

Menn, W., et al., The absolute flux of protons and helium at the top of the atmosphere using IMAX, *Astrophysical Journal*, *533*, 281–297, 2000.

Menn, W., et al., The PAMELA space experiment, *Advances in Space Research*, *51*, 209–218, 2013.

Minnie, J., Observational constraints on the heliospheric diffusion tensor for galactic cosmic rays, Master's thesis, Potchefstroom University for CHE, South Africa, 2002.

Minnie, J., An ab initio approach to the heliospheric modulation of galactic cosmic rays, Ph.D. thesis, North-West University, South Africa, 2006.

Minnie, J., J. W. Bieber, W. H. Matthaeus, and R. A. Burger, Suppression of particle drifts by turbulence, *Astrophysical Journal*, *670*, 1149–1158, 2007.

Miralles, M. P., and J. E. Sánchez Almeida, The Sun, the solar wind, and the heliosphere, Springer-Praxis, Chichester, UK, 2011.

Mocchiutti, E., et al., PAMELA and electrons, *Nuclear Instruments and Methods in Physics Research A*, *630*, 28–35, 2011.

Moore, R., and D. Rabin, Sunspots, *Annual Review of Astronomy and Astrophysics*, *23*, 239–266, 1985.

Moraal, H., Proton modulation near solar minimum periods in consecutive solar cycles, in *Proceedings of the International Cosmic Ray Conference, 6,* 140-143, 1990.

Moraal, H., and L. J. Gleeson, Three-dimensional models of the galactic cosmic-ray modulation, in *Proceedings of the International Cosmic Ray Conference, 12,* 4189-4194, 1975.

Moraal, H., and M. S. Potgieter, Solutions of the spherically-symmetric cosmic-ray transport equation in interplanetary space, *Astrophysics and Space Science*, *84*, 519–533, 1982.

Moraal, H., L. J. Gleeson, and G. M. Webb, Effects of charged particle drifts on the modulation of the intensity of galactic cosmic rays, in *Proceedings of the International Cosmic Ray Conference, 3,* 1-6, 1979.

Moskalenko, I. V., A. W. Strong, J. F. Ormes, M. S. Potgieter, and U. W. Langner, Secondary antiprotons in cosmic rays, in *Proceedings of the International Cosmic Ray Conference, 5,* 1868-1871, 2001.

Moskalenko, I. V., A. W. Strong, J. F. Ormes, and M. S. Potgieter, Secondary antiprotons and propagation of cosmic rays in the Galaxy and heliosphere, *Astrophysical Journal*, *565*, 280–296, 2002.

Müller, H. R., P. C. Frisch, V. Florinski, and G. P. Zank, Heliospheric response to different possible interstellar environments, *Astrophysical Journal*, *647*, 1491–1505, 2006.

Munini, R., Solar modulation of cosmic ray electrons and positrons measured by the PAMELA experiment during the 23rd solar minimum, Ph.D. thesis, University of Trieste, Italy, 2015.

Ndiitwani, D. C., A study of the time-dependent modulation of galactic cosmic rays in the heliosphere, Master's thesis, North-West University, South Africa, 2005.

Ndiitwani, D. C., S. E. S. Ferreira, M. S. Potgieter, and B. Heber, Modelling cosmic ray intensities along the Ulysses trajectory, *Annales Geophysicae*, *23*, 1061–1070, 2005.

Ngobeni, M. D., and M. S. Potgieter, The heliospheric modulation of cosmic rays: Effects of a latitude dependent solar wind termination shock, *Advances in Space Research*, *46*, 391–401, 2010.

Ngobeni, M. D., and M. S. Potgieter, Modelling the effects of scattering parameters on particle-drift in the solar modulation of galactic cosmic rays, *Advances in Space Research*, *56*, 1525–1537, 2015.

Ngobeni, R. D., Modeling of galactic cosmic rays in the heliosphere, Ph.D. thesis, North-West University, South Africa, 2015.

Nndanganeni, R. R., Modeling of electrons in the heliosphere, Ph.D. thesis, North-West University, South Africa, 2016.

Ofman, L., The origin of the slow solar wind in coronal streamers, *Advances in Space Research*, *33*, 681–688, 2004.

Opher, M., J. F. Drake, B. Zieger, and T. I. Gombosi, Magnetized jets driven by the Sun: The structure of the heliosphere revisited, *Astrophysical Journal Letters*, *800*, L28, 2015.

Paizis, C., et al., Amplitude evolution and rigidity dependence of the 26-day recurrent cosmic ray decreases: COSPIN/KET results, *Journal of Geophysical Research*, *104*, 28241–28248, 1999.

Palmer, I. D., Transport coefficients of low-energy cosmic rays in interplanetary space, *Reviews of Geophysics and Space Physics*, *20*, 335–351, 1982.

Parker, E. N., Cosmic-ray modulation by solar wind, *Physical Review*, *110*, 1445–1449, 1958.

Parker, E. N., Interplanetary Dynamical Processes, Interscience Publishers, New York, USA, 1963.

Parker, E. N., The passage of energetic charged particles through interplanetary space, *Planetary and Space Science*, *13*, 9–49, 1965.

Parker, E. N., A history of early work on the heliospheric magnetic field, *Journal of Geophysical Research*, *106*, 15797–15802, 2001.

Peaceman, D. W., and H. H. Rachford, The numerical solution of parabolic and elliptic differential equations, *Journal of the Society for Industrial and Applied Mathematics*, *3*, 28–41, 1955.

Pei, C., J. W. Bieber, B. Breech, R. A. Burger, J. Clem, and W. H. Matthaeus, Cosmic ray diffusion tensor throughout the heliosphere, *Journal of Geophysical Research (Space Physics)*, *115*, A03103, 2010a.

Pei, C., J. W. Bieber, R. A. Burger, and J. Clem, A general time-dependent stochastic method for solving Parker's transport equation in spherical coordinates, *Journal of Geophysical Research (Space Physics)*, *115*, A12107, 2010b.

Perko, J. S., and L. A. Fisk, Solar modulation of galactic cosmic rays. V - Time-dependent modulation, *Journal of Geophysical Research*, *88*, 9033–9036, 1983.

Pesses, M. E., D. Eichler, and J. R. Jokipii, Cosmic ray drift, shock wave acceleration, and the anomalous component of cosmic rays, *Astrophysical Journal Letters*, *246*, L85–L88, 1981.

Peterson, J. D., A new look at galactic polar radio emission and the local interstellar electron spectrum, in *Proceedings of the International Cosmic Ray Conference, 4,* 251-254, 1999.

Phillips, J. L., et al., Ulysses solar wind plasma observations from pole to pole, *Geophysical Research Letters*, *22*, 3301–3304, 1995.

Picozza, P., et al., PAMELA: A payload for antimatter matter exploration and light-nuclei astrophysics, *Astroparticle Physics*, *27*, 296–315, 2007.

Picozza, P., et al., Dark matter research and the PAMELA space mission, in *Proceedings of the American Institute of Physics Conference, 1166,* 141-150, 2009.

Pogorelov, N. V., S. T. Suess, S. N. Borovikov, R. W. Ebert, D. J. McComas, and G. P. Zank, Three-dimensional features of the outer heliosphere due to coupling between the interstellar and interplanetary magnetic fields. IV. Solar cycle model based on Ulysses observations, *Astrophysical Journal*, *772*, 2, 2013.

Potgieter, M. S., The modulation of galactic cosmic rays as described by a three-dimensional drift model, Ph.D. thesis, Potchefstroom University for CHE, South Africa, 1984.

Potgieter, M. S., Heliospheric terminal shock acceleration and modulation of the anomalous cosmic-ray component, *Advances in Space Research*, *9*, 21–24, 1989.

Potgieter, M. S., Time-dependent cosmic-ray modulation - Role of drifts and interaction regions, *Advances in Space Research*, *13*, 239–249, 1993.

Potgieter, M. S., Heliospheric modulation of galactic electrons: Consequences of new calculations for the mean free path of electrons between 1 MeV and ∼10 GeV, *Journal of Geophysical Research*, *101*, 24411–24422, 1996.

Potgieter, M. S., The heliospheric modulation of galactic cosmic rays at solar minimum, *Advances in Space Research*, *19*, 883–892, 1997.

Potgieter, M. S., The modulation of galactic cosmic rays in the heliosphere: Theory and models, *Space Science Reviews*, *83*, 147–158, 1998.

Potgieter, M. S., Heliospheric modulation of cosmic ray protons: Role of enhanced perpendicular diffusion during periods of minimum solar modulation, *Journal of Geophysical Research*, *105*, 18295–18304, 2000.

Potgieter, M. S., Solar cycle variations and cosmic rays, *Journal of Atmospheric and Solar-Terrestrial Physics*, *70*, 207–218, 2008.

Potgieter, M. S., Cosmic rays in the inner heliosphere: Insights from observations, theory and models, *Space Science Reviews*, *176*, 165–176, 2013a.

Potgieter, M. S., Solar modulation of cosmic rays, *Living Reviews in Solar Physics*, *10*, 3, 2013b.

Potgieter, M. S., The charge-sign dependent effect in the solar modulation of cosmic rays, *Advances in Space Research*, *53*, 1415–1425, 2014a.

Potgieter, M. S., Very local interstellar spectra for galactic electrons, protons and helium, *Brazilian Journal of Physics*, *44*, 581–588, 2014b.

Potgieter, M. S., and R. A. Burger, The modulation of cosmic-ray electrons, positrons and helium nuclei as predicted by a drift model with a simulated wavy neutral sheet, *Astronomy and Astrophysics*, *233*, 598–604, 1990.

Potgieter, M. S., and S. E. S. Ferreira, The importance of perpendicular diffusion in the heliospheric modulation of cosmic ray electrons, *Advances in Space Research*, *23*, 463–466, 1999.

Potgieter, M. S., and L. J. Haasbroek, The simulation of base-line cosmic-ray modulation for the Ulysses trajectory, in *Proceedings of the International Cosmic Ray Conference, 3,* 457-460, 1993.

Potgieter, M. S., and U. W. Langner, Heliospheric modulation of cosmic-ray positrons and electrons: Effects of the heliosheath and the solar wind termination shock, *Astrophysical Journal*, *602*, 993–1001, 2004.

Potgieter, M. S., and H. Moraal, A drift model for the modulation of galactic cosmic rays, *Astrophysical Journal*, *294*, 425–440, 1985.

Potgieter, M. S., and H. Moraal, Acceleration of cosmic rays in the solar wind termination shock. I - A steady state technique in a spherically symmetric model, *Astrophysical Journal*, *330*, 445–455, 1988.

Potgieter, M. S., and R. R. Nndanganeni, The solar modulation of electrons in the heliosphere, *Astrophysics and Space Science*, *345*, 33–40, 2013a.

Potgieter, M. S., and R. R. Nndanganeni, A local interstellar spectrum for galactic electrons, *Astroparticle Physics*, *48*, 25–29, 2013b.

Potgieter, M. S., J. A. le Roux, and R. A. Burger, Interplanetary cosmic ray radial gradients with steady state modulation models, *Journal of Geophysical Research*, *94*, 2323–2332, 1989.

Potgieter, M. S., J. A. le Roux, L. F. Burlaga, and F. B. McDonald, The role of merged interaction regions and drifts in the heliospheric modulation of cosmic rays beyond 20 AU - A computer simulation, *Astrophysical Journal*, *403*, 760–768, 1993.

Potgieter, M. S., R. A. Burger, and S. E. S. Ferreira, Modulation of cosmic rays in the heliosphere from solar minimum to maximum: A theoretical perspective, *Space Science Reviews*, *97*, 295–307, 2001a.

Potgieter, M. S., U. W. Langner, and S. E. S. Ferreira, Cosmic ray electron to positron ratios in the heliosphere, *Advances in Space Research*, *27*, 523–528, 2001b.

Potgieter, M. S., E. E. Vos, M. Boezio, N. De Simone, V. Di Felice, and V. Formato, Modulation of galactic protons in the heliosphere during the unusual solar minimum of 2006 to 2009, *Solar Physics*, *289*, 391–406, 2014a.

Potgieter, M. S., E. E. Vos, and R. R. Nndanganeni, The first very local interstellar spectra for galactic protons, helium and electrons, in *Proceedings of the 14th ICATPP Conference on Astroparticle, Particle, Space Physics and Detectors for Physics Applications*, edited by

S. Giani, C. Leroy, L. Price, P. G. Rancoita, and R. Ruchti, 2014b.

Potgieter, M. S., E. E. Vos, R. Munini, M. Boezio, and V. Di Felice, Modulation of galactic electrons in the heliosphere during the unusual solar minimum of 2006 – 2009: A modeling approach, *Astrophysical Journal*, *810*, 141, 2015.

Prinsloo, P. L., Acceleration of cosmic rays in the outer heliosphere, Master's thesis, North-West University, South Africa, 2016.

Ptuskin, V. S., Origin of galactic cosmic rays: Sources, acceleration and propagation, in *Proceedings of the International Cosmic Ray Conference, 10,* 317-328, 2005.

Ptuskin, V. S., I. V. Moskalenko, F. C. Jones, A. W. Strong, and V. N. Zirakashvili, Dissipation of magnetohydrodynamic waves on energetic particles: Impact on interstellar turbulence and cosmic-ray transport, *Astrophysical Journal*, *642*, 902–916, 2006.

Raath, J. L., A comparative study of cosmic ray modulation models, Master's thesis, North-West University, South Africa, 2014.

Raath, J. L., M. S. Potgieter, R. D. Strauss, and A. Kopp, The effect of magnetic field modifications on the modulation of cosmic rays in the heliosphere, *ArXiv e-prints*, 2015a.

Raath, J. L., R. D. Strauss, and M. S. Potgieter, New insights from modeling the neutral heliospheric current sheet, *Astrophysics and Space Science*, *360*, 24, 2015b.

Richardson, J. D., C. Wang, and K. I. Paularena, The solar wind: From solar minimum to solar maximum, *Advances in Space Research*, *27*, 471–479, 2001.

Richardson, J. D., J. C. Kasper, C. Wang, J. W. Belcher, and A. J. Lazarus, Cool heliosheath plasma and deceleration of the upstream solar wind at the termination shock, *Nature*, *454*, 63–66, 2008.

Roberts, D. A., J. Giacalone, J. R. Jokipii, M. L. Goldstein, and T. D. Zepp, Spectra of polar heliospheric fields and implications for field structure, *Journal of Geophysical Research (Space Physics)*, *112*, A08103, 2007.

Rossi, B., and S. Olbert, Introduction to the physics of space, McGraw-Hill, New York, USA, 1970.

Sanders, J., and E. Kandrot, CUDA by example – An introduction to general purpose GPU programming, Addison-Wesley, Boston, USA, 2010.

Scarf, F. L., and D. A. Gurnett, A plasma wave investigation for the Voyager mission, *Space Science Reviews*, *21*, 289–308, 1977.

Scherer, K., and H. Fichtner, The return of the bow shock, *Astrophysical Journal*, *782*, 25, 2014.

Scherer, K., H. Fichtner, R. D. Strauss, S. E. S. Ferreira, M. S. Potgieter, and H. J. Fahr, On cosmic ray modulation beyond the heliopause: Where is the modulation boundary?, *Astrophysical Journal*, *735*, 128, 2011.

Schlickeiser, R., On the interplanetary transport of solar cosmic rays, *Journal of Geophysical Research*, *93*, 2725–2729, 1988.

Schlickeiser, R., Cosmic ray astrophysics, Springer, Germany, 2002.

Schwenn, R., Solar wind sources and their variations over the solar cycle, *Space Science Reviews*, *124*, 51–76, 2006.

Shalchi, A., Extended nonlinear guiding center theory of perpendicular diffusion, *Astronomy and Astrophysics*, *453*, L43–L46, 2006.

Shalchi, A., Nonlinear cosmic ray diffusion theories, Springer, Berlin, Germany, 2009.

Shalchi, A., A unified particle diffusion theory for cross-field scattering: Subdiffusion, recovery of diffusion, and diffusion in three-dimensional turbulence, *Astrophysical Journal Letters*, *720*, L127–L130, 2010.

Shalchi, A., and R. Schlickeiser, The parallel mean free path of heliospheric cosmic rays in composite slab/two-dimensional geometry. I. The damping model of dynamical turbulence, *Astrophysical Journal*, *604*, 861–873, 2004.

Shalchi, A., J. W. Bieber, and W. H. Matthaeus, Nonlinear guiding center theory of perpendicular diffusion in dynamical turbulence, *Astrophysical Journal*, *615*, 805–812, 2004.

Sheeley, N. R., Jr., et al., Measurements of flow speeds in the corona between 2 and 30 $R_{\odot}$, *Astrophysical Journal*, *484*, 472–478, 1997.

Shikaze, Y., et al., Measurements of 0.2–20 GeV/n cosmic-ray proton and helium spectra from 1997 through 2002 with the BESS spectrometer, *Astroparticle Physics*, *28*, 154–167, 2007.

Simpson, J. A., D. Hamilton, G. Lentz, R. B. McKibben, A. Mogro-Campero, M. Perkins, K. R. Pyle, A. J. Tuzzolino, and J. J. O'Gallagher, Protons and electrons in Jupiter's magnetic field: Results from the University of Chicago Experiment on Pioneer 10, *Science*, *183*, 306–309, 1974.

Simpson, J. A., M. Zhang, and S. Bame, A solar polar North-South asymmetry for cosmic-ray propagation in the heliosphere: The ULYSSES pole-to-pole rapid transit, *Astrophysical Journal Letters*, *465*, L69–L72, 1996.

Smith, C. W., and J. W. Bieber, Solar cycle variation of the interplanetary magnetic field spiral, *Astrophysical Journal*, *370*, 435–441, 1991.

Smith, E. J., Interplanetary magnetic field over two solar cycles and out to 20 AU, *Advances in Space Research*, *9*, 159–169, 1989.

Smith, E. J., The heliospheric current sheet, *Journal of Geophysical Research*, *106*, 15819–15832, 2001.

Smith, E. J., The global heliospheric magnetic field, in *The Heliosphere through the Solar Activity Cycle*, edited by A. Balogh, L. J. Lanzerotti, and S. T. Suess, Springer-Praxis, Chichester, UK, 2008.

Smith, E. J., Solar cycle evolution of the heliospheric magnetic field: The Ulysses legacy, *Journal of Atmospheric and Solar-Terrestrial Physics*, *73*, 277–289, 2011.

Steenkamp, R., Shock acceleration as source of the anomalous component of cosmic rays in the heliosphere, Ph.D. thesis, Potchefstroom University for CHE, South Africa, 1995.

Sternal, O., N. E. Engelbrecht, R. A. Burger, S. E. S. Ferreira, H. Fichtner, B. Heber, A. Kopp, M. S. Potgieter, and K. Scherer, Possible evidence for a Fisk-type heliospheric magnetic field. I. Analyzing Ulysses/KET electron observations, *Astrophysical Journal*, *741*, 23, 2011.

Stix, M., The Sun: An introduction, Springer, Berlin, Germany, 2004.

Stone, E. C., R. E. Vogt, F. B. McDonald, B. J. Teegarden, J. H. Trainor, J. R. Jokipii, and W. R. Webber, Cosmic ray investigation for the Voyager missions: Energetic particle studies in the outer heliosphere – and beyond, *Space Science Reviews*, *21*, 355–376, 1977.

Stone, E. C., A. C. Cummings, F. B. McDonald, B. C. Heikkila, N. Lal, and W. R. Webber, Voyager 1 explores the termination shock region and the heliosheath beyond, *Science*, *309*, 2017–2020, 2005.

Stone, E. C., A. C. Cummings, F. B. McDonald, B. C. Heikkila, N. Lal, and W. R. Webber, An asymmetric solar wind termination shock, *Nature*, *454*, 71–74, 2008.

Stone, E. C., A. C. Cummings, F. B. McDonald, B. C. Heikkila, N. Lal, and W. R. Webber, Voyager 1 observes low-energy galactic cosmic rays in a region depleted of heliospheric ions, *Science*, *341*, 150–153, 2013.

Strauss, R. D., Modelling of anomalous cosmic rays, Master's thesis, North-West University, South Africa, 2010.

Strauss, R. D., Modelling of cosmic rays in the heliosphere by stochastic processes, Ph.D. thesis, North-West University, South Africa, 2013.

Strauss, R. D., and M. S. Potgieter, Where does the heliospheric modulation of galactic cosmic rays start?, *Advances in Space Research*, *53*, 1015–1023, 2014a.

Strauss, R. D., and M. S. Potgieter, Is the highest cosmic-ray flux yet to come?, *Solar Physics*, *289*, 3197–3205, 2014b.

Strauss, R. D., M. S. Potgieter, and S. E. S. Ferreira, The heliospheric transport and modulation of multiple charged anomalous oxygen revisited, *Astronomy and Astrophysics*, *513*, A24, 2010a.

Strauss, R. D., M. S. Potgieter, S. E. S. Ferreira, and M. E. Hill, Modelling anomalous cosmic ray oxygen in the heliosheath, *Astronomy and Astrophysics*, *522*, A35, 2010b.

Strauss, R. D., M. S. Potgieter, I. Büsching, and A. Kopp, Modeling the modulation of galactic and jovian electrons by stochastic processes, *Astrophysical Journal*, *735*, 83, 2011a.

Strauss, R. D., M. S. Potgieter, A. Kopp, and I. Büsching, On the propagation times and energy losses of cosmic rays in the heliosphere, *Journal of Geophysical Research (Space Physics)*, *116*, A12105, 2011b.

Strauss, R. D., M. S. Potgieter, I. Büsching, and A. Kopp, Modelling heliospheric current sheet drift in stochastic cosmic ray transport models, *Astrophysics and Space Science*, *339*, 223–236, 2012.

Strauss, R. D., M. S. Potgieter, S. E. S. Ferreira, H. Fichtner, and K. Scherer, Cosmic ray modulation beyond the heliopause: A hybrid modeling approach, *Astrophysical Journal Letters*, *765*, L18, 2013.

Strong, A. W., and I. V. Moskalenko, Propagation of cosmic-ray nucleons in the Galaxy, *Astrophysical Journal*, *509*, 212–228, 1998.

Strong, A. W., I. V. Moskalenko, and O. Reimer, Diffuse continuum gamma rays from the galaxy, *Astrophysical Journal*, *537*, 763–784, 2000.

Strong, A. W., E. Orlando, and T. R. Jaffe, The interstellar cosmic-ray electron spectrum from synchrotron radiation and direct measurements, *Astronomy and Astrophysics*, *534*, A54, 2011.

Tanimori, T., et al., Discovery of TeV gamma rays from SN 1006: Further evidence for the supernova remnant origin of cosmic rays, *Astrophysical Journal Letters*, *497*, L25–L28, 1998.

Tautz, R. C., and A. Shalchi, Drift coefficients of charged particles in turbulent magnetic fields, *Astrophysical Journal*, *744*, 125, 2012.

Teufel, A., and R. Schlickeiser, Analytic calculation of the parallel mean free path of heliospheric cosmic rays. I. Dynamical magnetic slab turbulence and random sweeping slab turbulence, *Astronomy and Astrophysics*, *393*, 703–715, 2002.

Teufel, A., and R. Schlickeiser, Analytic calculation of the parallel mean free path of heliospheric cosmic rays. II. Dynamical magnetic slab turbulence and random sweeping slab turbulence with finite wave power at small wavenumbers, *Astronomy and Astrophysics*, *397*, 15–25, 2003.

Thomas, B. T., and E. J. Smith, The Parker spiral configuration of the interplanetary magnetic field between 1 and 8.5 AU, *Journal of Geophysical Research*, *85*, 6861–6867, 1980.

Thomas, B. T., and E. J. Smith, The structure and dynamics of the heliospheric current sheet, *Journal of Geophysical Research*, *86*, 11105–11110, 1981.

Usoskin, I. G., A history of solar activity over millennia, *Living Reviews in Solar Physics*, *5*, 2008.

Usoskin, I. G., G. A. Bazilevskaya, and G. A. Kovaltsov, Solar modulation parameter for cosmic rays since 1936 reconstructed from ground-based neutron monitors and ionization chambers, *Journal of Geophysical Research (Space Physics)*, *116*, A02104, 2011.

Usoskin, I. G., et al., Force-field parameterization of the galactic cosmic ray spectrum: Validation for Forbush decreases, *Advances in Space Research*, *55*, 2940–2945, 2015.

Venter, C., A. Kopp, A. K. Harding, P. L. Gonthier, and I. Büsching, Cosmic-ray positrons from millisecond pulsars, *Astrophysical Journal*, *807*, 130, 2015.

von Rosenvinge, T. T., F. B. McDonald, J. H. Trainor, and W. R. Webber, The modulation of galactic cosmic rays between 1 and 17 AU, in *Proceedings of the International Cosmic Ray Conference, 12,* 171, 1979.

Vos, E. E., Cosmic ray modulation processes in the heliosphere, Master's thesis, North-West University, South Africa, 2012.

Vos, E. E., and M. S. Potgieter, New modeling of galactic proton modulation during the minimum of solar cycle 23/24, *Astrophysical Journal*, *815*, 119, 2015.

Vos, E. E., and M. S. Potgieter, Global gradients for cosmic ray protons in the heliosphere during the solar minimum of cycle 23/24, *Solar Physics*, In press, 2016.

Vos, E. E., M. S. Potgieter, M. Boezio, N. De Simone, V. Di Felice, and V. Formato, Modulation mechanisms for galactic protons during the unusual solar minimum of 2009, in *Proceedings of the International Cosmic Ray Conference*, edited by R. C. Shellard, 2013a.

Vos, E. E., M. S. Potgieter, M. Boezio, V. Di Felice, N. De Simone, and V. Formato, Modulation of galactic electrons during the unusual solar minimum of 2009, in *Proceedings of the International Cosmic Ray Conference*, edited by R. C. Shellard, 2013b.

Wang, Y. M., Coronal holes and open magnetic flux, *Space Science Reviews*, *144*, 383–399, 2009.

Wang, Y. M., and N. R. Sheeley, Jr., Solar implications of Ulysses interplanetary field measurements, *Astrophysical Journal Letters*, *447*, L143–L146, 1995.

Webber, W. R., and P. R. Higbie, Limits on the interstellar cosmic ray electron spectrum below ∼1-2 GeV derived from the galactic polar radio spectrum and constrained by new Voyager 1 measurements, *Journal of Geophysical Research*, *113*, A11106, 2008.

Webber, W. R., and P. R. Higbie, Galactic propagation of cosmic ray nuclei in a model with an increasing diffusion coefficient at low rigidities: A comparison of the new interstellar spectra with Voyager data in the outer heliosphere, *Journal of Geophysical Research (Space Physics)*, *114*, A02103, 2009.

Webber, W. R., and D. S. Intriligator, Voyagers 1 and 2 in a shrunken and squashed heliosphere, *Journal of Geophysical Research (Space Physics)*, *116*, A06105, 2011.

Webber, W. R., and F. B. McDonald, Recent Voyager 1 data indicate that on 25 August 2012 at a distance of 121.7 AU from the Sun, sudden and unprecedented intensity changes were observed in anomalous and galactic cosmic rays, *Geophysical Research Letters*, *40*, 1665–1668, 2013.

Webber, W. R., R. L. Golden, S. J. Stochaj, J. F. Ormes, and R. E. Strittmatter, A measurement of the cosmic-ray ^{2}H and ^{3}He spectra and ^{2}H/^{4}He and ^{3}He/^{4}He ratios in 1989, *Astrophysical Journal*, *380*, 230–234, 1991.

Webber, W. R., F. B. McDonald, P. R. Higbie, and B. Heikkila, Recovery of 150-250 MeV cosmic ray proton intensities between 2004–2010 as measured near the Earth, at Voyager 2 and also in the heliosheath at Voyager 1 - A two zone heliosphere, *ArXiv e-prints*, 2011.

Webber, W. R., P. R. Higbie, and F. B. McDonald, The unfolding of the spectra of low energy galactic cosmic ray H and He nuclei as the Voyager 1 spacecraft exits the region of heliospheric modulation, *ArXiv e-prints*, 2013.

Wenzel, K. P., R. G. Marsden, D. E. Page, and E. J. Smith, The ULYSSES mission, *Astronomy and Astrophysics Supplement*, *92*, 207–219, 1992.

Whang, Y. C., and L. F. Burlaga, Anticipated Voyager crossing of the termination shock, *Geophysical Research Letters*, *27*, 1607–1610, 2000.

Wilcox, J. M., and N. F. Ness, Quasi-stationary corotating structure in the interplanetary medium, *Journal of Geophysical Research*, *70*, 5793–5805, 1965.

Williams, T., The influence of the wavy heliospheric neutral sheet on the modulation of cosmic rays (in Afrikaans), Ph.D. thesis, Potchefstroom University for CHE, South Africa, 1990.

Zank, G. P., Interaction of the solar wind with the local interstellar medium: A theoretical perspective, *Space Science Reviews*, *89*, 413–688, 1999.

Zhang, M., A markov stochastic process theory of cosmic-ray modulation, *Astrophysical Journal*, *513*, 409–420, 1999.

Zhao, L. L., G. Qin, M. Zhang, and B. Heber, Modulation of galactic cosmic rays during the unusual solar minimum between cycles 23 and 24, *Journal of Geophysical Research (Space Physics)*, *119*, 1493–1506, 2014.

Zurbuchen, T. H., A new view of the coupling of the Sun and the heliosphere, *Annual Review of Astronomy and Astrophysics*, *45*, 297–338, 2007.

Zurbuchen, T. H., N. A. Schwadron, and L. A. Fisk, Direct observational evidence for a heliospheric magnetic field with large excursions in latitude, *Journal of Geophysical Research*, *102*, 24175–24182, 1997.

Acknowledgements

It is my pleasure to thank the following persons and institutions for their support:

- Prof M.S. Potgieter, my supervisor, for his much needed guidance, and expertise throughout this study, as well as the care and attention to detail with which he has helped me to finish this work.
- The PAMELA-group, for giving me access to preliminary PAMELA data. In particular I would like to thank Drs M. Boezio, V. Di Felice and R. Munini for preparing all the PAMELA data used in this work, and for their assistance with data-related queries.
- Mr J. Gieseler, for supplying me with Ulysses data and for his help with data-related queries.
- Dr R.R. Nndanganeni, Mr J.L. Raath, Mr D. Bisschoff and Mr L. Prinsloo, for their time and assistance during the many insightful research discussions we had.
- Drs N.E. Engelbrecht and R.D. Strauss, for their advice during formal and informal research discussions.
- Mrs M.P. Sieberhagen, Mrs E. van Rooyen, and Mrs L. van Wyk, for their assistance and for handling all of my administrative matters.
- Mr M. Holleran and Mr C. Ackerman for their assistance with computer-related problems and queries.
- Mr I.D Davids, for his friendship, and for the privilege of having shared the office with him throughout my PhD.
- Mrs C. Vorster, for her help with the language editing of this thesis.
- The South African National Space Agency, the National Research Foundation and the Center for Space Research at the North-West University, for financial support throughout my studies.

A special thanks goes to:

- My wife, Jana, for her continual love, and for being by my side throughout this journey.
- My brother and friend, Jacques, as well as my parents, for their support during my studies and for the example that they set for me.
- My parents-in-law, for their support and encouragement.
- Above all, I would like to thank my Heavenly Father for giving me the opportunity to study and appreciate a small portion of the Universe we live in.

Etienne Eben Vos
Center for Space Research,
North-West University
October, 2016.